The Role of the *Leishmania mexicana* Amastigote Flagellum in Parasite-Host Interactions



A thesis submitted for the degree of Doctor of Philosophy
in the University of Oxford Trinity Term 2017

Jessica Valli
St Edmund Hall
Sir William Dunn School of Pathology

"It was the best of times, it was the *blurst* of times?"

- Charles Montgomery Burns

Abstract

Cilia and flagella are important organelles with roles in motility and signalling across eukaryotes. *Leishmania* species possess both a motile 9+2 flagellum and an immotile 9+0 flagellum in different life-cycle stages. While several roles have been defined for the motile promastigote flagellum, the importance of the amastigote flagellum has long eluded understanding, but recent evidence suggests a potential role for this organelle in parasite-host interactions.

In this thesis, serial block-face scanning electron microscopy and transmission electron tomography were used to build comprehensive high-resolution models of *Leishmania mexicana* amastigotes within parasitophorous vacuoles and to precisely define parasite-host connectivity. This provided previously unavailable three-dimensional insight into both parasite and host structures and allowed us to propose a model of amastigote positioning during vacuole maturation. Analysis of the connectivity between the amastigote flagellum and the PV membrane identified membranous extensions of the flagellar membrane as well as evidence suggestive of vesicular trafficking.

In pursuit of functional insight into the amastigote flagellum, we assessed null mutants of components of the BBSome trafficking complex, and of the kinetoplastid-specific trafficking protein, KHARON1, for their ability to infect and replicate within macrophages to determine whether a correctly populated flagellar membrane is required for survival within the intracellular environment. Intriguingly, while KHARON1-null amastigotes were unable to survive within macrophages and exhibited a failure of cytokinesis as well as a cell-shape defect, knockout of individual BBSome components did not significantly impair survival of intracellular amastigotes.

This thesis offers insight into the complexities of intracellular survival and provides evidence which ties in with the emerging field of flagellar vesicles as a delivery mechanism for virulence factors, and has thus contributed to the complex body of evidence towards finally defining the role of the *Leishmania* amastigote flagellum.

Acknowledgements

I would like to start by thanking my supervisor, Dr Eva Gluenz, for her support throughout my time in her lab. I honestly appreciated her advice, patience and encouragement through difficult experiments and exciting results alike.

I am also very grateful for all of the knowledge imparted by Professor Keith Gull and his post-docs: Samuel Dean, Helen Farr, Flavia Moreira-Leite, Jack Sunter, Vladimir Varga and Richard Wheeler, as well as Helen Banks. I feel very fortunate to have had the opportunity to learn from them and I am sure that my research has been the better for it.

I greatly enjoyed my collaboration with members of Scott Landfear's lab; Khoa Tran and Marco Sanchez were a pleasure to work with and helped to make my visit both scientifically successful and a lovely experience.

I owe my sanity to Laura Makin, Tom Beneke, Michael Fiebig, and Felix Castellanos; my fellow PhD researchers, and what's more, my friends. Through steep learning curves and long hours, it was always reassuring to know that they were there with me. I have to thank my family for always being proud of me and believing in me even when I had doubts. Last but not least, I want to thank Ross Madden, who made me believe that I could actually do this.

This work was funded by the Medical Research Council and the Edward Penley Abraham Trust.

Declaration

No portion of the work referred to in this thesis has been submitted in support of an application for another degree or qualification at this or any other university or institute of learning.

Table of Contents

1 Introduction 2
1.1 Eukaryotic Cilia and Flagella 2
1.1.1 Distinctions between eukaryotic cilia and flagella 2
1.1.2 Cytoskeletal ultrastructure of eukaryotic cilia 2
1.1.3 Ciliary function: motility 6
1.1.4 Ciliary function: sensing environmental stimuli 7
1.1.5 Trafficking of ciliary proteins 8
1.1.6 Evolution of eukaryotic cilia 10
1.1.7 Ciliopathies: the role of ciliary dysfunction in human disease 10
1.2 *Leishmania mexicana* 13
1.2.1 Leishmaniasis 13
1.2.2 The *Leishmania* life cycle 13
1.2.3 *Leishmania* ultrastructure 16
1.2.4 *Leishmania*-host interactions 19
1.2.5 *Leishmania mexicana* as a model organism for ciliary/flagellar research 20
1.3 Aims and Strategy 21

2 Materials and Methods 24
2.1 Trypanosomatid Culture 24
2.1.1 Cell lines and *in vitro* culture of promastigotes 24
2.1.2 *In vitro* differentiation and culture of axenic amastigotes 24
2.2 Transgenic Trypanosomatid Cell Lines 24
2.2.1 Fluorescent cell lines for vacuole progression studies 24
2.2.2 *L. mexicana* KHARON1 (KH1) knockout and add-back cell lines and *T.brucei* KHARON1 (KH1) RNAi cell lines 25
2.2.3 *L. mexicana* endogenously-tagged BBSome cell lines 25
2.2.4 *L. mexicana* BBSome knockout mutants 27
***2.3 Immunoblotting* 33**
2.4 Macrophage Infections 34
2.5 Light Microscopy 34
2.5.1 Imaging of mNeonGreen-tagged cells 34
2.5.2 Airyscan Imaging of Vacuole Progression 35
2.6 Electron Microscopy 35
2.6.1 Fixation of samples for electron microscopy 35
2.6.2 Transmission Electron Microscopy Sample Preparation and Imaging 36
2.6.3 Serial Block-Face Scanning Electron Microscopy (3View) Sample Preparation and Imaging 36
2.7 Flow Cytometry 37

3 Interaction of *L. mexicana* amastigotes with the parasitophorous vacuoles of host macrophages 40
3.1 Preface 40
3.2 Results 44
3.2.1 Optimisation of 3View sample preparation protocol 44
3.2.2 *L. mexicana* amastigotes are observed in three main orientations within parasitophorous vacuoles 50
3.2.3 Different vacuole types may represent steps in the progression of vacuole maturation 54
3.2.4 Amastigotes within tight vacuoles possess membranous flagellar extensions 56

3.2.5 Preliminary evidence of vesicular activity 61
3.3 Discussion 65

4 Characterisation of KHARON1 function; a cross-species comparison..... 70
4.1 Preface 70
4.2 Results 72
4.2.1 Knockout of KHARON1 does not affect *L. mexicana* promastigote cell body or flagellar morphology..... 72
4.2.2 ΔKHARON1 mutant amastigotes have typical flagellar axonemes but irregular flagellar tips..... 75
4.2.3 ΔKHARON1 mutant intracellular amastigotes are unusually round compared to wild type cells..... 78
4.2.4 RNAi knockdown of *kharon1* in *Trypanosoma brucei* causes flagellar and nuclear irregularities..... 81
4.3 Discussion 84

5 Characterisation of the *Leishmania mexicana* BBSome complex function..... 88
5.1 Preface 88
5.2 Results 91
5.2.1 *Leishmania mexicana* BBS proteins contain evolutionarily conserved functional domains 91
5.2.2 The BBSome complex localises to the base of the flagellum in promastigotes and axenically differentiated amastigotes, and the small GTPase BBS3 localises along the length of the flagellum in each lifecycle stage..... 94
5.2.3 Individual components of the BBSome are not essential for *in vitro* survival or for ciliogenesis in *Leishmania mexicana* promastigotes..... 96
5.2.4 Interdependence of BBSome subunits..... 99
5.2.5 Knockout of BBS3 causes mislocalisation of the *Leishmania mexicana* orthologue of calflagin..... 99
5.2.6 Knockout of BBS2 causes clumping of *Leishmania mexicana* promastigotes. 102
5.2.7 BBS2 is not required for successful differentiation of *L. mexicana* into axenic amastigotes..... 107
5.2.8 Individual components of the BBSome are not essential for the successful infection of murine bone marrow derived macrophages by *Leishmania mexicana* promastigotes or for their intracellular survival as amastigotes..... 109
5.3 Discussion 111

6 Conclusions and Outlook..... 116
6.1 Addressing thesis aims..... 116
6.2 A potential role for the amastigote flagellum in modulating PV formation? 116
6.3 Trafficking of flagellar membrane proteins..... 119
6.4 Specialisation of the amastigote posterior pole..... 120
6.5 Future Work..... 121
6.6 Concluding Remarks..... 122

7 References..... 123

8 Appendix 141
8.1 List of Supplementary Materials 141

List of Figures and Tables

1. Introduction

Figure 1.1. Ciliary and flagellar beats 3
Figure 1.2. Conserved ultrastructure of the 9+2 cilium 5
Figure 1.3. Conservation of cilia across eukaryotic groups suggests presence in Last Eukaryotic Common Ancestor 11
Figure 1.4. Endemicity of visceral and cutaneous leishmaniasis 14
Figure 1.5 The digenetic *Leishmania* life cycle 15
Figure 1.6. Ultrastructure of *Leishmania* promastigotes and amastigotes 17

2. Materials and Methods

Figure 2.1. CRISPR-Cas9 facilitated endogenous C-terminal tagging of *Leishmania mexicana* BBS proteins 26
Figure 2.2 CRISPR-Cas9 facilitated double knockout of of *Leishmania mexicana* BBS proteins in a single round 28
Figure 2.3. *Leishmania mexicana* BBS2 add-back 30
Figure 2.4. Double knockout of *Leishmania mexicana* BBS2 by classical homologous recombination 32
Table 2.1 Antibody dilutions for Western Blot Analysis 33

3. Interactions of *Leishmania mexicana* amastigotes with the parasitophorous vacuoles of host macrophages

Figure 3.1. Three-dimensional electron microscopy techniques 43
Figure 3.2. 3View imaging of TEM prepared or 3View prepared samples 47
Table 3.1. 3View sample preparation conditions tested for improving microtubule resolution 48
Figure 3.3. 3View sample preparation conditions tested for improving microtubule resolution 49
Table 3.2. Details of final 3View datasets 50
Figure 3.4. Different amastigote positions and parasitophorous vacuole shapes observed by 3View microscopy 51
Figure 3.5. Live cell imaging confirms the presence of previously-unobserved bulging parasitophorous vacuoles 53
Figure 3.6 3View data suggest that different vacuole types may represent steps in progression of vacuole maturation 55
Figure 3.7 Live vacuole progression imaging 57
Figure 3.8. Amastigotes within tight vacuoles possess membranous flagellar extensions 59
Figure 3.9. Flagellar membrane activity of intracellular amastigotes 60
Figure 3.10. Preliminary evidence of vesicular activity on flagellar and PV membranes 62
Figure 3.11. Further evidence of vesicular activity on flagellar and PV membranes 63
Figure 3.12. Live cell analysis of flagellum and PV membrane activity 64

4. Characterisation of KHARON1 function; a cross species comparison

Figure 4.1. KHARON1-null *Leishmania mexicana* promastigotes show comparable cell morphology to wild types 73
Figure 4.2. KHARON1-null *Leishmania mexicana* promastigotes show comparable flagellar morphology to wild types 74
Figure 4.3. KHARON1-null *Leishmania mexicana* intracellular amastigotes show comparable flagellar morphology to wild types..... 76
Figure 4.4. Atypical flagellar tips in KHARON1-null *Leishmania mexicana* amastigotes 77
Figure 4.5. KHARON1-null *Leishmania mexicana* intracellular amastigotes have a rounded cell morphology 79
Figure 4.6. KHARON1-null *Leishmania mexicana* intracellular amastigotes fail to undergo cytokinesis 80
Figure 4.7. Ultrastructural flagellar phenotypes of bloodstream form *Trypanosoma brucei* following RNAi against KHARON1 mRNA..... 82
Figure 4.8. Ultrastructural nuclear phenotypes of bloodstream form *T. brucei* following RNAi against KHARON1 mRNA 83

5. Characterisation of the *Leishmania mexicana* BBSome complex function

Table 5.1. Accession numbers of BBS genes in *Leishmania spp.* 92
Figure 5.1. Conserved InterPro domains in *Leishmania mexicana* BBS proteins 93
Figure 5.2. Localisation of BBS proteins in *Leishmania mexicana* 95
Figure 5.3. PCR confirmation of BBS gene knockout..... 97
Figure 5.4. *Leishmania mexicana* ΔBBS clones show no significant viability defects. ... 98
Figure 5.5. Interdependence of BBS proteins in *Leishmania mexicana* 100
Figure 5.6. Knockout of BBS3 causes partial mislocalisation of a putative calflagin but does not affect localisation of SMP1 or ARL-3A..... 101
Figure 5.7. Double knockout of BBS2 by classical homologous recombination 103
Figure 5.8. Clumping of *Leishmania mexicana* promastigotes occurs only in absence of both BBS2 alleles 105
Figure 5.9 ΔBBS2 promastigotes exhibit a striking clumping phenotype, which is not rescued by expression of BBS2 from the β-tubulin locus 106
Figure 5.10 Clumps formed by BBS2 knockouts incorporate labelled cells in co-culture 108
Figure 5.11 ΔBBS2 cells complete axenic differentiation but show changes in stage-specific markers at an accelerated rate 110
Figure 5.12. Knockout of individual BBS proteins does not impair ability of *Leishmania mexicana* to infect or survive within macrophages..... 112

Abbreviations

Δ	Knockout
[ ]	Add-back
9v	**9** **v**ariable
AB	**A**dd-**b**ack
AXA	**Ax**enic **a**mastigote
BBS	**B**ardet-**B**iedl **S**yndrome
BMDM	**B**one **m**arrow-**d**erived **m**acrophage
CRISPR	**C**lustered **r**egularly **i**nterspaced **s**hort **p**alindromic **r**epeats
FIB-SEM	**F**ocused **i**on **b**eam **s**canning **e**lectron **m**icroscopy
GP	**G**lyco**p**rotein
HASP	**H**ydrophilic **a**cylated **s**urface **p**rotein
IFT	**I**ntra**f**lagellar **t**ransport
KH1	**KH**ARON**1**
KO	**K**nock**o**ut
EM	**E**lectron **m**icroscopy
LAMP	**L**ysosome **a**ssociated **m**embrane **p**rotein
LPG	**L**ipo**p**hospho**g**lycan
MOI	**M**ultiplicity **o**f **i**nfection
ORF	**O**pen **r**eading **f**rame
PFR	**P**ara**f**lagellar **r**od
PRO	**Pro**mastigote
PV	**P**arasitophorous **v**acuole
RNAi	**R**ibo**n**ucleic **a**cid **i**nterference
SBF-SEM	**S**erial **b**lock-**f**ace **s**canning **e**lectron **m**icroscopy
SEM	**S**canning **e**lectron **m**icroscopy
sgRNA	**S**ingle **g**uide **r**ibo**n**ucleic **a**cid
SMP	**S**mall **m**yristoylated **p**rotein
TEM	**T**ransmission **e**lectron **m**icroscopy
UTR	**U**n**t**ranslated **r**egion
WT	**W**ild **t**ype

CHAPTER 1

INTRODUCTION

1 Introduction

1.1 Eukaryotic Cilia and Flagella

1.1.1 Distinctions between eukaryotic cilia and flagella

Cilia and flagella are specialised centriole-derived organelles that project from the surfaces of eukaryotic cells. The two terms are often used interchangeably, and the component structures are, in fact, identical. There are, however, several distinctions commonly applied in determining which term to use. Historically, the term flagella has been used to describe long protrusions present in only one or very few copies (e.g. the single flagellum of spermatozoa), while cilia has been used to describe shorter protrusions, present in larger numbers (e.g. cilia involved in mucociliary clearance in respiratory pathways) (Brokaw, 1972). Distinct ciliary and flagellar waveforms have been defined, describing the movements produced by these organelles. Ciliary waveforms are characterised by an asymmetric beat starting with an effective stroke, in which a bend is formed at the base of the cilium resulting in the movement of surrounding fluid parallel to the cell surface in the direction of the stroke (**Fig 1.1 A**) (Gray, 1930). This is then followed by a recovery stroke, in which the bend propagates up the cilium, allowing it to return to its initial position (**Fig 1.1 A**) (Gray, 1930). Flagellar beats, on the other hand, consist of nearly symmetrical beats, propagating from one end of the flagellum to the other, resulting in a movement of surrounding fluid parallel to the flagellum length (**Fig 1.1 B**) (Brokaw, 1965; Gray, 1955). As is often the case in describing biological systems, this classification into two beat types represents an over-simplification, and in reality, there is a large diversity of beat waveforms in terms of amplitude and frequency. Moreover, certain organisms, including several trypanosomatid parasites, exhibit both ciliary and flagellar beats (Gadelha et al., 2007; Holwill, 1965), while cilia of the mammalian embryonic node display an altogether different, helical movement in which they twist about their base while remaining rigid along their length, causing counter-clockwise rotational movement of the surrounding fluid (**Fig 1.1 C**) (Brokaw, 2005). For the purposes of this thesis, the term cilia will be used when referring to structures conserved across eukaryotes, while flagella will be used specifically for describing these in the kinetoplastid protozoa examined herein.

1.1.2 Cytoskeletal ultrastructure of eukaryotic cilia

All eukaryotic cilia contain a cytoskeletal axoneme comprised of microtubule doublets arranged symmetrically around a central axis. The outer microtubule doublets consist of pairs of microtubules formed of α/β-tubulin heterodimers, with each pair comprising a complete A-tubule containing 13

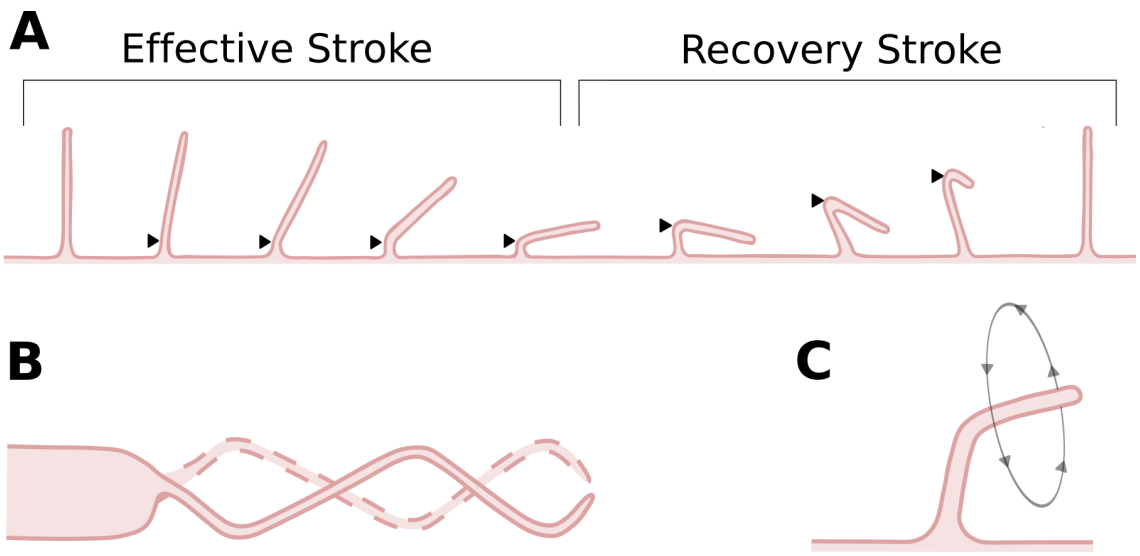


Figure 1.1. Ciliary and flagellar beats. (A) Ciliary beat; effective stroke moves fluid in direction of stroke, and recovery stroke returns cilium to starting position. Arrow = point of ciliary bend. **(B)** Flagellar beat; symmetric beats move fluid parallel to flagellum. **(C)** Nodal ciliary beat; helical movement propels surrounding fluid in counter-clockwise direction.

parallel protofilaments, and an incomplete B-tubule containing only 10 (Nicastro et al., 2011; Ringo, 1967a; Sui and Downing, 2006; Warner and Satir, 1973). Cilia are classified by the number of symmetrical outer microtubule doublets as well as the presence or absence of a central pair of single microtubules. The most commonly occurring organisations are 9+2 and 9+0 axonemes, which contain nine outer microtubule doublets, and either two central microtubules or no central pair, respectively (Porter, 1956). Traditionally, the 9+2 classification was considered to represent motile cilia, and the 9+0 classification to represent non-motile cilia (Porter, 1956). However, recent evidence has shown that these lines are somewhat blurred, as mammalian 9+2 olfactory cilia are immotile, while embryonic 9+0 nodal cilia produce the helical movement described above (Brokaw, 2005; Lidow and Menco, 1984; Menco, 1984). While a nine-fold symmetry is largely conserved throughout eukaryotes, there are a number of exceptions. The simplest axoneme discovered to date is the 3+0 arrangement found in the male gamete of the protozoan parasite, *Diplauxis hatti* (Prensier et al., 1980). At the other end of the scale, 12+0 and 14+0 axonemes have been documented in the sperm of several arthropod species (Baccetti et al., 1973). Similarly, variations also exist in in the number of central microtubules, outside of the standard pair or complete absence, with 9+1 and 9+3 axonemes having been observed in the sperm of flatworms and arthropods, respectively (Dallai et al., 1995; Henley et al., 1969). To date, the only known example of a vertebrate deviation from the standard 9+2 or 9+0 axoneme structures is in the notochordal plate of the rabbit embryo, where the cilia exhibit a combination of 9+0, 9+2 and 9+4 axonemes (Feistel and Blum, 2006).

In addition to the outer microtubule doublets and central pair, there are a number of other highly conserved structures that make up the ciliary axoneme. Cilia are templated from the cell's mature centriole, which docks at the plasma membrane to produce a nucleation site for ciliogenesis (Sorokin, 1962, 1968). Once in this context, the centriole is referred to as the basal body, and in most cilia consists of nine symmetrically-arranged triplet microtubules (Gibbons and Grimstone, 1960; Sorokin, 1968). As is the case in the axoneme proper, only the A tubule is complete and contains 13 protofilaments; in the basal body both the B and C tubules are incomplete and contain only 10 protofilaments (Nicastro et al., 2011; Ringo, 1967a; Sui and Downing, 2006; Warner and Satir, 1973; Wilsman and Farnum, 1983). Axonemal decorations known as transition fibres emerge from between the A- and B-tubules at the distal end of the microtubule triplets, and this is shortly followed by the end of the C-tubules (Gibbons and Grimstone, 1960). The A- and B-tubules then extend into a region known as the transition zone, which is bounded at its proximal and distal ends by the terminal and basal plates, respectively (Dute and Kung, 1978; Gilula and Satir, 1972; Wolfe, 1970). The transition zone is characterised by the presence of microtubule decorations known as Y-shaped linkers, which tether the outer doublets to the ciliary membrane and to a structure known as the ciliary necklace (Anderson, 1974; Gilula and Satir, 1972). Together, the transition fibres and the transition zone make up the ciliary gate, which plays an important role in selective trafficking to the cilium (Williams et al., 2011) (see section 1.1.5).

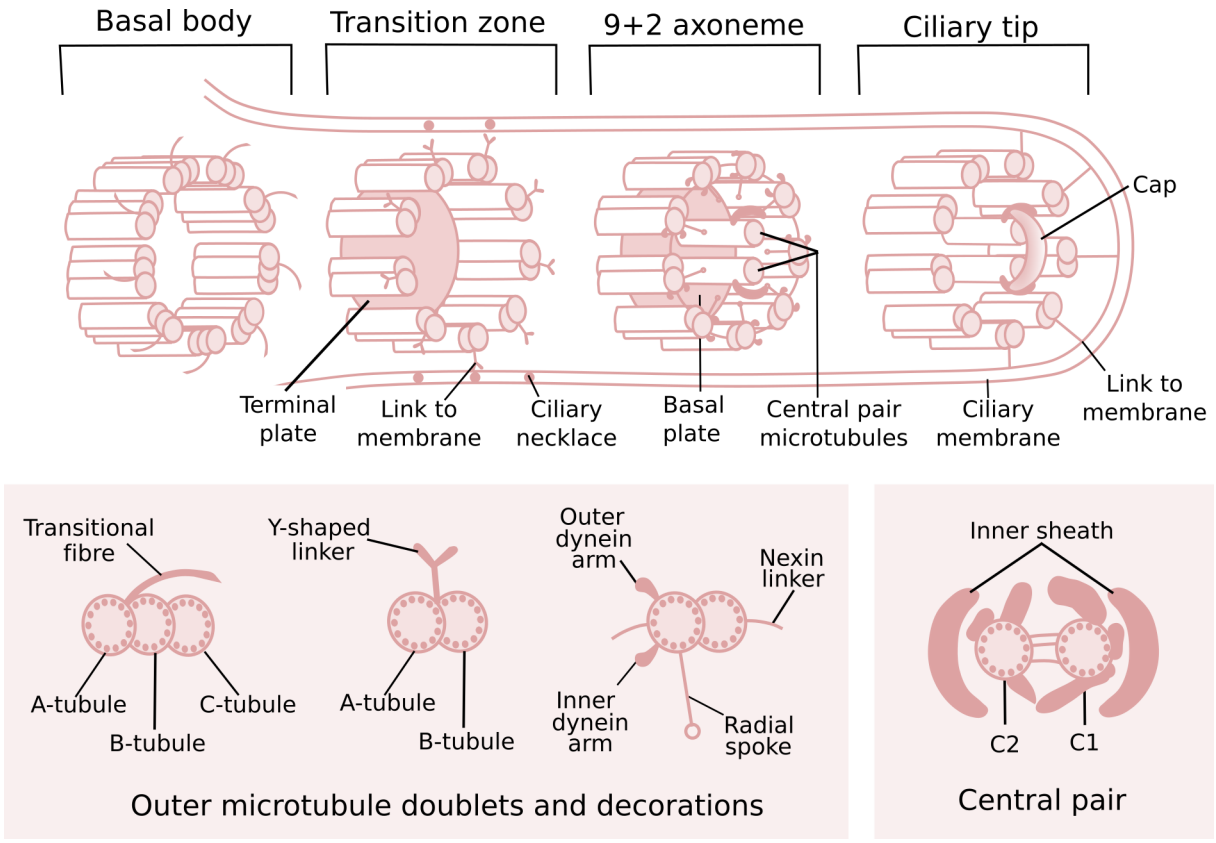


Figure 1.2. Conserved ultrastructure of the 9+2 cilium. Basal body: outer microtubule triplets (A-tubule: 13 protofilaments, B- and C- tubules: 10 protofilaments); transitional fibres at distal end. Transition zone: outer microtubule doublets (A-tubule: 13 protofilaments, B-tubules: 10 protofilaments); Y-shaped linkers tethered to ciliary membrane. 9+2 axoneme: outer microtubule doublets; inner and outer dynein arms, nexin links and radial spokes; central pair (C1 and C2 with decorations) and inner sheath. Ciliary tip: outer microtubule doublets linked to ciliary membrane, and central pair capping structure. Cross section views from distal end.

In 9+2 cilia, the central pair of singlet microtubules nucleates at the end of the transition zone, defining the start of the cilium proper (Ringo, 1967b). Within this part of the cilium are several microtubule decorations which are regularly spaced along the axoneme and which work in tandem to coordinate ciliary function. Dynein motor protein complexes known as the inner and outer dynein arms are linked to the A-tubule of each outer doublet, and have ATPase activity involved in ciliary bending (Afzelius, 1959; Gibbons and Rowe, 1965) (see section 1.1.3). Adjacent outer doublets are connected by nexin links to one another, and by radial spokes to a sheath surrounding the central pair (Afzelius, 1959; Gibbons, 1965; Warner and Satir, 1974). Each central pair microtubule, termed C1 and C2, additionally has its own accessory proteins, which interact with the radial spokes (Adams et al., 1981; Dutcher et al., 1984; Smith and Lefebvre, 1997). The ciliary axoneme ends in a capping structure that links the outer doublets and central pair to the ciliary membrane (Dentler and Rosenbaum, 1977; Sale and Satir, 1977). See **Figure 1.2** for an overview of the 9+2 ciliary structure. The conserved structures of 9+0 cilia have been less well characterised, save for the defining lack of the central pair, the additional absence of the dynein arms, and a frequent collapse of the nine-fold symmetrical structure of the outer doublets towards the distal end (Allen, 1965; Barnes, 1961; Dahl, 1963; Sorokin, 1962).

1.1.3 Ciliary function: motility

Ciliary motility is an ATP-dependent process (Hoffmann-Berling, 1955), which uses conserved mechanisms in all motile cilia, regardless of whether they exhibit a ciliary or flagellar beat. The ATPase activity that generates the force required for motility is carried out by the dynein arms, which are located on the A-tubule of each microtubule outer doublet, and interact with the B-tubule of the neighbouring doublet to produce sliding of doublets relative to one another (Gibbons and Rowe, 1965; Satir, 1965; Summers and Gibbons, 1971). As the microtubule doublets remain anchored at the basal body, this inter-doublet sliding results in bending of the cilium. Regulation of this bending to produce beats capable of forward propulsion or generation of extracellular flow is mediated by other axonemal structures. The radial spokes appear to be central to this process, through detachment and reattachment to the central sheath (Warner and Satir, 1974), and are proposed to be important for translation of symmetric bends into asymmetric waveforms (Brokaw et al., 1982). Evidence has shown that the radial spokes and central complex are, however, dispensable for high-frequency oscillating beats, consistent with the existence of motile 9+0 cilia (Yagi and Kamiya, 2000). The nexin links, which form the dynein regulatory complex, are also thought to play a crucial role in regulating dynein activity (Heuser et al., 2009; Oda et al., 2013; Wirschell et al., 2013). Motile cilia are used for cell propulsion throughout eukaryotic groups from protozoa to mammalian sperm, but ciliary motility has also evolved to carry out a range of different functions. In many higher eukaryotes, including mammals, motile cilia are crucial for functions such as mucociliary clearance in the respiratory tract and in establishment of right-left asymmetry during development (Nonaka et al., 1998; Wanner et al., 1996).

1.1.4 Ciliary function: sensing environmental stimuli

Cilia have now been shown to have diverse sensory and signalling functions, including mechanoreception, chemoreception, photoreception and extracellular signalling. These functions are often, though certainly not always, performed by 9+0 cilia, which in mammalian cells are referred to as primary cilia (Sorokin, 1968). Primary cilia are present on nearly all mammalian cell types and are dynamically regulated during the cell cycle; they are generally present in G0/G1, are resorbed before mitotic entry, and are re-assembled after cytokinesis (Jensen et al., 1987; Rieder et al., 1979; Sorokin, 1968).

The earliest recognition of the sensory roles of cilia came from evidence of photoreception by rod and cone receptor cells in the mammalian retina. These cells possess a specialised structure derived from 9+0 cilia, referred to as the outer segment (Robertis, 1956). Rhodopsin receptors localised within the outer segments of rod cells respond to photons of light by activating the G-protein transducin, which in turn activates a cyclic GMP phosphodiesterase, increasing hydrolysis of the secondary messenger, cyclic GMP (cGMP) (Katsanis et al., 2000). The decreased cGMP levels trigger the closing of cGMP-gated cation channels, resulting in hyperpolarisation of the cell and subsequent inhibition of synaptic transmission (Fesenko et al., 1985; Haynes and Yau, 1985). Similar signalling cascades have been found to be involved in mammalian olfaction, where the interaction of odorants with GPCRs in the membrane of olfactory cilia results in increased levels of cyclic AMP, which in turn triggers the opening of cyclic nucleotide-gated ion channels to produce depolarisation of the cell (Boekhoff et al., 1990; Nakamura and Gold, 1987).

Mechano-sensory roles of cilia have also been elucidated in detail, most prominently in the case of detection of fluid flow by kidney primary cilia. Primary cilia are present on the apical surface of epithelial cells that line the kidney nephron, extending into the lumen of the renal tubules and ducts (Andrews and Porter, 1974). These cilia bend in response to fluid flow (Roth et al., 1988; Schwartz et al., 1997), which initiates an influx of extracellular Ca^{2+}, subsequently inducing release of intracellular calcium stores (Praetorius and Spring, 2001). Mechano-reception by cilia has since been described in several other systems including osteogenic responses of bone cells to fluid flow (Malone et al., 2007) and reception of sound vibrations by *Drosophila* antennae (Gong et al., 2004). Primary cilia have also been implicated in the modulation of Sonic Hedgehog (Shh) (Huangfu and Anderson, 2006) and Wnt (Simons et al., 2005) signalling pathways in mammalian cells, which are central to processes such as embryonic cell differentiation and cell proliferation. Primary cilia are now generally considered to act as cell "antennae"; consistent with this is the presence of numerous tissue-specific receptors localised to ciliary membranes, including somatostatin receptors and serotonin receptors in neuronal cells (Brailov et al., 2000; Händel et al., 1999).

1.1.5 Trafficking of ciliary proteins

Proteomic studies of *Chlamydomonas* and *Trypanosoma* flagella and mammalian cilia have shown that cilia are composed of hundreds of different proteins (Broadhead et al., 2006; Gherman et al., 2006; Ishikawa et al., 2012; Pazour et al., 2005). However, no protein synthesis occurs within the flagellum, meaning that ciliary components are produced within the main cell compartment and must then translocate to the cilium. Although the ciliary membrane is continuous with the plasma membrane, and the ciliary compartment equivalent to the cell cytosol, protein compositions differ greatly between ciliary compartments and the rest of the cell (Hu et al., 2010; Tyler et al., 2009). This suggests that mechanisms exist to mediate selective targeting and prevent random diffusion of macromolecules into this organelle (recently reviewed in Stephen et al., 2017).

The transition fibres at the distal end of the basal body, along with the transition zone have been proposed to act as a "ciliary gate" to prevent the random diffusion of both membrane proteins and large soluble proteins (Garcia-Gonzalo and Reiter, 2012; Nachury et al., 2010). For membrane proteins, a select few proteins, such as Smoothened, have been observed diffusing laterally from the plasma membrane to the ciliary membrane (Milenkovic et al., 2009). However, for the vast majority of ciliary proteins, this does not appear to be an available entry route. Indeed, experiments using fluorescence recovery after photobleaching have shown that several plasma membrane and ciliary membrane proteins, while mobile, do not travel across the boundary between these two compartments (Hu et al., 2010). Similarly, microinjection of mammalian cells with fluorescent dextran molecules of various sizes has suggested that the transition zone represents a size-exclusion barrier, limiting the diffusion of soluble proteins over 40kDa in size (Kee et al., 2012). This "ciliary gate" structure is thought to resemble the nuclear pore, and several nuclear pore components have, in fact, been localised to the ciliary base (Kee et al., 2012). Larger proteins must therefore be actively transported into the cilium.

With very few exceptions, trafficking of proteins in all eukaryotic cilia during ciliogenesis and for ciliary function is mediated at least in part by a process known as Intraflagellar Transport (IFT), which was first detected in the unicellular green alga *Chlamydomonas reinhardtii* (Kozminski et al., 1993). During ciliogenesis, axonemes are assembled by addition of components at the distal end (Binder et al., 1975; Johnson and Rosenbaum, 1992; Rosenbaum and Child, 1967; Witman, 1975); pre-assembled protein complexes and axonemal components are therefore loaded onto the IFT machinery for trafficking to the ciliary tip. Inner dynein arm components in *Chlamydomonas reinhardtii* were the first identified IFT cargo (Piperno et al., 1996), but many cargoes have since been identified, including tubulins and ciliary turnover products (recently reviewed in Bhogaraju et al., 2013 and Lechtreck, 2015). IFT components are currently known to comprise 20 proteins, which organise into two subcomplexes: IFT-A and IFT-B (Bhogaraju et al., 2013; Cole et al., 1998; Piperno and Mead, 1997). The IFT-B subcomplex is thought to be the main mediator of anterograde transport from the base of the cilium to the tip, and transport in

this direction is driven by heterotrimeric kinesin-II motors (Cole et al., 1998; Kozminski et al., 1995). The IFT-A subcomplex, on the other hand, is thought to mainly function in returning IFT-B to the ciliary base by retrograde transport, which is driven by cytoplasmic dyneins (Pazour et al., 1999; Porter et al., 1999). However, there is some evidence that IFT-A may be required for anterograde transport of certain ciliary membrane proteins such as Smoothened and a subset of ciliary G-protein coupled receptors (Liem et al., 2012; Mukhopadhyay et al., 2010), and that IFT-B components are involved in transporting the BBSome (see Chapter 5) out of cilia (Eguether et al., 2014; Liew et al., 2014), suggesting that both IFT sub-complexes participate in both ciliary import and export.

While the mechanisms involved in IFT and the role this plays in actively transporting proteins into cilia have been well-defined, there remains a lack of clarity when it comes to mechanisms of selectively targeting proteins for transport to the cilium. Despite the wealth of research performed on the subject in recent years, a conserved sequence for targeting proteins to the primary cilium remains to be identified. Until recently, only two ciliary targeting sequences had been identified: the VxPx motif found in rhodopsin (Deretic et al., 2005), polycystin-2 in kidney tubule epithelial cells (Geng et al., 2006) and olfactory cyclic-nucleotide-gated channel B1 (Jenkins et al., 2006), and the Ax(S/A)xQ motif found in the somatostatin receptor SSTR3 (Berbari et al., 2008). In recent years, however, additional targeting sequences have been recognised, including an M-G-XX-X-S/T myristoylation sequence in nephronophthisis 3 (NPHP3) in renal epithelial cells, a FDRELYL motif in inositol polyphosphate-5-phosphatase E (INPP5E), which has been linked to the ciliopathy Joubert's syndrome (Humbert et al., 2012; Nakata et al., 2012), an FK/FR motif, found in the transmembrane protein Smoothened (Smo) and in rhodopsin (Deretic and Wang, 2012; Lodowski et al., 2013), and an NPM motif identified in the flagellar glucose transporter LmxGT1 in *Leishmania mexicana* (Tran et al., 2012). Several lipid modifications have also been found to promote ciliary membrane localisation, including N-myristoylation of NPHP3 (Humbert et al., 2012; Nakata et al., 2012) and dual acylation in trypanosomatid ciliary membrane proteins including the *Leishmania spp*. small myristoylated protein 1 (SMP-1) and the *T. cruzi* flagellar calcium binding protein (FCaBP), which contain both myristoylation and palmitoylation sites and are targeted to the flagellar membrane (Godsel and Engman, 1999; Maric et al., 2011; Tull et al., 2012).

Current understanding of ciliary targeting is further complicated by the presence of adaptor proteins that mediate the interactions of cargo with the IFT machinery, to allow entry to the cilium (Emmer et al., 2010). One such adaptor is the BBSome complex, which functions as a membrane coat complex (see section 5.1 for further detail) (Jin et al., 2010). Different targeting sequences may therefore have co-evolved with different adaptor proteins.

1.1.6 Evolution of eukaryotic cilia

Cilia are found in eukaryotes ranging from protists to mammals, with primary cilia present on the apical surfaces of nearly all non-proliferating cells in vertebrates. The nearly-ubiquitous presence of cilia across eukaryotes and the degree of conservation of the characteristic structures have led to the hypothesis that cilia were present in the last eukaryotic common ancestor (LECA), and that several evolutionarily-independent losses resulted in the wide-ranging eukaryotic organisms lacking cilia (e.g. yeasts, and several plants and amoebozoa; **Fig 1.3**) (Carvalho-Santos et al., 2010; Cavalier-Smith, 2002; Hodges et al., 2010). Since their discovery, several mechanisms have been proposed for the appearance of cilia in the LECA. The principal hypotheses that have gained support are that they arose: 1) through endosymbiosis between a spirochete and an archaebacterial host cell (Dolan et al., 2002; Sagan, 1967), 2) through viral infection of a host cell with a self-assembling RNA virus exhibiting a capsid with nine-fold symmetry which would form the basis of the centriolar cartwheel (Satir et al., 2007), or 3) autogenously by duplication and divergence of pre-existing microtubule organising centre components (Cavalier-Smith, 1978; Mitchell, 2004; Pickett-Heaps, 1974). There is little evidence in support of the two former hypotheses, as no bacterial, archaeal or viral orthologues have been identified for conserved regions of centriolar components (Carvalho-Santos et al., 2010; Jékely and Arendt, 2006). Moreover, many of the components of centrioles and cilia, including the tubulins, dynein motors and IFT particles represent paralogues of cytosolic proteins, supporting the hypothesis that cilia could have evolved by duplication of existing structures (Dutcher, 2003; Jékely and Arendt, 2006; Wickstead and Gull, 2007).

1.1.7 Ciliopathies: the role of ciliary dysfunction in human disease

Ciliary dysfunction represents the underlying cause of many heritable human diseases, known collectively as ciliopathies. The term ciliopathy was coined in 1984 to describe aberrant axonemal structures in children with recurrent respiratory tract infections (Cornillie et al., 1984). However, ciliary dysfunction was first recognised as a cause of human disease in 1976, when a link was drawn between male infertility and chronic respiratory conditions caused by immotile cilia (Afzelius, 1976); a condition now known as Primary Ciliary Dyskinesia (PCD) (Rossman et al., 1981). Numerous ciliopathies have since been characterised, including Polycystic Kidney Disease (PKD), Bardet-Biedl Syndrome (BBS), Joubert Syndrome (JBTS), Meckel-Gruber Syndrome (MKS) and Nephronophthisis (NPHP) (recently reviewed in Reiter and Leroux, 2017). Most known ciliopathies vary in severity across cases, and show extensive pleiotropism, as one might expect given the range of ciliary functions throughout the human body. However, there are several types of defects that are common to many of these disorders.

Perhaps the most well-characterised pathogenic mechanisms in ciliary dysfunction are those underlying the reproductive defects resulting from immotile sperm amongst men with PCD (Munro et al., 1994). However, the underlying ultrastructural defects vary significantly between cases, with sperm

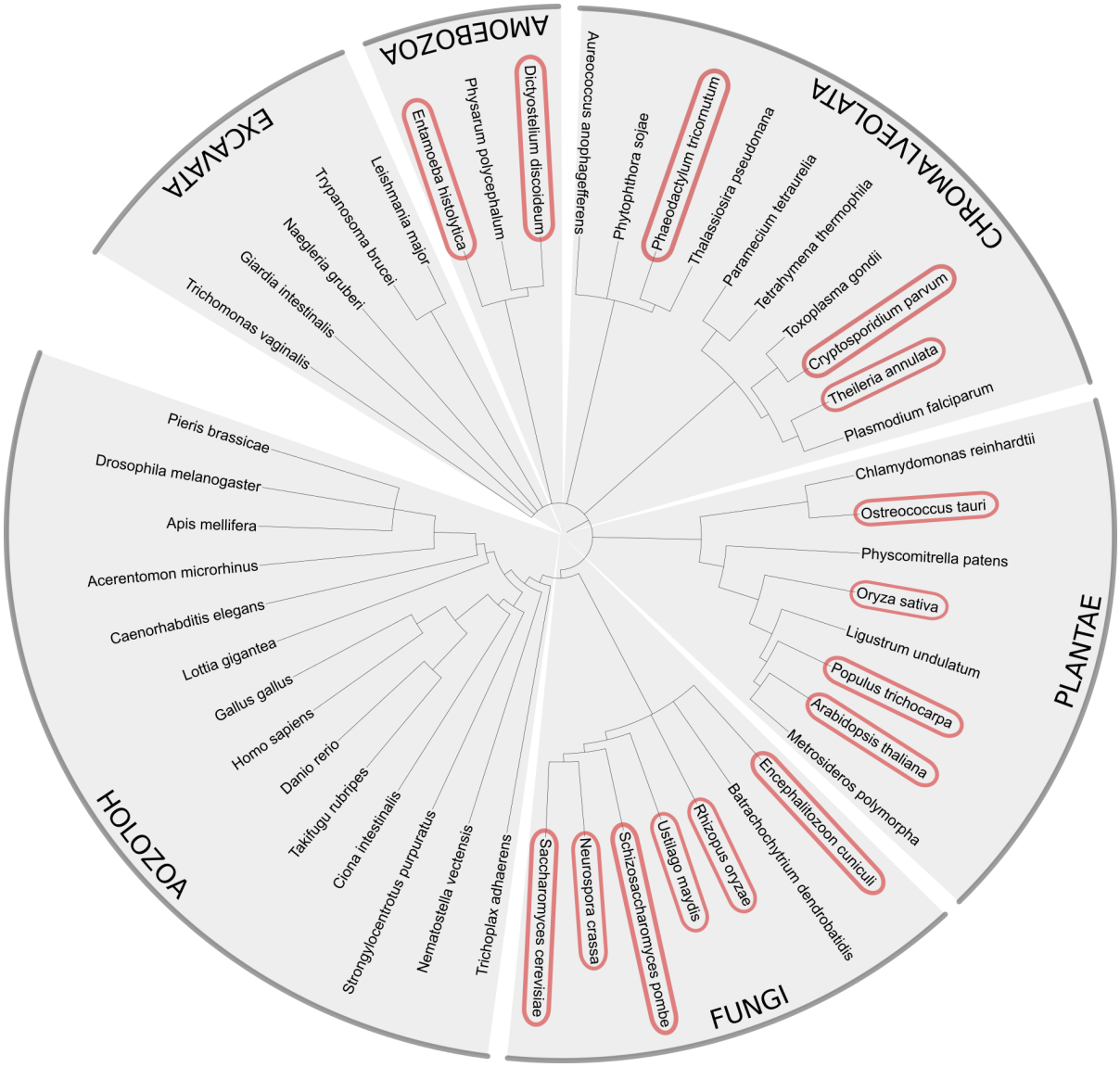


Figure 1.3. Conservation of cilia across eukaryotic groups suggests presence in the Last Eukaryotic Common Ancestor. Cilia are present in organisms within every major eukaryotic group, but absence of cilia in subsets of Fungi, Plantae, Chromalveolata and Amoebozoa groups (red circled) suggests several evolutionarily independent losses. After **(Carvalho-Santos et al., 2010; Hodges et al., 2010).** Phylogenetic tree produced using Interactive Tree of Life **(Letunic and Bork, 2016)**.

exhibiting 9+0 axonemes, a lack of inner and/or outer dynein arms, or abnormal numbers of outer microtubule doublets (Afzelius, 1976; Neugebauer et al., 1990; Pedersen and Rebbe, 1975; Yokota et al., 1993). The role of ciliary dysfunction in female reproduction remains unclear. While women with PCD have been shown to have immotile endometrial cilia, it is unclear how important this is for transport of the ovum along the fallopian tubes (Jean et al., 1979; McComb et al., 1986; Pedersen, 1983). Reproductive defects in other ciliopathies, such as BBS and Alström Syndrome, usually take the form of hypogonadism, but the underlying molecular defects involved remain unclear (Joy et al., 2007; Mozaffarian et al., 1979; Toledo et al., 1977). The axonemal defects associated with sperm immotility in PCD can likewise produce respiratory defects through impaired clearance of mucus from airways. The axonemal defects discussed above can result in either completely immotile cilia, or in disruption of the ciliary beat pattern (Chilvers et al., 2003). As the cilia in the respiratory pathway depend on highly regulated synchronised beating to produce metachronic waves (Katsanis et al., 2000), the lack of coordinated beating resulting from these defects results in critically-impaired mucociliary clearance (Chilvers et al., 2003). The inability to clear mucus from the airways of PCD patients typically results in conditions such as sinusitis or chronic bronchitis, affecting both the upper and lower respiratory tracts (Lucas and Leigh, 2014). Respiratory defects can also result from non-motile ciliary dysfunction. For example, mutations of the transition zone protein meckelin/TMEM67 (transmembrane protein 67), which represent the most common MKS-causing mutations, are associated with pulmonary hypoplasia (Abdelhamed et al., 2013). TMEM67 has been identified as a receptor in Wnt signalling pathways, and evidence suggests that this protein is essential for correct pulmonary morphogenesis during development (Abdelhamed et al., 2015).

The most prevalent clinical manifestations across ciliopathies are cystic disorders of the kidneys. Identification of underlying mutations have begun to provide insight into potential pathogenic mechanisms that contribute to cystogenesis in these diseases. PKD, for example, is most commonly caused by mutations in the genes PKD1 and PKD2, encoding the ciliary proteins polycystin 1 and 2 (Hughes et al., 1995; Mochizuki et al., 1996). Polycystin 1 and 2 are involved in mechanosensation of laminar fluid flow, regulating calcium entry into primary cilia in the kidney tubule with downstream effects on several signalling pathways (Nauli et al., 2003; Saigusa and Bell, 2015). siRNA knockdown of the mouse orthologue of PKD2 has been shown to completely abolish flow-dependent calcium-entry into kidney primary cilia (Jin et al., 2014). The low intracellular calcium levels allow elevated levels of cyclic AMP to over-activate signalling pathways involved in cell proliferation and fluid secretion, resulting in the formation of cysts (Yamaguchi et al., 2004). Given the widespread functions of cilia throughout the human body, both during development and in adult life, and the range of mutations that can impair their activity, it is clear that research into cilia and ciliopathies remains both relevant and necessary.

1.2 *Leishmania mexicana*

1.2.1 Leishmaniasis

The term leishmaniasis describes a spectrum of diseases caused by protozoan parasites of the *Leishmania* genus, of which there are over 20 human-infective species. The disease comprises three main forms: cutaneous, mucocutaneous, and visceral leishmaniasis (World Health Organization, 2017). Cutaneous leishmaniasis (e.g. *L. major, L. mexicana, L. tropica*) represents the most common form of the disease and causes skin lesions which are often self-healing but can leave permanent scars or disabilities (World Health Organization, 2017). Mucocutaneous leishmaniasis (e.g. *L. braziliensis*) involves destruction of mucous membranes within the nose, mouth and throat (World Health Organization, 2017). Finally, visceral leishmaniasis (e.g. *L. donovani, L. infantum*) represents the most severe form of the disease, infecting the liver and spleen, and is fatal if left untreated in over 95% of cases (World Health Organization, 2017). Leishmaniasis is endemic in countries across the Americas, the Mediterranean basin, the Middle East, Central Asia, and Northern Africa (**Fig 1.4**) (World Health Organisation, 2016a; World Health Organization, 2016b). Incidence of the disease is highly correlated with risk factors including socioeconomic conditions; particularly poor sanitary conditions and malnutrition (Desjeux, 2001). However, increasing population mobility and climate change have to led to an increase in cases in more affluent regions and an emergence of the disease in Europe (González et al., 2010; Muccio et al., 2015; Ready, 2010). Estimates suggest that each year up to a million new cases of leishmaniasis emerge, and up to 30, 000 deaths result from the disease (World Health Organization, 2017). Several treatments for leishmaniasis exist, including pentavalent antimonials, which have been pharmaceutically available since the 1940s, and more recently developed drugs such as amphotericin B, miltefosine and pentamidine (Cardoso et al., 2014). However, the effectiveness of these treatments varies depending on the *Leishmania* species, with some species displaying reduced sensitivity (Croft, 2001). Moreover, these treatments can be highly toxic with adverse side-effects and are expensive, which given the socioeconomic conditions of the areas with the highest incidence of disease, means that they are often inaccessible to those in need (reviewed in Freitas-Junior et al., 2012; Singh et al., 2012). These shortcomings, combined with the emergence of resistance to several treatments, mean that the development of new anti-leishmanial drugs remains essential, and cell biology research uncovering potential targets is thus invaluable.

1.2.2 The *Leishmania* life cycle

The lifecycle of *Leishmania* species is digenetic, progressing through both sandfly and mammalian hosts. The parasites adopt specifically-adapted morphologies and metabolic profiles to suit the specific environment within each host. The females of over 90 species of sandfly of the family *Phlebotominae* are

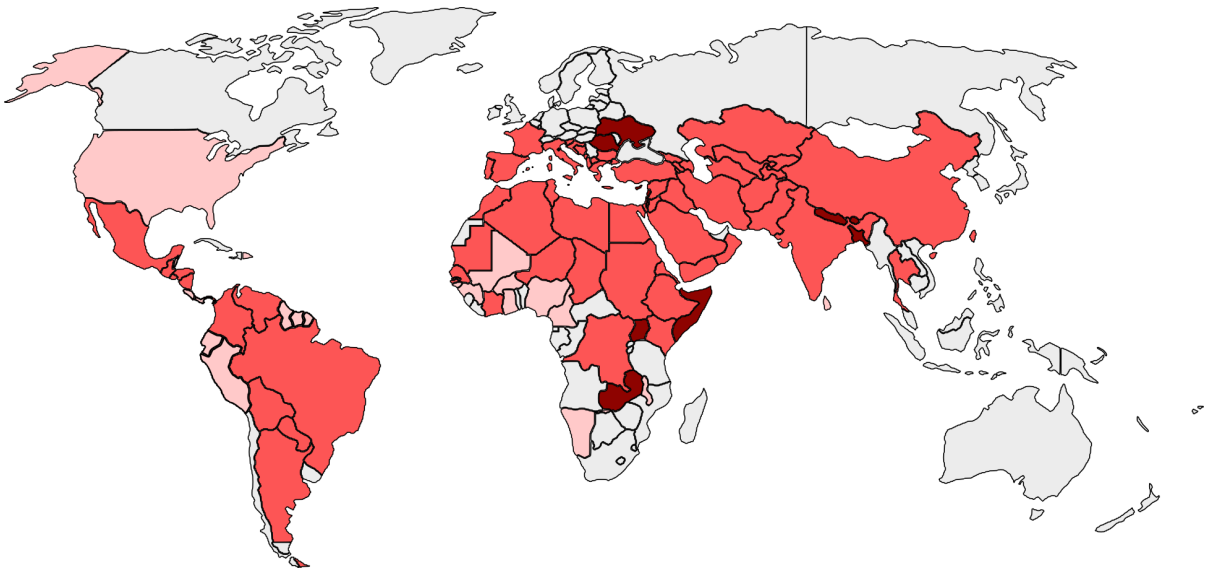


Figure 1.4. Endemicity of visceral and cutaneous leishmaniasis. Visceral leishmaniasis. Visceral and cutaneous leishmaniasis. Cutaneous leishmaniasis. After **(World Health Organisation, 2016a; World Health Organization, 2016b).**

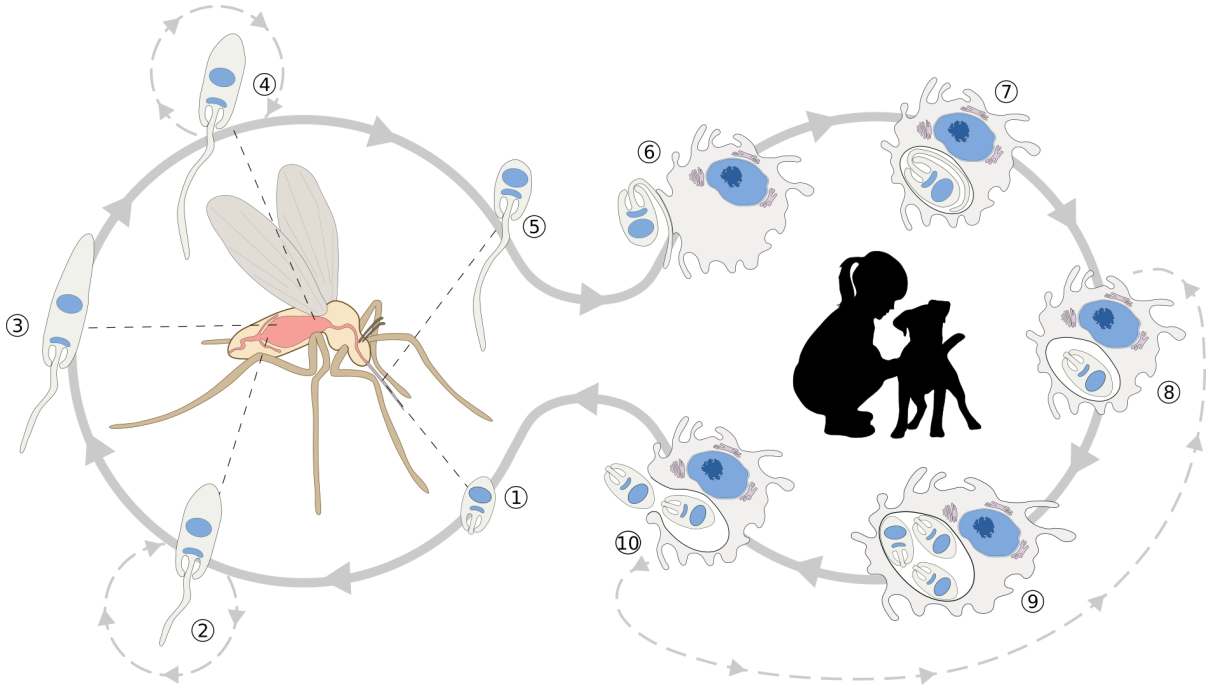


Figure 1.5 The digenetic *Leishmania* life cycle. (1) Uptake of amastigotes by phlebotomine sandfly during bloodmeal. (2) Differentiation to proliferative procyclic promastigotes in the midgut. (3) Differentiation to migratory nectomonad promastigote for migration through gut. (4) Differentiation to proliferative leptomonad promastigotes. (5) Differentiation to mammalian infective metacyclic promastigotes. (6) Adherence of metacyclic promastigotes to macrophages after transmission to mammalian skin. (7) Phagocytosis of metacyclic promastigotes by macrophages. (8) Differentiation to amastigotes. (9) Replication of amastigotes within PV. (10) Egress from macrophages for re-uptake or transmission.

known to carry and transmit *Leishmania* (World Health Organization, 2017); within this host, *Leishmania* parasites adopt a promastigote morphology and proliferate within the sandfly digestive tract (Chang and Dwyer, 1976). Within mammalian hosts, the parasites adopt an amastigote morphology and are phagocytosed by macrophages, where they replicate inside of parasitophorous vacuoles (Chang and Dwyer, 1976).

Leishmania are initially ingested by female phlebotomine sandflies as amastigotes (**Fig 1.5 1**) from the skin of an infected host during a bloodmeal (Bates, 2007). As the parasites arrive in the sandfly midgut, they differentiate into proliferative procyclic promastigote forms (**Fig 1.5 2**) to adapt to the decreased temperature and increased pH (Bates and Rogers, 2004; Kamhawi, 2006). The procyclic forms then undergo further differentiation for anterior migration; first into strongly motile nectomonad promastigotes (**Fig 1.5 3**), then into proliferative leptomonad promastigotes (**Fig 1.5 4**), and finally into infective metacyclic promastigotes (**Fig 1.5 5**) (Bates, 2007; Gossage et al., 2003; Rogers et al., 2002). During subsequent blood meals, infected sandflies transfer saliva containing promastigotes (predominantly metacyclic) into the mammalian skin resulting in transmission of the disease (Bates, 2007). From their location in the skin, metacyclic promastigotes interact with macrophages, neutrophils and dendritic cells that are recruited to the site (**Fig 1.5 6**), and are rapidly phagocytosed and compartmentalised into phagolysosome-derived parasitophorous vacuoles (PVs; **Fig 1.5 7**) (Gueirard et al., 2008; Laskay et al., 2003; van Zandbergen et al., 2004). Following uptake, the increased temperature and low pH in the parasitophorous vacuoles stimulates differentiation into amastigotes (**Fig 1.5 8**) (Garlapati et al., 1999; Zilberstein and Shapira, 1994). Finally, after replicating inside of parasitophorous vacuoles (**Fig 1.5 9**), amastigotes egress from macrophages (**Fig 1.5 10**) in association with phagolysosomal components, allowing for re-uptake by nearby uninfected macrophages or transmission to the sandfly (Real et al., 2014).

1.2.3 *Leishmania* ultrastructure

Cell body length is typically 6-12μm in promastigotes, and 2-5μm in amastigotes (Rogers et al., 2002). Despite the morphological and metabolic adaptations of each life cycle stage, *Leishmania* promastigotes and amastigotes share many of the same ultrastructural components. Both contain a microtubule array making up the subpellicular cytoskeleton (**Fig 1.6 A**). These subpellicular microtubules associate with the plasma membrane and represent the basic scaffold of the cell, defining morphology (Dwyer, 1980). The subpellicular microtubules do not continue into the region of the flagellar pocket, and all endo- and exocytosis is thus thought to occur through this opening (Overath and Engstler, 2004). Notable subcellular organelles include a nucleus, endoplasmic reticulum, lysosomal compartment (multi-vesicular tubule in promastigotes; megasome in amastigotes), golgi apparatus, a flagellum which protrudes from the cell body via the flagellar pocket, and a single mitochondrion (**Fig 1.6 B**) (Alberio et al., 2004; Coombs et al., 1986; Waller and McConville, 2002). The mitochondrion of *Leishmania spp*., and

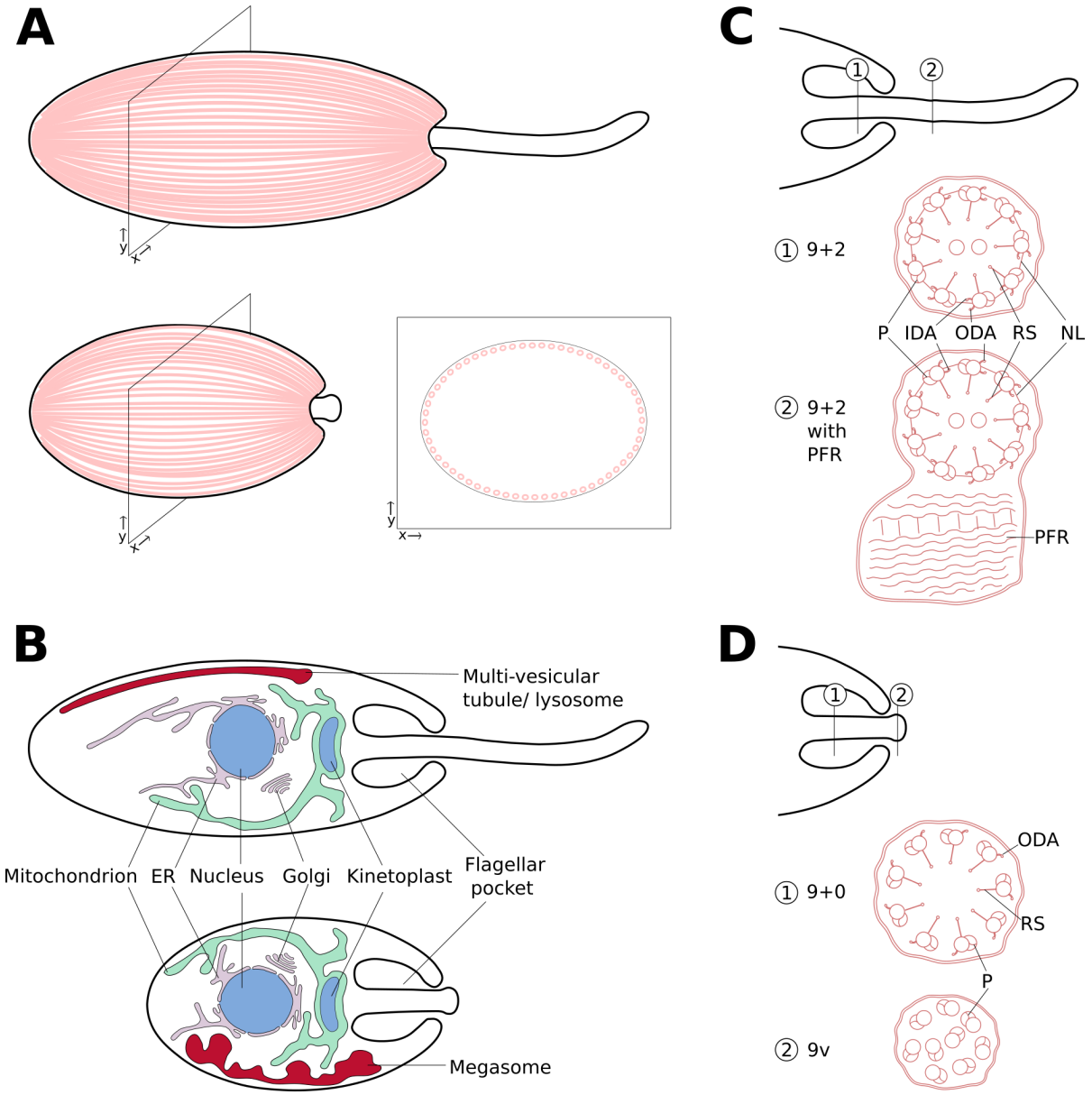


Figure 1.6. Ultrastructure of *Leishmania* promastigotes and amastigotes. (A) Subpellicular microtubule array defines cell morphology. Represented longitudinally and in cross-section. **(B)** Subcellular organisation of organelles: nucleus; single mitochondrion with DNA concentrated at kinetoplast; endoplasmic reticulum (ER); golgi apparatus; flagellum protruding from flagellar pocket; lysosomal compartments (multi-vesicular tubule in promastigote; megasome in amastigote). **(C)** Promastigote flagellum axoneme: canonical 9+2 arrangement, with outer (ODA) and inner (IDA) dynein arms, radial spokes (RS), nexin links (NL) and ponticuli (P). Kinetoplastid-specific paraflagellar rod (PFR) structure upon exit from flagellar pocket. **(D)** Amastigote flagellum axoneme: 9+0 arrangement lacking central pair and all microtubule decorations except outer dynein arms (ODA) and radial spokes (RS) at proximal end, and ponticuli (P) along length of B-tubules. Collapse of nine-fold symmetry at distal end into 9variable (9v) structure.

indeed of all kinetoplastids, is unique in that the mitochondrial DNA is concentrated at a single location, known as the kinetoplast (**Fig 1.6 B**) (Stuart, 1983). The kinetoplast is associated with the basal body via the tripartite attachment complex (Ogbadoyi et al., 2003). Several of these organelles represent morphological markers which can be used to define cell cycle stage, including the nucleus, kinetoplast, and flagellum, which are each present in a single copy in non-dividing cells, and replicate once per cell cycle (Ambit et al., 2011; Wheeler et al., 2011). The first stage of division of *Leishmania spp.* (as shown for *L. mexicana, L. major,* and *L. amazonensis* promastigotes) is the formation of a new flagellum from a duplicated basal body, followed by the duplication of nuclear and mitochondrial DNA (Ambit et al., 2011; da Silva et al., 2013; Wheeler et al., 2011). The order in which cells complete nuclear and kinetoplast division appears to be species specific; *L. mexicana* completes nuclear division before kinetoplast segregation, but the opposite is true for *L. major* (Ambit et al., 2011; Wheeler et al., 2011). Interestingly, *L. amazonensis* and *L. donovani* appear to possess proportions of cells carrying out organelle duplication in either order (da Silva et al., 2013; Minocha et al., 2011).

The major morphological difference between promastigotes and amastigotes is in the ultrastructure of the flagellum. Promastigotes possess a long, motile flagellum; unique amongst duplicated organelles, the promastigote flagellum continues growing over multiple cell cycles (Wheeler et al., 2011). As is the case for most motile flagella, the axoneme is composed of a canonical 9+2 arrangement, with microtubule decorations in the axoneme proper, including inner and outer dynein arms, nexin links, radial spokes and central pair decorations (**Fig 1.6 C**) (Gluenz et al., 2010a). The B-tubules contain bridge-like structures, referred to as ponticuli, which were first identified in *Trypanosoma brucei* (Vaughan et al., 2006). These structures represent a post-assembly modification of the outer doublets, and as such are not present in newly assembled flagella (**Fig 1.6 C**) (Vaughan et al., 2006). Upon exiting the flagellar pocket, the promastigote flagellum contains a kinetoplastid-specific extra-axonemal structure known as the paraflagellar rod (PFR; **Fig 1.6 C**) (Maga et al., 1999; Vickerman, 1962). This structure, which comprises a paracrystalline latticework of cytoskeletal filaments, lies parallel to the axoneme (Bastin et al., 1996; Maga et al., 1999). The PFR has been shown to be essential for motility in *Leishmania mexicana*, where knockout mutants of the genes encoding the component proteins PFR1 and PFR2 exhibit severe defects in flagellar wave propagation and swimming velocity (Maga et al., 1999; Santrich et al., 1997). In the promastigote form, the flagellum has several elucidated roles, including motility and attachment within the sandfly gut (Krüger and Engstler, 2015; Warburg et al., 1989), and is also expected to be involved in kinetoplast segregation, as is the case for *T. brucei* (Robinson and Gull, 1991). The amastigote flagellum, meanwhile, is severely reduced in length, barely protruding past the flagellar pocket (Gluenz et al., 2010b). In this life cycle stage, the flagellum is immotile and the axoneme adopts a 9+0 conformation, lacking the central pair as well as most of the microtubule decorations; outer dynein arms and radial spokes remain visible at the proximal end of the flagellum, while no decorations are observed towards the distal end (**Fig 1.6 D**) (Gluenz et al., 2010b; Wheeler et al., 2015). Ponticuli

remain visible along the length of the B-tubules in non-newly assembled flagella (Vaughan et al., 2006; Wheeler et al., 2015). The amastigote flagellum also lacks a PFR structure; a rare occurrence amongst kinetoplastid flagella (Bates et al., 1992; Gluenz et al., 2010b). Shortly prior to exit of the flagellar pocket, the axoneme of the amastigote flagellum loses the nine-fold symmetry of the outer doublets as some doublets progressively occupy more central positions (Gluenz et al., 2010b). Towards the distal end, a reduction in the number of doublets, or a reduction to singlet microtubules is sometimes observed, leading to the classification of these axonemes as 9-variable (9v) (Gluenz et al., 2010b). The axonemal arrangements of the amastigote flagellum show striking parallels to the structure of primary cilia (Dahl, 1963; Gluenz et al., 2010b). This has led to the suggestion that the amastigote flagellum could perform either sensory or signalling roles by serving as a specialised platform for either receptors or trafficking proteins (Gluenz et al., 2010b). During differentiation from the promastigote to the amastigote form, the morphological changes in the flagellum occur through two pathways: by *de novo* synthesis during cell division, and by remodelling of an existing flagellum by disassembly (Wheeler et al., 2015). Despite our current understanding of the mechanisms of flagellar differentiation, the biological incentives behind this remodelling remain unclear.

1.2.4 *Leishmania*-host interactions

Leishmania-host interactions have been studied in both the sandfly and the mammalian host, elucidating key differences in the parasite's mechanisms of survival in each environment. One of the major host defences to which *Leishmania* parasites are subjected within the sandfly is the secretion of digestive enzymes such a trypsin, aminopeptidase, carboxypeptidase, and alpha-glucosidase after ingestion of a bloodmeal (Borovsky and Schlein, 1987; Dillon and Lane, 1993). *Leishmania* have evolved species-specific resistance to digestion by these enzymes. The sandfly *Phlebotominae papatasi*, for example, exhibits natural resistance to many *Leishmania* species, but is susceptible to infection by *L. major* (Schlein and Jacobson, 1998). Studies have shown that production of proteolytic enzymes by *P. papatasi* is inhibited or delayed during infection with *L. major* but is unaffected by infection with *L. donovani* (Dillon and Lane, 1993b; Schlein and Romano, 1987). *L. major* is therefore able to survive where other species do not by reducing the levels of digestive enzymes to which it is exposed (Dillon and Lane, 1993b; Schlein and Romano, 1987). The surface glycoconjugate, lipophosphoglycan (LPG), has been implicated in early parasite resistance to digestion, but its mechanisms of action in this process remain unclear (Sacks et al., 2000). LPG plays additional roles in promastigote survival within the sandfly midgut, including attachment to the epithelial lining (Kamhawi et al., 2000; Sacks et al., 1995). *L. major* and *L. donovani LPG1*-deficient mutants exhibited a complete inability to persist within the midgut, and *in vitro* experiments correlated this result with an inability to bind to the epithelial cells (Sacks et al., 2000). Persistence in the midgut was completely restored by reintroduction of *LPG1*, confirming the involvement of the surface glycoconjugate in this process (Sacks et al., 2000). Attachment to the

epithelial cells is essential for protecting *Leishmania* promastigotes from clearance by the peristaltic action of the midgut, and thus plays a central role in the induction of a successful infection.

Within the mammalian host, *Leishmania* parasites have been shown to affect numerous cellular processes in order to evade the immune response, gain access to nutrients, and promote proliferation and persistent infection. *Leishmania* tactics for immune evasion within macrophages are particularly reliant on inhibiting production of microbicidal molecules and cytokines, and preventing antigen presentation to T lymphocytes (Gregory and Olivier, 2005). Unlike most intracellular parasites, *Leishmania* species do not prevent the acidification of the macrophage phagolysosome, and instead adapt to the amastigote form which is able to thrive within these harsh conditions (Burchmore and Hart, 1995; Ghosh and Mukherjee, 2000; Mazareb et al., 1999). They are, however, susceptible to nitric oxide (NO; Liew et al., 1990) and reactive oxygen species (ROS; Murray and Nathan, 1999; Murray et al., 1982), and have thus developed mechanisms to inhibit production of these microbicidal agents. Macrophage production of NO and ROS is regulated in part by protein kinase C (PKC) function (Severn et al., 1992), and *Leishmania* promastigote surface conjugates such as lipophosphoglycan (LPG), while able to scavenge oxygen radicals (Chan et al., 1989; McNeely and Turco, 1990), also appear to specifically inhibit PKC function (McNeely, 1987; McNeely et al., 1989; Olivier et al., 1992). *Leishmania* infection additionally causes changes in cytokine secretion by macrophages. This occurs both through increased production of cytokines which inhibit macrophage functions, such as Interleukin 10 (IL-10; Kane and Mosser, 2001), and through inhibited production of cytokines involved in the inflammatory response, such as Interleukin 12 (IL-12; Carrera et al., 1996). Modulation of many of these host processes by intracellular *Leishmania* involves disruption of macrophage signalling pathways. For example, *Leishmania* have been shown to prevent activation of mitogen-activated protein kinases (MAPKs), which regulate macrophage processes including production of pro-inflammatory cytokines and NO (Nandan et al., 1999; Seger and Krebs, 1995). Inhibition of these MAPKs by *Leishmania* is mediated by parasite modulation of macrophage protein tyrosine kinases and protein tyrosine phosphatases (PTPs; Blanchette et al., 1999; Forget et al., 2006), and a specific role for the *Leishmania* surface Glycoprotein 63 (GP63) has been elucidated in cleavage of PTPs and subsequent MAPK inactivation (Gomez et al., 2009; Hallé et al., 2009).

1.2.5 *Leishmania mexicana* as a model organism for ciliary/flagellar research

Due to the pervasive nature of ciliary defects in human disease, research into ciliary cell biology and function remains an area of keen interest. Much of our knowledge to date about cilia comes from the study of unicellular flagellated organisms. *Leishmania mexicana* represents a particularly attractive model for ciliary/flagellar research for a number of reasons:

1. The presence of a 9+2 axoneme in the promastigote form and a 9+0 or 9v axoneme in the amastigote form allows us to study both motile and non-motile flagella within a single organism and can shed light on the requirements of certain axonemal structures for different functions.

2. Both promastigote and amastigote forms can be cultured and differentiated under controlled conditions *in vitro* (Bates, 1994; Pan, 1984).

3. The *L. mexicana* genome has been sequenced and the annotations revised using transcriptomics data (Fiebig et al., 2015; Rogers et al., 2011). Comparative transcriptomics between life cycle stages has additionally provided information about stage-specific expression levels of thousands of genes (Fiebig et al., 2015).

4. Recent advances in genetic tools for this species allow for rapid gene manipulation using CRISPR-Cas9 facilitated editing (Beneke et al., 2017).

1.3 Aims and Strategy

While the role of the amastigote flagellum has remained elusive, a number of potential functions have been proposed, including roles in flagellar pocket formation and kinetoplast segregation. However, the proposed role in parasite-host communication is of particular interest, as insight into this could shed light on the mechanisms of intracellular survival and potentially provide future drug targets in the fight against leishmaniasis. The objective of this thesis was therefore to explore the putative roles of the amastigote flagellum in parasite-host interactions; specifically in providing a platform for either receptor-ligand interactions or vesicular trafficking.

There are few known proteins in the *L. mexicana* flagellar membrane, and even fewer known to localise there in the amastigote form. The afore-mentioned research question was therefore addressed using a combination of structural, molecular and genetic approaches. Previous research in the Gluenz lab has shown that the tip of the amastigote flagellum is often in close contact with the PV membrane, which contributed to the initial suggestion of a sensory function for this organelle (Gluenz et al., 2010b). A major aim of this research was therefore to build comprehensive high-resolution models of intracellular *Leishmania* amastigotes, to precisely define the connectivity between the parasite and the host cell, and to identify any evidence of vesicular trafficking or remodelling of host cell structures. This was achieved through the use of two 3-dimensional electron microscopy techniques: electron tomography and serial block-face scanning electron microscopy (SBF-SEM). However, structural information alone cannot provide functional insight into the putative role of the amastigote flagellum in either sensing or modulating the intracellular environment. The structural approach was therefore complemented by

analysis of mutants with putative defects in trafficking of flagellar membrane proteins. Null mutants of components of the BBSome trafficking complex, and of the kinetoplastid-specific trafficking protein, KHARON1, were assessed for their ability to infect and replicate within macrophages to determine whether an intact flagellum, and a correctly populated flagellar membrane, are required for survival within the intracellular environment.

CHAPTER 2

MATERIALS AND METHODS

2 Materials and Methods

2.1 Trypanosomatid Culture

2.1.1 Cell lines and *in vitro* culture of promastigotes

All cell lines were derived from a starting culture of wild type *Leishmania mexicana mexicana* strain MNYC/BZ/62/M379 promastigotes. Promastigote cell lines were cultured at 28°C in complete M199 medium, pH7.4: M199 powder (Invitrogen, 31100019) supplemented with 26 mM $NaHCO_3$, 40 mM 4-(2-hydroxyethyl)-1-piperazineethanesulfonic acid (HEPES), 5 µg/ml haemin and 9.1% v/v heat inactivated foetal calf serum (FCS) of South American origin (Invitrogen, 10500064). Promastigote cell lines were maintained at densities allowing for logarithmic growth ($1x10^5$-$2x10^7$/ml) by regular subculture. Cell density was measured using a CASY model TT cell counter and analyser system (Roche Innovatis AG) fitted with a 60 µm capillary, and a dead cell size cut-off of 2.5 µm.

2.1.2 *In vitro* differentiation and culture of axenic amastigotes

For differentiation into axenic amastigotes, log phase promastigote cell lines were first split to a density $1x10^5$ cells/ml and incubated for 5 days in M199 medium at 28°C to allow for growth into stationary phase. The stationary phase promastigotes were then differentiated by seeding at a density of $1x10^6$ cells/ml in SM5.5 medium, pH5.5: Schneider's drosophila medium (Life Technologies, 21720024), supplemented with 16.7% v/v heat inactivated FCS of South American origin (Invitrogen, 10500064) and 25 mM 2-morpholin-4-ylethanesulfonic acid (MES) hydrate, followed by incubation for 72h at 34°C/5% CO_2.

2.2 Transgenic Trypanosomatid Cell Lines

2.2.1 Fluorescent cell lines for vacuole progression studies

Studies on amastigote positioning and vacuole formation by fluorescence microscopy used two cell lines that had previously been produced in the Gluenz lab:

1. Wild type *L. mexicana* promastigotes with a C-terminal enhanced green fluorescent protein (eGFP) tag on the plasma membrane Glucose Transporter 2 (GT2; LmxM.36.6290) (Burchmore

et al., 2003), and a C-terminal mCherry tag on the flagellar membrane Small Myristoylated Protein 1 (SMP1; LmxM.20.1310) (Tull et al., 2004).

2. Cas9 and T7 polymerase-expressing *L. mexicana* promastigote cells with a C-terminal mCherry tag on the flagellar membrane Small Myristoylated Protein 1 (SMP1; LmxM.20.1310) (Tull et al., 2004).

2.2.2 *L. mexicana* KHARON1 (KH1) knockout and add-back cell lines and *T.brucei* KHARON1 (KH1) RNAi cell lines

ΔKH1 knockout and ΔKH1[intKH1] add-back cell lines were provided by Scott Landfear (OHSU, OR, USA), and were produced by members of the Landfear lab as described in Tran et al., 2013 and Tran et al., 2015, respectively. *T. brucei kharon1* RNAi cell lines were produced by Marco Sanchez in the Landfear lab (OHSU, OR, USA), as described in Sanchez et al., 2016.

2.2.3 *L. mexicana* endogenously-tagged BBSome cell lines

Each BBS protein was endogenously tagged at the C-terminus with the *Branchiostoma lanceolatum*-derived fluorescent protein, mNeonGreen (Shaner et al., 2013), by CRISPR-Cas9-facilitated replacement (Beneke et al., 2017) (**Fig 2.1**). Tagging constructs were amplified by polymerase chain reaction (PCR) from the pPOT.v4 BLAST-mNeonGreen-BLAST plasmid (Dean et al., 2015), using the Expand High Fidelity (Hifi) Polymerase (Sigma 04738250001). Long-primer PCR added 30 bp homology regions to the end of the BBS gene open reading frame (ORF), and the start of the adjacent 3' untranslated region (UTR) (**Fig 2.1 A**). Each reaction mix contained 5 µl 10x Expand High Fidelity Buffer with 15 mM $MgCl_2$, 1 µl 10 mM dNTPs, 30ng pPOT.v4 plasmid, 1 µl 100 µM forward primer, 1 µl 100 µM reverse primer and 0.5 µl Hifi polymerase, made up to 50 µl with ddH_2O. Thermocycling parameters included an initial 5-minute denaturation at 94°C, 35 cycles of 30 seconds denaturation at 94°C, 30 seconds annealing at 65°C and 2.5 minutes extension at 72°C, and a final 7 minute extension at 72°C.

Additional PCR reactions were performed to produce ~100 bp DNA sequence templates for single guide RNAs (sgRNAs) using a site-specific forward primer and a conserved sgRNA backbone reverse primer (**Fig 2.1 B**). sgRNA sequences were selected using the Eukaryotic Pathogen CRISPR guide RNA/DNA design tool (Peng and Tarleton, 2015). For each gene, sgRNA templates were produced for a site directly upstream of the open reading frame. Each PCR reaction, performed using the Expand High Fidelity (Hifi) Polymerase (Sigma 04738250001), contained 5 µl 10x Expand High Fidelity Buffer with 15 mM $MgCl_2$, 1 µl 10 mM dNTPs, 1 µl 100 µM site-specific forward primer, 1 µl 100 µM conserved gRNA backbone reverse primer and 0.5 µl Hifi polymerase, made up to 50 µl with ddH_2O. Thermocycling parameters consisted of an initial 30-second step at 98°C for denaturation, followed by 35 cycles of 10

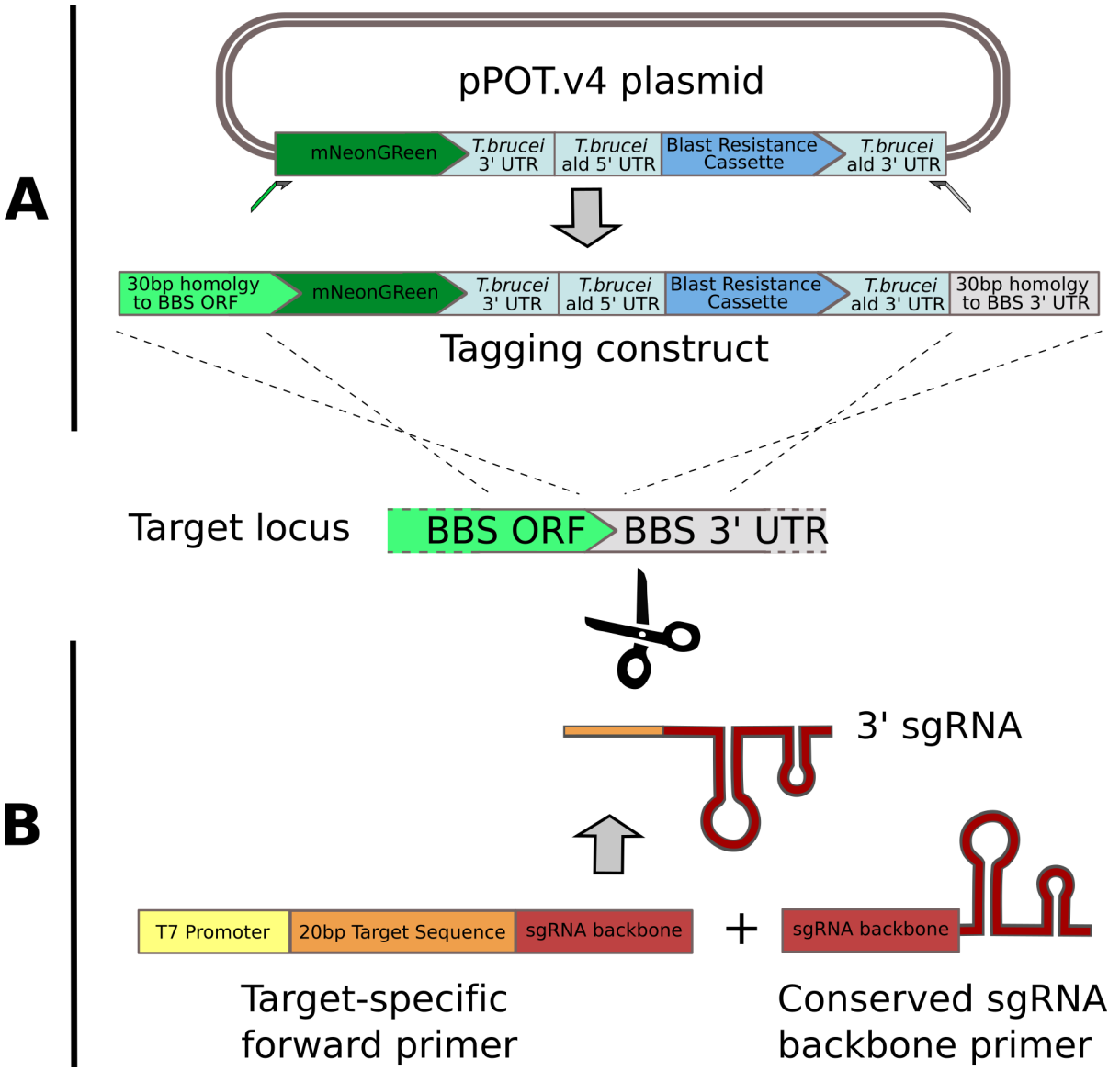


Figure 2.1. CRISPR-Cas9 facilitated endogenous C-terminal tagging of *Leishmania mexicana* BBS proteins. (A) Tagging constructs produced by PCR from template of circular pPOT.v4 BLAST-mNeonGreen-BLAST plasmid **(Dean et al., 2015)**. During PCR, long primers add 30 bp homology regions corresponding to the end of BBS gene ORF and start of adjacent 3' UTR at the target locus. This produces a linear PCR product used as the tagging construct. **(B)** sgRNA templates produced by PCR with conserved sgRNA backbone primer and site-specific forward primer targeting a site directly upstream of the gene ORF. During PCR, the forward and reverse primers anneal to produce a linear PCR product, which serves as a template for the sgRNA. Expression of Cas9 and T7 polymerase in transfected cells allows for CRISPR-Cas9 facilitated replacement, and *in vivo* transcription of sgRNA templates, respectively **(Beneke et al., 2017)**.

seconds denaturation at 98°C, 30 seconds annealing at 60°C and 15 seconds extension at 72°C, with a final 10 minute extension at 72°C.

Cas9- and T7 polymerase-expressing *L. mexicana* promastigotes (Beneke et al., 2017) were transfected with the pPOT.v4 tagging construct and the 3' sgRNA template, using the Amaxa Nucleofector IIb (Lonza) programme X-001. The constructs were transfected into $5x10^6$ Cas9T7 cells resuspended in Roditi buffer (66.7 mM Na_2HPO_4, 23.3 mM NaH_2PO_4, 5 mM KCl, 50 mM HEPES pH7.3, 143 µM $CaCl_2$). The expression of the T7 polymerase in the cell line allowed for *in vivo* transcription of the sgRNA from the transfected DNA templates (Beneke et al., 2017). Tagged cells were selected for with 5 µg/ml blasticidin after recovery in M199 medium. Resulting populations were screened for fluorescent signal by live-cell imaging.

2.2.4 *L. mexicana* BBSome knockout mutants

2.2.4.1 Generation of BBS1, BBS2, BBS3, BBS4, BBS5, BBS7, BBS8 and BBS9 null mutants by CRISPR-Cas9 facilitated replacement

Double knockouts for each of the *L. mexicana* BBS proteins were produced in a single round of CRISPR-Cas9-facilitated replacement as described in Beneke et al., 2017. Knockout constructs were produced by long-primer PCR using the pT plasmid system (Beneke et al., 2017), using a combination of the pT-puro and pT-neo plasmids (**Fig 2.2 A**). The long-primer PCR added 30 bp homology flanks corresponding to regions in the 5' and 3' UTRs of each gene, using the Expand High Fidelity (Hifi) Polymerase (Sigma 04738250001). Each reaction mix contained 5 µl 10x Expand High Fidelity Buffer with 15 mM $MgCl_2$, 1 µl 10 mM dNTPs, 30ng pT plasmid, 1 µl 100 µM forward primer, 1 µl 100 µM reverse primer and 0.5 µl Hifi polymerase, made up to 50 µl with ddH_2O. Thermocycling parameters consisted of an initial 5-minute denaturation at 94°C, 35 cycles of 30 seconds denaturation at 94°C, 30 seconds annealing at 65°C and 2.5 minutes extension at 72°C, and a final 7 minute extension at 72°C.

Additional PCR reactions were performed to produce ~100 bp DNA sequence templates for sgRNAs using a site-specific forward primer and a conserved sgRNA backbone reverse primer (**Fig 2.2 B**). sgRNA sequences were selected using the Eukaryotic Pathogen CRISPR guide RNA/DNA design tool (Peng and Tarleton, 2015). For each gene, sgRNA templates were produced for sites upstream and downstream of the open reading frame. Each PCR reaction contained 5 µl 10x Expand High Fidelity Buffer with 15 mM $MgCl_2$, 1 µl 10 mM dNTPs, 1 µl 100 µM specific forward primer, 1 µl 100 µM conserved gRNA backbone reverse primer and 0.5 µl Expand High Fidelity (Hifi) Polymerase (Sigma 04738250001), made up to 50 µl with ddH_2O. Thermocycling parameters consisted of an initial 30 second denaturation at 98°C, followed by 35 cycles of comprising 10 seconds denaturation at 98°C, 30 seconds annealing at 60°C and 15 seconds extension at 72°C, with a final 10 minute extension at 72°C.

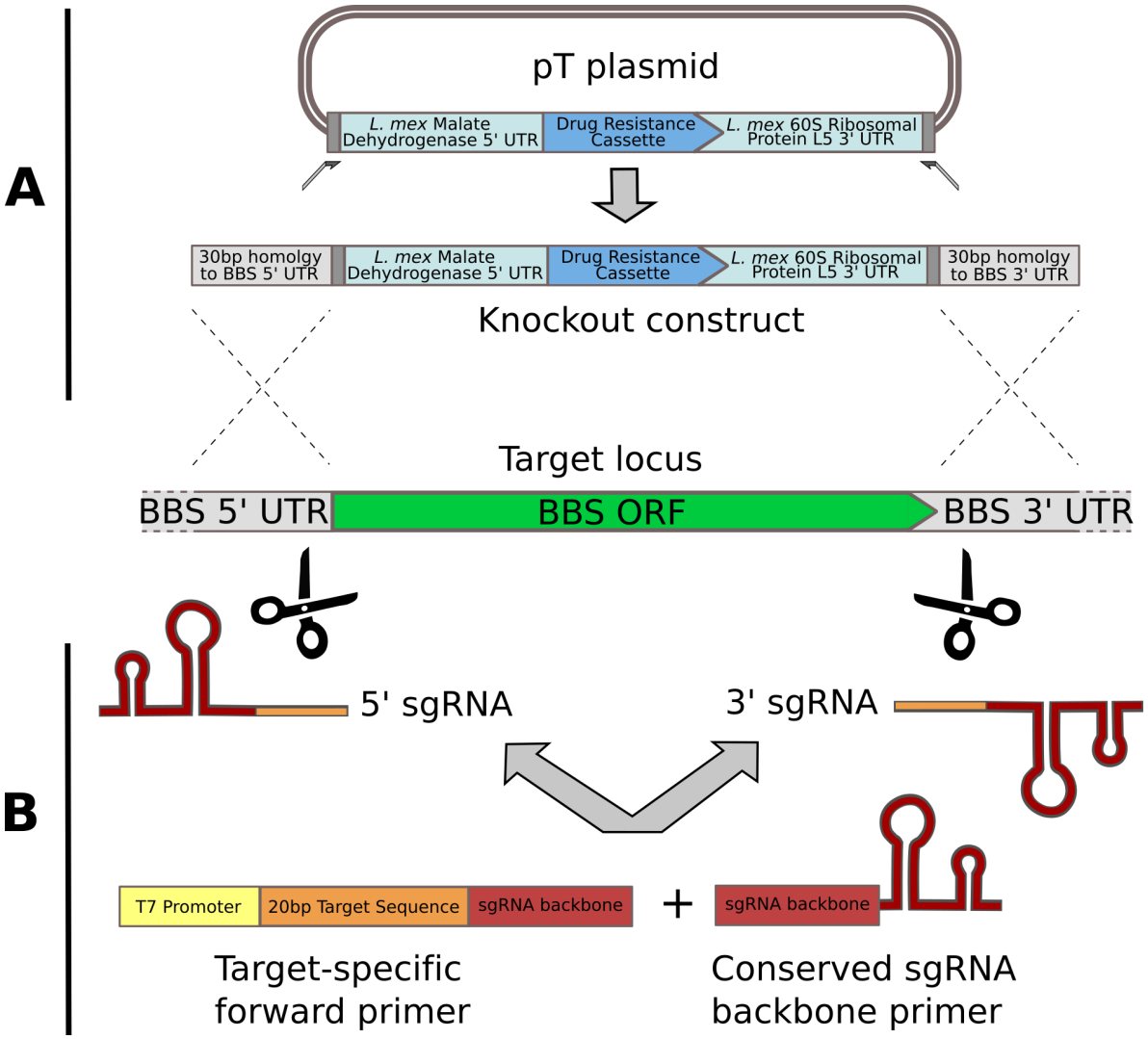


Figure 2.2 CRISPR-Cas9 facilitated double knockout of *Leishmania mexicana* BBS proteins in a single round. (A) Knockout constructs containing puromycin and neomycin drug resistance cassettes produced by PCR from template of circular pT-puro and pT-neo plasmids **(Beneke et al., 2017)**. During PCR, long primers add 30 bp homology regions corresponding to the end of BBS gene 5' UTR and the start of 3' UTR at the target locus. This produces a linear PCR product which is used as the knockout construct. **(B)** sgRNA templates produced by PCR with conserved sgRNA backbone primer and site-specific forward primer targeting sites directly downstream (5') and upstream (3') of the gene ORF. During PCR, the forward and reverse primers anneal to produce a linear PCR product, which serves as a template for the sgRNA. Expression of Cas9 and T7 polymerase in transfected cells allows for CRISPR-Cas9 facilitated replacement, and *in vivo* transcription of sgRNA templates, respectively **(Beneke et al., 2017)**.

For each knockout, Cas9 and T7 polymerase-expressing *L. mexicana* promastigotes were transfected with each of the pT-puro and a pT-neo knockout constructs, as well as both a 5′ and 3′ sgRNA template, using the Amaxa Nucleofector IIb (Lonza) programme X-001. The constructs were transfected into $1x10^7$ Cas9T7 cells resuspended in Roditi buffer (66.7 mM Na_2HPO_4, 23.3 mM NaH_2PO_4, 5 mM KCl, 50 mM HEPES pH7.3, 143 μM $CaCl_2$). The expression of the T7 polymerase in the cell line allowed for *in vivo* transcription of the sgRNA from the transfected DNA templates (Beneke et al., 2017). Double knockouts were selected for with 40 μg/ml G418 and 20 μg/ml puromycin on 96-well plates after recovery in 'magic' M199 medium (M199 powder, Invitrogen 31100019; 26 mM $NaHCO_3$; 40 mM HEPES; 2.5 μg/ml haemin; 100 μM adenine hemisulphate; 1.2 μg/ml biopterin; 20% v/v heat inactivated foetal calf serum of South American origin, Invitrogen 10500064). Resulting clones were screened by PCR for the correct incorporation of each knockout construct at the endogenous locus as well as for the absence of the relevant open reading frame.

2.2.4.2 Generation of BBS2 add-back cell line

An add-back cell line for the BBS2 knockout was produced by expressing the BBS2 ORF from the β-tubulin locus. An add-back construct was produced by insertion of the BBS2 ORF with a C-terminal 2x c-myc epitope tag into the pTadd plasmid (Beneke et al., 2017), using SpeI and EcoRI restriction sites (**Fig 2.3 A**). The BBS2 ORF was amplified from *L. mexicana* wild-type genomic DNA at 150 ng/μl by PCR, using the Expand High Fidelity (Hifi) Polymerase (Sigma 04738250001). Each reaction mix contained 5 μl 10x Expand High Fidelity Buffer with 15 mM $MgCl_2$, 1 μl 10 mM dNTPs, 30ng pTadd plasmid, 1 μl 100 μM forward primer, 1 μl 100 μM reverse primer and 0.5 μl Hifi polymerase, made up to 50 μl with ddH_2O. Thermocycling parameters consisted of an initial 5-minute denaturation at 94°C, followed by 35 cycles of 30 seconds denaturation at 94°C, 30 seconds annealing at 65°C and 2 minutes extension at 72°C, with a final 7 minute extension at 72°C.

All PCR products were purified, digested with the appropriate enzymes, and ligated into pTadd using T4 DNA Ligase (Roche 10136923) as per the manufacturer's instructions. After ligation, the plasmid was transformed into XL-1 blue competent *E. coli* by heat shock for 45 seconds at 42°C and selected for at 37°C on LB Agar plates containing 100 μg/ml ampicillin. Selected colonies were grown in LB medium and the plasmid was extracted using the QIAprep Spin Miniprep Kit (QIAGEN 27104). The final add-back construct was digested out of the plasmid using the restriction enzyme PacI (**Fig 2.3 B**), and ethanol precipitated prior to transfection. The add-back construct was transfected into $2x10^7$ CRISPR-generated knockout cells resuspended in Roditi buffer (66.7 mM Na_2HPO_4, 23.3 mM NaH_2PO_4, 5 mM KCl, 50 mM HEPES pH7.3, 143 μM $CaCl_2$), using the Amaxa Nucleofector IIb (Lonza) programme X-001.

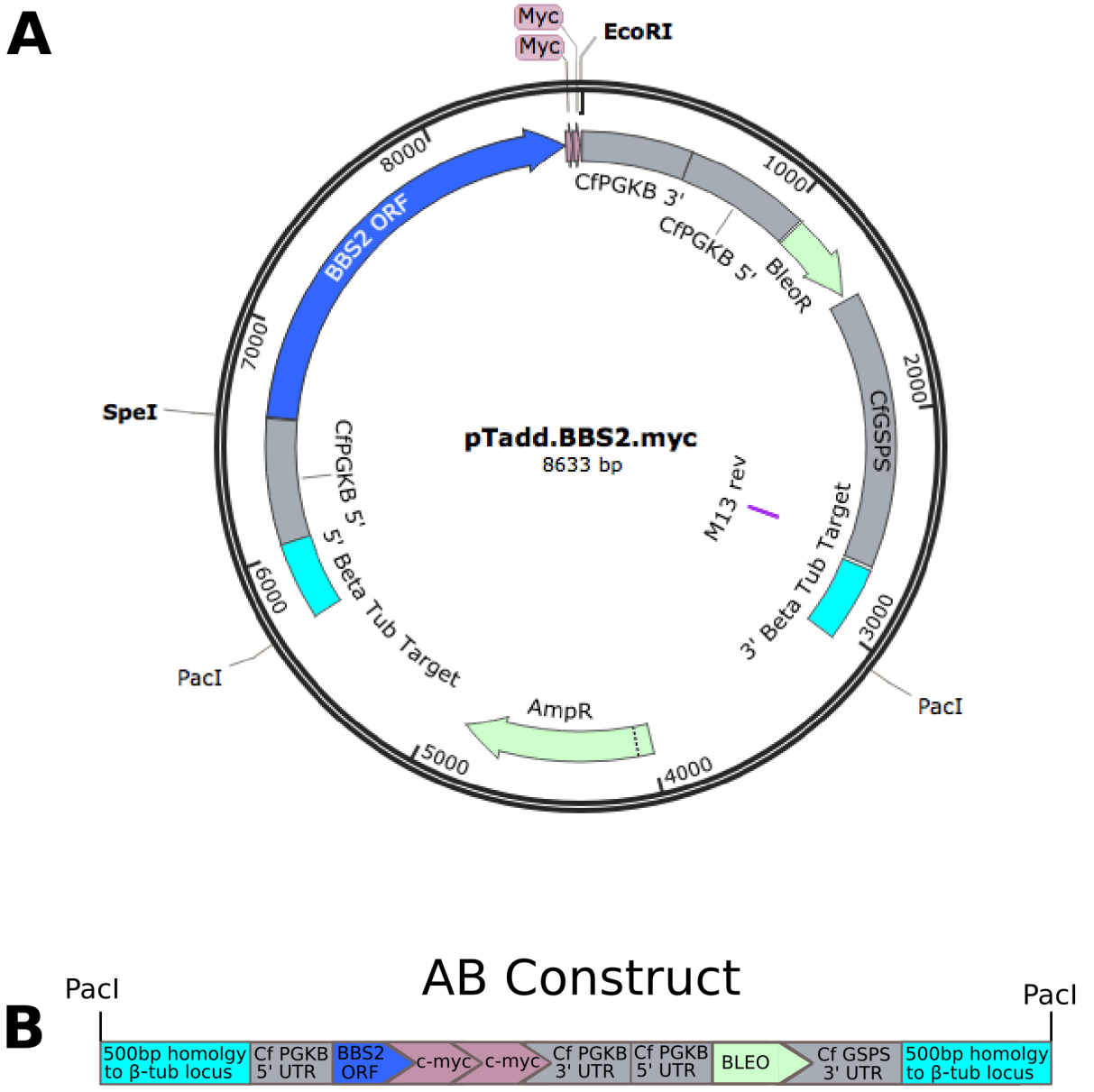


Figure 2.3. ***Leishmania mexicana*** **BBS2 add-back. (A)** Add-back plasmid produced from plasmid pTadd **(Beneke et al., 2017)**. BBS2 ORF produced by PCR from wild type *L. mexicana* genomic DNA. BBS2 ORF with 2x c-myc epitope tag inserted using restriction enzymes sites for SpeI and EcoRI by ligation with T4 ligase. Final plasmids purified from competent XL-1 blue *E. coli*. Plasmid maps made in SnapGene. **(B)** Add-back construct for insertion into β-tubulin locus was digested from the plasmid using the restriction enzyme PacI, and the resulting linear segment transfected into ΔBBS2 cells.

Transfectants were selected for with 25 μg/ml phleomycin on 96-well plates after recovery in 'magic' M199 medium. Clones were screened by western blot for expression of the myc-tagged BBS2 protein.

2.2.4.3 Generation of BBS2 null mutants by classical homologous recombination

Two knockout plasmids were produced for BBS2 knockout, one containing a puromycin-resistance cassette, and the other containing a hygromycin-resistance cassette. Both BBS2 plasmids were adapted from plasmid pJ1170 (**Fig 2.4 A**) (Dean et al., 2015). The eYFP coding sequence of the original pJ1170 plasmid was replaced with either a puromycin- or hygromycin-resistance cassette, and flanking regions of 500 bp of homology to the endogenous BBS2 5′ and 3′ UTRs were added either side of exogenous UTRs from *Crithidia fasciculata* for targeting of the knockout constructs (**Fig 2.4 A**). The 500 bp homology regions were amplified from *L. mexicana* wild-type genomic DNA at 150 ng/μl by PCR, using the Expand High Fidelity (Hifi) Polymerase (Sigma 04738250001). Each reaction mix contained 5 μl 10x Expand High Fidelity Buffer with 15 mM $MgCl_2$, 1 μl 10 mM dNTPs, 0.5 μl gDNA, 1 μl 100 μM forward primer, 1 μl 100 μM reverse primer and 0.5 μl Hifi polymerase, made up to 50 μl with ddH_2O. Thermocycling parameters consisted of an initial 5-minute denaturation at 94°C, followed by 25 cycles of 30 seconds denaturation at 94°C, 30 seconds annealing at 55°C and 1.5 minutes extension at 72°C, with a final 7 minute extension at 72°C. All PCR products were purified, digested with the appropriate enzymes, and ligated into pJ1170 using T4 DNA Ligase (Roche 10136923) as per the manufacturer's instructions. After each ligation stage, the plasmid was transformed into XL-1 blue competent *E. coli* by heat shock for 45 seconds at 42°C and selected for at 37°C on LB Agar plates containing 100 μg/ml ampicillin. Selected colonies were grown up in LB medium and plasmids were extracted using the QIAprep Spin Miniprep Kit (QIAGEN 27104). The final knockout constructs were digested out of the plasmids using the restriction enzymes NotI and SpeI (**Fig 2.4 B**), and ethanol precipitated prior to transfection.

BBS2 knockout mutants were produced by two successive rounds of homologous recombination using the Amaxa Nucleofector IIb (Lonza) programme X-001 for transfection. Each construct was transfected into $2x10^7$ wild type *L. mexicana* promastigotes resuspended in Amaxa Human T-cell Nucleofector solution (Lonza VPA-1002) and selected for with either 20 μg/ml puromycin or 32 μg/ml hygromycin on 96-well plates after recovery in 'magic' M199 medium. Resulting clones were screened for correct incorporation of the transfected knockout construct and one positive clone from each cell line was then transfected with the second knockout construct; cell lines containing a puromycin knockout construct were transfected with the hygromycin knockout construct and vice versa. Transfectants were selected for with both 20 μg/ml puromycin and 32 μg/ml hygromycin on 96-well plates. Resulting clones were screened for the correct incorporation of each knockout construct at the endogenous locus as well as for the absence of the BBS2 open reading frame using two independent primer pairs.

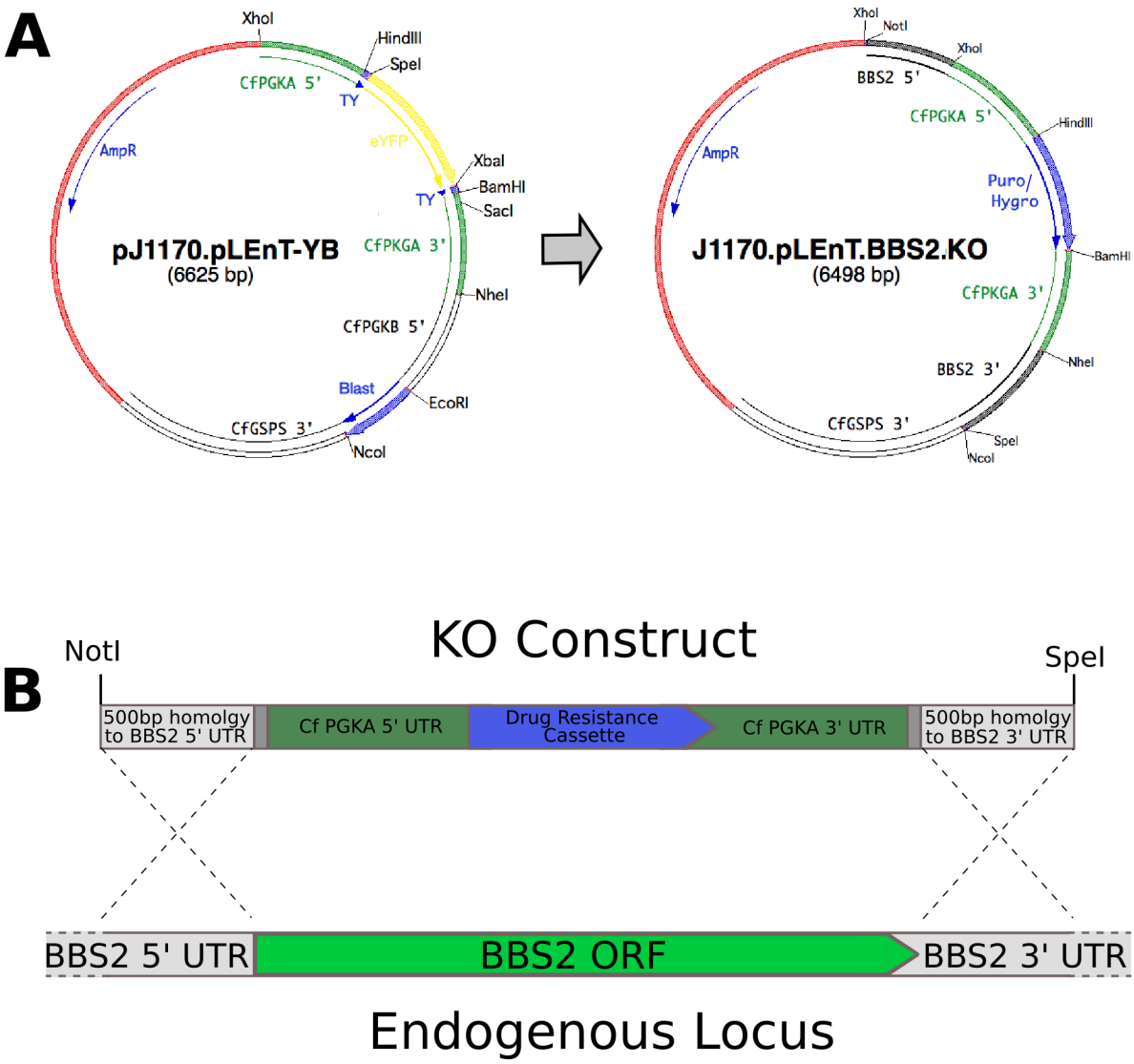


Figure 2.4. Double knockout of *Leishmania mexicana* BBS2 by classical homologous recombination. (A) Knockout plasmids produced from plasmid pJ1170 **(Dean et al., 2015)**. eYFP coding sequence of original plasmid replaced with either a puromycin or hygromycin resistance cassette. 500 bp homology to BBS2 5' UTR and 3'UTR produced by PCR from wild type *L. mexicana* genomic DNA by PCR and incorporated either side of *Crithidia fasciculata* exogenous UTRs from original plasmid by ligation with T4 ligase. Final plasmids purified from competent XL-1 blue *E. coli*. Plasmid maps made in Gene Construction Kit. **(B)** Knockout constructs were digested from the plasmids using the restriction enzymes NotI and SpeI, and the resulting linear segment transfected into *L. mexicana* wild type promastigotes. Double knockout achieved by two consecutive rounds of homologous recombination with puromycin and hygromycin drug selection.

2.3 Immunoblotting

For Western Blot analysis, whole cell lysates were produced as follows. Cells were pelleted at 800xg for 5 minutes, followed by removal of the supernatant and resuspension in 1ml PBS. Cells were re-pelleted at 800xg for 5 minutes, and all of the PBS was removed and replaced with boiling 1x laemmli buffer at a volume of 10 µl per $5x10^6$ cells. Laemmli-resuspended pellets were incubated at 95°C for 5 minutes, and then placed at -20°C until required. For whole cell lysates produced from axenically-differentiated amastigotes, protease inhibitors were included in both the washing step and the final laemmli resuspension. Protease inhibitors consisted of Leupeptin hydrochloride (Sigma LS783) at a concentration of 100 µM, Pepstatin A (Sigma P4265) at a concentration of 15 µM, Phenylmethanosulfonylfluoride (PMSF; Cell Signalling Technology 8553S) at a concentration of 1mM, and E-64 (Sigma E3132) at a concentration of 10 µM. 10 µl of each lysate was separated on 10% SDS-PAGE gels, and the separated proteins were transferred to nitrocellulose membranes (Sigma GE10600012) by overnight wet transfer at 120mA for 14 hours.

Membranes were blocked for 1 hour in blocking buffer comprised of 1x tris-buffered saline (TBS, 200 mM Tris, 3 M NaCl, pH 7.4) supplemented with 0.05% v/v Tween-20 (Sigma P2287) and 5% w/v skimmed powdered milk (Marvel). Membranes were incubated under agitation for 1 hour in relevant primary antibody diluted in blocking buffer at the dilutions listed in **table 2.1**. Membranes were then washed 3x 10 minutes in blocking buffer, before being incubated under agitation for 1 hour in relevant secondary antibody diluted in blocking buffer at the dilutions listed in **table 2.1**. Membranes were then washed a for further 3x 10 minutes in blocking buffer, and finally rinsed in 1x TBS. Bands were resolved by addition of the Western Lightning Plus-ECL enhanced chemiluminescence substrate (PerkinElmer NEL103001EA) and exposure of Carestream Kodak X-OMAT LS autoradiographic film (Sigma F1274).

Table 2.1 Antibody dilutions for Western Blot Analysis.

Primary Antibody	**Antibody Origin**	**Dilution**
Mouse IgG_1 anti-myc epitope monoclonal antibody 4A6	EMD Millipore 05-724	1:2,000 dilution from 1mg/ml stock
Monoclonal mouse IgG L13D6 (PFR1-specific in *Leishmania*) (Kohl et al., 1999)	Gift from Keith Gull, Oxford	1:20 dilution from hybridoma supernatant
Rabbit polyclonal anti-hydrophilic acylated surface protein B (HASP B) (Flinn et al., 1994)	Gift from Deborah Smith, York	1:2,000 dilution from affinity-purified serum
Secondary Antibody	**Antibody Origin**	**Dilution**
Rabbit anti-mouse IgG peroxidase-conjugated antibody	Sigma A9044	1:20,000 from the stock concentration
Polyclonal goat anti-rabbit peroxidase-conjugated antibody	Dako P0448	1:5,000 from the stock concentration

2.4 Macrophage Infections

Murine bone-marrow derived macrophages (BMDMs) were previously generated by members of the Gluenz lab from the femora, humeri and tibiae of C57BL/6 mice, and frozen after differentiation (Fiebig, 2014; Wheeler, 2012). Differentiation from monocytes into macrophages had been established for these cells by staining with anti-mouse F4/80, anti-mouse MAC1, and anti-mouse GR-1 (Fiebig, 2014; Wheeler, 2012). Once thawed, these were cultured in high glucose Dulbecco's Modified Eagle Medium (DMEM; Sigma D6429), supplemented with 9.1% v/v heat inactivated foetal calf serum of South American origin (Invitrogen, 10500064) and 10ng/ml recombinant human macrophage colony-stimulating factor (MCSF; R&D Systems 216-MC), at 37°C for four days before infection, with a replacement of medium after 2 days.

RAW 264.7 cells which had been stably transfected with LAMP1-GFP (RAW 264.7 LAMP1-GFP) by Lentivirus transfection without drug selection were provided by the Michael Hensel lab, Universität Osnabrück, Germany (Krieger et al., 2014), and were cultured in high glucose Dulbecco's Modified Eagle Medium (DMEM; Sigma D6429), supplemented with 9.1% v/v heat inactivated foetal calf serum of South American origin (Invitrogen, 10500064) at 37°C. These cells were sub-cultured every 3 days until required for infection, starting at passage 12 and continuing until passage 14. For infection of either BMDMs or RAW 264.7 Lamp1-GFP cells, *L. mexicana* promastigotes were split to a density of $1x10^5$ cells/ml and allowed to grow into stationary phase over 5 days. Stationary phase promastigotes were then added to macrophages at a multiplicity of infection (MOI) of 10:1 and allowed 2 hours to adhere and infect at 34°C/5% CO_2. After 2 hours, remaining extracellular parasites were removed by 5 washes and infected macrophages were incubated in fresh medium at 34°C/5% CO_2 for the duration of the required time-course.

2.5 Light Microscopy

2.5.1 Imaging of mNeonGreen-tagged cells

For live cell imaging of fluorescently-tagged cell lines, 1ml of mid-logarithmic phase *L. mexicana* promastigote cultures were transferred to Eppendorf tubes and pelleted at 800xg for 5 minutes. Pelleted cells were washed once in 1ml PBS containing 1 µg/ml Hoechst 33342 (Thermo Fisher H3570), and then resuspended in 100 µl PBS. 1 µl of each final cell suspension was transferred to a well of a 10-well diagnostic microscope slide (ThermoFisher ER-308B-CE24) and covered using a 22 x 64 mm No. 0 cover slip (Scientific Laboratory Supplies MIC3208).

Slides were imaged on a Leica DM5500B microscope with a Leica 63x (NA 1.4) HCX PL APO oil immersion objective and an Andor Neo 5.5 sCMOS camera. Cells were imaged using phase contrast, as well as fluorescence using a GFP filter cube for mNeonGreen signal and an A4 filter cube for Hoechst signal. Images were captured using MicroManager (Edelstein et al., 2010) and were processed in ImageJ (Schneider et al., 2012).

2.5.2 Airyscan Imaging of Vacuole Progression

For imaging of amastigote orientation and vacuole development, BMDMs were infected with *L.mex* WT/GT2::eGFP/SMP1::mCherry cells and RAW264.7 Lamp1-GFP macrophages were infected with *L.mex* Cas9T7/SMP1::mCherry cells, following the infection protocol described in section 2.4. These infections were performed in 35/10 mm glass-bottomed petri dishes (Greiner 627861) with macrophages seeded at a density of $2x10^4$ BMDMs/plate or $1x10^4$ RAWs/plate. BMDMs infected with *L.mex* WT/GT2::eGFP/SMP1::mCherry cells were incubated at 34°C for 2 days, before addition of 250 µg/ml 10000MW Cascade Blue fluorophore-conjugated Dextran (Thermo Fisher D1976) and incubation for a further 24 hours. Prior to imaging, cells were washed 3x in DMEM, and then cultured in Fluorobrite DMEM Medium (Thermo Fisher A1896701) + 9.1% v/v heat inactivated foetal calf serum of South American origin (Invitrogen, 10500064) for the duration of the imaging time-course. RAW264.7 Lamp1-GFP macrophages infected with *L.mex* Cas9T7/SMP1::mCherry cells were incubated for 3 days after infection, washed once in DMEM, and then cultured in Fluorobrite DMEM Medium (Thermo Fisher A1896701) + 9.1% v/v heat inactivated foetal calf serum of South American origin (Invitrogen, 10500064) for the duration of the imaging time-course.

Samples were imaged on an inverted Zeiss LSM 880, with a Zeiss 63x (NA 1.4) Plan Apochromat oil immersion objective, and a Zeiss Airyscan 32 GaAsp PMT detector array. A solid state 561 nm laser was used for excitation of mCherry, an argon laser at 488 nm for excitation of eGFP, and a solid state 405 nm laser for excitation of the Cascade Blue Dextran. Images were captured using Zeiss Zen System software and underwent Airyscan processing in this software. Further processing was performed in ImageJ (Schneider et al., 2012).

2.6 Electron Microscopy

2.6.1 Fixation of samples for electron microscopy

L. mexicana and infected macrophage cell lines were fixed in 2.5% glutaraldehyde by addition of 1/10 volume of 25% glutaraldehyde directly to the culture and incubated at room temperature for 5 minutes. Cells were subsequently pelleted for 10 minutes at 800xg for parasite cultures or 300xg for infected

macrophage cultures. Cells were resuspended in 1ml of buffered fixative (2.5% glutaraldehyde and 2% formaldehyde in 100 mM sodium phosphate buffer, pH 7.4, for TEM samples, or in 100 mM PIPES buffer, pH7.4, for SBF-SEM samples), and then centrifuged for 1 minute at maximum speed in a table-top centrifuge to form a firm pellet. The supernatant was discarded and the pellets carefully overlaid with fresh buffered fixative and stored at 4°C. *T. brucei* bloodstream form samples were fixed by essentially the same method except with the inclusion of 50 mM sucrose in the buffered fixative.

2.6.2 Transmission Electron Microscopy Sample Preparation and Imaging

Fixed samples were washed in 100 mM sodium phosphate buffer, followed by incubation at 4°C for 1 hour in 1% aqueous osmium tetroxide in 100 mM sodium phosphate buffer. Samples were subsequently washed with ddH_2O and then incubated in the dark at 4°C for 2 hours in 2% aqueous uranyl acetate. After a final washing step in ddH_2O, samples were dehydrated through a graded series of 30%, 50%, 70%, 90% and 100% ethanol incubations and embedded in Agar 100 epoxy resin.

Sections (90 nm for ultrathin-section TEM and 150 nm for tomography) were cut on a Leica Ultracut 7 microtome, post stained with lead citrate and imaged in a Tecnai 12 Transmission Electron microscope (Hillsboro, OR, USA) at 120 kV. Images were captured with a Gatan Ultrascan 1000 CCD camera or Gatan OneView 4k x4k CMOS camera using SerialEM (Mastronarde, 2014) or Gatan Microscopy Suite 3 software. Tomograms were acquired in two perpendicular axes with tilt series acquired from -55° to 55° in 1° increments. Dual axis tomograms were reconstructed in the IMOD graphical user interface programme, eTomo (Mastronarde, 2014). Ultrathin section images were processed in ImageJ, while reconstructed tomograms were segmented in IMOD (Mastronarde, 2014).

2.6.3 Serial Block-Face Scanning Electron Microscopy (3View) Sample Preparation and Imaging

Fixed samples were washed in 100 mM PIPES buffer and then embedded in a mix of 4% low melting point agarose and 4% gelatin from porcine skin. Excess agarose/gelatin was removed and samples were prepared following an optimised version of the protocol defined by Deerinck et al. (2010). Briefly, samples were incubated at 4°C for 1h in a 1:1 mix of 3% potassium ferricyanide in 200 mM PIPES buffer and 4% aqueous osmium tetroxide. Washes in ddH_2O were performed between each of the subsequent heavy metal staining steps, which consisted of 1% thiocarbohydrazide (TCH) in ddH_2O for 20 minutes at room temperature, 2% aqueous osmium tetroxide for 30 minutes at 4°C, 1% uranyl acetate overnight at 4°C, and lead aspartate (20 mM lead nitrate and 30 mM aspartic acid) for 30 minutes at room temperature. Final washes in ddH_2O were performed prior to dehydration through a graded series of

30%, 50%, 70%, 90% and 100% ethanol incubations followed by 100% acetone incubations. The samples were then embedded in Durcupan ACM epoxy resin, then mounted and trimmed as described in (Deerinck et al., 2010).

Serial block face images were captured with a Zeiss Merlin Compact Field Emission Gun Scanning Electron Microscope (FEG-SEM) with Variable Pressure (VP) mode and a Gatan 3View System using Digital Micrograph, with an accelerating voltage of 3kV, variable pressure of 45Pa, an aperture size of 30 μm, an axial resolution of 50 nm or 100 nm and lateral resolutions as stated in the results. Image stacks were processed using ImageJ and segmented in IMOD (Mastronarde, 2014). The contrast was normalised across the slices of each stack using a brightness normalising macro written by Richard Wheeler for ImageJ (Wheeler, n.d.), and the slices of each stack were then aligned using the ImageJ StackReg plug-in (Thévenaz et al., 1998). Finally, stacks were converted to 8-bit TIFF stacks and then converted to MRC stacks using the raw2mrc IMOD programme (Mastronarde, 2014), with the x,y,z and offset parameters specified. Infected vacuoles were segmented in IMOD, and the volume inside of reconstructed parasitophorous vacuoles was measured using the IMOD programme imodinfo, specifying option -c (Mastronarde, 2014).

2.7 Flow Cytometry

Prior to infection of BMDMs, stationary phase promastigotes were stained with carboxyfluorescein succinimidyl ester (CFSE) as per the manufacturer's instructions. Briefly, stationary phase promastigotes were washed once in PBS, followed by incubation for 15 minutes at 28°C in 1ml PBS + 10 μM CFSE (BioLegend 423801). Cells were then pelleted at 800xg for 5 minutes, and resuspended in 1ml M199 medium and incubated for a further 30 minutes at 28°C. During this incubation step, cell density was counted from a small aliquot using a CASY model TT cell counter and analyser system (Roche Innovatis AG) fitted with a 60 μm capillary, and a dead cell size cut-off of 2.5 μm. After a final wash in PBS, stained cells were resuspended in DMEM/9.1% FCS at an appropriate concentration. Infection of BMDMs proceeded as described in section 2.4. At each time-point, BMDMs were detached from surfaces by incubation in TrypLE Express trypsin-like enzyme (Thermo Fisher 12604013) for 10 minutes at 34°C. Detached cells were pelleted at 300xg for 3 minutes and washed in PBS. Cells were fixed in 4% formaldehyde for 20 minutes, before a final resuspension in 200 μl PBS and transfer to a 96-well plate.

Flow cytometry measurements were performed using a BD Accuri C6 Flow Cytometer (BD Biosciences). Fluorescent events were differentiated by excitation at 488nm and detection with an FL1 533/30 nm filter. Forward/side scatter data were gated to exclude cell debris and extracellular *Leishmania*, and uninfected controls were used to define intensity cut-offs for uninfected cells. Each condition was

performed in triplicate. However, one replicate showed duplicated populations in the scatter plots and was therefore excluded. The mean of the remaining two duplicates was calculated for each condition at each time point.

CHAPTER 3

INTERACTION OF *LEISHMANIA MEXICANA* AMASTIGOTES WITH THE PARASITOPHOROUS VACUOLES OF HOST MACROPHAGES

3 Interaction of *L. mexicana* amastigotes with the parasitophorous vacuoles of host macrophages

The work presented in this chapter relied on optimisation of 3View sample preparation techniques, which were performed in collaboration with Errin Johnson, the Electron Microscope Facility Manager at the Sir William Dunn School of Pathology, University of Oxford. The results and figures presented in section 3.2.1 are therefore based on data that resulted from this collaboration. All other data and figures presented in this chapter are wholly my own work unless otherwise stated.

3.1 Preface

Parasitic organisms employ a range of mechanisms for evading host immune responses and gaining access to nutrients. Popular amongst these is refuge within host cell digestive compartments. *Leishmania* amastigotes adopt this strategy and reside within mammalian macrophages in parasitophorous vacuoles of phagolysosomal origin. After transmission to a mammalian host, *Leishmania* promastigotes are ingested by mammalian dermal macrophages by phagocytosis (Chang and Dwyer, 1976). Uptake of *Leishmania* promastigotes occurs through receptor-mediated phagocytosis, and several host receptors have been implicated in this process including complement receptors 1 and 3 (CR1 & CR3) and mannose receptors (reviewed in Ueno and Wilson, 2012). Orientation during attachment to the host cell and subsequent uptake has been widely debated, with contradictory studies showing attachment occurring predominantly via the flagellum (Chang, 1978; Forestier et al., 2011), or via either the flagellum or the posterior pole (Chang, 1979; Courret et al., 2002; Pearson et al., 1983). It appears that orientation during this process may be species specific, with species such as *L. major* and *L. aethiopica* displaying consistent flagellar attachment, and species such as *L. donovani* displaying greater variation (Rittig et al., 1998). Flagellum motility has also been implicated in intracellular re-orientation after engulfment (Forestier et al., 2011). Pre-infection treatment of *Leishmania* with cytochalasin D or nocodazole, showed that inhibition of actin polymerisation, but not microtubule polymerisation, significantly reduced parasite uptake, providing evidence that the parasite actively participates in the uptake process (Forestier et al., 2011). This result has been proposed as evidence for a role of actin-based flagellar motility in *Leishmania* uptake, but this has yet to be confirmed (Forestier et al., 2011).

The parasites are initially contained within phagosomal compartments derived from the macrophage plasma membrane (Muller et al., 1980a, 1980b). These vacuoles are then remodelled via fusion with lysosomes and late endocytic compartments to produce mature parasitophorous vacuoles (PVs) (Alexander and Vickerman, 1975; Courret et al., 2002; Desjardins et al., 1994). Intracellular *Leishmania*

have been shown to use virulence factors to either subvert or hijack macrophage processes involved in pathogen degradation and phagolysosome maturation; particularly well-characterised are the roles of the GPI-anchored surface glycoconjugates lipophosphoglyan (LPG) and glycoprotein 63 (GP63) (Desjardins and Descoteaux, 1997; Matheoud et al., 2013). GP63 has been shown to interfere with presentation of *Leishmania* antigens to T-cells, through cleavage of host cell membrane fusion machinery causing increased proteolytic activity within the phagosome (Matheoud et al., 2013). LPG, meanwhile, causes delayed fusion of the phagosome with lysosomes and late endosomes, by inserting into the phagosome membrane and thus reducing its fusogenic properties (Desjardins and Descoteaux, 1997). The parasitophorous vacuole represents an acidic environment, maintaining an average pH of around 5.0 (Antoine et al., 1990), and contains active acid hydrolases, sulfatases and phosphatases of host cell origin (Antoine et al., 1990, 1987; Prina et al., 1990). *Leishmania* do not appear to inhibit the production or activity of these proteases and have even been shown to stimulate lysosomal enzymatic activity in infected macrophages (Prina et al., 1990). Intracellular *Leishmania* adapt to these conditions through differentiation to the acidophilic amastigote form, and the delayed maturation of the PV caused by LPG may be of particular importance in allowing this adaptation to occur (Desjardins and Descoteaux, 1997). While this form maintains an intracellular pH of around 7.0 (Glaser et al., 1988), the amastigote's metabolic processes occur optimally in an acidic extracellular environment (Burchmore and Hart, 1995; Ghosh and Mukherjee, 2000; Mazareb et al., 1999).

PV size and occupancy are dependent upon *Leishmania* species. Most *Leishmania* species reside within small PVs, each containing only a single amastigote (Antoine et al., 1998; Real and Mortara, 2012). *Leishmania* of the mexicana complex, however, are found within much larger vacuoles, which can contain numerous amastigotes (Antoine et al., 1998; Real and Mortara, 2012). As well as representing an important source of nutrient acquisition (Borges et al., 1998; Russell et al., 1992), fusion with endocytic compartments is likely to play a role in the formation of these larger vacuoles. There is evidence to suggest that increased vacuole size may facilitate intracellular survival of amastigotes by producing a dilution effect on nitric oxide and reactive oxygen species (Wilson et al., 2008). Amastigotes of *Leishmania* species that reside within large PVs have been shown to remain bound to the vacuole membrane rather than floating freely within the lumen (Benchimol and de Souza, 1981). However, some ultrastructural studies suggest attachment via the flagellar tip, whilst others suggest attachment via other regions such as the posterior end (Benchimol and de Souza, 1981; Gluenz et al., 2010b). The major limiting factor in reconciling these previous studies is the lack of three-dimensional information. Therefore, a comprehensive description of amastigote positioning within a three-dimensional context, and the nature of the interactions involved in amastigote-PV binding remain to be elucidated. The functional significance of this binding is also of interest, in terms of whether this could be required for amastigote viability or could promote remodelling of host cell structures to produce the characteristically large vacuoles. These mechanisms are likely to bear directly on *Leishmania*

pathogenicity and understanding of these therefore has important implications in the search for therapeutic targets.

Electron microscopy represents a fundamental technique for exploring ultrastructural questions such as that of amastigote positioning and attachment. Since its first use for analysis of cells by Porter et al. in 1945, electron microscopy has profoundly influenced our understanding of biological structures. A rapidly expanding area of electron microscopy is the acquisition of three-dimensional information. Traditionally, 3D information could be acquired by either transmission electron microscopy of serial sections or by transmission electron tomography. Serial section TEM has been used to define structures ranging from the entire nervous system of the nematode, *Caenorhabditis elegans* (Hall and Russell, 1991; White et al., 1986), to synapses in the mammalian retina (Anderson et al., 2011). However, this technique is very labour intensive and time-consuming, depending on the collection and imaging of each individual ultrathin section, and alignment of micrographs for reconstruction. Continuity of sections is critical, and this method is thus plagued with issues from accidental loss of sections to generation of artefacts from holes, shrinkage/stretching, or precipitation of heavy metal stains on individual sections (Peddie and Collinson, 2014). While serial section TEM can provide sub-nanometre lateral (x and y) resolution, it is limited in axial (z) resolution by sectioning thickness capabilities (usually ~50 nm) (De Groot, 1988). In reality, the lateral resolution of plastic embedded samples is limited by the deposition of heavy metals onto structures, but this can be overcome by the use of cryo-TEM techniques (Weston et al., 2009).

3D information can be gathered from a single section by TEM tomography, where a thicker section is imaged at a series of tilt angles, which can be reconstructed into a three-dimensional tomogram, providing axial resolution of features within the slice (Penczek et al., 1995). A major shortcoming of this method due to technical limitations and the increased thickness of sections at high tilts, is the inability to image to ± 90°, resulting in a 'missing wedge' of information in Fourier space, which translates to a loss of lateral information and an axial stretching of features (Radermacher, 1992). This can be somewhat minimised by capturing two tilt series offset by 90° in the rotation plane of the specimen (dual-axis tomography; **Fig 3.1 A**) (Mastronarde, 1997; Penczek et al., 1995)**.** As is the case with serial section TEM, better resolution can be achieved by tomography of cryo-EM samples, though this often limits image capture to a single tilt axis due to rapid radiation damage to the sample (Guesdon et al., 2013). Electron tomography is able to provide an axial resolution down to 2 nm (Bárcena and Koster, 2009). Tomography generally imposes a limit on the volume that can be imaged (typically < 1 μm unless using a high-voltage TEM) (Martone et al., 2013), though this can be increased by combining tomography with serial sectioning to image larger volumes while maintaining better axial resolution. Additional limitations of tomography include the time required to capture tilt series and generate tomograms.

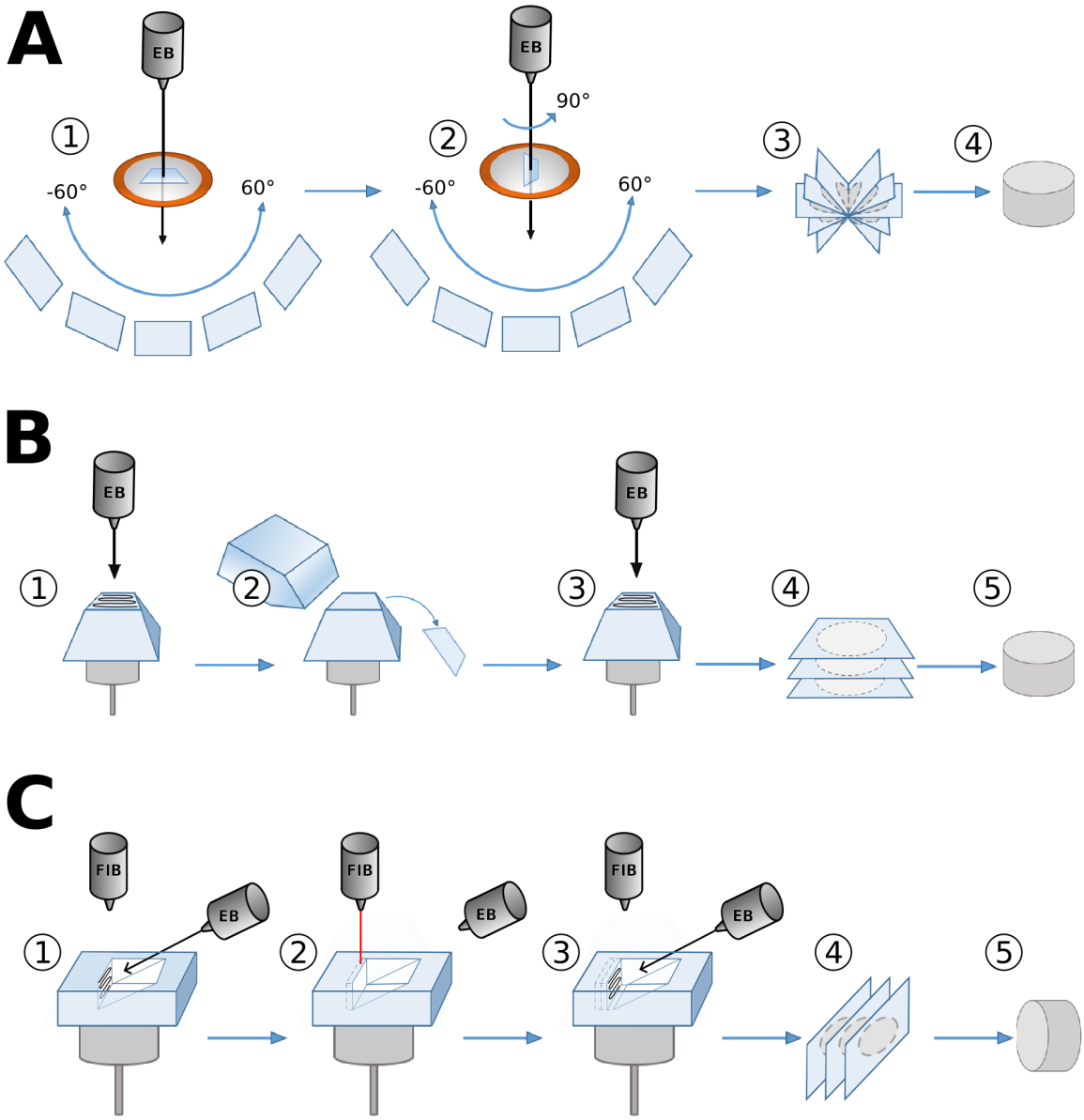


Figure 3.1. Three-dimensional electron microscopy techniques. (A) Dual axis transmission electron tomography. 1: transmitted electron beam (EB) is captured at a series of tilt angles. 2: grid is rotated 90° in plane perpendicular to electron beam (EB), and new tilt series imaged. 3: Tilt series are combined and reconstructed into a 3D tomogram. 4: 3D models of structures of interest can be segmented from tomograms. **(B)** Serial block-face scanning electron microscopy (SBF-SEM). 1: Block-face is imaged by raster scanning electron beam (EB). 2: Ultrathin section is removed by a diamond knife within the vacuum chamber. 3: Newly-revealed block-face is imaged. 4: Repetition allows for automated imaging of serial sections. 5: 3D models of structures of interest can be segmented from image stacks. **(C)** Focused ion beam scanning electron microscopy (FIB-SEM). 1: Region of block-face imaged by raster scanning electron beam (EB). 2: Ultrathin section removed by milling with a focused gallium ion beam (FIB). 3: Newly-revealed block-face region is imaged. 4: Repetition allows for automated imaging of serial sections. 5: 3D models of structures of interest can be segmented from image stacks.

Recently, two similar scanning electron microscopy (SEM) techniques have been developed for imaging data directly from a resin-embedded sample block-face, with both automated image acquisition and in-chamber serial sectioning. In serial block-face SEM (SBF-SEM; **Fig 3.1 B**) sections are cut from the block-face by a diamond knife inside of the vacuum chamber (Denk and Horstmann, 2004), while in Focused Ion Beam SEM (FIB-SEM; **Fig 3.1 C**) they are removed using a focused gallium ion beam (Knott et al., 2008). In each of these techniques, the removed sections are discarded meaning that imaged areas cannot be revisited. However, as well as automating the traditionally labour-intensive process of serial image capture, these techniques reduce sectioning artefacts, such as compression and distortion, through imaging of the block-face rather than the removed section, and improve the axial resolution as compared to manual sectioning (Denk and Horstmann, 2004; Knott et al., 2008). SBF-SEM, which has now been commercialised as 3View (Gatan, USA), has the advantage of allowing imaging of large volumes, currently only limited by the physical constraints of the in-chamber ultramicrotome (Marx, 2013). With optimal specimens, lateral resolution has been reported down to 5 nm (Vihinen et al., 2013) and section cutting thickness down to 25 nm (Briggman et al., 2011; Friedrich et al., 2013; Vihinen et al., 2013). FIB-SEM, while being limited in the volume that can be assessed, has the advantage of providing greatly increased axial resolution, reportedly down to 3 nm (Wei et al., 2012). These recent advances have vastly improved our ability to reveal high-resolution three-dimensional information about ultrastructure.

The aim of the work presented in this chapter was therefore to build high-resolution 3D models of intracellular amastigotes in order to determine amastigote positioning and to precisely define the connectivity between the amastigote flagellum and the parasitophorous vacuole membrane, towards elucidating the role of this organelle in parasite-host communication.

3.2 Results

3.2.1 Optimisation of 3View sample preparation protocol

In order to investigate the question of amastigote orientation within parasitophorous vacuoles, bone marrow-derived macrophages were infected with wild type *L. mexicana* stationary phase promastigotes as described in section 2.4 and fixed at 24 and 72 hours post-infection. The fixed samples were prepared as described in section 2.6.3 and imaged by serial block-face scanning electron microscopy (SBF-SEM)/ 3View to capture 3-dimensional information. SBF-SEM produces micrographs which more closely resemble TEMs than SEMs. However, TEM and SBF-SEM differ in the types of electrons detected and how these contribute to contrast in the image, and there are therefore different requirements for sample preparation. As the name suggests, TEM detects electrons that are transmitted through a sample; contrast therefore depends on differences in density in different parts of the sample, as regions of lower

density will allow more electrons to be transmitted, translating to lighter regions in the micrograph (Burge, 1973). In biological samples, there is generally little difference in density between different structures within the area of interest, and these therefore need to be differentially stained with heavy metals to produce contrast in the micrograph (Burge, 1973). SBF-SEM is obviously a scanning electron microscopy technique meaning that electrons do not have to pass through the sample to be detected. With conventional SEM, low-energy secondary electrons are detected as they are knocked out of the electron shells of atoms in the sample by the electron beam (Seiler, 1983). This is therefore independent of sample density and instead relies on the differential ability of these secondary electrons to escape from depressions or projections in the sample to produce contrast, and consequently provides an image of the sample surface topography (Seiler, 1983). With SBF-SEM, however, yet another type of electron is detected: high-energy backscattered electrons. These occur when the electron beam collides with the nuclei of atoms in the sample and is deflected back (Denk and Horstmann, 2004). As is the case with TEM, this technique relies on differences in sample density to produce contrast, but it has different requirements in terms of how much contrast is produced and the need for conductivity in the sample (Denk and Horstmann, 2004).

Specific optimisation of the sample preparation protocol was therefore required to produce enough contrast for structures of interest to be discerned. SBF-SEM specific protocols have already been defined for introducing maximal contrast and conductivity into samples (Deerinck et al., 2010; Tapia et al., 2012). However, these techniques have mainly been optimised for imaging of brain tissue, which represents a dense sample that becomes highly conductive when stained (Peddie and Collinson, 2014). Imaging of less dense samples, and in particular of cell suspensions, presents new challenges in terms of sensitivity to electron dose due to regions of low-conductivity and the accumulation of local negative charge, producing imaging artefacts (Peddie and Collinson, 2014). Technical advances such as the availability of variable pressure systems, which inject nitrogen gas into the vacuum chamber to neutralise the charge on the sample, provide some relief from this issue (Moncrieff et al., 1978; Robinson, 1975). However, introduction of gas into the vacuum chamber also reduces image resolution (Moncrieff et al., 1978; Robinson, 1975).

We therefore resolved to optimise existing SBF-SEM sample preparation protocols for use with cell suspension samples, to minimise the need for variable pressure, and thus retain high resolution. The protocol defined by Deerinck et al. (2010) for SBF-SEM imaging of mammalian tissue was adapted for use on *Leishmania* and *Leishmania*-infected macrophage cell pellets. This starting protocol was selected for its enhanced membrane contrast (Deerinck et al., 2010), as the focus of this research was on amastigote positioning, and it was therefore essential to be able to resolve membranes surrounding the amastigote and the parasitophorous vacuole. The major optimisation requirement for our samples was in increasing the conductivity of regions in between the pelleted cells. This was achieved by embedding pelleted cells into a mix of 4% low-melting point agarose and 4% gelatine before beginning staining

with heavy metals. Embedding in this mix at later points in the protocol was found to be less effective in reducing charging in the sample, as the agarose and gelatine did not stain sufficiently under these conditions. Other minor adaptations to the protocol were included to reduce cellular extraction and to maximise resin infiltration (for finalised protocol, see section 2.6.3). **Figure 3.2** shows comparative 3View images of samples prepared according to the traditional TEM protocol, and according to our optimised 3View protocol. This clearly shows the difference in resolution of both macrophage and *Leishmania* structures observable. Of particular significance to this work was the ability to discern the membranes of the flagellum tip and of the parasitophorous vacuole, though resolution was still limited when these were found in close apposition.

One shortcoming of the finalised protocol was the inability to discern microtubules. A number of conditions were experimented with, either replacing or supplementing steps in the protocol with tannic acid to increase contrast on the microtubules. The tested conditions are summarised in **Table 3.1.** 3 pairs of conditions were tested including tannic acid at different points in the protocol (**Table 3.1 A-B, C-D, & E-F**). Each pair consisted of one sample prepared in sodium cacodylate buffer and one prepared in PIPES buffer. PIPES buffer has previously been shown to improve retention of cellular material (Baur and Stacey, 1977), and we hypothesised that this might result in increased staining of the cytoplasm under the extensive heavy metal staining requirements of the 3View preparation protocol, which could make it harder to discern microtubules. Conditions were therefore duplicated with samples prepared in either sodium cacodylate buffer or PIPES buffer to determine if differential extraction of cellular material affected the ability to discern microtubules. The previously optimised protocol was included as a control (**Table 3.1 G**).

A comparison of conditions A (cacodylate buffer) and B (PIPES buffer), which replaced the usual thiocarbohydrazide (TCH) incubation step in the protocol with 1% tannic acid, showed no significant difference in extraction of cellular materials or contrast resulting from the difference in buffer (**Figure 3.3 A).** Further comparison was therefore only carried out on the conditions prepared in PIPES buffer (B, D, F and G; **Figure 3.3 B**). Conditions B and D, which comprised tannic acid incubations instead of the TCH step or in the buffered fixative, respectively, appeared to produce an increase in the beam-reactivity of the sample, meaning that the samples were extremely unstable and could not be imaged at high magnifications (**Figure 3.3 B**). It is unclear why this should be the case, as increased heavy metal deposition in the sample generally increases sample stability. Imaging of conditions F and G at higher magnifications showed that addition of tannic acid after the TCH step (condition F) slightly increased microtubule staining as compared to the control protocol (condition G; **Figure 3.3 B inset images**). However, this was not sufficient to resolve individual microtubules. This sample preparation condition additionally appeared to reduce the overall contrast between structures and the ability to resolve membranes. Given the focus of the current 3View analyses on amastigote positioning, it was deemed most important to be able to resolve membranes and the tannic acid step was therefore not included in

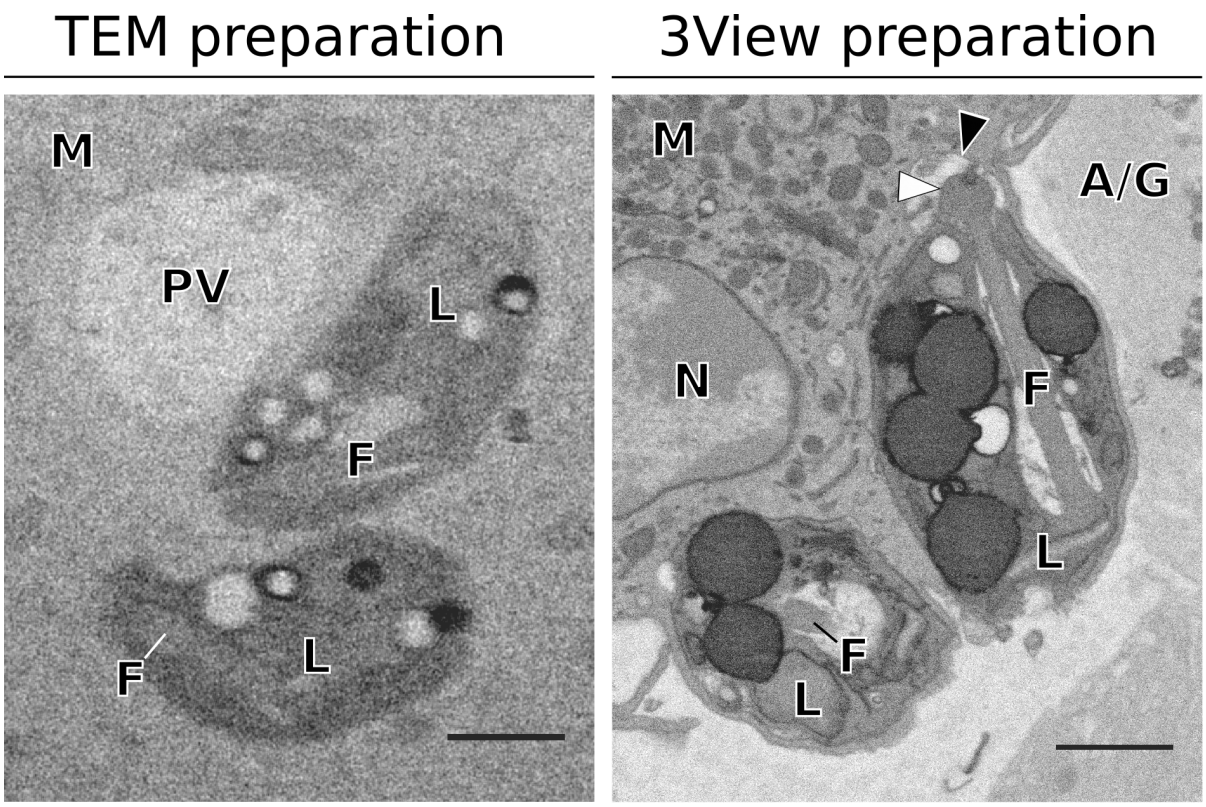


Figure 3.2. 3View imaging of TEM prepared or 3View prepared samples. Image of TEM prepared sample shows two *L. mexicana* amastigotes (L) inside of a macrophage (M), with a visible parasitophorous vacuole (PV); the flagella (F) of both amastigotes are visible; note that no membranes are discernible. Image of 3View prepared sample shows two *L. mexicana* amastigotes (L) inside of a macrophage (M), with a visible macrophage nucleus (N); the flagella (F) of both amastigotes are visible; both the flagellar membrane (white arrow) and the parasitophorous vacuole membrane (black arrow) can be discerned. The pelleted cells are embedded in a mix of 4% agarose and 4% gelatine (A/G) to reduce beam reactivity in areas between cells. Scale bars = 1 µm.

Table 3.1. 3View sample preparation conditions tested for improving microtubule resolution. Paired conditions A-B, C-D and E-F test tannic acid staining at different stages in the protocol. Each pair contains one sample prepared in Sodium Cacodylate buffer and one sample prepared in PIPES buffer. Condition G represents control condition, which is protocol as previously optimised.

	A	B	C	D	E	F	G
Primary Fix	2.5% glut in culture - 3 mins	2.5% glut in culture - 3 mins	2.5% glut in culture - 3 mins	2.5% glut in culture - 3 mins	2.5% glut in culture - 3 mins	2.5% glut in culture - 3 mins	2.5% glut in culture - 3 mins
Buffered Fix	2.5% glut + 2% PFA in 100mM cacodylate + 2mM CaCl2 - over weekend	2.5% glut + 2% PFA in 100mM PIPES + 2mM CaCl2 - over W/E	2.5% glut + 2% PFA + 0.1% tannic acid in 100mM cacodylate + 2mM CaCl2 - over W/E	2.5% glut + 2% PFA + 0.1% tannic acid in 100mM PIPES + 2mM CaCl2 - over weekend	2.5% glut + 2% PFA in 100mM cacodylate + 2mM CaCl2 - over W/E	2.5% glut + 2% PFA in 100mM PIPES + 2mM CaCl2 - over W/E	2.5% glut + 2% PFA in 100mM PIPES + 2mM CaCl2 - over W/E
Wash	Wash 5x30min in 100mM cacodylate + 2mM CaCl2; 4th wash +1% glycine	Wash 5x30min in 100mM PIPES + 2mM CaCl2; 4th wash + 1% glycine	Wash 5x30min in 100mM cacodylate + 2mM CaCl2; 4th wash +1% glycine	Wash 5x30min in 100mM PIPES + 2mM CaCl2; 4th wash + 1% glycine	Wash 5x30min in 100mM cacodylate + 2mM CaCl2; 4th wash +1% glycine	Wash 5x30min in 100mM PIPES + 2mM CaCl2; 4th wash + 1% glycine	Wash 5x30min in 100mM PIPES + 2mM CaCl2; 4th wash + 1% glycine
Agarose/gelatin	Embed in 4% low melting point agarose + 4% gelatin from porcine skin, type A	Embed in 4% low melting point agarose + 4% gelatin from porcine skin, type A	Embed in 4% low melting point agarose + 4% gelatin from porcine skin, type A	Embed in 4% low melting point agarose + 4% gelatin from porcine skin, type A	Embed in 4% low melting point agarose + 4% gelatin from porcine skin, type A	Embed in 4% low melting point agarose + 4% gelatin from porcine skin, type A	Embed in 4% low melting point agarose + 4% gelatin from porcine skin, type A
Osmium (1)	1h 2% osmium tetroxide + 1.5% potassium ferricyanide	1h 2% osmium tetroxide + 1.5% potassium ferricyanide	1h 2% osmium tetroxide + 1.5% potassium ferricyanide	1h 2% osmium tetroxide + 1.5% potassium ferricyanide	1h 2% osmium tetroxide + 1.5% potassium ferricyanide	1h 2% osmium tetroxide + 1.5% potassium ferricyanide	1h 2% osmium tetroxide + 1.5% potassium ferricyanide
Wash	Wash 5 x 5 mins in ddH2O	Wash 5 x 5 mins in ddH2O	Wash 5 x 5 mins in ddH2O	Wash 5 x 5 mins in ddH2O	Wash 5 x 5 mins in ddH2O	Wash 5 x 5 mins in ddH2O	Wash 5 x 5 mins in ddH2O
TCH	-	-	20 mins TCH	20 mins TCH	20 mins TCH	20 mins TCH	20 mins TCH
Wash	-	-	Wash 5 x 5 mins in ddH2O	Wash 5 x 5 mins in ddH2O	Wash 5 x 5 mins in ddH2O	Wash 5 x 5 mins in ddH2O	Wash 5 x 5 mins in ddH2O
Tannic Acid	2h 1% tannic acid	2h 1% tannic acid	-	-	2h 1% tannic acid	2h 1% tannic acid	-
Wash	Wash 5 x 5 mins in ddH2O	Wash 5 x 5 mins in ddH2O	-	-	Wash 5 x 5 mins in ddH2O	Wash 5 x 5 mins in ddH2O	-
Osmium (2)	30 mins 2% osmium tetroxide	30 mins 2% osmium tetroxide	30 mins 2% osmium tetroxide	30 mins 2% osmium tetroxide	30 mins 2% osmium tetroxide	30 mins 2% osmium tetroxide	30 mins 2% osmium tetroxide
Wash	Wash 5 x 5 mins in ddH2O	Wash 5 x 5 mins in ddH2O	Wash 5 x 5 mins in ddH2O	Wash 5 x 5 mins in ddH2O	Wash 5 x 5 mins in ddH2O	Wash 5 x 5 mins in ddH2O	Wash 5 x 5 mins in ddH2O
Uranyl Actetate	1% uranyl acetate overnight	1% uranyl acetate overnight	1% uranyl acetate overnight	1% uranyl acetate overnight	1% uranyl acetate overnight	1% uranyl acetate overnight	1% uranyl acetate overnight
Wash	Wash 5 x 5 mins in ddH2O	Wash 5 x 5 mins in ddH2O	Wash 5 x 5 mins in ddH2O	Wash 5 x 5 mins in ddH2O	Wash 5 x 5 mins in ddH2O	Wash 5 x 5 mins in ddH2O	Wash 5 x 5 mins in ddH2O
Lead Aspartate	-	-	30 mins lead aspartate	30 mins lead aspartate	30 mins lead aspartate	30 mins lead aspartate	30 mins lead aspartate
Wash	-	-	Wash 5 x 5 mins in ddH2O	Wash 5 x 5 mins in ddH2O	Wash 5 x 5 mins in ddH2O	Wash 5 x 5 mins in ddH2O	Wash 5 x 5 mins in ddH2O
EtOH dehydration	30%, 50%, 70%, 90%, 100%, 100% (dry) EtOH, AC, AC: 10min each	30%, 50%, 70%, 90%, 100%, 100% (dry) EtOH, AC, AC: 10min each	30%, 50%, 70%, 90%, 100%, 100% (dry) EtOH, AC, AC: 10min each	30%, 50%, 70%, 90%, 100%, 100% (dry) EtOH, AC, AC: 10min each	30%, 50%, 70%, 90%, 100%, 100% (dry) EtOH, AC, AC: 10min each	30%, 50%, 70%, 90%, 100%, 100% (dry) EtOH, AC, AC: 10min each	30%, 50%, 70%, 90%, 100%, 100% (dry) EtOH, AC, AC: 10min each
Durcupan Infiltration	25% 2h, 50% o/n, 75% 2h, 100% 8h, 100% o/n, 100% 4h, 100% o/n, 100% 4h	25% 2h, 50% o/n, 75% 2h, 100% 8h, 100% o/n, 100% 4h, 100% o/n, 100% 4h	25% 2h, 50% o/n, 75% 2h, 100% 8h, 100% o/n, 100% 4h, 100% o/n, 100% 4h	25% 2h, 50% o/n, 75% 2h, 100% 8h, 100% o/n, 100% 4h, 100% o/n, 100% 4h	25% 2h, 50% o/n, 75% 2h, 100% 8h, 100% o/n, 100% 4h, 100% o/n, 100% 4h	25% 2h, 50% o/n, 75% 2h, 100% 8h, 100% o/n, 100% 4h, 100% o/n, 100% 4h	25% 2h, 50% o/n, 75% 2h, 100% 8h, 100% o/n, 100% 4h, 100% o/n, 100% 4h
Embedding	Embed in 100% Durcupan	Embed in 100% Durcupan	Embed in 100% Durcupan	Embed in 100% Durcupan	Embed in 100% Durcupan	Embed in 100% Durcupan	Embed in 100% Durcupan

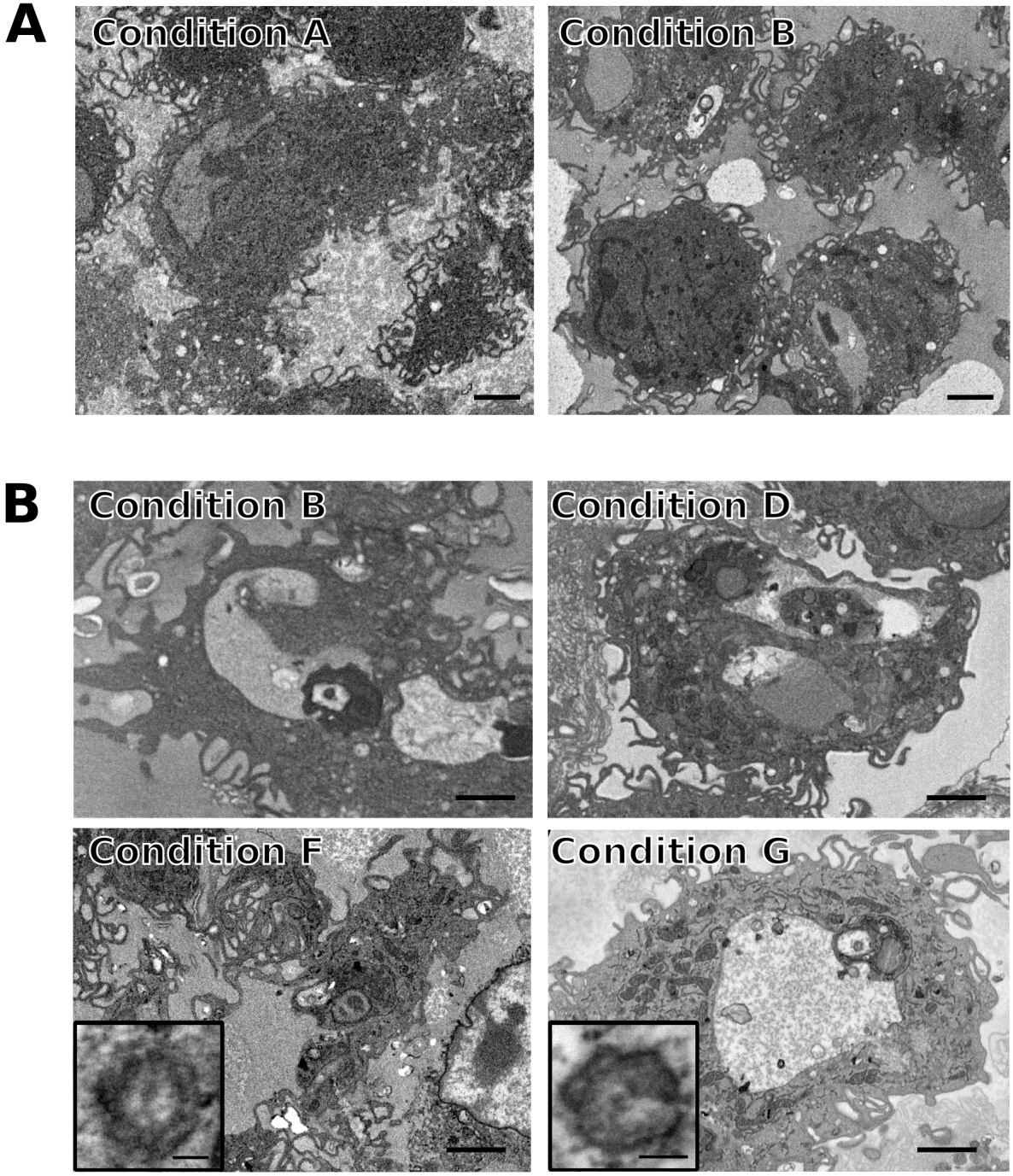


Figure 3.3. 3View sample preparation conditions tested for improving microtubule resolution. (A) Comparison of samples prepared in either Sodium Cacodylate buffer (condition A) or in PIPES buffer (condition B). Different buffers showed no significant difference in extraction of cellular materials or contrast within samples. Scale bars = 2 µm. **(B)** Samples prepared in PIPES buffer. Condition B: 1% tannic acid instead of TCH incubation. Condition D: 0.1% tannic acid in buffered fixative. Condition F: 1% tannic acid after TCH incubation. Condition G: control; previously optimised protocol without tannic acid. Main image scale bars = 2 µm. Inset images in conditions F and G show flagellar profiles, scale bars = 100 nm.

the final protocol. The ability to resolve microtubules is not critical for this research, but future 3View analyses of *Leishmania* may benefit from revisiting this issue.

3.2.2 *L. mexicana* amastigotes are observed in three main orientations within parasitophorous vacuoles

Four final datasets were produced by 3View: two image stacks of 24-hour infected macrophages and two of 72-hour infected macrophages. The magnification, lateral resolution, slice number and thickness, and final volume are summarised in **Table 3.2.** See **Supplementary Video S3.1** for an example of 3View stack data.

Table 3.2. Details of final 3View datasets

Time Point	Magnification	Resolution	Slices	Volume (x*y*z µm)
24 hours	x3500	8.0 nm	220 x 100 nm	64.16 x 64.16 x 22.00
24hours	x3500	5.4 nm	323 x 100 nm	64.80 x 64.80 x 32.30
72 hours	x5000	5.6 nm	398 x 50 nm	40.49 x 42.00 x 19.90
72 hours	x3500	5.4 nm	326 x 100 nm	64.80 x 64.80 x 32.60

The 3View image stacks were used to reconstruct large volumes of infected parasitophorous vacuoles. In total 108 infected vacuoles were reconstructed across the four datasets. The aim was to provide 3-dimensional information which had not previously been available, to reconcile the conflicting views of amastigote positioning previously observed in different ultrastructural studies. The reconstructions allowed for grouping of infected vacuoles into three main amastigote position / PV shape combinations:

1. Amastigotes bound within tight vacuoles, with contact on all sides (referred to as tight; **Fig 3.4 A**),

2. Amastigotes embedded into the PV membrane by their posterior ends, with no flagellar contact (referred to as open; **Fig 3.4 B**), and

3. Amastigotes with both their posterior ends and flagellar tips in contact with the PV membrane, with the main vacuole volume bulging laterally away from the amastigote (referred to as bulging; **Fig 3.4 C**).

These 3-dimensional reconstructions provide an explanation for the different orientations previously observed. It is easy to imagine how single ultrathin slices showing cross sections at different angles could present different views; for example, a bulging vacuole sectioned in different ways could suggest posterior-only or tip-only contact, despite the reality being contact at both ends (**Fig 3.4 D**). It is worth

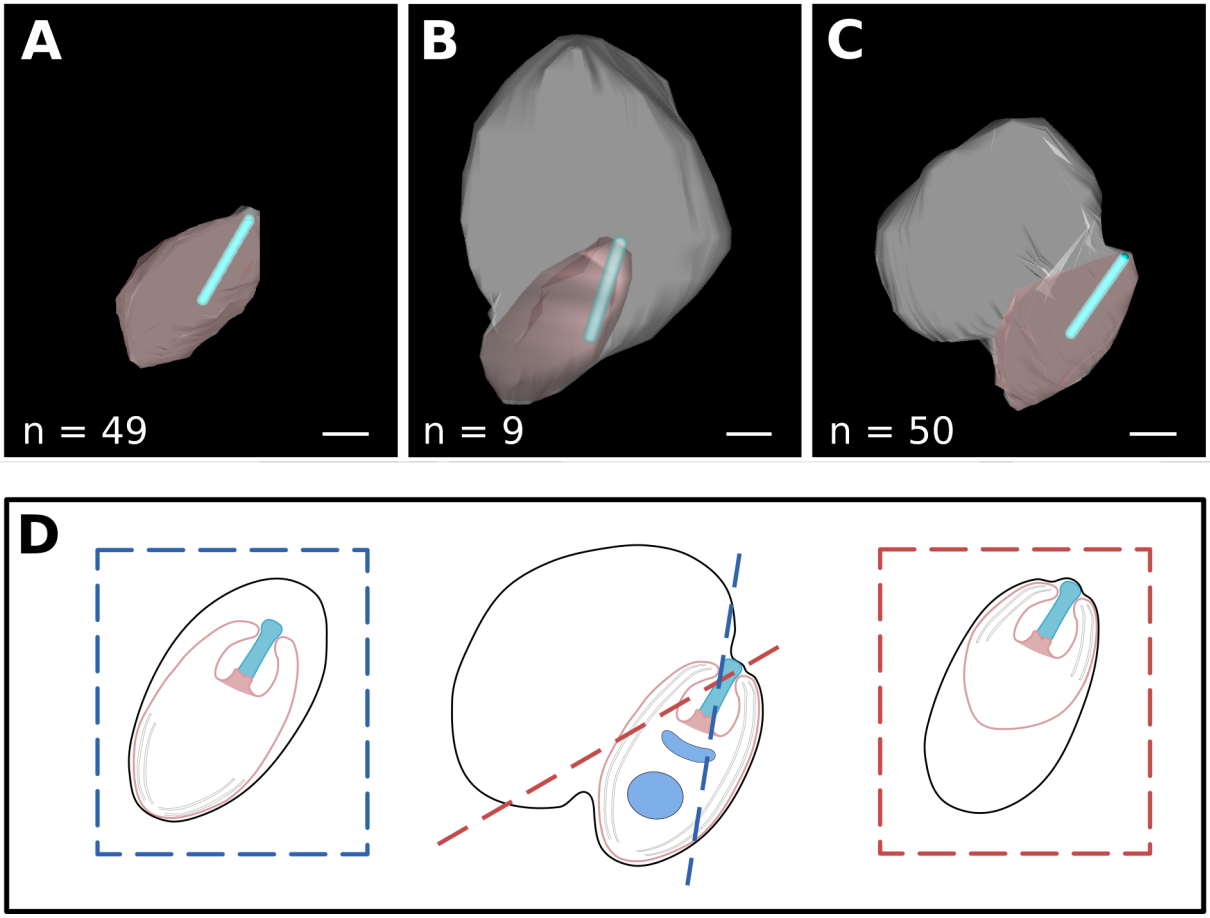


Figure 3.4. Different amastigote positions and parasitophorous vacuole shapes observed by 3View microscopy. Reconstructions of amastigotes within: (A) tight vacuole, membrane contact on all sides; (B) open vacuole, posterior end embedded in PV membrane, no flagellar contact; (C) bulging vacuole, posterior end and flagellar tip contact, vacuole volume bulging away from amastigote. White = PV; pink = amastigote; cyan = flagellum. Scale bars = 1 µm. (D) Theory of how observed vacuoles could provide differing views of amastigote attachment depending on sectioning angle. Different cross-sections through a bulging vacuole show views that give the impression of posterior-only (blue-dashed) or tip-only (red-dashed) contact.

noting, however, that the 3D reconstructions show that posterior-only contact does occur, while no evidence was observed of tip-only contact. The results also provide evidence of a previously unobserved orientation, as the third vacuole type with a bulging volume and both flagellum and posterior end contact had not previously been described. It was hypothesised that this was due to the difficulty of visualising this vacuole type without the use of 3-dimensional techniques, which had not previously been accessible.

It was nevertheless important to ensure that this was representative of the situation in live cells, and that the point of contraction (**Fig 3.5 A**) was not simply an artefact resulting from collapse of the PV during fixation. To this end, live cell imaging was employed in conjunction with Airyscan processing (Engelmann et al., 2014; Huff, 2015), to validate the result. Airyscan is a new detection technique for use with confocal laser scanning microscopy. The detector is formed of 32 hexagonal detector elements, each of which collects a pinhole-like image (Huff, 2015). The central element lies on the optical axis and collects an image similar to what would be collected by traditional scanning confocal microscopy (Huff, 2015). Each of the other detectors additionally collects an image, but these images are displaced relative to the optical axis (Huff, 2015). Airyscan detection is able to significantly increase signal-to-noise by using the surrounding elements to re-map light that would be rejected by traditional confocal imaging, allowing for resolution down to 140 nm in the x and y dimensions and 400 nm in the z dimension (Huff, 2015).

Murine bone marrow derived macrophages were infected with wild-type *L. mexicana* promastigotes expressing an endogenous C-terminal enhanced green fluorescent protein (eGFP) tag on the plasma membrane Glucose Transporter 2 (GT2; LmxM.36.6290) (Burchmore et al., 2003), and an endogenous C-terminal mCherry tag on the flagellar membrane Small Myristoylated Protein 1 (SMP1; LmxM.20.1310) (Tull et al., 2004). Infected macrophages were then allowed to take up blue fluorescent dextran for 24 hours before imaging in order to fill the empty spaces within the parasitophorous vacuoles and thus assess vacuole shape. Fluorescent dextran conjugates are membrane-impermeant unless taken up by host cells by fluid-phase endocytosis (Swanson, 1988). They accumulate in lysosomal compartments (Swanson, 1988), making them ideal for studies on the parasitophorous vacuole. Dextran signals were observed as bulging areas closely abutted to amastigotes (**Fig 3.5 B**), and reconstructions showed that the dextran signal often wrapped around the amastigotes (**Fig 3.5 C**). These results are consistent with what one would expect to see for vacuoles that remained tight around most of the amastigote surface, and then bulged out providing an area that could be filled by endocytosed dextran. However, it was not entirely possible, based on these data alone, to exclude the possibility that the dextran could be contained within separate, closely-abutting vacuoles to those containing the amastigotes.

In order to exclude this possibility, it was necessary to use a macrophage cell line containing a fluorescent tag in the parasitophorous vacuole membrane. RAW 264.7 macrophages with a stably GFP-

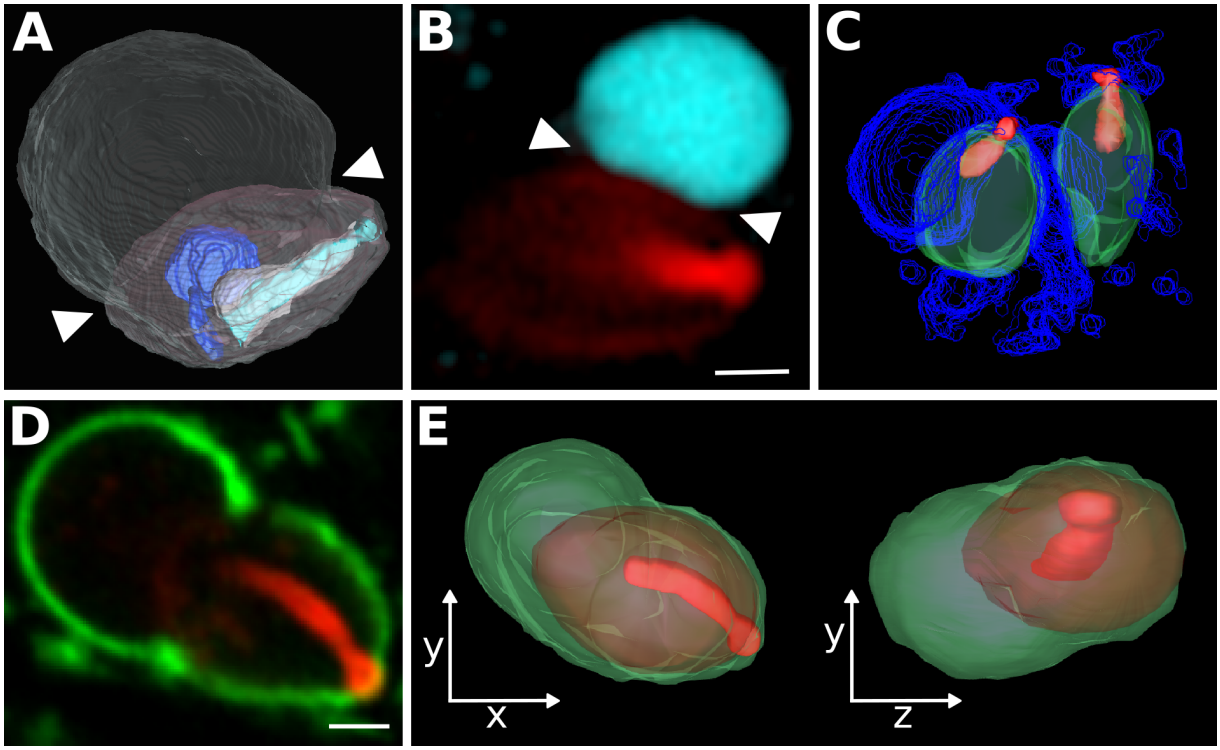


Figure 3.5. Live cell imaging confirms the presence of previously-unobserved bulging parasitophorous vacuoles. (A) 3View reconstructions of bulging vacuole type. White = PV; pink = amastigote cell surface; cyan = flagellum; blue = nucleus and kinetoplast. It was necessary to confirm that the contraction point (arrows) of the bulging vacuoles observed by 3View were not fixation artefacts. **(B)** Bulging type vacuole observed in live cells by Airyscan confocal microscopy. Red = flagellar membrane (SMP1::mCherry); cyan = dextran. Fluorescent dextran uptake by infected macrophages produced bulging areas closely abutted to amastigotes, with interfaces (arrows) reminiscent of the contraction observed by 3View; scale bar = 1 µm. **(C)** Reconstruction of fluorescent dextran signals observed in live cells by Airyscan confocal microscopy shows that these areas wrap around amastigotes. Red = flagellar membrane (SMP1::mCherry); green = amastigote cell surface membrane (GT2::GFP); blue = dextran **(D)** Airyscan confocal image of *Leishmania*-infected RAW 264.7 LAMP1-GFP macrophages show fluorescent PV membrane signals consistent with bulging vacuoles. Red = flagellar membrane (SMP1::mCherry); green = PV membrane (LAMP1::GFP). Scale bar = 1 µm. **(E)** 3D reconstruction cells shown in (D); views from different angles confirm bulging vacuole shape. Red = flagellar membrane (SMP1::mCherry); green = PV membrane (LAMP1::GFP).

tagged lysosomal-associated membrane protein 1 (LAMP1) were kindly donated by the Michael Hensel lab, Universität Osnabrück, Germany (Krieger et al., 2014). The RAW 264.7 LAMP1-GFP macrophages were infected with Cas9T7 *L. mexicana* cells expressing a C-terminal mCherry tag on the flagellar membrane protein SMP1 (LmxM.20.1310) (Tull et al., 2004) and were imaged 72 hours post infection. 18 out of the 48 infected vacuoles imaged by Airyscan detection showed a clear bulging shape, with the LAMP1-GFP signal tightly surrounding a portion of the amastigote, but with a region bulging away from the parasite (**Fig 3.5 D & E**). These data therefore confirm that the bulging vacuole shape observed by 3View is representative of the live situation and not simply a fixation artefact.

3.2.3 Different vacuole types may represent steps in the progression of vacuole maturation

Based on the 3View data, we postulated that the different vacuole types observed could represent sequential steps in the progression of vacuole formation. This hypothesis was based on a number of factors. The most convincing argument for this based on the 3View data is the analysis of PV volume; different vacuole types showed a clear trend of increasing volume from tight vacuoles, through bulging vacuoles, to open vacuoles (mean volumes = 9.9 μm^3, 28.0 μm^3 and 65.4 μm^3 respectively; **Fig 3.6 A**). Despite far fewer open vacuoles being observed than either of the other categories (tight = 49; bulging = 50; open = 9), a Spearman's Rank analysis suggested a statistically significant positive correlation between PV type (1 = tight; 2 = bulging; 3 = open) and volume ($\rho = 0.707199$; $p < 0.001$).

This hypothesis was also supported by the occurrence of multi-occupancy vacuoles within the different reconstructed vacuole categories. Vacuoles which were tight around the entire amastigote were never observed to contain more than a single parasite (**Fig 3.6 B**), while only 6% (3 out of 50) of the reconstructed bulging vacuoles (**Fig 3.6 B**) but over 50% (5 out of 9) of the reconstructed open vacuoles (**Fig 3.6 B & C**) were found to contain more than a single amastigote. These multi-occupancy vacuoles could arise either as a result of amastigote division after phagocytosis, or through fusion of parasitophorous vacuoles containing individual amastigotes (Real and Mortara, 2012; Real et al., 2010). In either case, these events would be expected to occur at later stages in the infection process than single occupancy vacuoles.

Finally, 3 out of the 9 reconstructed open vacuoles contained amastigotes that were in the process of division, as determined by the presence of two flagella. There were also dividing amastigotes observed in the tight and bulging vacuoles (3 and 1, respectively), but these represented a much smaller subset of the total number of vacuoles reconstructed, and this could therefore be indicative of the open vacuoles representing a later stage in the infection. Given the small number of open vacuoles upon which these observations are based, it is important to consider the possibility that these reconstructed

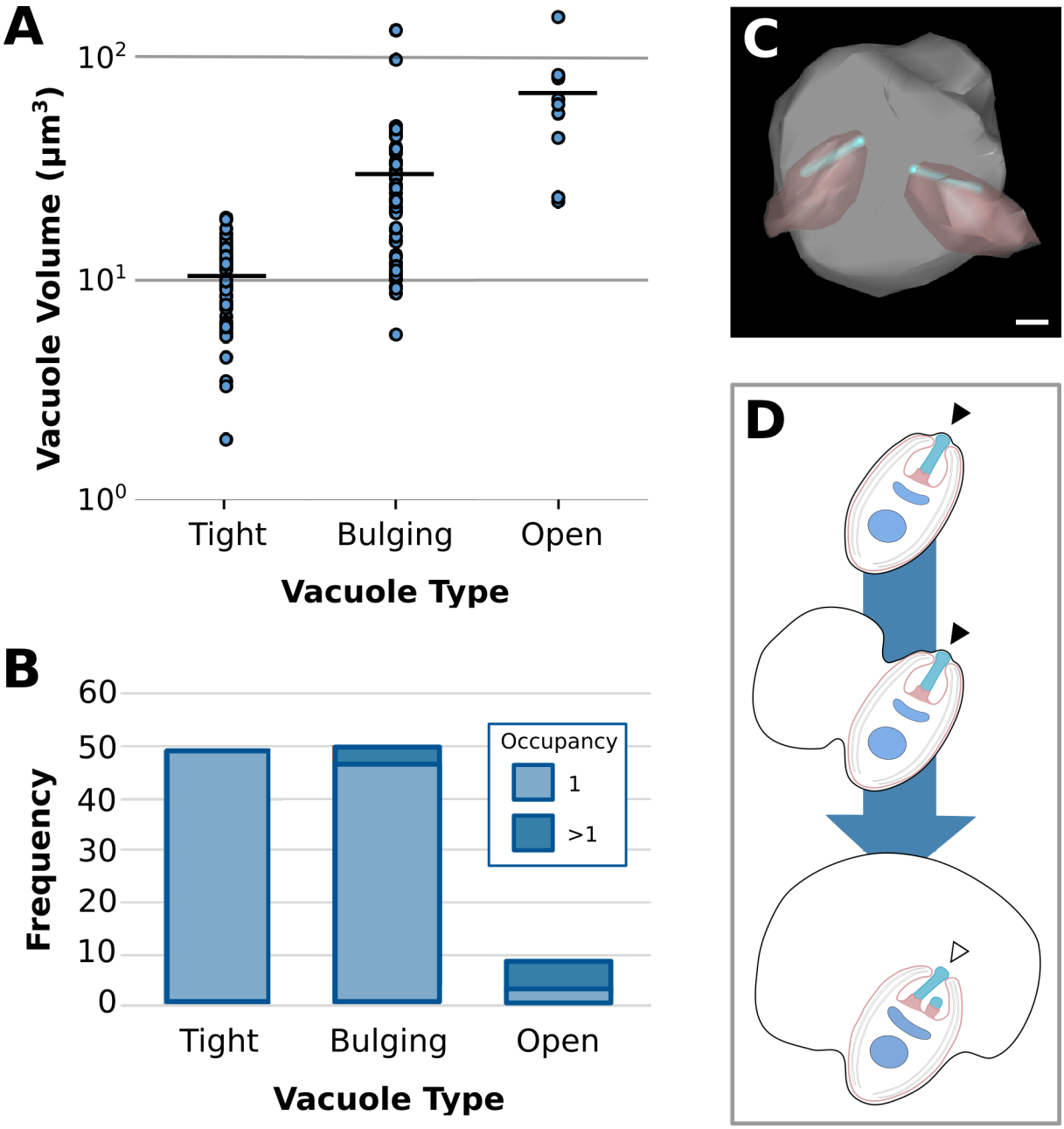


Figure 3.6 3View data suggest that different vacuole types may represent steps in progression of vacuole maturation. (A) Vacuole volume increases from tight to bulging to open vacuoles. Graph shows individual data points, each representing a fully reconstructed vacuole (n = 108), and a bar representing mean volume. Spearman's Rank analysis shows a statistically significant positive correlation between PV type (1 = tight; 2 = bulging; 3 = open) and volume ($\rho = 0.707199$; $p < 0.001$). (B) Occurrence of multi-occupancy vacuoles in different vacuole types. (C) Reconstruction of a multi-occupancy open vacuole. Scale bar = 1 µm. (D) Proposed model of amastigote positioning during parasitophorous vacuole maturation. Black arrows = flagellar contact with PV membrane. White arrow = no flagellar contact.

vacuoles may not be representative of the entire population of open vacuoles. However, the convergence of these different pieces of evidence has led us to propose a model of parasitophorous vacuole maturation whereby soon after phagocytosis, amastigotes are found within tight vacuoles, which then increase in volume, with the main vacuole volume initially bulging laterally away from the amastigote, before opening out fully (**Fig 3.6 D**). In this model, tip interactions are frequent in the early stages of vacuole development, but infrequent in later stages. Posterior end contact, however, appears to be maintained throughout vacuole maturation. Interestingly, this suggests that parasite orientation changes with vacuole development.

While the 3View data indicate that vacuole maturation may progress as defined by this model, it is not possible to confirm this from fixed samples, even by comparison of different time points, given the incidence of parasite egress and re-infection. Indeed, the 3View data summarised herein represent samples that were fixed at either 24 or 72 hours post-infection. Two time points were selected in order to maximise the likelihood of observing all different vacuole types occurring throughout infection. However, the results from each time point were combined and not treated separately because of the inability to discern how long individual macrophages had been infected. Therefore, in order to confirm the hypothesis presented by this model, one would need to observe maturation of individual vacuoles by time-lapse microscopy.

To this end, RAW 264.7 LAMP1-GFP macrophages infected with Cas9T7 SMP1::mCherry *L. mexicana* cells were imaged at 1, 15, and 30 minute intervals for up to 240 minutes per cell. The results showed some evidence of vacuoles progressing from a rounder shape to develop a bulging form (**Fig 3.7**) over 30 minute (**Fig3.7 A**) and 60 minute (**Fig 3.7 B**) intervals. However, there were no clear examples of vacuoles progressing from a characteristically tight form to a bulging form, or from a bulging form to an open form. It is possible that these changes may not occur within the time frames observed. If this is the case, method optimisation will be required to overcome current technical limitations including the limit on the number of image stacks that can be captured due to photo-bleaching of the fluorescent tags, and tracking of individual vacuoles, as the macrophages and amastigotes move significantly over even short time-courses. While the time-lapse imaging cannot, in this case, confirm the proposed model of vacuole formation, the observed results are consistent with this sequence of events.

3.2.4 Amastigotes within tight vacuoles possess membranous flagellar extensions

While the 3View imaging provided the ability to investigate amastigote positioning within the context of whole parasitophorous vacuoles, it was unable to provide the resolution required to assess whether the flagellar contact observed in the tight and bulging vacuoles could be functionally significant or whether this was largely incidental based on the availability of space. Remodelling of host cell structures

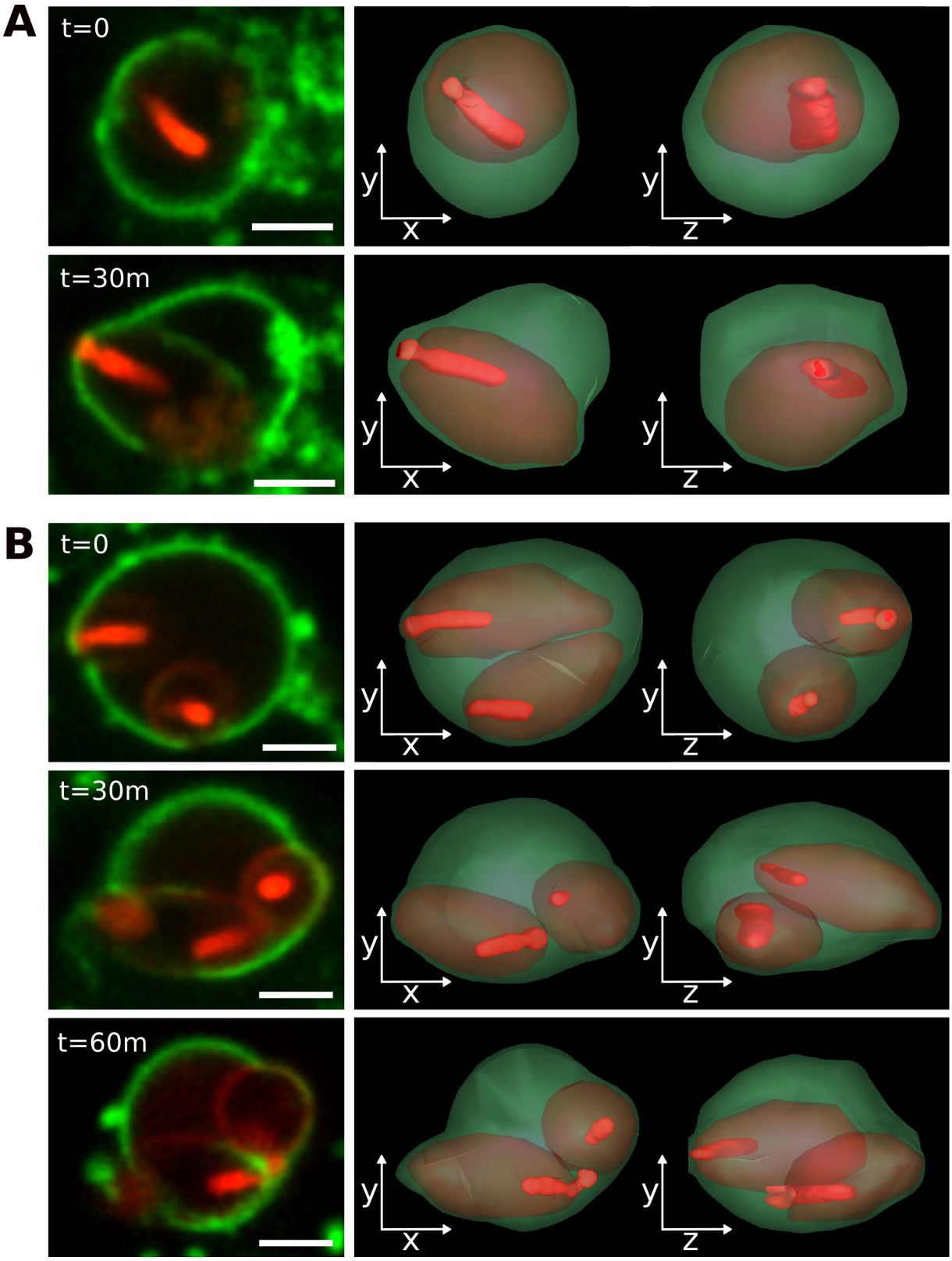


Figure 3.7 Live vacuole progression imaging. *Leishmania*-infected RAW 264.7 LAMP1-GFP macrophages show fluorescent PV membrane signals that develop into a bulging form. Images are each averaged intensities from 9 z-slices. Scale bars = 2 µm. (A) A single occupancy vacuole develops a bulging form over 30 minutes. (B) A multi-occupancy vacuole takes on a bulging form over 60 minutes.

is a common theme amongst intracellular parasites, and we hypothesised that the maintained flagellar contact observed in vacuoles could be required for communication with the macrophage to modulate vacuole development, and in particular to promote increases in vacuole size. To address this possibility, the point of contact between the flagellum and the PV membrane in tight or bulging vacuoles was imaged by TEM tomography, to provide much higher resolution access to this interface. Bone marrow-derived macrophages were infected with wild type *L. mexicana* stationary phase promastigotes as described in section 2.4 and fixed at 24 and 72 hours post-infection. The fixed samples were prepared as described in section 2.6.2 and imaged at tilts of -55° to 55° in 1° increments, in two axes.

In over 50% of the tomograms captured from samples fixed 24 hours post-infection (5 out of 8), the flagellar tips were observed to have narrow tubular extensions of the flagellar membrane, which we termed streamers (**Fig 3.8; Videos S3.2 & S3.3**). These were continuous with the flagellar membrane and did not appear to contain any axonemal components. All examples of streamers were observed in amastigotes bound within tight vacuoles, and the PV membrane closely-followed the contour of the streamers (**Fig 3.8; Videos S3.2 & S3.3**). Streamers were additionally observed by Airyscan imaging of bone marrow derived macrophages infected with stationary phase promastigotes expressing the GT2::eGFP and SMP1::mCherry tags, which were imaged live 24 and 72 hours post-infection. This showed that the streamers were SMP1-positive, confirming that they are derived from the parasite flagellar membrane (**Fig 3.9**). The Airyscan imaging was also used to determine what proportion of amastigotes possessed neat flagellar membranes with no membrane activity (**Fig 3.9 A**), or flagellar membranes exhibiting budding (**Fig 3.9 B**) or streamers (**Fig 3.9 C**). Across both the 24 and 72-hour time points, over 40% (33 out of 79) of the observed amastigotes showed some form of flagellar membrane extrusion, with streamers representing the more common occurrence (**Fig 3.9 D**).

Streamers were seen in many of the 24-hour tomograms but were not observed in any of the 72-hour tomograms (0 out of 13). However, they were still observed at 72-hours post-infection during live-cell imaging. Culture of *L. mexicana* stationary phase promastigotes in DMEM/ 9.1% FCS/ 10ng/ml rh-MCSF (the medium in which macrophage infections are performed) at 34°C for 72 hours resulted in a complete shortening of flagellar length in 96% of observed cells (n = 51) (**Fig 3.9 E**). It is therefore particularly interesting that streamers were still observed at 72 hours post-infection in the Airyscan confocal images. It is worth noting that it is not possible to define time post-infection for individual cells, as amastigotes may have escaped from ruptured macrophages to re-infect new ones, or remained in the medium for a significant duration before being phagocytosed. However, given the nearly ubiquitous presence of short flagella in amastigotes cultured at 34°C for 72 hours, it is reasonable to conclude that the vast majority of intracellular amastigotes observed at 72 hours would have completed flagellar shortening.

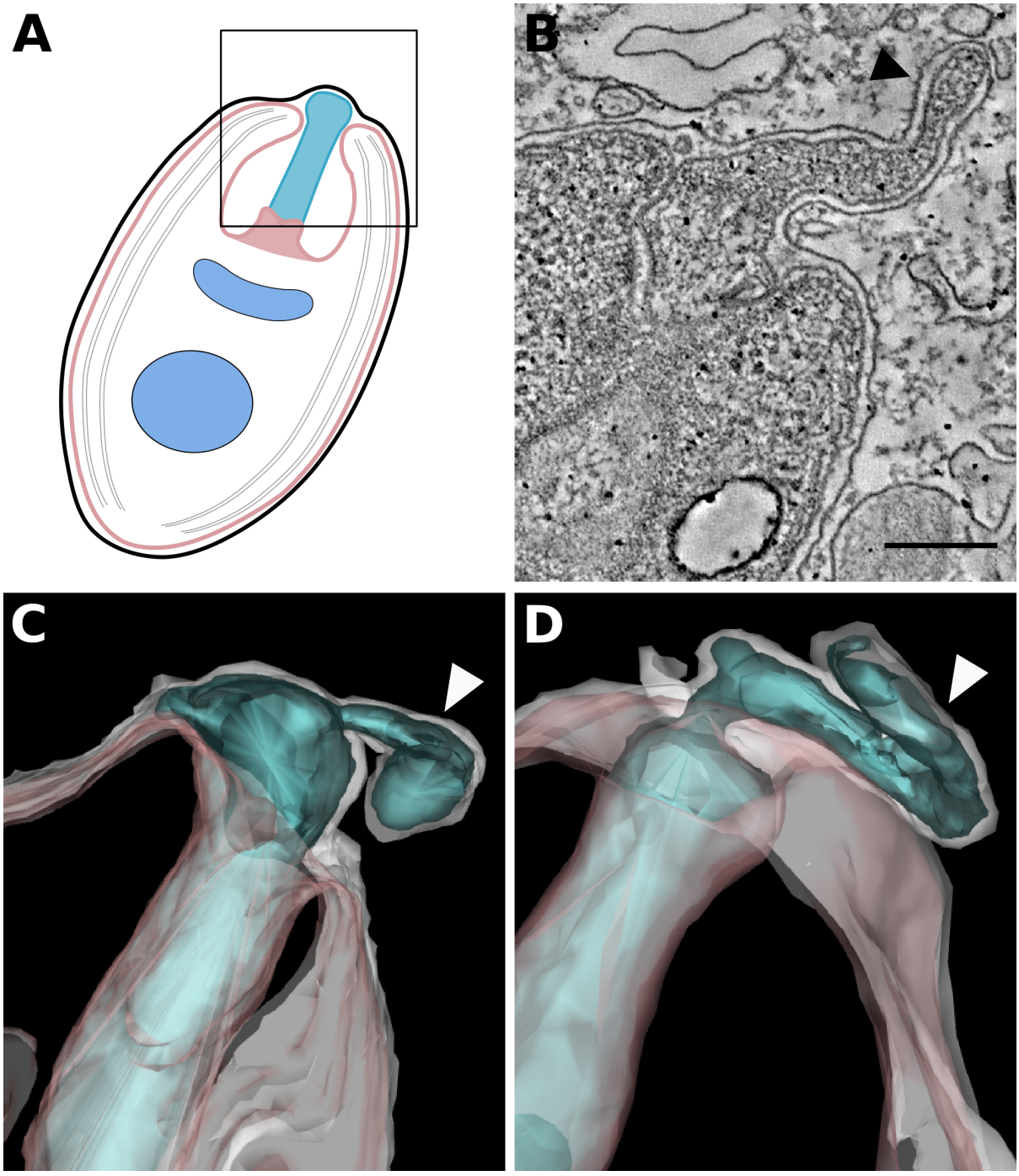


Figure 3.8. Amastigotes within tight vacuoles possess membranous flagellar extensions. (A) Diagram of amastigote within a tight vacuole. Black outline = PV; pink = amastigote cell surface and flagellar pocket membranes; cyan = flagellar membrane; blue = nucleus and kinetoplast. Black box represents region shown in B-D. (B) Single slice from a dual axis tomogram showing a flagellar membrane streamer (black arrow). Scale bar = 200 nm. (C and D) Reconstructions of amastigotes with flagellar membrane streamers (white arrows); PV membrane closely follows contours of streamers. White = PV; pink = amastigote cell surface and flagellar pocket membranes; cyan = flagellar membrane. Tomograms from which C and D are reconstructed can be found in **Supplementary Videos S3.2 and S3.3**.

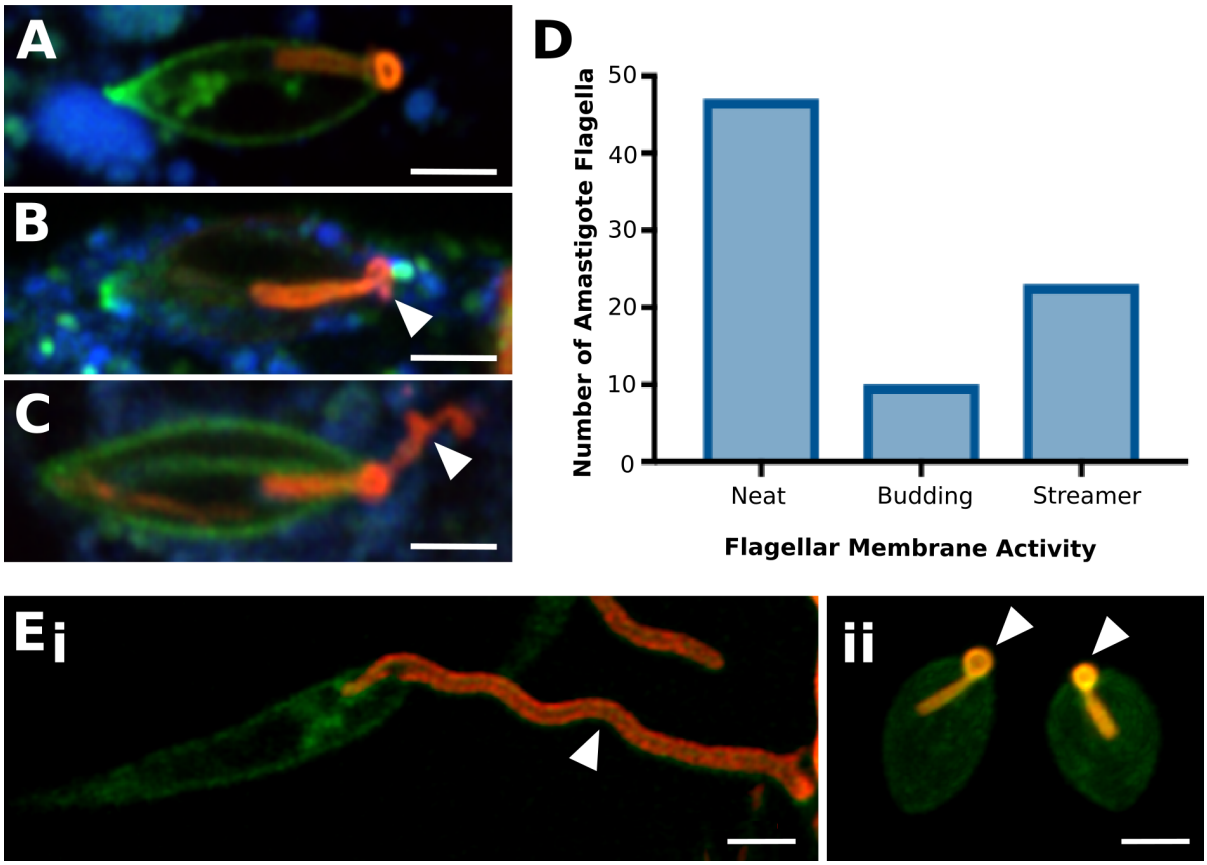


Figure 3.9. Flagellar membrane activity of intracellular amastigotes. (A-C) Airyscan confocal images of intracellular amastigotes expressing the GT2::eGFP cell surface marker (green) and SMP1::mCherry flagellar membrane marker (red). Macrophages additionally contain endocytosed dextran (blue). Intracellular amastigotes exhibit either neat flagellar membranes (A) or flagellar membranes with budding (B; arrow) or streamers (C; arrow). **(D)** Number of amastigotes with neat flagellar membranes or displaying budding or streamers; n = 79. **(E) i)** Stationary phase promastigotes cultured in M199 at 28°C have long flagella (arrow). **ii)** Transfer to DMEM/ 9.1% FCS and culture at 34°C for 72 hours results in complete flagella shortening (arrows) in 96% of observed cells. Scale bars = 2 µm.

3.2.5 Preliminary evidence of vesicular activity

The tomography analysis focused on amastigotes bound within either tight or bulging vacuoles, where the tip of the flagellum was in close proximity to the PV membrane. Open vacuoles were excluded from the analysis because the volume that would need to be imaged to determine activity occurring between the flagellum and PV membrane would be beyond the scope of this technique. However, in a small subset of the imaged tomograms, the flagellum did not appear to be in direct association with the vacuole membrane, and this allowed for preliminary observations of vesicular activity between the flagellar and parasitophorous vacuole membranes.

The clearest example is shown in **Figure 3.10** and in **Supplementary Video S3.4.** In this cell, vesicular structures were observed on both the flagellar membrane and on the PV membrane (**Fig 3.10 A**). Reconstruction of this tomogram showed that the vesicular structures on the flagellum and PV membranes almost appeared to bridge the gap between the two (**Fig 3.10 B**), and that vesicular activity on the PV membrane was particularly focused in the region nearest the flagellar tip (**Fig 3.10 C**). It is not possible to determine from the tomography data whether the vesicular structures are budding from or fusing with the membranes they are associated with and indeed if this represents trafficking in a particular direction. Other tomograms showed vesicular structures between the flagellum tip and PV membrane (**Fig 3.11 A-C**), though in some cases it was not possible to determine which membrane these were associated with (**Fig 3.11 B**).

We once again turned to time-lapse microscopy and Airyscan detection in order to determine the origin of vesicular structures and to look for evidence of incorporation of membrane from one structure into the other. RAW 264.7 LAMP1-GFP macrophages infected with Cas9T7 SMP1::mCherry *L. mexicana* cells were imaged at 1 minute intervals for up to 10 minutes per cell. Although budding of vesicular structures from the flagellar membrane was observed in individual frames (**Fig 3.12**), it was difficult to determine whether abscission occurred. It was also particularly challenging to assess activity of the PV membrane. While the LAMP1::GFP provides delimitation of the PV border, the fluorescent signals from other lysosomal compartments within the macrophage obscure activity which is specifically associated with this vacuole membrane. In many of the observed cells, the LAMP1 signal was denser in the region of the flagellar tip than around the rest of the amastigote (**Fig 3.12**), but the signal could not be resolved into budding structures. The SMP1::mCherry and LAMP1::GFP signals were seen to co-localise in some cases, as determined by the observation of yellow signal in regions of overlap (**Fig 3.12**). However, this may represent a limit on the resolution of this technique.

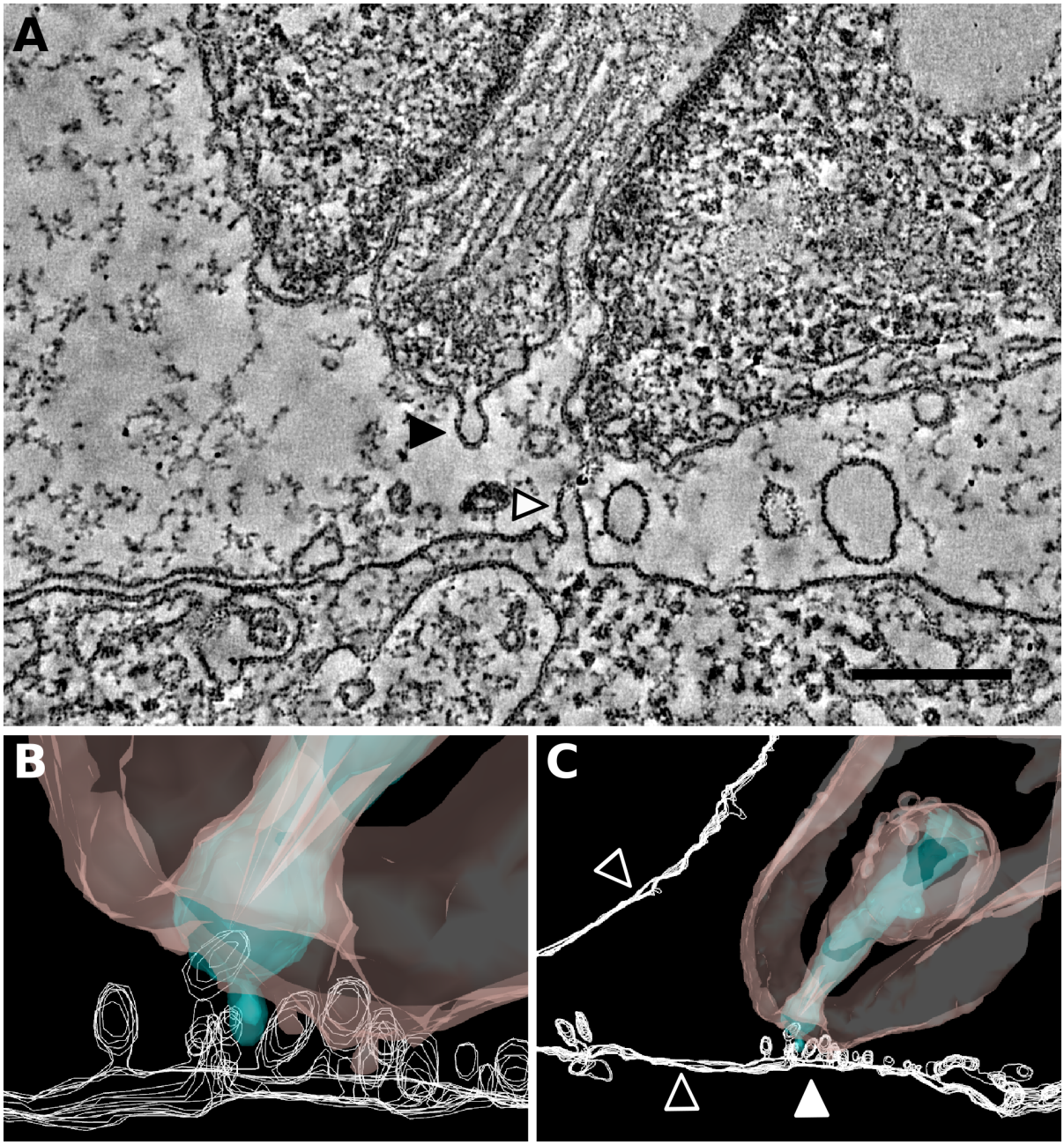


Figure 3.10. Preliminary evidence of vesicular activity on flagellar and PV membranes. (A) Single slice from a dual axis tomogram showing vesicular structures on both the flagellar (black arrow) and PV (white arrow) membranes. Scale bar = 200 nm. Full tomogram in Supplementary Video S3.4 (B) Tomogram reconstruction shows vesicular structures bridging gap between flagellum tip and PV membrane. Vesicles are represented in the same colour as the membrane they are associated with but this does not necessarily denote origin. (C) Wider view of tomogram reconstruction shows a particular focus of vesicular activity on the PV membrane in the region nearest the flagellum (filled arrow) as compared to other areas of the PV membrane (unfilled arrows).

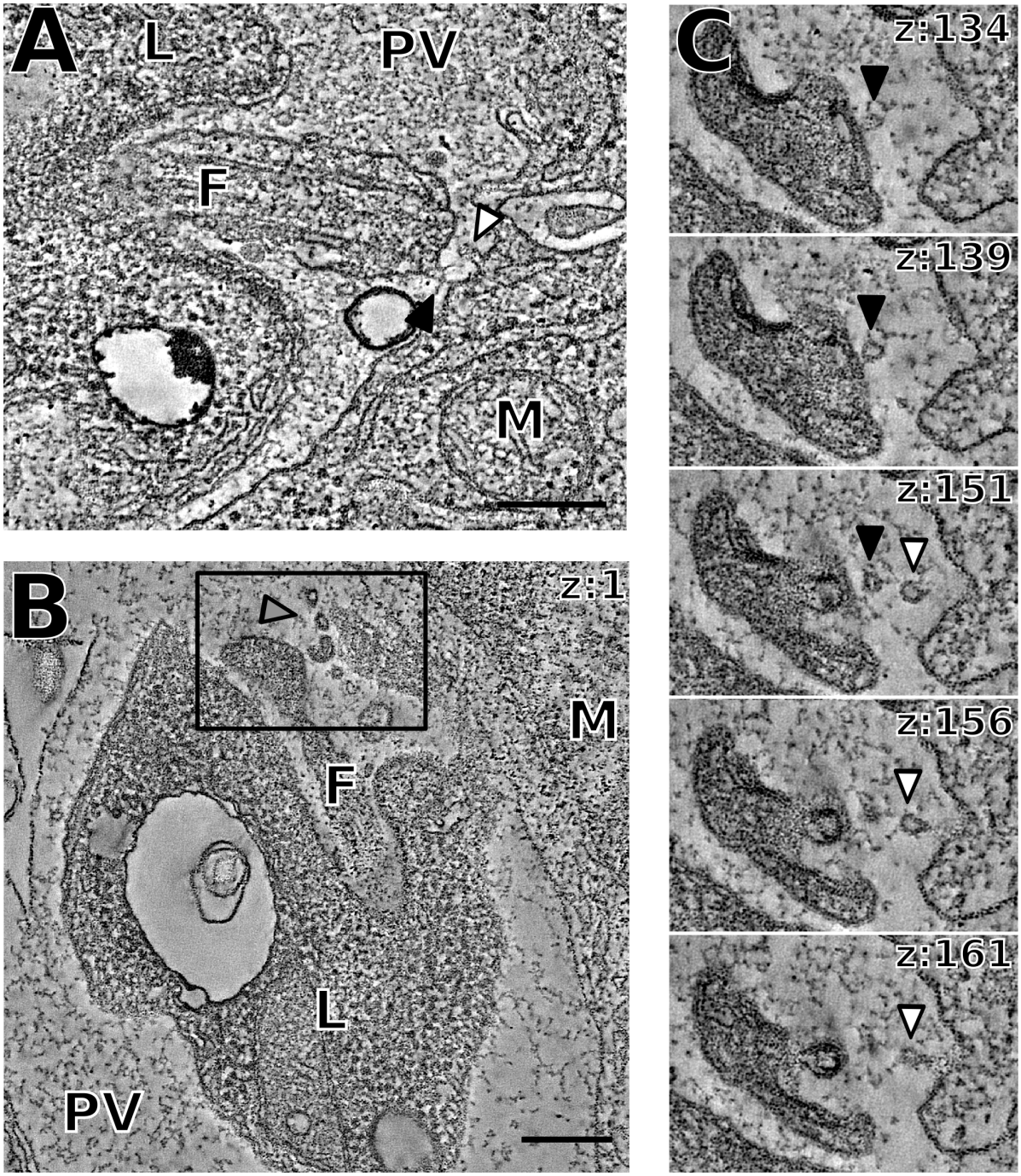


Figure 3.11. Further evidence of vesicular activity on flagellar and PV membranes. Reconstructed tomograms show the flagella (F) of *L. mexicana* amastigotes (L), within the parasitophorous vacuoles (PV) of macrophages (M). **(A)** Single slice from a dual axis tomogram showing vesicular structures on both the flagellar (black arrow) and PV (white arrow) membranes. Scale bar = 200 nm. **(B)** Single slice (z:1) from a dual axis tomogram showing vesicular structures of unknown origin (grey arrow). Black box represents region displayed in (C). Scale bar = 200 nm. **(C)** Series of z-slices from the tomogram in (B) showing vesicular structures on both the flagellar (black arrow) and PV (white arrow) membranes. Slice number shown in top right corner. Slice thickness = 0.8 nm.

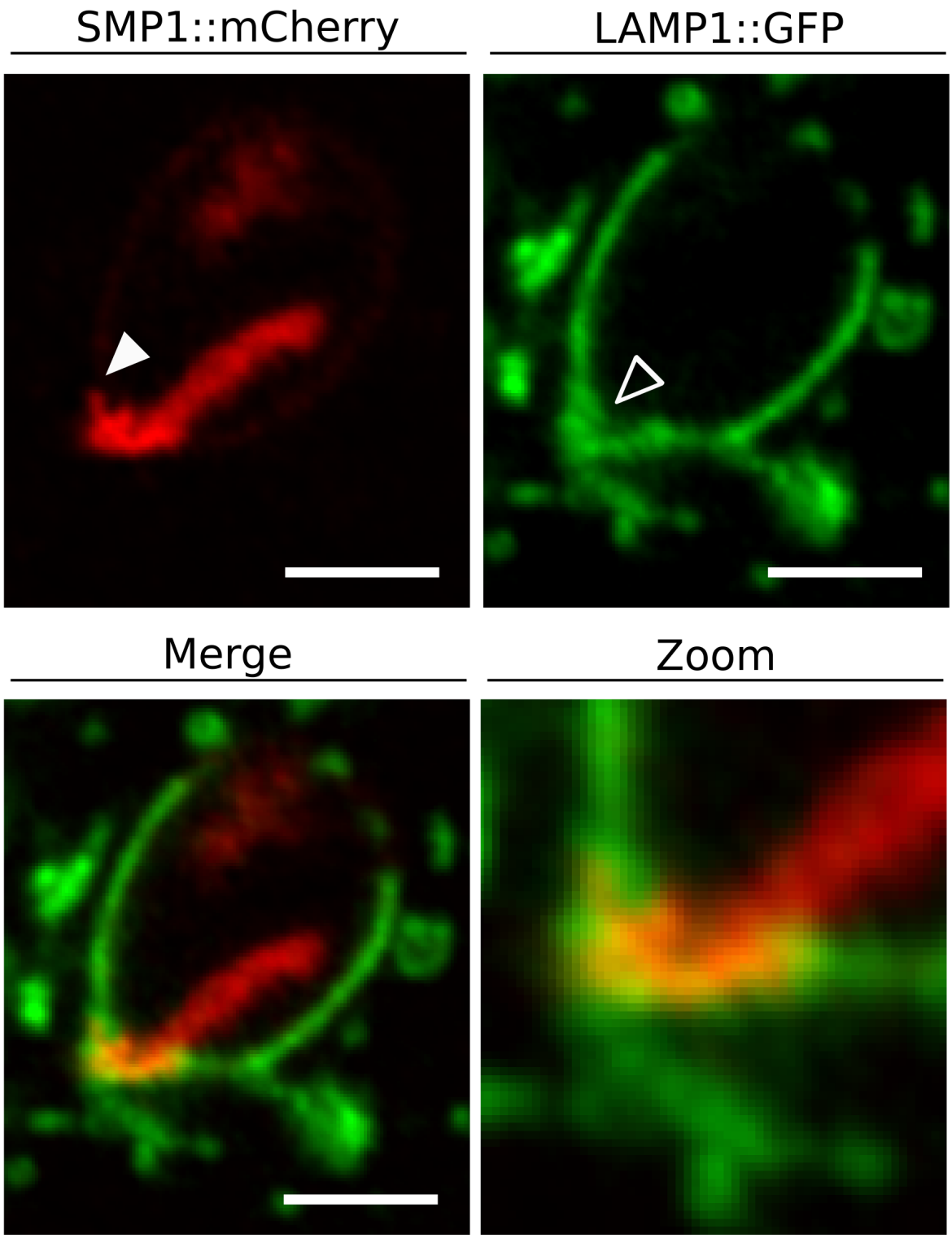


Figure 3.12. Live cell analysis of flagellum and PV membrane activity. Airyscan confocal images of intracellular amastigotes expressing the SMP1::mCherry flagellar membrane marker (red) in macrophages expressing LAMP1::GFP (green). Budding vesicular structures were observed on the flagellar membrane (SMP1::mCherry; filled arrow). PV membrane appeared denser in region of flagellum contact (LAMP1::GFP; unfilled arrow). Merge shows yellow signal, suggesting co-localisation. Scale bars = 2 µm.

3.3 Discussion

The aim of these ultrastructural analyses was to elucidate the role of the flagellum in amastigote positioning within the parasitophorous vacuole and determine whether there is evidence that this could play a role in parasite-host communication.

The results showed that amastigotes within parasitophorous vacuoles adopted three main orientations; flagellum and posterior pole contact in tight vacuoles, flagellum and posterior pole contact in bulging vacuoles, and posterior pole-only contact in open vacuoles. One of the key controversies in the field of *Leishmania* subsistence within parasitophorous vacuoles is the question of parasite orientation during attachment. Early studies on *L. donovani* positioning in parasitophorous vacuoles proposed three categorisations of amastigote positioning: completely enclosed in tight vacuoles, partially adhered in distended vacuoles, and free floating in large vacuoles (Chang and Dwyer, 1976). However, the existence of free-floating amastigotes has been strongly debated, and it is suggested that these observations may result from analysis of single ultrathin section transmission electron microscopy or imaging of few numbers of serial sections (Benchimol and de Souza, 1981; Chang and Dwyer, 1976). Early transmission electron microscopy studies in *L. donovani* and *L. amazonensis* suggested that adhered amastigotes remained attached to the PV membrane via their posterior poles (Benchimol and de Souza, 1981; Chang and Dwyer, 1976; Lang et al., 1994; Leao et al., 1995). More recently, however, *L. mexicana* amastigotes were found to be predominantly oriented with their flagellar tips in close association with the PV membrane, leading to the suggestion of a potential functional significance in parasite-host communication (Gluenz et al., 2010b). It remained unclear whether this contradictory observation represented a species-specific difference or whether differences resulted from the sampling techniques. The major limiting factor in these previous studies which we sought to overcome was the lack of three-dimensional information.

The results presented in this chapter provide an explanation for the conflicting previously-observed views of amastigote attachment to the PV membrane, and therefore provide the first reconciliation of these previous studies. It is clear from the results discussed herein that *L. mexicana* amastigotes remain in contact with the PV membrane via their posterior end. However, these data demonstrate that amastigote contact with the PV membrane is more complex than previously thought, as sites of contact appear to change with vacuole development. Access to three-dimensional electron microscopy techniques and advances in the resolution of light microscopy allowed us to reveal a previously-undescribed parasitophorous vacuole shape and associated amastigote orientation; with both flagellar tip and posterior pole contact, but a conspicuous bulging vacuole volume. Based on observations of trends in vacuole size and occupancy, we have proposed a model of amastigote positioning during vacuole development, whereby amastigotes are initially found within tight vacuoles, which increase in volume with the main volume initially bulging laterally away from the amastigote, before opening out

fully leaving only the posterior pole in contact with the vacuole membrane. This model allows us to make a number of predictions which will remain to be tested; amongst these is the hypothesis that the amastigote modulates vacuole development. As has previously been discussed, one of the hypothesised functions of the amastigote flagellum is in providing a platform for communication with the host either through receptor-ligand interactions or vesicular trafficking. In the proposed model of vacuole development, tip interactions are frequent in the early stages of development. A testable prediction stemming from this model is therefore that these tip interactions may be functionally significant, for example in allowing the parasite to modulate vacuole size increase.

Remodelling of host-cell structures by intracellular parasites has been well-characterised in many organisms, particularly amongst apicomplexans, and has been shown to be involved in all stages of parasite infection, from invasion to nutrient acquisition and egress. Apicomplexans of the genera *Plasmodium, Toxoplasma* and *Cryptosporidium*, for example, have been shown to induce *de novo* polymerisation of host-cell F-actin to produce a ring structure facilitating invasion (Elliott and Clark, 2000; Gonzalez et al., 2009). *Leishmania* are known to modulate host cell processes in a number of ways, including the delayed fusion of the parasitophorous vacuole with lysosomes and late endosomes, which is mediated by the promastigote surface membrane glycoconjugate lipophosphoglycan (LPG) (Desjardins and Descoteaux, 1997; Scianimanico et al., 1999). Indeed, several secreted virulence factors have been shown to play fundamental roles in *Leishmania* infection, including LPG, GP63, and histidine secretory acid phosphatase, which interfere with various macrophage signalling pathways (reviewed in Lambertz et al., 2012). The *Leishmania* secretome has now been shown to also include several proteases, heat shock proteins, proteins with predicted oxidoreductase activity, and putative kinases (Silverman et al., 2008). The secreted population of proteins is therefore enriched in numerous proteins that are likely to play important roles in *Leishmania* adaptation to the intracellular environment, and in disruption of macrophage processes. However, bioinformatics analysis has shown that very few of these secreted proteins contain a classical N-terminal secretion signal peptide, and evidence suggests that secretion in *Leishmania* may progress primarily through vesicle-based secretion rather than classical pathways (Silverman et al., 2011; Silverman et al., 2008).

An emerging field of research suggests a role for the flagella of parasites in delivery of virulence factors. The first evidence of a functional role for flagellar-derived vesicles came not from the field of parasite-host communication, but instead from studies on cell division of the green alga *Chlamydomonas reinhardtii* (Wood et al., 2013). In this context, vesicles shed from the flagella of *C. reinhardtii* daughter cells deliver the protease, vegetative lytic enzyme (VLE), to the encapsulating mother cell wall causing degradation and subsequent 'hatching' of daughter cells (Wood et al., 2013). Flagellar-derived vesicles have also been identified in kinetoplastids, where membranous tubules were observed to bud from the flagellum of *Trypanosoma spp.* and fragment into vesicles (Szempruch et al., 2016). These vesicles were shown to be enriched for parasite virulence factors and were able to transfer serum resistance from *T.*

rhodesiense to the susceptible *T. brucei* (Szempruch et al., 2016). *T. brucei* vesicles were additionally able to fuse with erythrocytes and have been implicated in parasite-to-host transfer of virulence factors, possibly underlying the anaemia associated with acute trypanosomiasis by promoting increased clearance of erythrocytes (Szempruch et al., 2016). Of particular relevance to the scope of this thesis, vesicles budding from the flagellar pocket of *Leishmania donovani* in the parasitophorous vacuoles of macrophages were observed and appeared to be trafficked from the PV into the macrophage cytosol and even to nearby uninfected macrophages (Silverman et al., 2010, 2008). Taken together, these findings across different organisms have led to the hypothesis that vesicles could additionally bud from the *Leishmania* flagellar membrane as a means of trafficking virulence factors to the host.

Our detailed examination of the interface between the flagellum and the PV membrane in tight vacuoles revealed the presence of tubular extensions of the flagellar membrane, closely followed in contour by the PV membrane. Intriguingly, these were observed after 72 hours of culture by live-cell imaging. The morphological events and timings of disassembly of the axoneme during differentiation have been elucidated in detail in *L. mexicana*. The flagellum shortens to extend just past the flagellar pocket in most cells during the first 16 hours of differentiation (Wheeler et al., 2015). The first axonemal structures to be disassembled are the PFR, central pair and inner dynein arms, which are mostly lost by 18 hours, but complete loss of the radial spokes and other components characteristic of the 9+2 axoneme to form a 9v flagellum can take up to 72 hours (Wheeler et al., 2015). The mechanisms and timings of flagellar membrane shortening, however, are much less well understood. Nevertheless, our imaging of stationary phase promastigotes cultured at 34°C in macrophage medium for 72 hours showed a complete shortening of the flagellum in 96% of the imaged cells. This suggests that the streamers observed in the intracellular amastigotes after 72 hours of infection are not simply remnants of the flagellar shortening process.

Preliminary evidence of vesicular structures associated with both the flagellar and PV membranes was also observed, with a particular concentration of PV membrane activity in the region nearest the flagellar tip. These results therefore provide the first definitive structural evidence of apparent shedding of vesicular structures and streamers from the tip of the flagellar membrane and are consistent with the potential role of the amastigote flagellum in vesicular trafficking. However, the molecular mechanisms involved in this membranous shedding and the functional significance remain to be elucidated.

The results presented in this chapter additionally raise interesting questions about the role of the amastigote posterior pole. While flagellar contact with the parasitophorous vacuole membrane varied with vacuole shape, contact of the posterior pole was found to be ubiquitous. It will be of future interest to determine whether this region of the amastigote acts simply to anchor the parasite to the vacuole membrane, or whether contact in this region could have additional functions. The purpose of this

amastigote anchoring to the vacuole membrane also remains to be determined, and future analyses could investigate whether this contributes to intracellular survival.

CHAPTER 4

CHARACTERISATION OF KHARON1 FUNCTION; A CROSS-SPECIES COMPARISON

4 Characterisation of KHARON1 function; a cross-species comparison

The work presented in this chapter is the result of collaboration between myself, my supervisor Eva Gluenz and several members of the Landfear lab at the Oregon Health & Science University, USA. The LmxKHARON1 data were published under the title of "Kharon1 Null Mutants of *Leishmania mexicana* Are Avirulent in Mice and Exhibit a Cytokinesis Defect within Macrophages" in PLOS ONE (2015; 10, e0134432), and the TbKHARON data were published as "KHARON is an Essential Cytoskeletal Protein Involved in the Trafficking of Flagellar Membrane Proteins and Cell Division in African Trypanosomes" in the Journal of Biological Chemistry (2016; 291, 19760-19773). My contribution focused on ultrastructural analysis of the mutant phenotypes by electron microscopy, and thus all of the electron microscope-based analyses reported in these publications are my work. After our collaboration on the LmxKHARON1 work, I visited the Landfear lab in 2015, where I prepared the TbKHARON RNAi samples from cell lines produced by Marco Sanchez. The data and figures presented in this chapter are all my own work unless otherwise stated.

4.1 Preface

The *Leishmania mexicana* protein KHARON1 (KH1), encoded by the gene LmxM.36.5850, is a 520 amino acid protein with a predicted molecular weight of 57kDa (Aslett et al., 2010), and was first identified by the Landfear lab at the Oregon Health & Science University (Tran et al., 2013). This protein is well-conserved across kinetoplastids but is absent in other eukaryotes (Tran et al., 2013). The protein sequence contains no domains recognised by either Interpro or PFAM classification. Using *in vivo* crosslinking of *L. mexicana* promastigote proteins and tandem affinity purification (TAP), members of the Landfear group selectively identified KHARON1 as an interacting partner of the flagellar glucose transporter, LmxGT1 (Tran et al., 2013). Interestingly, they were able to pull down KHARON1 only by targeting a TAP-tagged wildtype isoform of LmxGT1, but not a tagged mutant lacking the flagellar targeting signal (Tran et al., 2013).

L. mexicana expresses three closely-related glucose transporter isoforms: LmxGT1, LmxGT2 and LmxGT3 (Burchmore and Landfear, 1998). Only LmxGT1, however, is localised to the flagellar membrane, while LmxGT2 and LmxGT3 both localise to the pellicular membrane (Burchmore et al., 2003). The three isoforms show large regions of sequence identity, and the main differences occur in the N-terminal regions, with LmxGT1 possessing an N-terminal extension required for flagellar targeting (Burchmore and Landfear, 1998; Tran et al., 2012). The selective absence of KHARON1 in pull-downs

with an LmxGT1 flagellar targeting signal null mutant suggests that KHARON1 specifically interacts with this flagellar targeting domain (Tran et al., 2013).

Knockout of KHARON1 causes mislocalisation of GFP-tagged LmxGT1, as observed by fluorescence microscopy and immuno-EM, resulting in an absence of the glucose transporter in the flagellar membrane outside of the flagellar pocket compartment (Tran et al., 2013). KHARON1 is therefore proposed to regulate the sorting of this glucose transporter from the flagellar pocket to the flagellum proper (Tran et al., 2013). LmxGT1 has been linked to promastigote sensing of extracellular glucose depletion resulting in the transition to stationary phase (Rodriguez-Contreras et al., 2015). This suggests an interesting role for KHARON1 in the trafficking of sensory flagellar proteins. Immunofluorescence analyses, however, have shown that KHARON1 does not appear to be involved in flagellar trafficking of episomally-expressed *L. major* aquaglyceroporin AQP1, which plays a role in water homeostasis and osmotaxis (Figarella et al., 2007; Tran et al., 2013). Neither is it involved in trafficking of dually acylated flagellar-targeted proteins, such as the *L. mexicana* small myristoylated protein 1 (SMP1) or the *T. cruzi* flagellar calcium binding protein, TcFCaBP, which has previously been shown to correctly localise to the flagellar membrane in *Leishmania* species (Maric et al., 2011; Tran et al., 2013; Tull et al., 2012). Given the specificity of KHARON1 towards the flagellar glucose transporter over the pellicular isoforms, but the concurrent lack of effect on the targeting of several other flagellar membrane proteins, it remains unclear what subset of proteins are trafficked in a KHARON1-dependent manner.

Immunofluorescence and immuno-EM probing of HA-tagged KHARON1 have shown it to be localised at the base of the flagellum, at the subpellicular microtubules, and at the mitotic spindle in both the promastigote and amastigote lifecycle stages (Sanchez et al., 2016; Tran et al., 2015, 2013), while immunoblotting after subcellular fractionation suggests that it is cytoskeletally-associated (Tran et al., 2013). KHARON1-null mutant (ΔKH1) promastigotes show no reduced viability, and have been shown to successfully differentiate into amastigote-like forms under axenic conditions, after which they survive in culture at a rate comparable to wild types (Tran et al., 2015, 2013). Surprisingly, ΔKH1 intracellular amastigotes are unable to persist within macrophages and, in a mouse model of infection, do not form lesions and are completely cleared from the infected mice (Tran et al., 2015, 2013). Fluorescence microscopy of GFP-tagged LmxGT1 during intracellular differentiation has shown downregulation of this transporter in amastigote forms, though some expression is still visible within 24 hours of infection (Rodriguez-Contreras et al., 2015). It is therefore possible that correct localisation of this glucose transporter is crucial during the early stages of infection, and that its mislocalisation could result in initial defects with downstream phenotypes producing impaired survival. However, there is currently no evidence to support this, and as such, the precise role of KHARON1 in survival in macrophages remains unknown.

Despite the lack of understanding of the underlying causes of poor ΔKH1 intracellular viability, the critical requirement of KHARON1 for the disease-causing lifecycle stage makes this protein an ideal candidate for investigating the role of flagellar membrane proteins in survival in macrophages. The aim of the work presented in this chapter was therefore to gain insight into the underlying causes of the poor ΔKH1 viability inside of macrophages by assessing the ultrastructural phenotypes present in the null-mutant. The following questions were of particular interest:

1. Do ΔKH1 cells exhibit ultrastructural flagellar defects and, following on from this, do differences in the ultrastructural phenotypes of ΔKH1 promastigotes and amastigotes provide clues about the difference in survival between the lifecycle stages?

2. Is there any evidence of involvement of the amastigote flagellum in the poor viability of the ΔKH1 intracellular amastigotes; specifically, do ΔKH1 amastigote flagellar tips maintain contact with the parasitophorous vacuole membrane?

4.2 Results

4.2.1 Knockout of KHARON1 does not affect *L. mexicana* promastigote cell body or flagellar morphology

Knockout of KHARON1 had previously been shown to have no effect on the viability of *L. mexicana* promastigotes (Tran et al., 2013). In order to further investigate whether the loss of this gene had more subtle effects in this life cycle stage, transmission electron microscopy (TEM) was used to assess the ultrastructural phenotype. As KHARON1 was identified as an interacting partner of the flagellar membrane glucose transporter LmxGT1 (Tran et al., 2013), the analysis particularly focused on detection of any flagellar defects, such as changes to the structure of the axoneme or membrane irregularities.

The ΔKH1 promastigotes showed no evident differences in overall cell morphology in comparison to wild type cells. Longitudinal views of ΔKH1 promastigotes in the ultrathin sections showed typical organelle morphology and distribution; cells had a single, or in some cases dividing, nucleus and kinetoplast, with a long flagellum extending out of the flagellar pocket (**Fig 4.1**). When scrutinised more comprehensively in both longitudinal and transverse sections, the flagella of the ΔKH1 promastigotes showed all of the structures that are characteristic of a motile kinetoplastid flagellum; they showed nine-fold symmetry along the length of the flagellum, with nine triplet microtubules in the basal body, nine doublet microtubules in the transition zone, a 9+2 axoneme with a central pair, and the presence of the paraflagellar rod upon exit from the flagellar pocket (**Fig 4.2**). Rotational averaging (Gadelha et al., 2006) of the axonemes highlighted the presence of ponticuli, transitional fibres, nexin links, Y-shaped linkers,

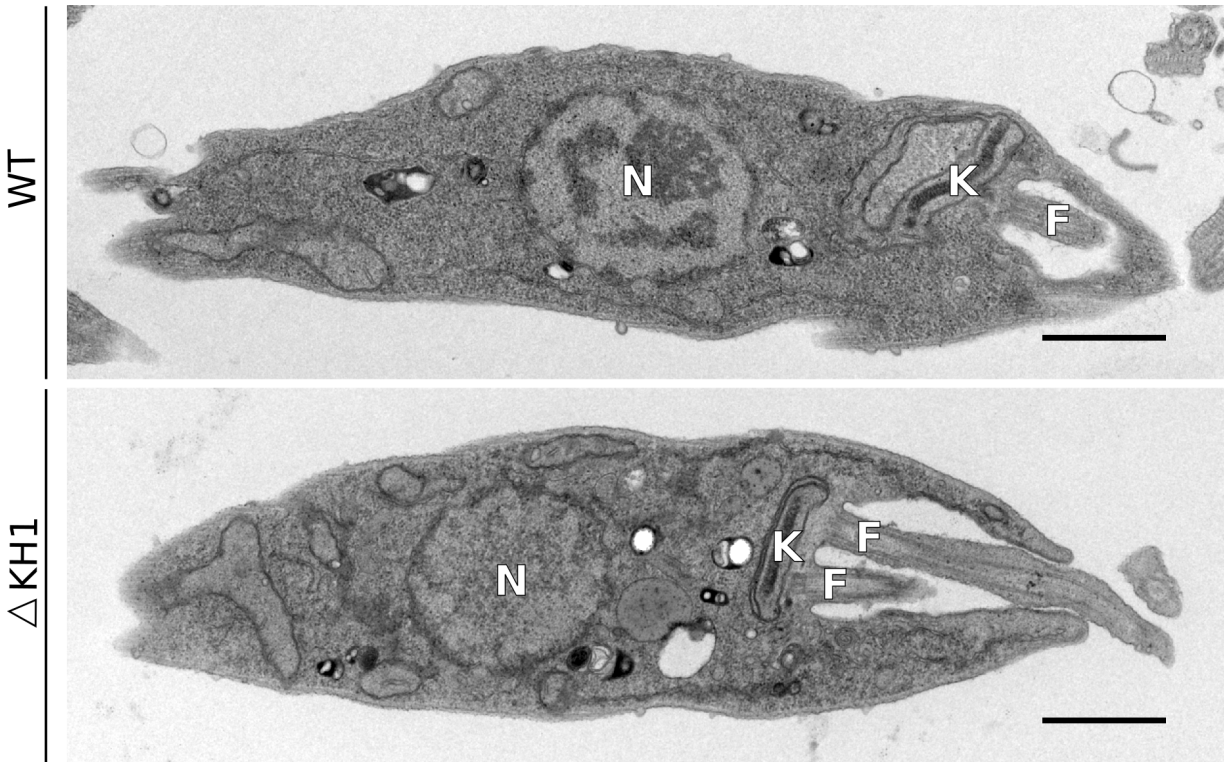


Figure 4.1. KHARON1-null *Leishmania mexicana* promastigotes show comparable cell morphology to wild types. Transmission electron micrographs show presence of a single nucleus (N) and kinetoplast (K) and either a single or two dividing flagella (F) in wild type (WT) and KHARON1-null (ΔKH1) promastigotes. Scale bars = 1 μm.

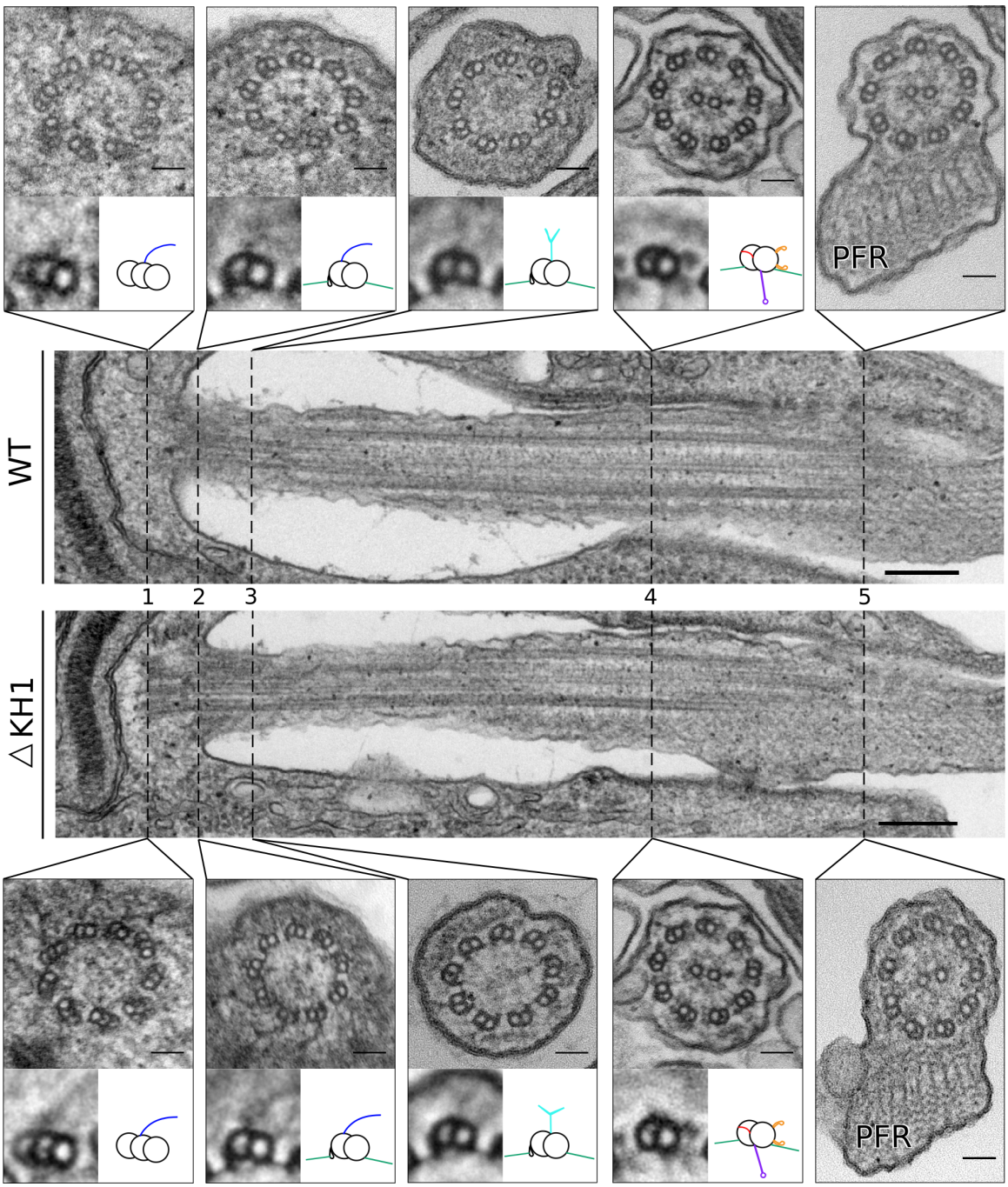


Figure 4.2. KHARON1-null *Leishmania mexicana* promastigotes show comparable flagellar morphology to wild types. Transmission electron micrographs show wild type (WT) and KHARON1-null (ΔKH1) longitudinal flagella, with cross sections of (1) the basal body, (2) the proximal transition zone, (3) the distal transition zone, (4) the 9+2 axoneme arrangement, and (5) the 9+2 axoneme with associated paraflagellar rod (PFR). Each cross section is accompanied by a rotationally averaged **(Gadelha et al., 2006)** example of the microtubule triplets or doublets in that cross section, and a diagram highlighting the microtubule decorations present: ponticuli, transitional fibres, nexin links, Y-shaped linkers, radial spokes, and inner and outer dynein arms. Scale bars = 200 nm on longitudinal sections and 50 nm on cross sections.

radial spokes, and inner and outer dynein arms (**Fig 4.2**).

4.2.2 ΔKHARON1 mutant amastigotes have typical flagellar axonemes but irregular flagellar tips

The differential viability previously observed between the axenic and intracellular ΔKH1 amastigotes raised interesting questions about the mechanisms of survival in the parasitophorous vacuole (Tran et al., 2015, 2013). TEM analysis was used in these life cycle stages to identify any ultrastructural defects that might explain the loss of viability observed exclusively in the intracellular amastigotes. A particular focus was placed on determining whether ΔKH1 amastigote flagella maintained contact with the parasitophorous vacuole membrane. This flagellum-PV contact has previously been suggested to provide a platform for receptor-ligand interactions or vesicular trafficking, and it was therefore hypothesised that a loss of such contact could impede survival within macrophages.

Transverse sections of both intracellular and axenically-differentiated ΔKH1 amastigotes showed some axonemes still in the promastigote 9+2 arrangement, but these were rare and observed in similar proportions in the wild types. The majority of the observed ΔKH1 axonemes exhibited the characteristic amastigote 9+0 and collapsed 9v arrangements (Gluenz et al., 2010b), along with the expected loss of axonemal decorations (**Fig 4.3**). When observed longitudinally, however, almost 80% of the ΔKH1 mutants displayed unusual flagellar tip structures (11 out of 14), which often protruded further and appeared more bulbous than those of the wild type cells (9 out of 14; **Fig 4.4**). In rarer cases, flagella of intracellular amastigotes were observed that appeared to protrude from the cell at the level of the base of the flagellum, without any visible flagellar pocket (2 out of 14; **Fig 4.4**).

These irregular tip structures were, however, present in both the axenic and intracellular amastigotes, albeit in a much lower proportion of axenic amastigotes observed longitudinally (3 out of 10). There was therefore no indication that the differential survival of these cell types resulted directly from the defects in flagellar morphology. As axenic amastigotes have no need to modulate a vacuole environment and are not exposed to macrophage defence mechanisms, it is possible that the irregular flagellar tips could be defective in a mechanism that is essential for survival specifically within the PV environment. However, in intracellular amastigotes, there was no indication that the irregular tip structures lost contact with the parasitophorous vacuole membrane (**Fig 4.4**). Further exploration of the functions of the amastigote flagellar tip and of identification of trafficking substrates of KHARON1 in amastigotes are therefore required to assess how loss of this protein might impede flagellar function.

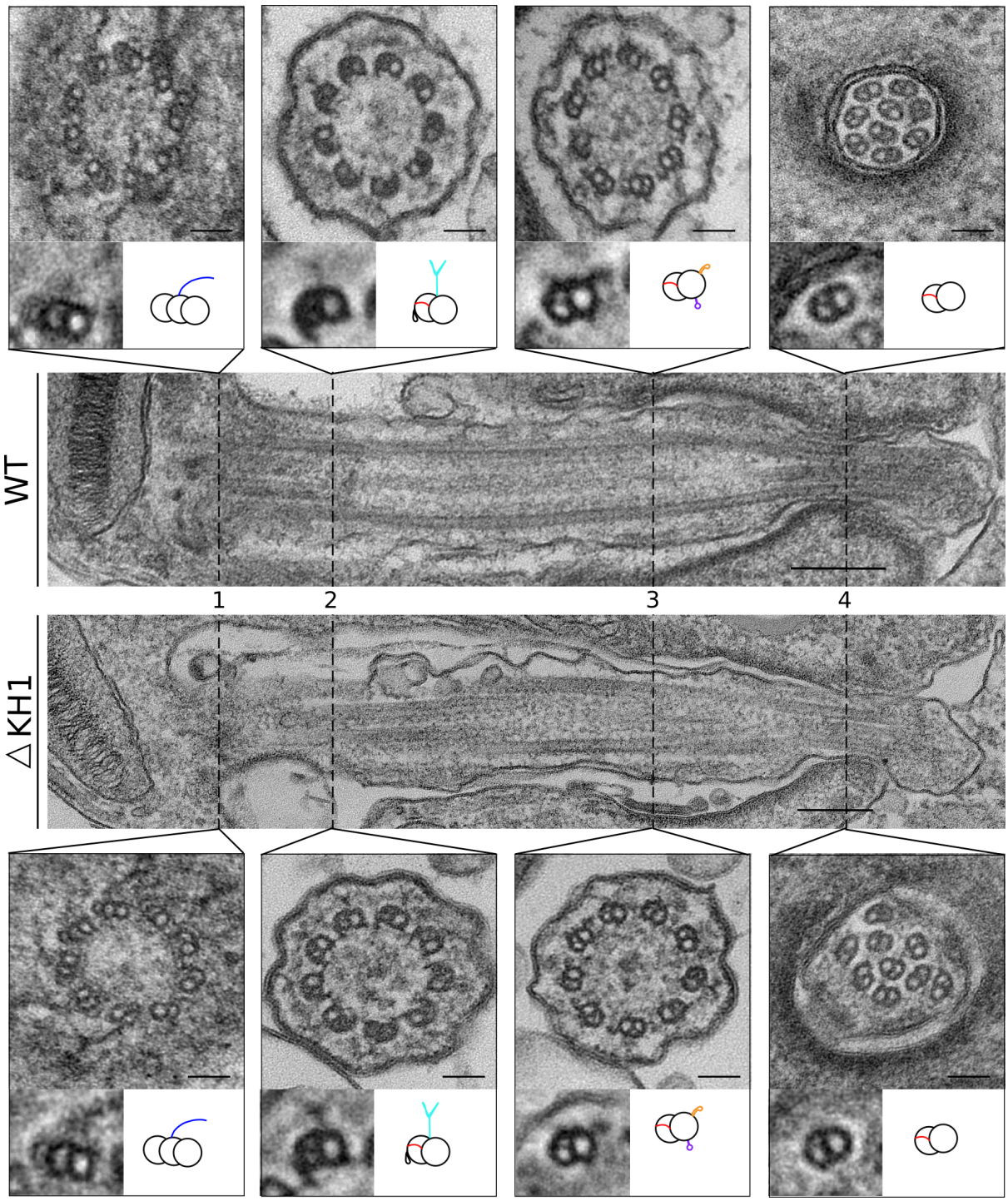


Figure 4.3. KHARON1-null *Leishmania mexicana* intracellular amastigotes show comparable flagellar morphology to wild types. Transmission electron micrographs show wild type (WT) and KHARON1-null (ΔKH1) longitudinal flagella, with cross sections of (1) the basal body, (2) the transition zone, (3) the 9+0 axoneme arrangement, and (4) the collapsed 9v axoneme arrangement. Each cross section is accompanied by a rotationally averaged **(Gadelha et al., 2006)** example of the microtubule triplets or doublets in that cross section, and a diagram highlighting the microtubule decorations present: ponticuli, transitional fibres, Y-shaped linkers, radial spokes, and outer dynein arms. Scale bars = 200 nm on longitudinal sections and 50 nm on cross sections.

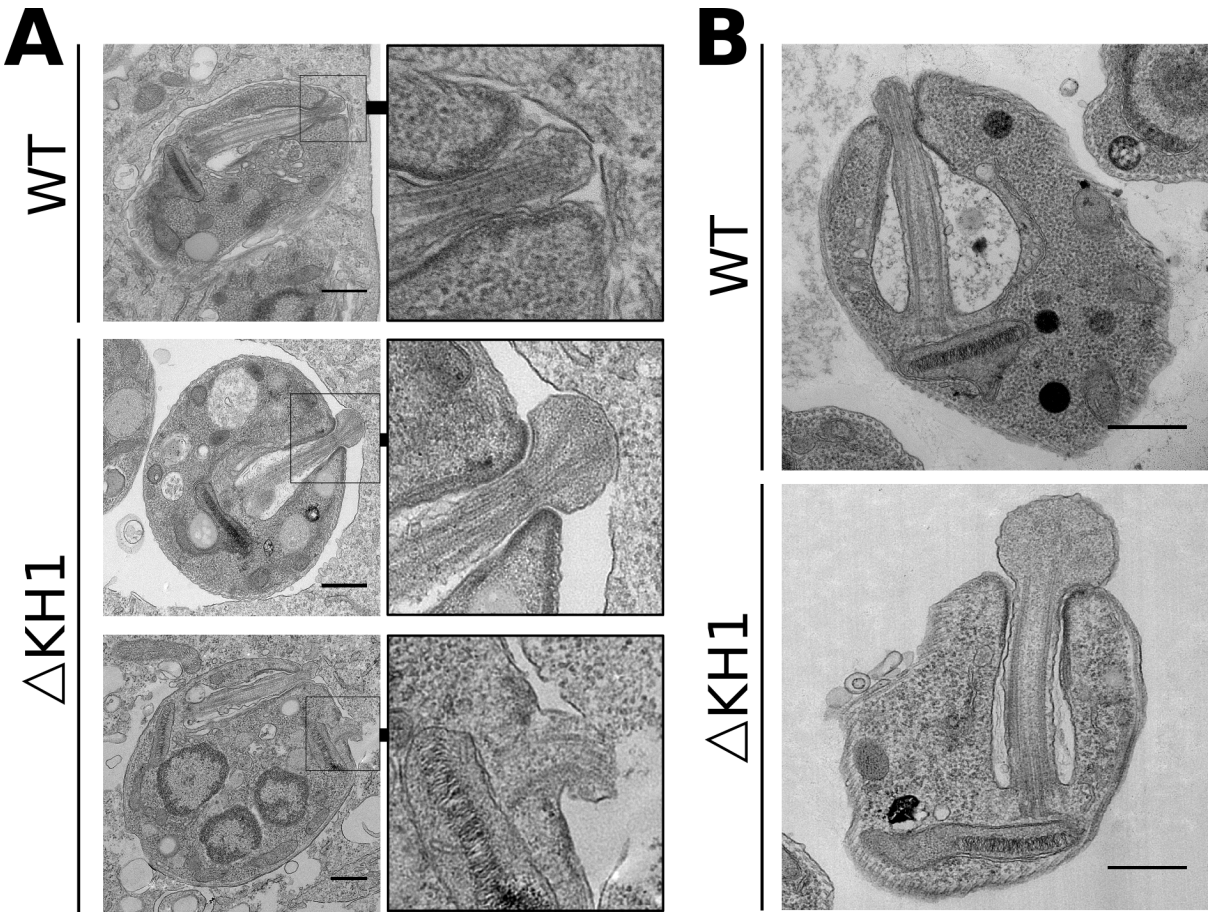


Figure 4.4. Atypical flagellar tips in KHARON1-null *Leishmania mexicana* amastigotes. Transmission electron micrographs show typical flagellar tip morphology in wild type (WT) cells, and a distended flagellar tip and protruding flagellum without a flagellar pocket in the KHARON1-null (ΔKH1) intracellular (A) and axenic (B) amastigotes. Note that ΔKH1 flagella of intracellular amastigotes still make contact with the parasitophorous vacuole membrane as is the case for the WT, despite the structural irregularities. Scale bars = 500nm

4.2.3 ΔKHARON1 mutant intracellular amastigotes are unusually round compared to wild type cells

Although the flagellar phenotype provided little insight into the differential survival of the axenic and intracellular amastigotes, there were additional defects observed exclusively in amastigotes residing within parasitophorous vacuoles.

The most manifest of these was a remodelling of the overall cell shape, from the characteristic elliptical shape of wild type amastigotes, to a strikingly round morphology; a phenotype which disappeared when a copy of the KHARON1 open reading frame was re-integrated into the endogenous locus (**Fig 4.5 A**). A circularity analysis ($4\pi[\text{area}/\text{perimeter}^2]$), assigning each cell an index between zero and one, showed a statistically significant increase in the mean circularity of ΔKH1 intracellular amastigotes when compared to the wild types (WT: $c = 0.20$, $n = 25$; ΔKH1: $c = 0.33$, $n = 34$; t-test; $p<0.01$). This phenotype was, interestingly, not observed in ΔKH1 axenically-differentiated amastigotes (**Fig 4.5 B**).

As previously mentioned, KHARON1 has been shown to localise along the flagellum and in the region of the subpellicular microtubules in amastigotes (Tran et al., 2013). A loss of function at the level of the subpellicular microtubules (see section 1.2.3) represented a likely candidate for a cause of the alteration in cell shape. However, close observation by ultrathin section TEM showed regularly-spaced microtubules of similar shape and proportions to the wild type subpellicular microtubules, with the characteristic lack of surrounding electron density, and there were no obvious visible defects which could account for the change in cell shape (**Fig 4.5 C**).

4.2.4 ΔKHARON1 mutant intracellular amastigotes undergo mitosis but not cytokinesis

As well as the cell shape remodelling, another intracellular amastigote-specific defect was observed, in the form of an apparent inability to undergo cytokinesis. The ΔKH1 intracellular amastigotes appeared to undergo mitosis normally, as characterised by the ability to replicate their flagella, nuclei and kinetoplasts. However, the mutants were never observed with cleavage furrows or the cell shape remodelling necessary for cytokinesis, as were present in the wild type intracellular amastigotes (**Fig 4.6 A**). Crucially, cytokinesis was observed in the ΔKH1 axenic amastigotes, suggesting that this defect was specific to the parasitophorous vacuole environment (**Fig 4.6 B**). In accordance with the inability to successfully divide, several ΔKH1 intracellular amastigotes possessed supernumerary nuclei, substantiating the proposed successful mitosis followed by unsuccessful cytokinesis (**Fig 4.6 C**). Indeed, the presence of more than two nuclei observed in multiple cells suggests that successive rounds of

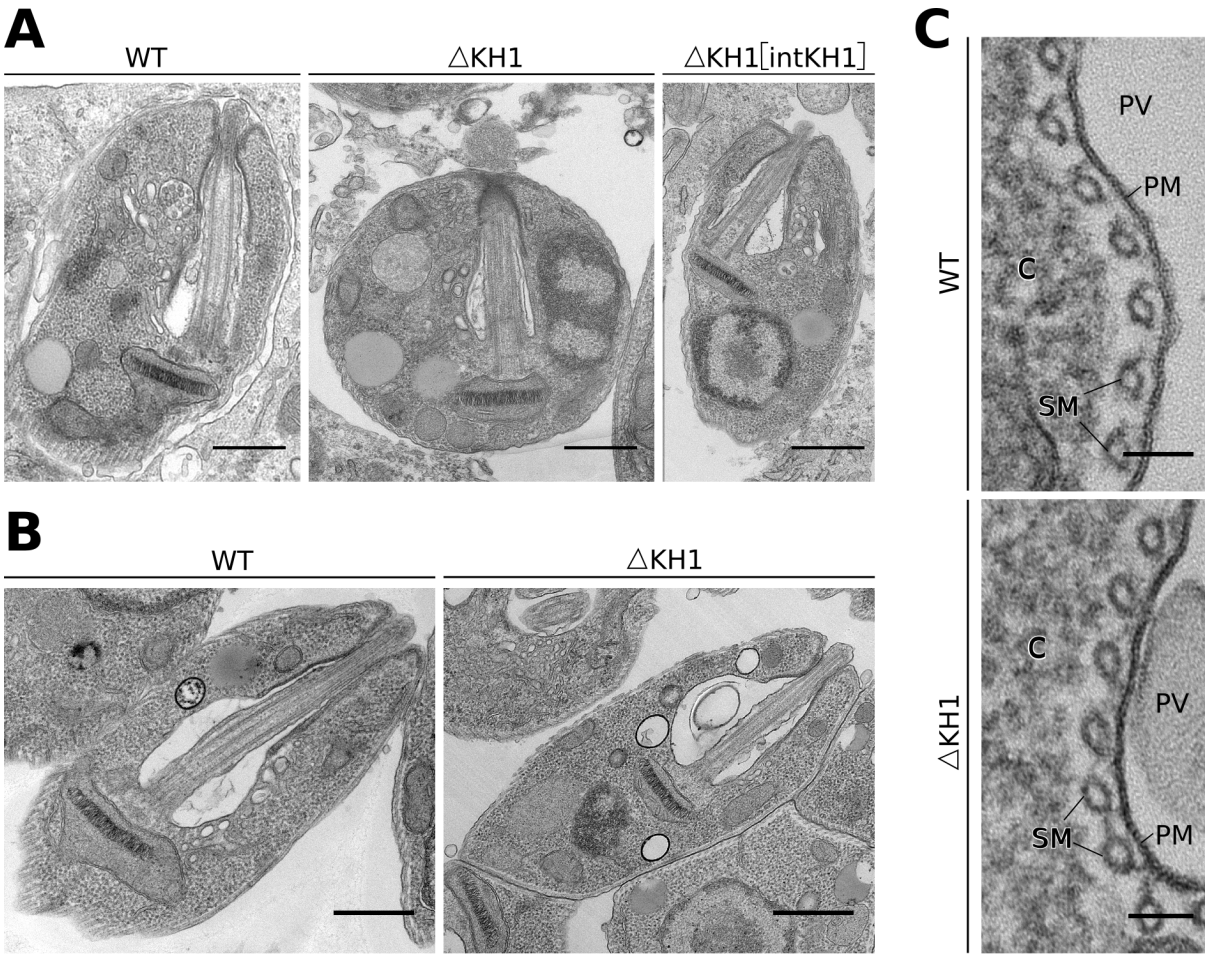


Figure 4.5. KHARON1-null *Leishmania mexicana* intracellular amastigotes have a rounded cell morphology. Transmission electron micrographs show: **(A)** typical cell morphology in wild type (WT) and add-back (ΔKH1[intKH1]) intracellular amastigotes, and rounded morphology of KHARON1-null (ΔKH1) intracellular amastigotes; a circularity analysis (4π[area/perimeter^2]) showed a statistically significant difference between WT and ΔKH1 cells (WT: c = 0.20, n = 25; ΔKH1: c = 0.33, n = 34; t-test; $p<0.01$); **(B)** ΔKH1 axenic amastigotes show typical morphology comparable to WT; and **(C)** no obvious differences between wild type (WT) and KHARON1-null (ΔKH1) intracellular amastigote subpellicular microtubules, suggesting these are not responsible for the remodelling in the mutants; C: amastigote cytoplasm, PM: amastigote plasma membrane, SM: amastigote subpellicular microtubules, PV: macrophage parasitophorous vacuole. Scale bars = 500 nm (A) and (B), 50 nm (C).

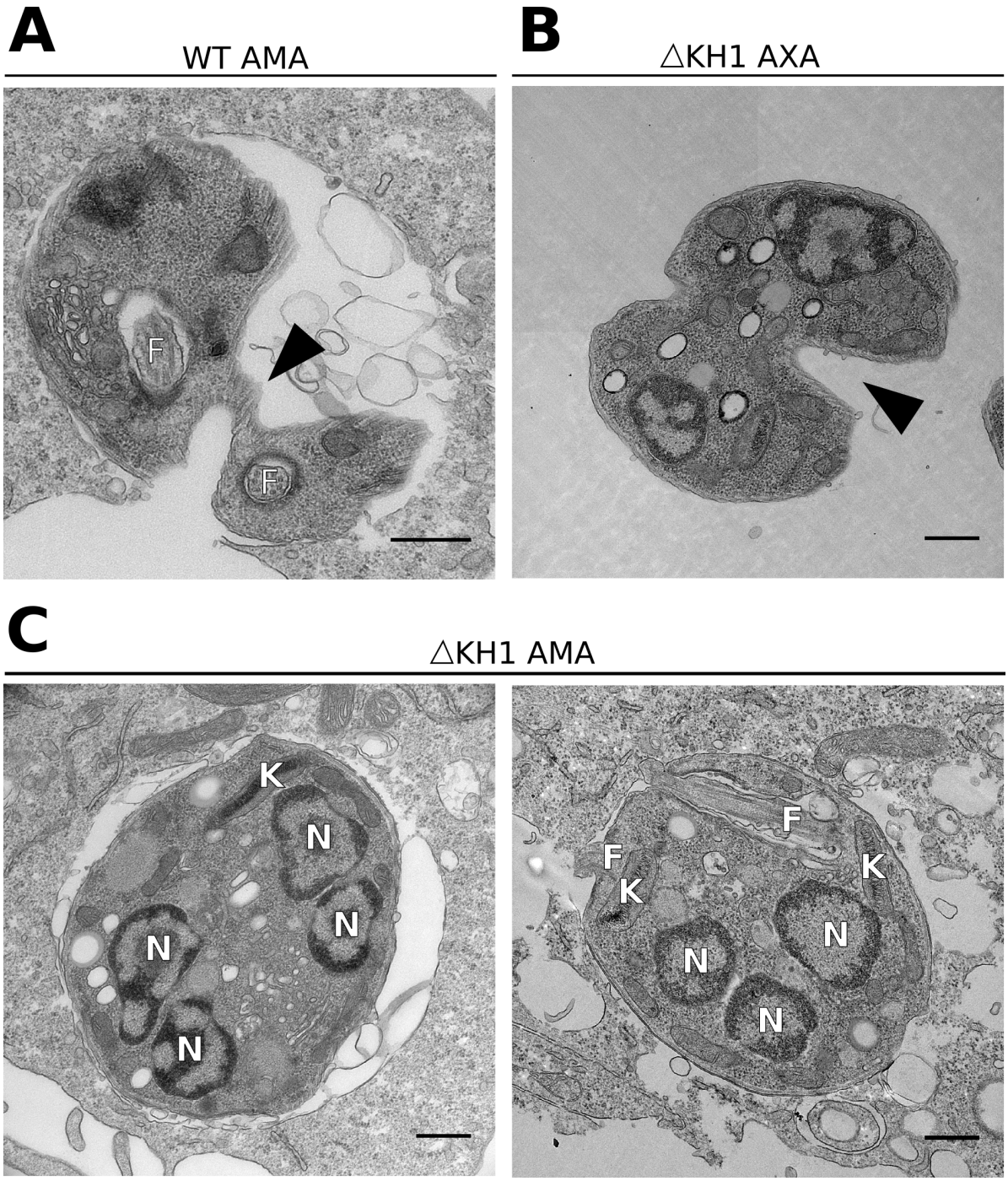


Figure 4.6. KHARON1-null *Leishmania mexicana* intracellular amastigotes fail to undergo cytokinesis. Transmission electron micrographs show occurrence of cytokinesis in **(A)** wild type intracellular amastigotes (WT AMA) and **(B)** KHARON1-null axenic amastigotes (ΔKH1 AXA) (note that this was not observed in ΔKH1 intracellular amastigotes); and **(C)** KHARON1-null intracellular amastigotes (ΔKH1 AMA) with supernumerary nuclei, indicating the occurrence of organelle replication, but absence of cytokinesis. Scale bars = 500 nm.

mitosis are completed without cytokinesis. The ultrastructural defects observed in the flagella of ΔKH1 mutants were subtle and of unclear significance. TEM analysis, however, revealed an apparent inability of mutant intracellular amastigotes to undergo cytokinesis. This defect is sufficient to explain the inability of these amastigotes to proliferate in macrophages, but the mechanism by which loss of KH1 results in a cytokinesis defect, and whether it is in any way linked to flagellar function, remains unclear.

4.2.5 RNAi knockdown of *kharon1* in *Trypanosoma brucei* causes flagellar and nuclear irregularities

In order to further characterise the role of KHARON1, Marco Sanchez in Scott Landfear's lab generated an RNAi knockdown of this gene in the related kinetoplastid parasite, *Trypanosoma brucei* (Sanchez et al., 2016). As the mammalian-infective stage of *T. brucei* represents an extracellular parasite, but is closely related to *Leishmania spp.*, it was hoped that these analyses might provide insight into whether the ΔKH1 survival defect was related to intracellular survival. The *L. mexicana* and *T. brucei* predicted protein sequences for KHARON1 show only 27% identity over the entire length and the *T. brucei* protein is considerably shorter, with only 411 amino acids compared to 520 in *L. mexicana* (Sanchez et al., 2016). Immunofluorescence detection of the TbKH1 protein endogenously tagged with either an N-terminal TY epitope tag or a C-terminal HA epitope tag showed that the localisation of KHARON1 in both *T. brucei* procyclic (Tb927.10.8940) and bloodstream forms (Tb427.10.8940) was analogous to that observed in the *L. mexicana* orthologue; at the base of the flagellum, at the subpellicular microtubules and at the mitotic spindle (Sanchez et al., 2016). Doxycycline induction of RNAi against *kharon1* mRNA severely compromised the growth of both *T. brucei* lifecycle stages and resulted in cell death by 72 hours in bloodstream forms and 12.5 days in procyclics (Sanchez et al., 2016). As with the *L. mexicana* intracellular amastigote knockout, the RNAi cell lines were able to undergo mitosis, but failed to undergo cytokinesis, resulting in cells with supernumerary nuclei, kinetoplasts and flagella (Sanchez et al., 2016). RNAi induction additionally caused detachment of the flagella from the cell body (Sanchez et al., 2016).

I performed TEM analysis on un-induced and induced RNAi bloodstream form cells to determine how the observed phenotypes affected the parasite's ultrastructure. The ultrastructural phenotypes could be characterised into two distinct groups: those affecting the flagella and those affecting the nuclei. The flagellar phenotypes included the detachment phenotype and presence in supernumerary copies that had been previously observed by light microscopy (Sanchez et al., 2016), but also included additional defects that were only identifiable at the ultrastructural level. Consistent with the cytokinesis failures, RNAi-induced cells were observed with multiple flagellar pockets, often each containing multiple flagella, frequently with the paraflagellar rod present within the flagellar pocket (**Fig 4.7 B**), while this was not observed for the un-induced cells (**Fig 4.7 A**). Similarly, induced cells sometimes possessed

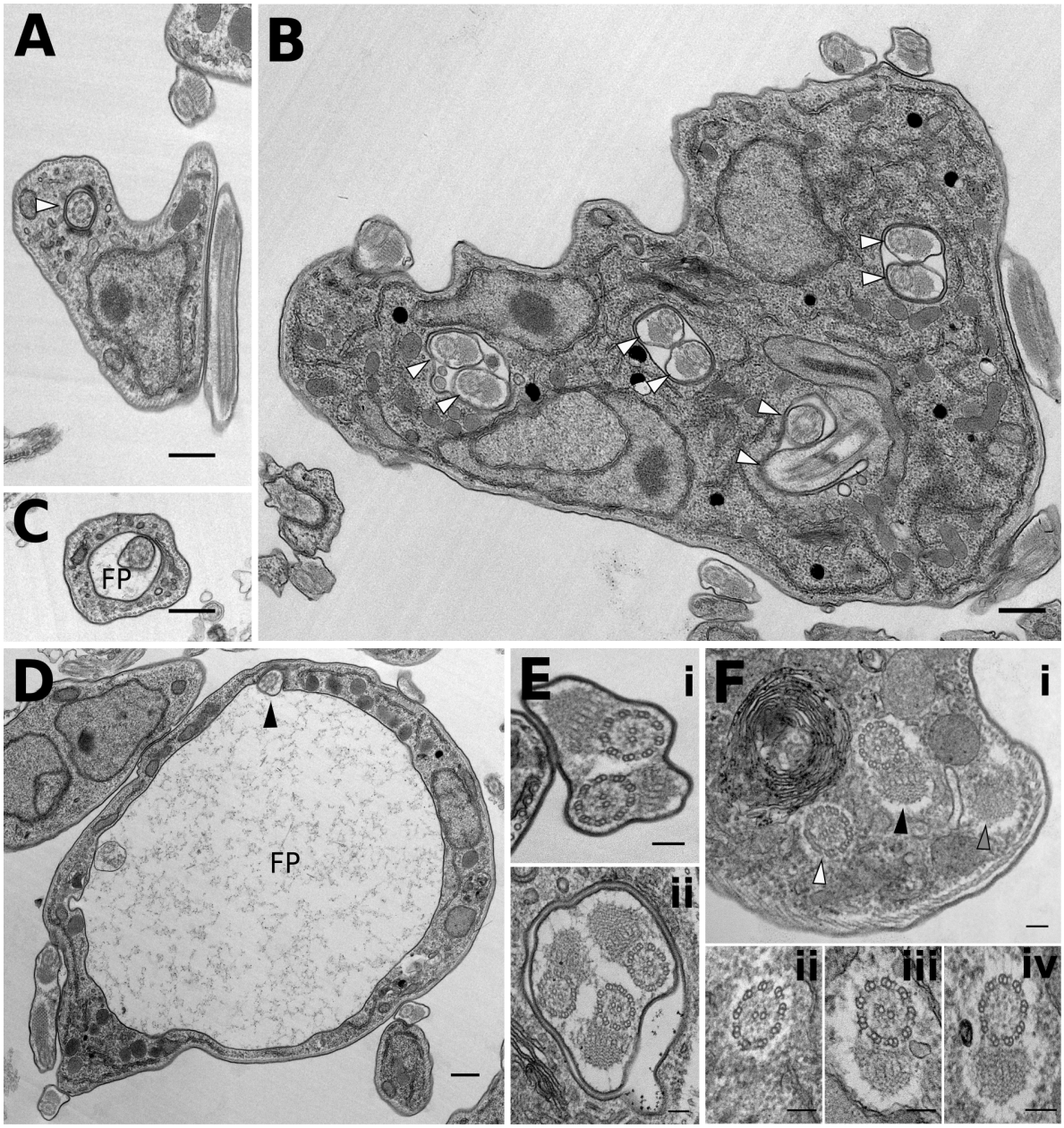


Figure 4.7. Ultrastructural flagellar phenotypes of bloodstream form *Trypanosoma brucei* following RNAi against *kharon1* mRNA. Transmission electron micrographs show: **(A)** an un-induced cell with a single flagellar pocket and flagellar profile (white arrow); **(B)** an RNAi-induced cell with multiple flagellar profiles (white arrows) within multiple flagellar pockets (note presence of paraflagellar rods in multiple flagellar profiles); **(C)** a normal sized flagellar pocket (FP) in an un-induced cell; **(D)** an enlarged flagellar pocket (FP) with single flagellar profile (black arrow) in an RNAi-induced cell; **(E)** multiple flagellar axoneme profiles within a single flagellar membrane, running either parallel (i & ii) or antiparallel (ii) to one another; and **(F)** axonemes within the cell body without a flagellar membrane or flagellar pocket either with (ii & iii) or without (iv) a central pair of microtubules, and with (iii & iv) or without (ii) a paraflagellar rod. Scale bars = 500 nm (A-D) and 100 nm (E-F).

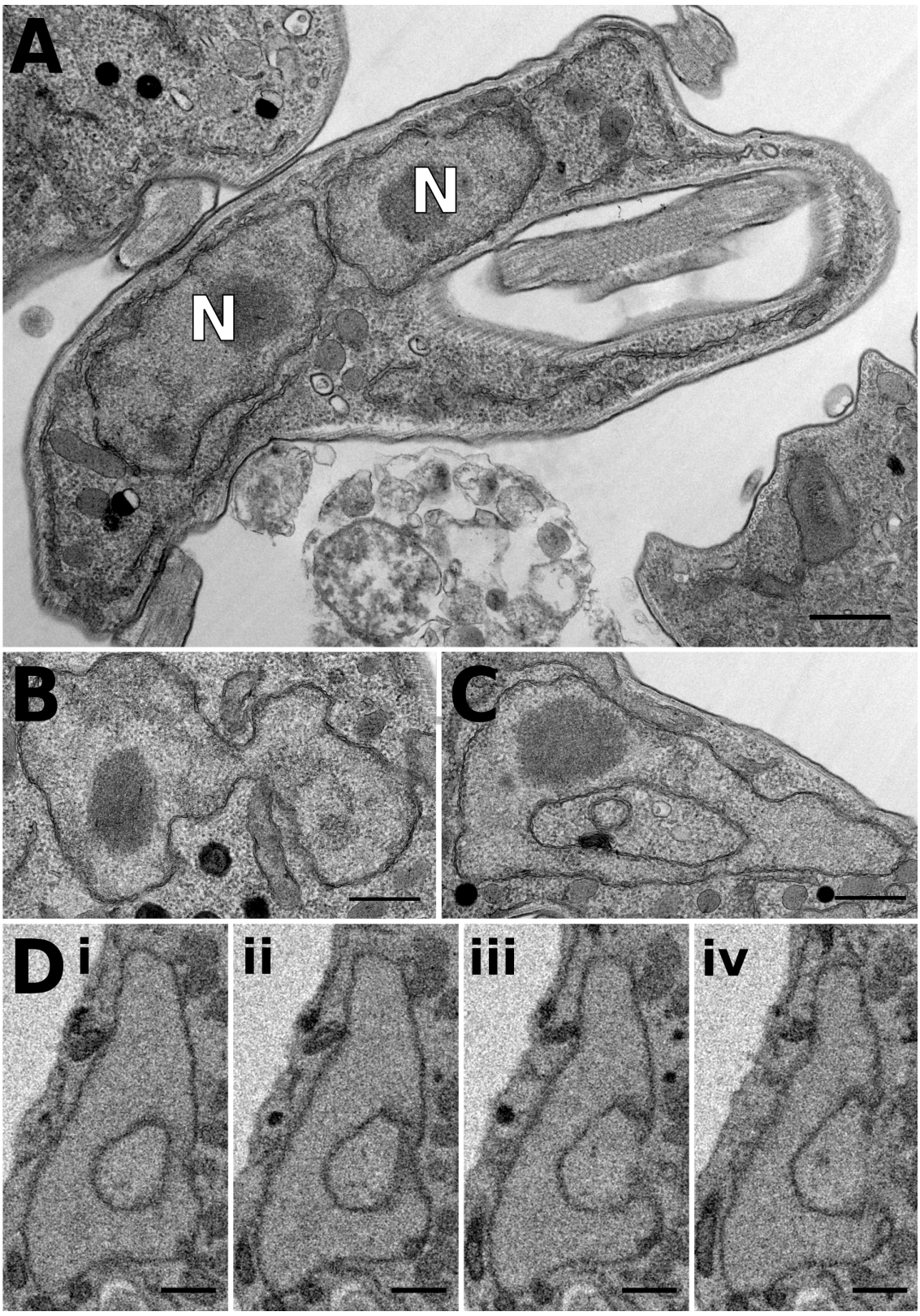


Figure 4.8. Ultrastructural nuclear phenotypes of bloodstream form *T. brucei* following RNAi against *kharon1* mRNA. Transmission electron micrographs (A-C) and serial block face scanning electron micrographs (D) show: **(A)** nuclei (N) abnormally close together; **(B)** multi-lobed nucleus; **(C)** nucleus with apparent membranous inclusions; and **(D)** four serial sections through a nucleus showing that an apparent membranous inclusion represents an invagination of the nuclear envelope. Scale bars = 500 nm.

enlarged flagellar pockets (**Fig 4.7 D**), as compared to the characteristic size observed in the un-induced conditions (**Fig 4.7 C**). Moreover, the induced cell lines showed irregularities in flagellar formation, including multiple axoneme profiles within a single flagellar membrane running either parallel (**Fig 4.7 E i & ii**) or antiparallel (**Fig 4.7 E ii**) to one another, and axonemes within the cell body without a flagellar membrane or flagellar pocket (**Fig 4.7 F**), either with (**Fig 4.7 F ii & iii**) or without (**Fig 4.7 F iv**) a central pair of microtubules, and with (**Fig 4.7 F iii & iv**) or without (**Fig 4.7 F ii**) a paraflagellar rod. The TEM analysis also highlighted nuclear phenotypes additional to the presence of this organelle in supernumerary copies, including separate nuclei very closely abutting one another, as would not be observed in the wild type (**Fig 4.8 A**), as well as nuclei of irregular shape (**Fig 4.8 B**). Interestingly, several nuclei initially appeared to have membranous inclusions (**Fig 4.8 B**). The use of 3-dimensional electron microscopy techniques was particularly informative in this case, as 3View microscopy showed that these were in fact invaginations of the nuclear envelope (**Fig 4.8 C**). It is important to note that while the presence of irregular, multi-lobed nuclei could give the impression of multiple nuclei, 3View analysis allowed us to confirm the presence of multiple distinct nuclei within cells as well.

4.3 Discussion

The aim of these ultrastructural analyses was to identify phenotypes in the *L. mexicana* KHARON1-null mutants that could explain their loss of viability inside of macrophages, and to determine whether flagellar defects could be responsible, for example through a loss of contact with the parasitophorous vacuole membrane.

The results showed that KHARON1-null amastigotes exhibited deformed flagellar tips, which were more bulbous in shape and appeared to protrude further from the flagellar pocket than in the wild type cells. However, the axonemal structures in this life cycle stage remained unchanged. This may suggest that the irregular flagellar tip structures resulted from a change in flagellar membrane properties, which, given the previously observed role of KHARON1 in promastigote cells (Tran et al., 2013), could follow the mistrafficking of one or more flagellar membrane proteins. One of the possible downstream effects of such mistrafficking could be a decrease in the shedding of flagellar membrane as vesicles, which is a proposed mechanism of delivery for parasite virulence factors to the host (see Chapter 3) (Makin, 2017). Alternatively, it is possible that rather than a change in flagellar membrane properties, the bulbous tips could result from an imbalance in trafficking of soluble components to the flagellum, resulting in an accumulation of excess material. A similar phenotype has previously been observed in procyclic *T. brucei*, where RNAi against the paraflagellar rod component PFR 1 resulted in accumulation of the other major component PFR 2 at the flagellar tip, producing a bulbous structure in this region (Bastin et al., 1999).

However, the implication of the irregular tip phenotype described herein for a flagellar role in survival is complicated by the fact that this phenotype was observed in axenically differentiated amastigotes, which were viable in culture, and not only in the intracellular amastigotes that failed to persist within macrophages. There are several possible alternate conclusions on the role of the flagellum based on these results:

1. The flagellar phenotype is not related to the loss of viability within macrophages.

2. The flagellar defect only becomes lethal after complete differentiation to the amastigote form. Gene expression studies have shown that while *L. mexicana* axenic amastigotes are not identical to intracellular amastigotes, they are much more similar to this life-cycle stage than to promastigotes (Fiebig et al., 2015). It is therefore possible that axenic amastigotes could represent an intermediate along the differentiation pathway and thus not rely on any function interrupted by this defect.

3. This phenotype represents the ultrastructural manifestation of a change in flagellar function, which is specifically essential within the parasitophorous vacuole; either for sensing environmental stimuli or for interactions with the host macrophage.

It is also important to note that despite their irregular morphology, the ΔKH1 intracellular amastigote flagellar tips maintained contact with the parasitophorous vacuole membrane. This contact has been postulated to be involved in the interactions between the parasite and the host macrophage, possibly through receptor-ligand binding (Gluenz et al., 2010b). If a flagellar defect were responsible for the poor survival of the intracellular amastigotes, this maintained contact would mean that either the defect affected flagellar function independent of the membrane contact, or that although the contact was maintained, the function served by this contact was nonetheless impaired. Given the orientations of wild type amastigotes within parasitophorous vacuoles defined by the structural analyses described in Chapter 3, it would be of interest to determine whether ΔKHARON1 amastigotes maintain posterior contact with the parasitophorous vacuole membrane or whether the loss of this contact could in any way contribute to their poor survival.

Aside from the flagellar phenotypes, the intracellular amastigotes exhibited a striking alteration of cell shape. This defect was specific to the parasitophorous vacuole environment and did not occur in axenic amastigotes, suggesting an interesting link between the cell shape defect and the failure of cytokinesis. As no visible defects were observed at the level of the subpellicular microtubules, it was not possible to determine whether this rounded cell morphology could represent an inability of the cell to undergo the remodelling necessary for cytokinesis. Conversely, it is also conceivable that the rounded cell shape could represent a downstream effect of the failure of cytokinesis, resulting from an increased cell volume. Finally, it remains to be determined whether the knockout of KHARON1 in *L. mexicana* in any

way impairs the formation or function of the mitotic spindle, given its localisation there (Sanchez et al., 2016), though the presence of multiple, separate nuclei suggests that this may remain intact.

While it remains unclear whether the flagellum is involved in the poor survival of ΔKHARON1 *L. mexicana* amastigotes within macrophages, the sequence of defects resulting in loss of viability in the RNAi knockdown of this gene in *T. brucei* bloodstream forms is more clear-cut. After doxycycline induction, bloodstream forms exhibited similar phenotypes to those occurring in the *L. mexicana* ΔKH1 intracellular amastigotes, including a failure of cytokinesis resulting in multinucleate and multiflagellate "monster" cells (Broadhead et al., 2006), followed by cell death by 72 hours. In this organism, the knockdown of *kharon1* also caused detachment of the flagellum from the cell body (Sanchez et al., 2016), which provides insight into the sequence of events leading to the failure of cytokinesis. The knockdown of *kharon1* in *T. brucei* bloodstream forms was shown to inhibit the trafficking of the calcium channel TbCaCh to the flagellar membrane (Sanchez et al., 2016). RNAi knockdown of this calcium channel has previously been shown to be sufficient to cause flagellar detachment in this life cycle stage (Oberholzer et al., 2011). In bloodstream forms, correct flagellar formation and motility is required for division (Broadhead et al., 2006; Ralston et al., 2006), and flagellar detachment thus results in the failure of cytokinesis (LaCount et al., 2002; Sunter et al., 2015; Woods et al., 2013). It is therefore plausible that the phenotypes observed in the *kharon1* RNAi blood stream form cells represent a sequence of events initiated by the mislocalisation of TbCaCh, causing flagellar detachment and, consequently, interrupted division.

The *T. brucei* flagellum is attached along the cell body length (Vickerman, 1969), and the tip of the new flagellum defines the point of initiation of cytokinesis (Kohl et al., 2003). While this is clearly not the case in *Leishmania,* the flagellum in this genus shares many commonalities with its *Trypanosoma* relative, including a connection to the kinetoplast via the tripartite attachment complex (Ogbadoyi et al., 2003). In *T. brucei*, kinetoplast segregation is controlled through this complex by movements of the basal bodies (Ogbadoyi et al., 2003; Robinson and Gull, 1991), and this function is likely conserved in *Leishmania.* While the *L. mexicana* ΔKH1 intracellular amastigotes were able to replicate their kinetoplasts, it is possible that the flagellum in this species may play another as-yet uncharacterised role in cell division and that a loss of this function results in the failure of cytokinesis. It is, however, important to remember that while there are many similarities between *L. mexicana* and *T. brucei*, there is enough evolutionary distance between them for many of their genes to possess different functionalities. This may be compounded in this case by the poor sequence identity in predicted KHARON1 protein sequences in these two species. Thus, while the specificity of the cytokinesis defect in *L. mexicana* to the parasitophorous vacuole environment suggests a potential link to the ability to sense environmental stimuli, one must be careful in drawing parallels to the sequence of defects in *T. brucei* bloodstream forms to suggest a flagellar role.

CHAPTER 5

CHARACTERISATION OF THE *LEISHMANIA MEXICANA* BBSOME COMPLEX FUNCTION

5 Characterisation of the *Leishmania mexicana* BBSome complex function

The results presented in this chapter include data based on work performed by an FHS student, Charlotte Laycock, on the role of BBS3 in flagellar membrane trafficking. While I was involved in experimental design for the project and provided the base ΔBBS3 cell line, Charlotte performed endogenous tagging of several flagellar membrane proteins over this knockout cell line to assess their localisation and additionally produced a BBS3 add-back cell line. The localisations included in section 5.2.5 therefore represent tagged cell lines that were produced and imaged by Charlotte. However, the presentation of these images in the figure and the discussion of these results are my own work. All other data and figures presented in this chapter are wholly my own work unless otherwise stated.

5.1 Preface

The BBSome is a multimeric protein complex named for the pleiotropic Bardet-Biedl Syndrome. Symptoms of the human disease include polydactyly, obesity, retinitis pigmentosa, hypogenitalism and impaired cognitive development (Bardet, 1920; Biedl, 1922; Laurence and Moon, 1995; Moini et al., 1975). Identification of the genes responsible led to the characterisation of the syndrome as a ciliopathy; a disease associated with ciliary dysfunction (Ansley et al., 2003; Badano et al., n.d.; Beales et al., 2001; Carmi et al., 1995; Katsanis et al., 2000; Kwitek-Black et al., 1993; Leppert et al., 1994; Mykytyn et al., 2001; Nishimura et al., 2001; Sheffield et al., 1994; Woods et al., 1999; Young et al., 1999). The BBSome is composed of a core complex of eight proteins, BBS1, BBS2, BBS4, BBS5, BBS7, BBS8, BBS9, and BBIP10 (BBSome Interacting Protein of 10kDa) that are widely conserved amongst ciliated eukaryotes (Hodges et al., 2010; Loktev et al., 2008; Nachury et al., 2007). The core complex is recruited to membranes by the small GTPase BBS3, also known as ARL6 (Fan et al., 2004; Jin et al., 2010; Mourão et al., 2014). Additional chaperonin-like BBS proteins, including BBS6, BBS10 and BBS12 are present in certain holozoan organisms (e.g. present in humans and zebrafish, but notably absent in *Drosophila*), and have been shown to be required for BBSome assembly in mammals (Hodges et al., 2010; Seo et al., 2010).

The BBSome has been implicated in several cellular processes, including microtubule anchoring, and ciliary extension (Kim et al., 2004; Kulaga et al., 2004; Price et al., 2012). However, it is most notably associated with the trafficking of ciliary proteins, with roles in both import and export of proteins in the ciliary membrane (Jin et al., 2010; Lechtreck et al., 2013, 2009; Nachury et al., 2007). Recent progress in elucidation of the mechanisms involved suggest that the BBSome may form a clathrin-like coat complex around ciliary cargo, and that association of BBS1 with Rabin8 is responsible for recruitment of $Rab8^{GTP}$

allowing for vesicle fusion to the ciliary-base (Jin et al., 2010; Nachury et al., 2007). Knockout of BBSome subunits in organisms ranging from *Chlamydomonas reinhardtii* and *Caenorhabditis elegans* to mammalian cells produces significant trafficking defects, such as disrupted ciliary localisation or, conversely, accumulation of ciliary proteins, and the complex has repeatedly been shown to be involved in trafficking of sensory receptors to cilia in these organisms (Berbari et al., 2008; Domire et al., 2011; Lechtreck et al., 2009; Nishimura et al., 2004; Wei et al., 2012; Kulaga et al., 2004). BBIP10 is required for the assembly of the BBSome complex, and, like several other BBSome subunits, is essential for ciliogenesis (Loktev et al., 2008). However, BBIP10 has also been shown to have a number of functions distinct from the rest of the BBSome subunits, including regulating microtubule polymerisation and acetylation (Loktev et al., 2008).

To date, there is no evidence of BBSome involvement in the trafficking of sensory proteins, or indeed any proteins, to the flagellar membrane of kinetoplastid parasites. However, the extensive conservation of the proteins within ciliated organisms portends a likely conserved function. Furthermore, while the complex has not been definitively implicated in flagellar protein trafficking in these organisms, several interesting phenotypes have resulted from the knockout of BBSome components in kinetoplastids. In *T. brucei*, knockout of BBS1 or BBS9, which were shown to substantially disrupt the BBSome complex, caused reduced virulence in a mouse model of infection, as measured by prolonged mouse survival (Langousis et al., 2016). Reduced virulence in the BBS1 knockout was rescued by re-introduction of an ectopic wild type copy of BBS1, showing that the phenotype did, in fact, result from a loss of the complex (Langousis et al., 2016). Despite being associated with vesicles at the flagellar pocket, and interacting with clathrin, the *T. brucei* BBSome complex appears to be dispensable for clathrin-mediated endocytosis (Langousis et al., 2016). It has, however, been implicated in post-endocytic sorting of a subset of surface membrane proteins, including transferrin and variant surface glycoprotein (VSG)-associated proteins (Langousis et al., 2016). Analyses of the BBSome in *Leishmania* to date have been less comprehensive, as no studies to our knowledge have targeted all of the components of the complex. However, knockout of BBS1 has been performed in *L. major* with intriguing results (Price et al., 2013). Most strikingly, the BBS1-null mutants showed a reduced ability to persist within macrophages *in vitro* and were unable to survive in a mouse model of infection (Price et al., 2013). An add-back cell line expressing the BBS1 ORF from the ribosomal RNA locus was able to partially rescue this phenotype, allowing parasites to survive in a mouse model of infection, albeit with later development of lesions and a reduced parasite burden per lesion (Price et al., 2013). Meanwhile, the knockout of BBS1 had no effect on promastigote viability and the only discernible phenotype in this life cycle stage was an accumulation of vacuole-like structures within the flagellar pocket region (Price et al., 2013). This study suggests an amastigote-specific role for BBS1, affecting the virulence of the parasite and its ability to survive within the parasitophorous vacuole environment. The molecular mechanisms underlying this reduced virulence, however, remain to be determined, as does any link between this phenotype and

trafficking of flagellar proteins by the BBSome. The aim of the work presented in this chapter was therefore to determine whether knockout of the BBSome components in *Leishmania mexicana* could impede intracellular amastigote survival as was observed for BBS1 in *L. major* and identify any defects that suggested impaired flagellar trafficking or a role for the amastigote flagellum in survival inside of macrophages.

At the beginning of this DPhil. project, research into *Leishmania* species was hampered by a paucity of genetic tools available for use in this organism. RNA interference (RNAi) represents an important pathway in eukaryotic cells through which double stranded RNA causes degradation of mRNA, thus reducing translation and protein expression (Fire et al., 1998). This pathway is involved in essential cellular processes including regulation of mRNA levels and chromatin silencing (Cerutti and Casas-Mollano, 2006), but has also been commandeered as a genetic tool by research scientists, facilitating loss-of-function analyses under both *in vitro* and *in vivo* conditions (Aigner, 2006; Shim and Kwon, 2010). The phylogenetic distribution of key components such as Argonaut and Dicer suggests that these may have been present in the last eukaryotic common ancestor (Cerutti and Casas-Mollano, 2006). This valuable tool has therefore been exploited for large-scale genetic screens in organisms from protozoa, such as *Trypanosoma brucei* (Alsford et al., 2011), to primary human BJ fibroblasts (Berns et al., 2004). However, several evolutionary lineages, including a subset of *Leishmania spp*., have lost many of the genes required for active RNA interference (Ivens et al., 2005; Lye et al., 2010; Robinson and Beverley, 2003). This therefore precludes the possibility of easily producing knockdown mutants for genes of interest in these species, meaning that loss-of-function analyses must rely on complete knockouts of genes. This is particularly problematic in *Leishmania*, due to the plasticity of the parasite's genome. Frequent variations in gene and chromosome copy number appear to represent the norm amongst *Leishmania spp.* and have been proposed as mechanisms for parasite adaptation to changing environments (Cruz et al., 1993; Rogers et al., 2011; Sterkers et al., 2011).

Another preferred technique for genetic manipulation in many organisms is through clustered regularly interspaced short palindromic repeats (CRISPR)-Cas9 mediated gene editing (Doudna and Charpentier, 2014; Zhang et al., 2014). This technique produces Cas9 nuclease-induced double stranded breaks at precise locations determined by sequence-specific single guide RNAs (sgRNAs), allowing for either gene disruption via mutations occurring during repair, or for efficient insertions into the target locus (Doudna and Charpentier, 2014; Zhang et al., 2014). At the start of this research project, CRISPR-Cas9 tools for use in kinetoplastid species were in their infancy. Studies in *T. cruzi*, *L. donovani* and *L. major* had successfully employed the technique to produce mutations resulting from repair of the induced double stranded breaks (Peng et al., 2015; Zhang and Matlashewski, 2015) or for incorporation of donor DNA (Lander et al., 2015; Sollelis et al., 2015; Zhang and Matlashewski, 2015). However, sgRNAs in these studies were either *in vitro* transcribed prior to transfection (Peng et al., 2015), or were transcribed *in vivo* from plasmids, which required several cloning steps to produce (Lander et al., 2015; Sollelis et

al., 2015; Zhang and Matlashewski, 2015). Following on from these studies, advances in the Gluenz lab produced an efficient, high-throughput method for CRISPR-Cas9 mediated gene editing using only single-step PCR-produced constructs (Beneke et al., 2017). This revolutionised *Leishmania* genome editing by allowing for sgRNA templates and DNA donor cassettes to be produced in mere hours, and for diploid genes to be knocked out in a single transfection round, often with targeted genes being undetectable in non-clonal transfected populations (Beneke et al., 2017).

These advances have been particularly significant for the scope of this research project with regards to the BBSome. Using the traditional knockout methods that were available when this research began, it was not feasible to target all of the individual components of the BBSome. Selection of components was limited by the need to target genes which were on chromosomes typically found in diploid copy number, to minimise the number of sequential transfection rounds and drug resistance markers required. BBS3 and BBS5 were excluded on this basis; chromosome 16, which contains BBS3, is typically found in triploid copy number, while chromosome 12, where BBS5 is located, has been shown to be present in both diploid and triploid copy numbers within single *L. m. mexicana MNYC/BZ/62/M379* cultures (Rogers et al., 2011). After a review of the available literature, BBS1 and BBS2 were initially selected for analysis; BBS1 to determine whether the loss of virulence observed in *L. major* (Price et al., 2013) was replicated in *L. mexicana*, and BBS2 because knockout of this gene in mice was reported to leave ciliogenesis intact, but to cause mislocalisation of rhodopsin away from the rod outer segment, a specialised structure derived from the ciliary membrane (Nishimura et al., 2004). However, the advent of the Gluenz lab CRISPR-Cas9 technique allowed for the scope of this investigation to broaden to incorporate all seven BBS components of the BBSome complex, as well as the small GTPase, BBS3. This allowed for a more comprehensive analysis of the role of the BBSome in *Leishmania mexicana*. BBIP10 was not included in this analysis due to its extra-ciliary role in regulating cytoplasmic microtubule stability (Loktev et al., 2008).

5.2 Results

5.2.1 *Leishmania mexicana* BBS proteins contain evolutionarily conserved functional domains

The seven core BBSome genes and BBS3 had previously been identified in *Leishmania major* (Hodges et al., 2010). The known *L. major* genes were therefore used to identify the *L. mexicana* orthologues through TriTrypDB (Aslett et al., 2010). The accession numbers for the known *L. major* genes and the identified *L. mexicana* orthologues are listed in **Table 5.1**, along with the predicted protein size calculated from the predicted protein sequence for each *L. mexicana* gene.

Table 5.1. Accession numbers of BBS genes in *Leishmania spp.* Accession numbers for *L. major* as previously defined **(Hodges et al., 2010)** and for *L. mexicana* as identified through TriTrypDB **(Aslett et al., 2010)**. Size calculated from predicted protein sequence.

BBS Gene	*L. major* Accession Number (Hodges et al., 2010)	*L. mexicana* Accession Number (Aslett et al., 2010)	*L. mexicana* Predicted Protein Size (kDa)
BBS1	LmjF.35.4180	LmxM.34.4180	64.4
BBS2	LmjF.30.0590	LmxM.29.0590	71.4
BBS3	LmjF.16.1380	LmxM.16.1380	20.5
BBS4	LmjF.36.2280	LmxM.36.2280	54.5
BBS5	LmjF.12.0680	LmxM.12.0680	46.0
BBS7	LmjF.29.0710	LmxM.08_29.0710	91.4
BBS8	LmjF.09.0440	LmxM.09.0440	60.2
BBS9	LmjF.32.1240	LmxM.31.1240	98.4

Analysis of the protein sequences for each of the *L. mexicana* BBS genes revealed several conserved functional domains by InterPro classification (Finn et al., 2017) (**Fig 5.1**). BBS3 is a known member of the ARF-like small GTPase superfamily. As such, this protein contains domains associated with this function, including a P-loop containing nucleoside triphosphate hydrolase domain (IPR027417) and a small GTP-binding protein domain (IPR005225) (Finn et al., 2017). BBS1, BBS4, BBS5 and BBS8 were found to contain domains associated with protein binding: BBS1 includes WD40-repeat-containing domains (IPR017986), both BBS1 and BBS7 contain WD40/YVTN repeat-like-containing domains (IPR015943), and BBS4 and BBS8 both include tetratricopeptide repeat (TPR)-containing domains (IPR013026) and tetratricopeptide-like helical domains (IPR011990) (Finn et al., 2017). Meanwhile, BBS5 contains PH domain-like regions (IPR011993) which are structurally similar to PH domains often associated with lipid-binding in signalling proteins, as well as DM16 repeats (IPR14003) of unknown function (Finn et al., 2017). BBS2 and BBS9, however, do not contain any domains associated with particular functions. This is somewhat surprising, as BBS2 has been found to contain WD40 repeats within organisms ranging from *Trypanosoma brucei* to *Homo sapiens* (Badano et al., 2003; Yamamoto, 2012).

TPR repeats, such as those in BBS4 and BBS8 are predicted to fold into extended alpha-solenoid structures (Fournier et al., 2013), and WD40 type repeats, such as those in BBS1 and BBS7, adopt a beta-propeller fold (Wall et al., 1995). These secondary protein structures represent the structural scaffolds of coat-forming complexes, such as clathrin (Devos et al., 2004), and the presence of these conserved domains is therefore consistent with a trafficking coat complex-forming function for the BBSome in *Leishmania* species (Jin et al., 2010).

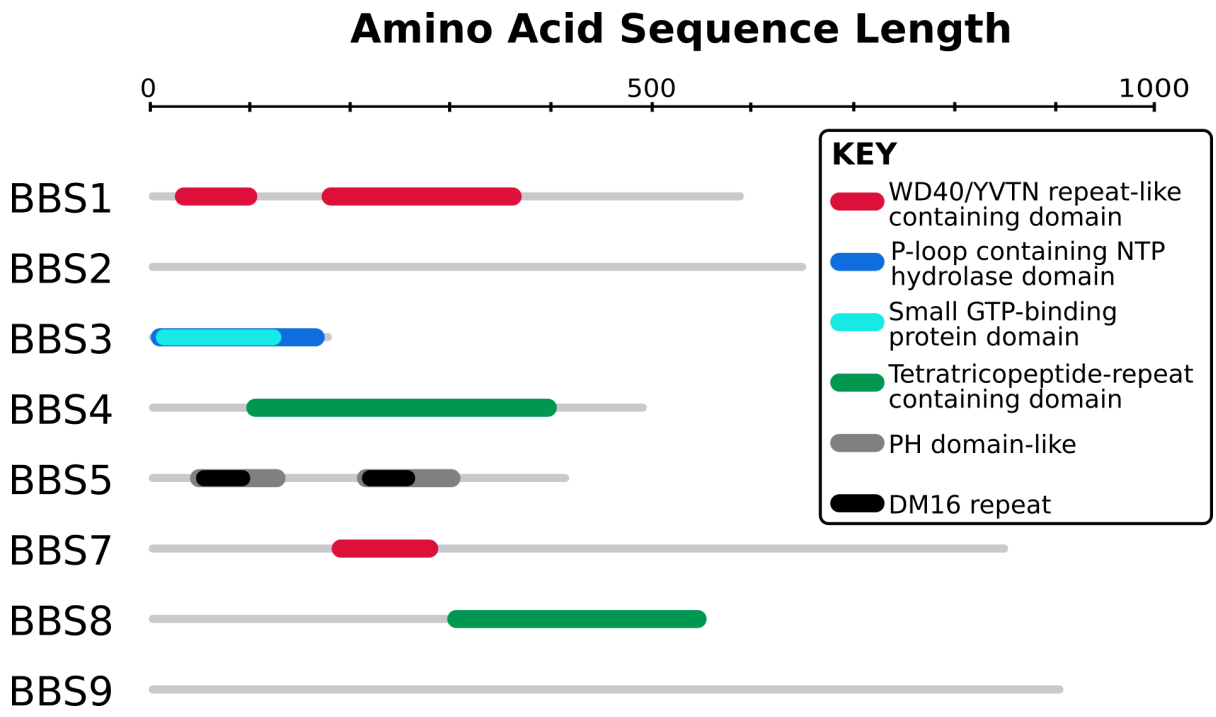


Figure 5.1. Conserved InterPro domains in *Leishmania mexicana* BBS proteins. WD40-repeat-containing domains (IPR017986) and WD40/YVTN repeat-like-containing domains (IPR015943). P-loop containing NTP hydrolase domain (IPR027417). Small GTP-binding protein domain (IPR005225). Tetratricopeptide repeat (TPR)-containing domains (IPR013026) and tetratricopeptide-like helical domains (IPR011990). PH domain-like regions (IPR011993). DM16 repeats (IPR14003).

5.2.2 The BBSome complex localises to the base of the flagellum in promastigotes and axenically differentiated amastigotes, and the small GTPase BBS3 localises along the length of the flagellum in each lifecycle stage.

In mammalian cells, the BBSome complex localises to the basal body, with BBS4 additionally found at centriolar satellites (Ansley et al., 2003; Kim et al., 2004; Nachury et al., 2007; Shah et al., 2008). There is, however, some variation in the reported localisations of the small GTPase BBS3, with some studies showing localisation only at centrosomes and basal bodies, and others showing localisation along the entire ciliary length (Jin et al., 2010; Wiens et al., 2010; Zhang et al., 2011). In *T. brucei*, immunofluorescence and immuno-EM on HA-tagged BBS proteins showed that the core complex localises to the base of the flagellum (Langousis et al., 2016), but attempts at localising BBS3 in this species using a polyclonal antibody showed a punctate cell body distribution in vesicular structures in both procyclic and bloodstream forms (Price et al., 2012). Meanwhile, the localisations of these proteins in *Leishmania* species had previously remained unresolved.

Endogenous C-terminal tagging of individual BBSome components with the *Branchiostoma lanceolatum*-derived green fluorescent protein, mNeonGreen (Shaner et al., 2013), was performed in *L. mexicana* promastigotes to determine the localisation of each component. These tagged promastigote cell lines were additionally differentiated axenically to amastigotes for 72 hours to determine whether the localisations remained the same in each life cycle stage. In both promastigotes (**Fig 5.2 A**) and axenic amastigotes (**Fig 5.2 B**), the seven core-complex subunits localised to the basal body region, with the fluorescent signals observed in close proximity but just anterior to the kinetoplast, while BBS3 localised to the flagellar membrane with an additional strong signal in the basal body region.

The localisations of the core BBSome components in *Leishmania mexicana* therefore reflect those observed within mammalian cells (Ansley et al., 2003; Kim et al., 2004; Nachury et al., 2007; Shah et al., 2008). The BBS3 localisation reflects observations from certain studies of mammalian cells, which show expression along the entire cilium (Jin et al., 2010; Zhang et al., 2011), but differs from those showing only basal body localisation (Wiens et al., 2010), and from the punctate cell body distribution observed in *T. brucei* (Price et al., 2012). Given the highly conserved localisations of the other components, it seems likely that the previously observed *T. brucei* localisation may represent a non-specific signal from the polyclonal antibody, at least in the procyclic form, especially given the absence of a specific signal at either the basal body or flagellum. Further support for the punctate localisation in bloodstream forms was produced by immunofluorescence of an overexpressed myc-tagged version of the protein (Price et al., 2012). However, endogenous C-terminal tagging of the protein with mNeonGreen by the TrypTag project has shown a localisation very similar to the one obtained in *Leishmania mexicana* herein (Gene

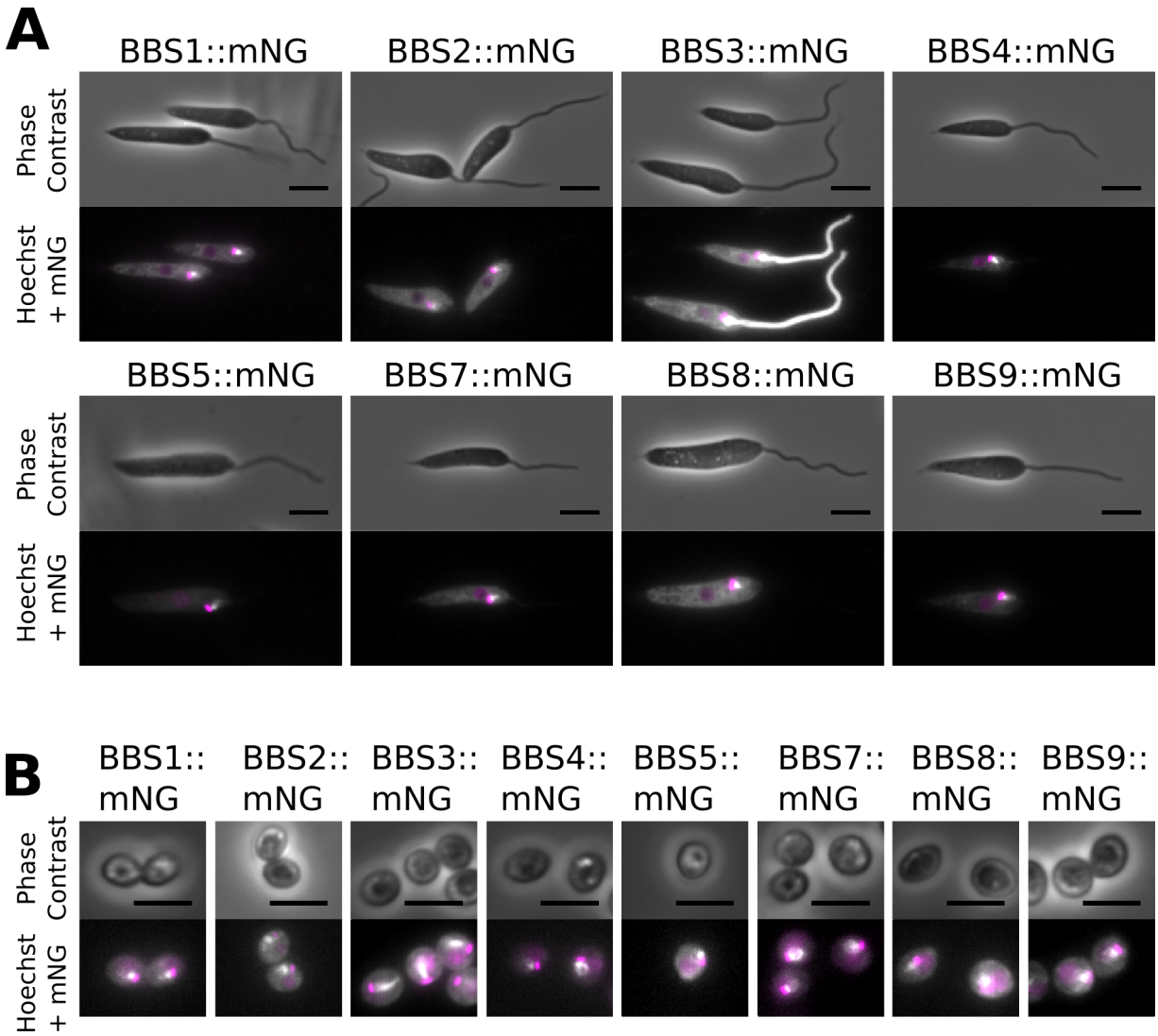


Figure 5.2. Localisation of BBS proteins in *Leishmania mexicana*. Imaging of endogenously tagged proteins in promastigotes (A) and axenically differentiated amastigotes (B). In each lifecycle stage, the seven BBSome complex proteins localise to the basal body region, while BBS3 localises along the length of the flagellum. Fluorescence is displayed as a merged channel where magenta = Hoechst signal from nucleus and kinetoplast, and white = mNeonGreen (mNG) signal. Scale bars = 5 μm.

Tb927.8.5060, transfection plate A168920160303 well E10, imaging plate D well A5; Dean et al., 2017). It remains to be determined whether the differences in reported expression along the entire cilium or exclusively at the base represent cell type- or cell cycle-specific differences, or whether they represent artefacts of the different methods used for visualisation. Overall, the localisations observed in *L. mexicana* are consistent with the hypothesis that the complex could be involved in flagellar membrane protein trafficking in this species.

5.2.3 Individual components of the BBSome are not essential for *in vitro* survival or for ciliogenesis in *Leishmania mexicana* promastigotes

In order to investigate the role of the BBSome in *Leishmania* viability and morphology, each component was knocked out in a single round, using the recently-developed Gluenz lab CRISPR-Cas9 mediated genome editing toolkit (Beneke et al., 2017). One clone of each resulting cell line (see section 2.2.4.1) was selected and confirmed as a complete knockout by PCR screening for the absence of the opening reading frame and the correct integration of two drug resistance constructs (**Fig 5.3**). Each knockout clone was split to a density of $1x10^5$cells/ml and allowed to grow for five days, well into stationary phase. Parasite density was measured daily for the duration of this growth. No significant viability defects were observed upon knockout of the individual BBS proteins in *L. mexicana* promastigotes, although ΔBBS5 and, to a lesser extent, ΔBBS7 cells took slightly longer to reach stationary phase (**Fig 5.4 A**). Knockout of individual subunits did not inhibit the formation of the promastigote flagellum (**Fig 5.2**). However, each produced a change in flagellar length.

When measured in mid-log phase promastigotes, the mean flagellar length in the Cas9T7 parental cell line was 15.7μm, but each knockout cell line showed a significant reduction in mean length (t-test, $p<0.001$); the mean flagellar length for each knockout was between 2 and 4μm shorter than that of the parental (**Fig 5.4 B**). Previous studies have similarly shown that the BBSome is not essential for ciliary assembly in many cell types (Lechtreck et al., 2009; Mykytyn et al., 2004). BBS3, however, has previously been implicated in flagellar extension in *T. brucei*, as RNAi knockdown resulted in decreased flagellum length, as measured by PFR signal by immunofluorescence (Price et al., 2012). While it is important to note that disruption of expression of certain proteins can shorten PFR-length without affecting overall flagellar length, this does not appear to be the case in the *T. brucei* knockdown. Interestingly, BBS1 knockout in *L. major* did not appear to have a significant impact on flagellar length, as measured by PFR signal by immunofluorescence (Price et al., 2013). It may be worth comparing flagellar length to cell body length in the measured cells, in order to determine proportions of different promastigote stages in each population.

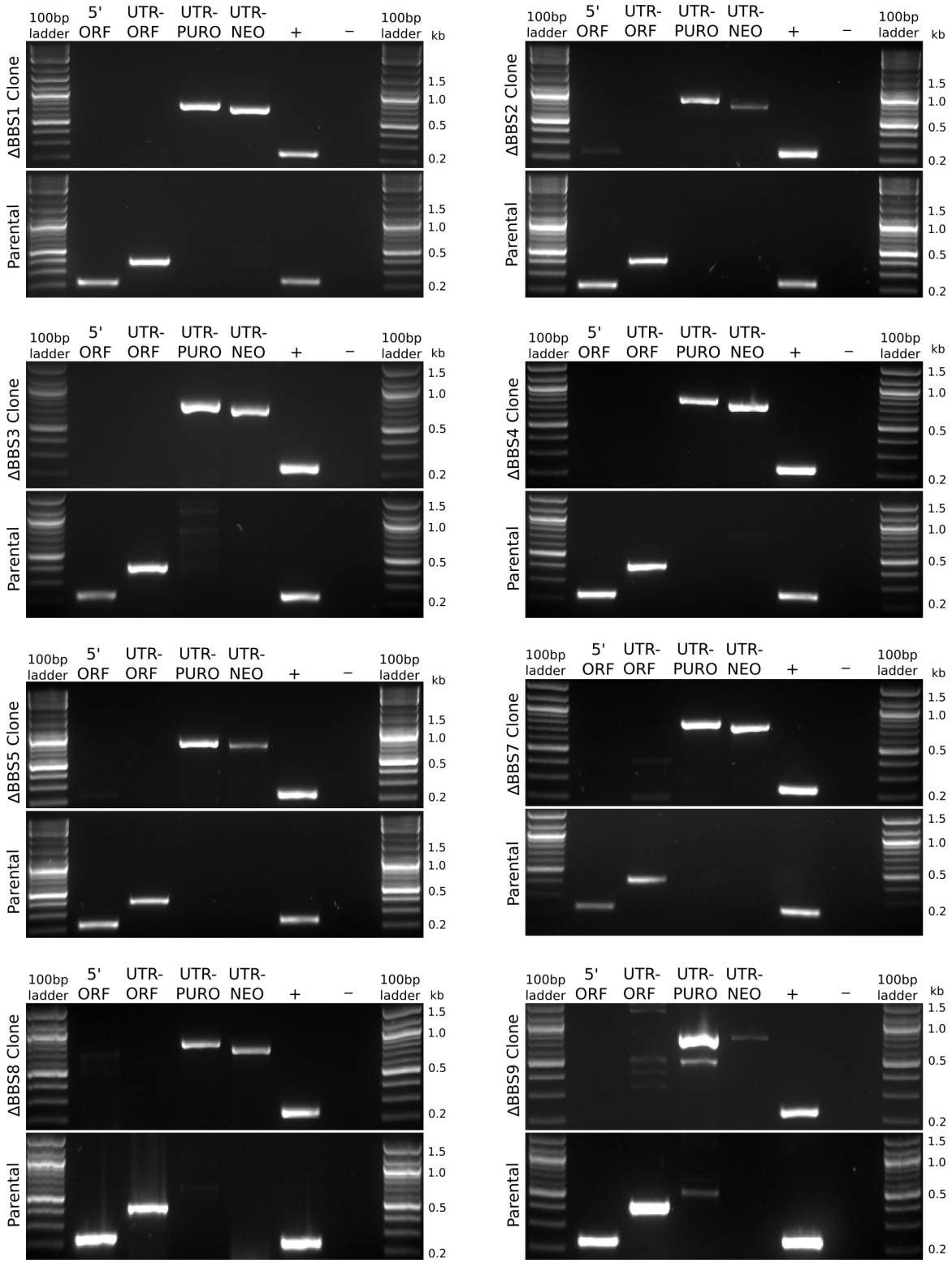


Figure 5.3. PCR confirmation of BBS gene knockout. Knockout clones were produced by a single round of CRISPR-Cas9-facilitated replacement of diploid ORF with constructs pT-puro and pT-neo. Transfectants screened for absence of ORF (5' ORF: primers against 225bp region 5' end of ORF; UTR-ORF: same reverse primer with a forward primer in the 5' UTR), and for correct integration of the pT-puro and pT-neo constructs (forward primer in 5' UTR and reverse primer in the puromycin or neomycin ORF). PCRs included a positive control (+; primers against PF16 ORF) and a no template control (-).

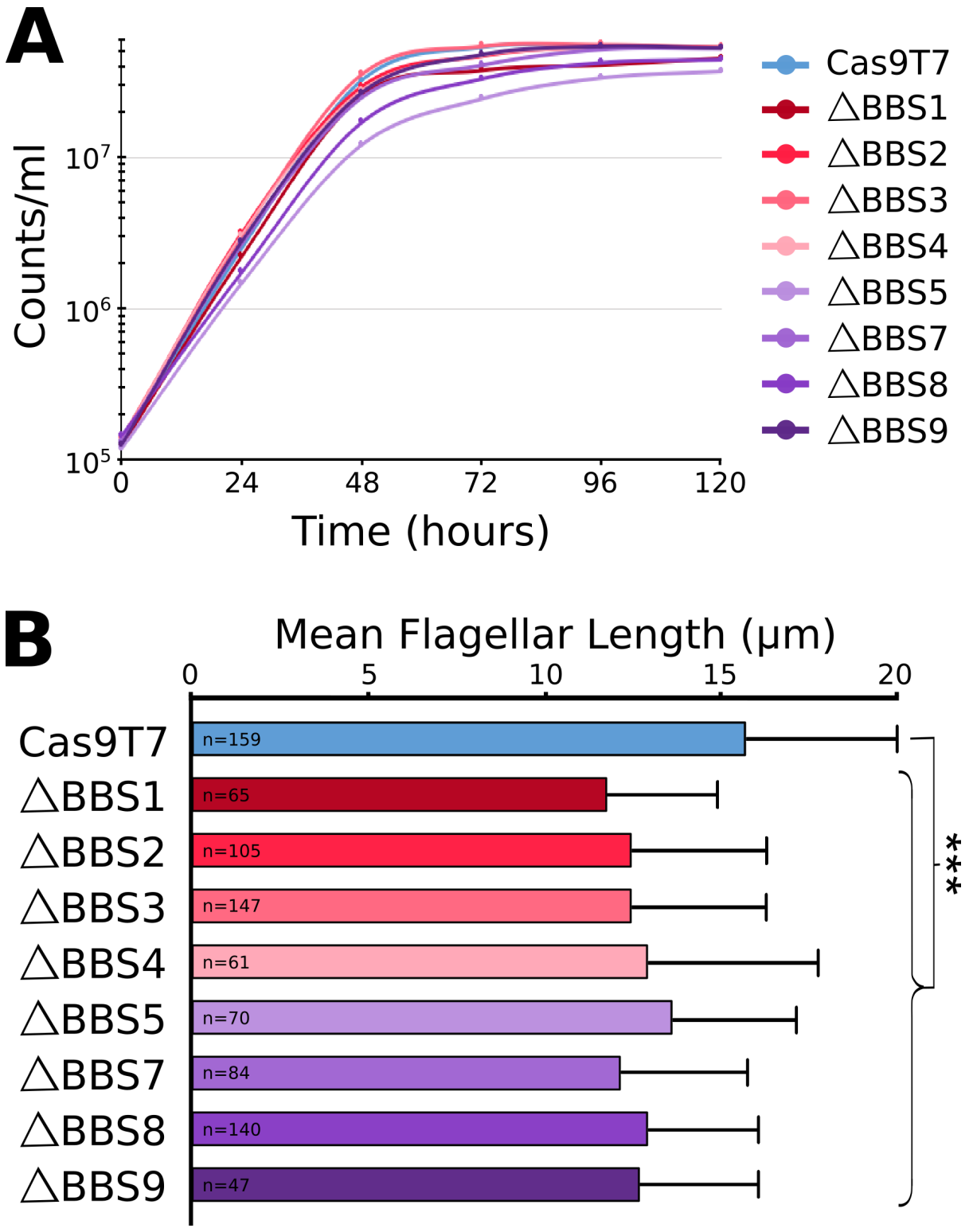


Figure 5.4. ***Leishmania mexicana*** **ΔBBS clones show no significant viability defects. (A)** Cells were split to a density of 1x10^{5}cells/ml and density was measured every 24 hours for 5 days. **(B)** Mean and SD of flagellar length in mid-log phase promastigotes of each cell line. All ΔBBS cells showed a significant reduction in flagellar length (t-test, *** = p<0.001).

5.2.4 Interdependence of BBSome subunits

Previous studies have elucidated the steps involved in assembly of the BBSome in mice and in *in vitro* culture of mammalian cells. These show that interaction of BBS7 with a complex of CCT proteins and with the chaperonin-like BBS proteins BBS6, BBS10 and BBS12 mediates the formation of an initial BBS2/BBS7 sub-complex (Seo et al., 2010; Zhang et al., 2012). This sub-complex is then able to bind BBS9, forming the core complex required for the integration of other subunits (Zhang et al., 2012). Once this core part of the complex has formed, BBS1, BBS5, and BBS8 are able to interact directly with BBS9, independently of one-another (Zhang et al., 2012). The final subunit to be incorporated is BBS4, which is dependent on the prior incorporation of BBS1 (Zhang et al., 2012). *In vitro* studies using human HEK293T cells showed that it is the initial formation of a sub-complex between BBS7 and the chaperonin-like BBS proteins that promotes the formation of the BBS/CCT complex (Seo et al., 2010). Although the *Leishmania* genome does not contain BBS6, BBS10, or BBS12, it does contain several homologues for the CCT chaperonins found in humans (Katsanis et al., 2000). It may therefore be the case that assembly of the BBSome in *Leishmania* is initiated by the formation of a BBS7/CCT complex, but that this can assemble without the help of other chaperones, or perhaps that other currently-unidentified proteins adopt the role of the chaperonin-like BBS proteins in this organism.

In order to determine whether BBSome assembly was similarly dependent on initial BBS2/BBS7 sub-complex formation in *Leishmania mexicana*, each BBS protein was C-terminally tagged as described in section 6.2.2 in the parental Cas9T7 cell line, as well as in the ΔBBS2 and ΔBBS7 cells. While the seven BBS complex components were localised to the basal body region in the parental cell line, there was no observable signal at this localisation for any of these proteins in either the ΔBBS2 or ΔBBS7 cell lines (**Fig 5.5**). Localisation of BBS3 along the length of the flagellum, however, was maintained in the knockout cell lines, although there additionally appeared to be greater levels of cell body signal than in the parental tagged cell line (**Fig 5.5**). In mice, BBS2 and BBS7 are dependent on one-another for stability and the protein levels of each significantly decrease in the absence of the other (Zhang et al., 2012). It remains to be determined whether the lack of observable localisation in the ΔBBS2 or ΔBBS7 cell lines represents a simple inability of the individual components to localise to the basal body region in the absence of the assembled complex, or whether this represents a decrease in protein levels due to destabilisation of the individual components.

5.2.5 Knockout of BBS3 causes mislocalisation of the *Leishmania mexicana* orthologue of calflagin

Endogenous C-terminal tagging of SMP1 (LmxM.20.1310; Tull et al., 2004), the small GTPase ARL-3A (LmxM.08_29.0880; A Cuvillier et al., 2000; Sahin et al., 2008), and a putative flagellar calcium-binding

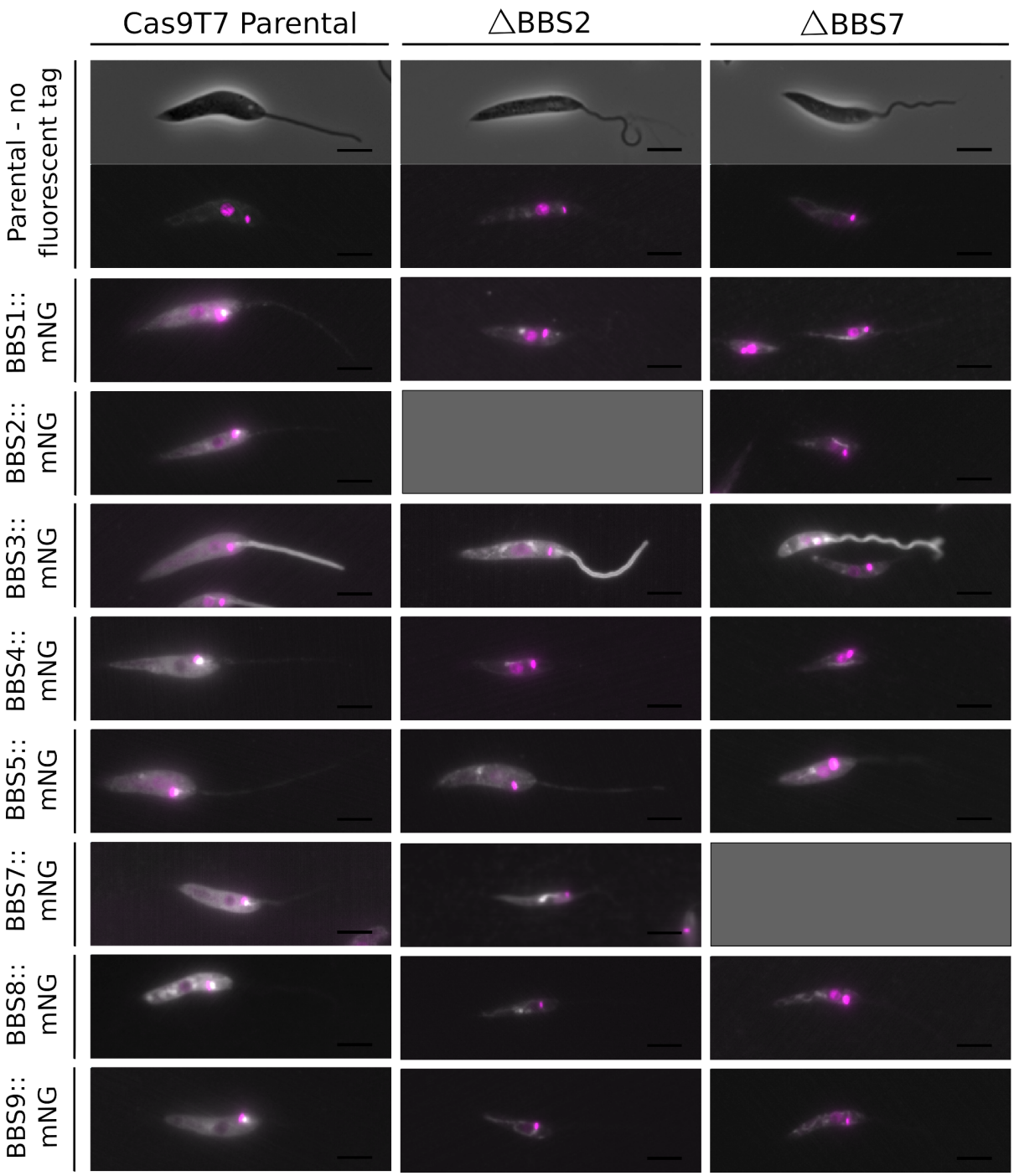


Figure 5.5. Interdependence of BBS proteins in *Leishmania mexicana*. BBSome complex proteins show no observable localisation in ΔBBS2 or ΔBBS7 cells. BBS3 is able to localise to the flagellum in these cell lines but shows an additional increase in cell body signal. Scale bars = 5 μm.

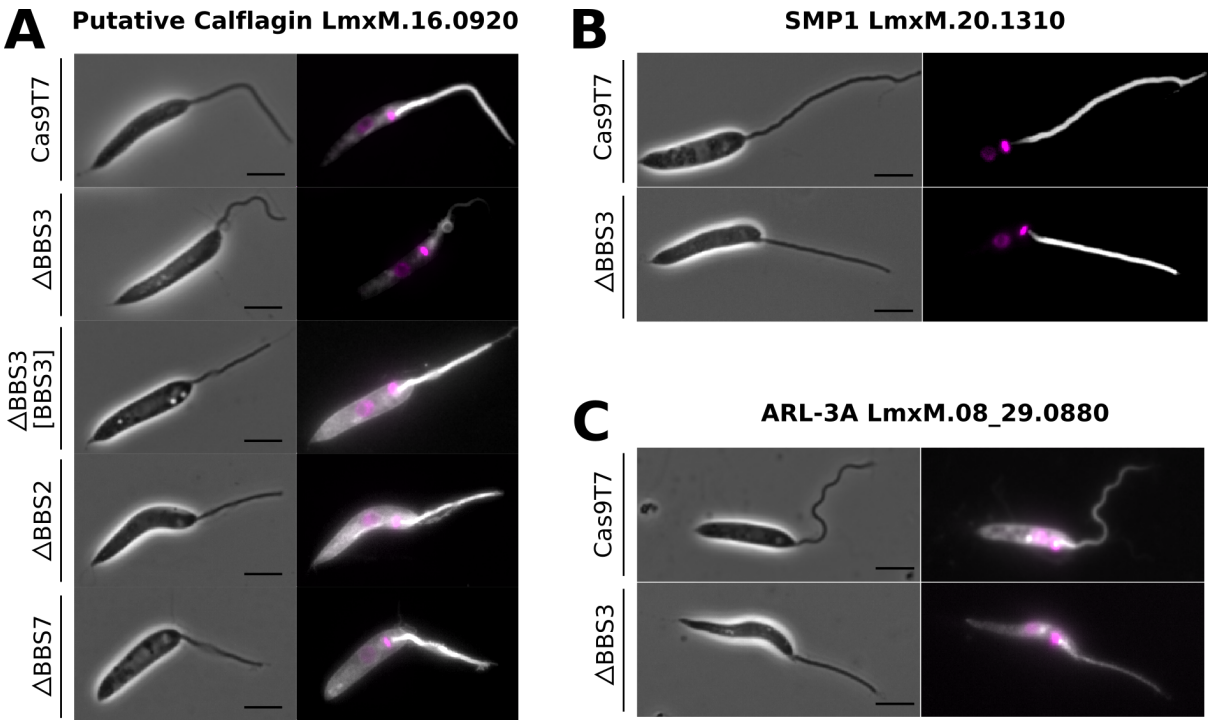


Figure 5.6. Knockout of BBS3 causes partial mislocalisation of a putative calflagin but has no effect on the localisation of SMP1 or ARL-3A. (A) Imaging of endogenously tagged putative calflagin (LmxM.16.0920) in parental (Cas9T7), BBS3 knockout (ΔBBS3) and add-back (ΔBBS3[BBS3]), and BBS2 (ΔBBS2) and BBS7 (ΔBBS7) knockout cell lines. **(B)** Imaging of endogenously tagged SMP1 (LmxM.20.1310) in parental (Cas9T7), and BBS3 knockout (ΔBBS3) cell lines. **(C)** Imaging of endogenously tagged ARL-3A (LmxM.08_29.0880) in parental (Cas9T7), and BBS3 knockout (ΔBBS3) cell lines. Fluorescence is displayed as a merged channel where magenta = Hoechst signal from nucleus and kinetoplast, and white = mNeonGreen (mNG) signal. Scale bars = 5 μm.

protein (calflagin; LmxM.16.0920), with the *Branchiostoma lanceolatum*-derived green fluorescent protein, mNeonGreen (Shaner et al. 2013), was performed in *L. mexicana* wild type, and ΔBBS3 promastigotes by an FHS student, Charlotte Laycock, to assess the role of the BBSome in the trafficking of flagellar membrane proteins. The ΔBBS3 cells showed a partial mislocalisation of the calflagin away from the flagellar membrane (**Fig 5.6 A**). This localisation varied across cells in the population; some cells exhibited a striking loss of fluorescent signal along the flagellum, while others retained more flagellar signal but displayed increased signal within the cell body.

Expression of an endogenous copy of BBS3 from the β-tubulin array was able to partially rescue flagellar localisation; in these cells, a strong flagellar membrane signal was restored, but there was significant additional signal within the cell body with an apparent edge-effect, suggesting localisation to the plasma membrane (**Fig 5.6 A**). The calflagin was additionally tagged in ΔBBS2 and ΔBBS7 promastigotes. Intriguingly, these cell lines maintained a strong flagellar membrane signal, but also showed increased cell body signal, which closely resembled the localisation in the BBS3 add-back (**Fig 5.6 A**). Although knockout of BBS3 caused mislocalisation of the calflagin, it had no apparent effect on the localisation of either SMP1 or the small GTPase, ARL-3A (**Fig 5.6 B & C**).

5.2.6 Knockout of BBS2 causes clumping of *Leishmania mexicana* promastigotes.

In addition to the reduction in flagellar length, the knockout of BBS2 produced a striking clumping phenotype in the promastigote form, which was visible by phase contrast microscopy as large, phase-bright rings. In addition to the CRISPR-Cas9 facilitated knockout, BBS2 knockouts were independently produced by two rounds of conventional homologous recombination (**Fig 5.7**), which allowed for comparison of the complete knockouts to cells expressing a single copy of the gene. Clumping was assessed independently in two ways:

1. Cells were split to $1x10^6$ cells/ml and allowed to grow for 24 hours in horizontally-oriented culture flasks. After 24 hours, the base of each flask was imaged on an upright phase contrast microscope (**Fig 5.8 A**). Culture in this orientation caused the clumps to settle at the base of the flask so care was taken not to disrupt these before imaging. Images were then analysed in ImageJ and phase bright rings counted using a macro that detects circles in images (**Fig 5.8 B**) (Wheeler, n.d.).

2. Cells were split to $1x10^6$ cells/ml and allowed to grow for 24 hours. After 24 hours, flasks were agitated to resuspend settled clumps and cells, and an aliquot was taken to measure cell density

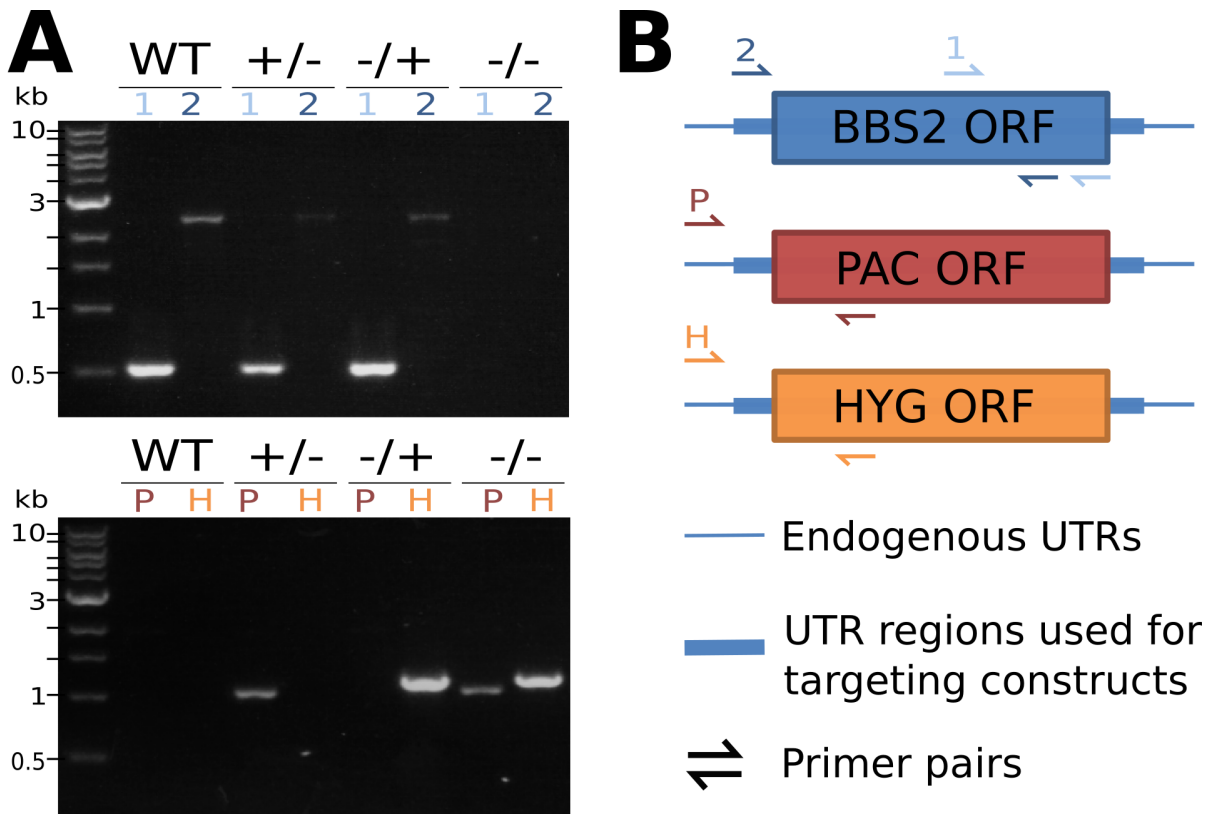


Figure 5.7. Double knockout of BBS2 by classical homologous recombination. (A) PCR screen of BBS2 single (+/- and -/+) and double knockout (-/-) cells. Knockouts were screened for absence of the ORF, using two independent primer sets (1 and 2) and for the correct 5' integration of the puromycin (P) and hygromycin (H) knockout constructs. Upper panel shows presence of ORF in WT and single KOs, but absence in double KO. Lower panel shows correct integration of either puromycin (P) or hygromycin (H) construct in the single KOs, and of both in the double KO. **(B)** Diagrammatic representation of primer locations. ORF screened using two independent primer pairs. 1 = 3' end of ORF; 2 = from 5' targeting region to 3' end of ORF. Correct integration screened using forward primer in 5' UTR outside of region used for targeting and reverse primer in relevant drug cassette. Puromycin resistance conferred by PAC ORF (P); hygromycin resistance conferred by HYG ORF (H).

using a Casy cell counter. Flasks were then vortexed to break up existing clumps, and a second aliquot was measured for cell density. A greater increase in cell density between the two measurements was taken as a measure of increased clumping (**Fig 5.8 C**).

One-way ANOVAs with post hoc Tukey HSD tests showed statistically significant differences between the double knockout and the other cell lines, both for the imaged clump counts (**Fig 5.8 B**; $F[3,8] = 81.0109$; $p < 0.001$. Tukey $p < 0.01$) and for the difference in fold-change in counts/ml between agitated and vortexed conditions over four 24 hour measurement periods (**Fig 5.8 C**; $F[3,12] = 22.8612$; $p < 0.001$. Tukey $p < 0.01$). Interestingly, cells expressing a single copy of the BBS2 gene did not exhibit a clumping phenotype (**Fig 5.8**), either suggesting that this phenotype occurred only in the complete absence of BBS2 and was not affected by a reduction in protein levels, or that regulatory mechanisms compensated for the presence of a single gene copy to maintain protein levels.

This was repeated using the CRISPR-Cas9 facilitated knockout cell line of BBS2, and several add-back clones derived from this, which contained a copy of the BBS2 ORF with a c-myc epitope tag expressed from the β-tubulin locus. Expression of the add-back protein was confirmed in five of the resulting clones by western blot using the anti-myc clone 4A6 monoclonal antibody (**Fig 5.9 A**). Degree of clumping was assessed in the parental Cas9T7 cell line, the BBS2 knockout and in the five positive add-back clones by imaging of the base of each flask after 24 hours of log-phase growth and counting of phase bright rings using the afore-mentioned macro. A one-way ANOVA confirmed that the BBS2 knockout and the addback clones all showed significantly greater clumping than the parental cell line (**Fig 5.9 B & C;** $F[6,14] = 9.0048$; $p < 0.001$. Tukey $p < 0.05$), although two of the add-back clones, E7 and G3, showed a possible slight reduction in clumping as compared to the knockout. The clumping phenotype was therefore not rescued by expression of the add-back construct.

The occurrence of a clumping phenotype in BBS2 knockout cell lines produced in two independent manners with different knockout constructs strongly implies that this phenotype results from the lack of BBS2. It is, however, unclear why this phenotype is not rescued in the add-back. It is possible that the protein levels expressed in the add-back could differ significantly from endogenous levels, and this may contribute to the lack of rescue. It was, however, not possible to compare protein expression levels between the wild-type BBS2 and the add-backs due to the lack of an anti-BBS2 antibody.

We proposed three possible mechanisms of ΔBBS2 clump formation, and predictions about what results each of these would produce during co-culture of the ΔBBS2 cells with a fluorescent reporter cell line:

1. Clumps resulting from a cytokinesis defect. Clumps would contain only unlabelled ΔBBS2 cells and no fluorescently labelled wild type reporter cells. ΔBBS2 cells within the clumps would be

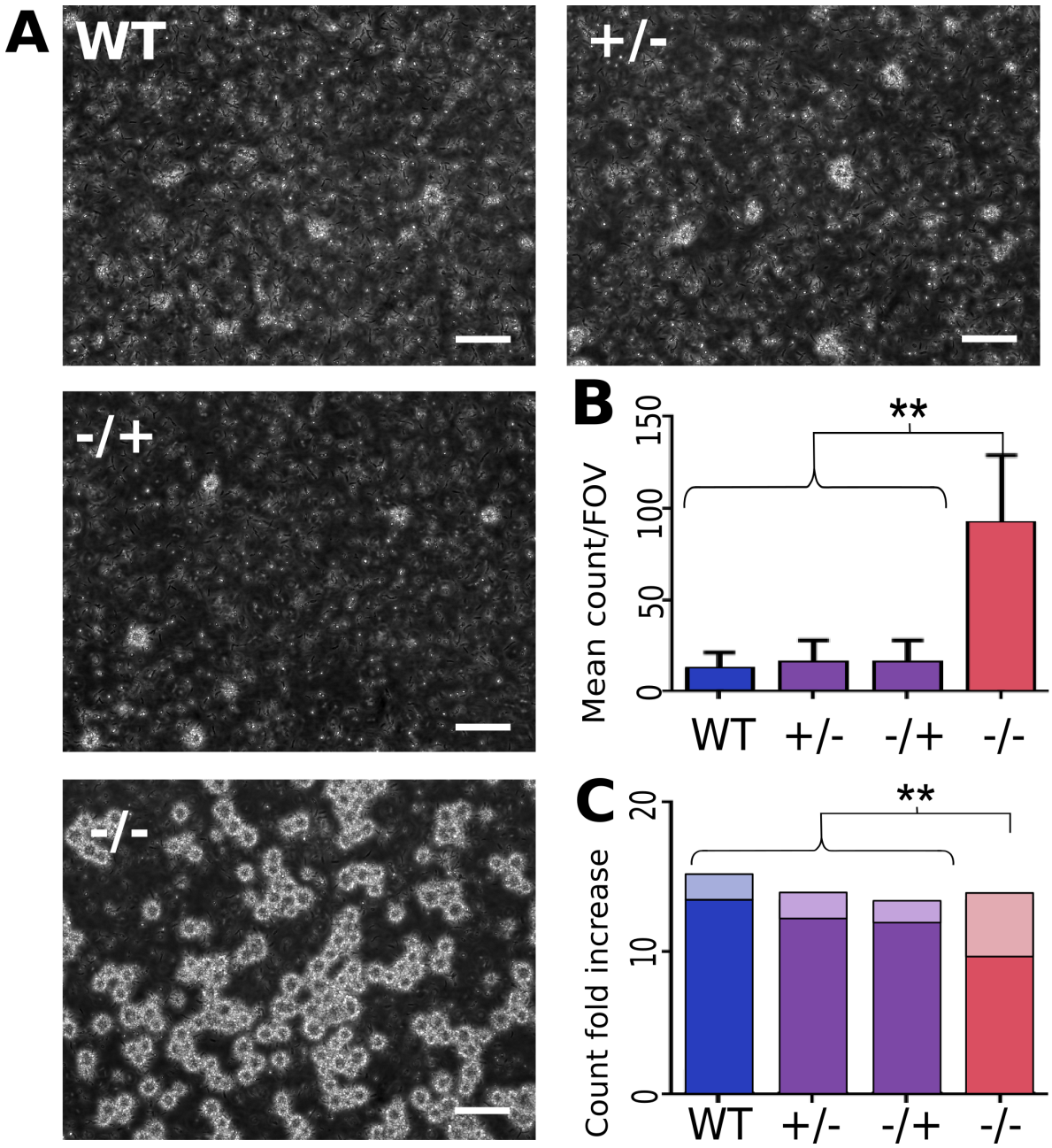


Figure 5.8. Clumping of *Leishmania mexicana* promastigotes occurs only in absence of both BBS2 alleles. (A) Phase contrast images show representative fields of view from base of flask containing wild type (WT) cells, BBS2 single knockouts (+/- and -/+), and BBS2 double knockout (-/-). Clumps appear as phase-bright rings. Scale bars = 100 µm. **(B)** Mean and SD of clump count per field of view over 3 days of measurements. The double knockout shows significantly more clumps than the wildtype or single knockouts (ANOVA + Tukey HSD; **= $p<0.01$). **(C)** Mean fold increase in counts over 24 hours. Faded region represents difference in count fold change between agitated and vortexed samples. The double knockout shows a significantly greater difference in fold change between the two conditions that than the wildtype or single knockouts (ANOVA + Tukey HSD; **= $p<0.01$).

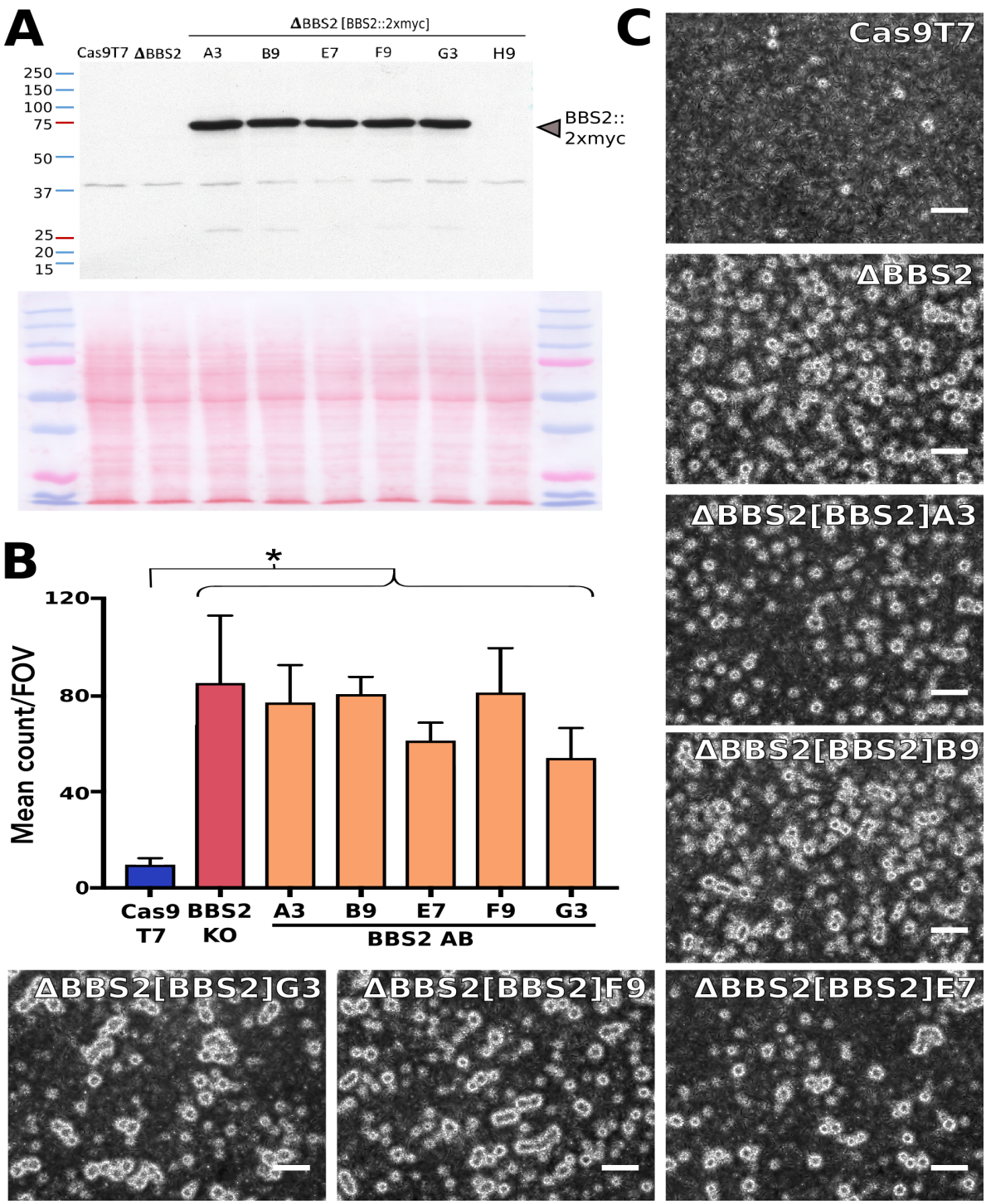


Figure 5.9. ΔBBS2 promastigotes exhibit a striking clumping phenotype, which is not rescued by expression of BBS2 from the β-tubulin locus. (A) Expression of BBS2::2xmyc confirmed in all but one of the add-back clones by Western blot using anti-myc monoclonal antibody 4A6 (Millipore EMD, 05-724) and anti-mouse IgG HRP-conjugated secondary antibody (Sigma, A9044). **(B)** Mean and SD of clump count per field of view from 3 days of measurements for Cas9T7, ΔBBS2, and 5 add-back clones. ΔBBS2 and add-back clones all show significantly more clumps than Cas9T7 parental (ANOVA + Tukey HSD; t-test, * = $p<0.05$). **(C)** Phase contrast images show representative fields of view from base of flask for each cell line. Scale bars = 100 μm.

expected to remain adhered via their posterior ends as cytokinesis proceeds in an anterior to posterior direction (**Fig 5.10 A i**) (Ambit et al., 2011).

2. Clumps resulting from an increase in the general adherent properties of the ΔBBS2 cells. Clumps would contain both unlabelled ΔBBS2 cells and labelled wild type reporter cells. Incorporation of the fluorescent cells would be expected to show random orientation of cells within the clumps (**Fig 5.10 A ii**).

3. Clumps resulting from a change in the flagellar properties of the ΔBBS2 cells. Clumps would contain both unlabelled ΔBBS2 cells and labelled wild type reporter cells. Incorporation of the fluorescent cells would be expected to show cells in a rosette formation with their flagella in the centre (**Fig 5.10 A iii**).

Therefore, in order to gain insight into the mechanism by which the increased clumping occurred in the BBS2 knockout, this was co-cultured with a wild type cell line expressing an SMP1::eGFP flagellar membrane tag and a GT2::mCherry pellicular membrane tag. After 24 hours of co-culture, the clumps contained both labelled and unlabelled cells (**Fig 5.10 B**), suggesting that these did not result from a cytokinesis defect. Moreover, the labelled cells were clearly oriented with their flagella in the centre, in a rosette formation, and the orientation of the Hoechst signal in the unlabelled cells was consistent with this (**Fig 5.10 B**). This suggests that the clumping of the BBS2 knockout results from an increase in adherence of cells to one-another in a cytokinesis-independent manner, and may indicate a change in flagellar membrane properties, as this seems to represent the point of attachment.

5.2.7 BBS2 is not required for successful differentiation of *L. mexicana* into axenic amastigotes

The conventionally-produced BBS2 knockout was additionally assessed for its ability to successfully differentiate into the amastigote form. To test this, stationary phase promastigotes were cultured under the axenic differentiation stimulatory conditions of an increased temperature of 34°C and decreased pH of 5.5 for 72 hours. Axenically-differentiated amastigotes differ somewhat from intracellular amastigotes in terms of gene expression (Fiebig et al., 2015), and metabolic profiles suggest that these may represent an intermediate stage in the differentiation process (Gupta et al., 1999). However, they are ideal for assessing the ability of a cell line to respond to temperature and pH stimuli, and to adapt their morphology appropriately. After differentiation, ΔBBS2 cells successfully adopted an amastigote-like morphology (**Fig 5.11 A**).

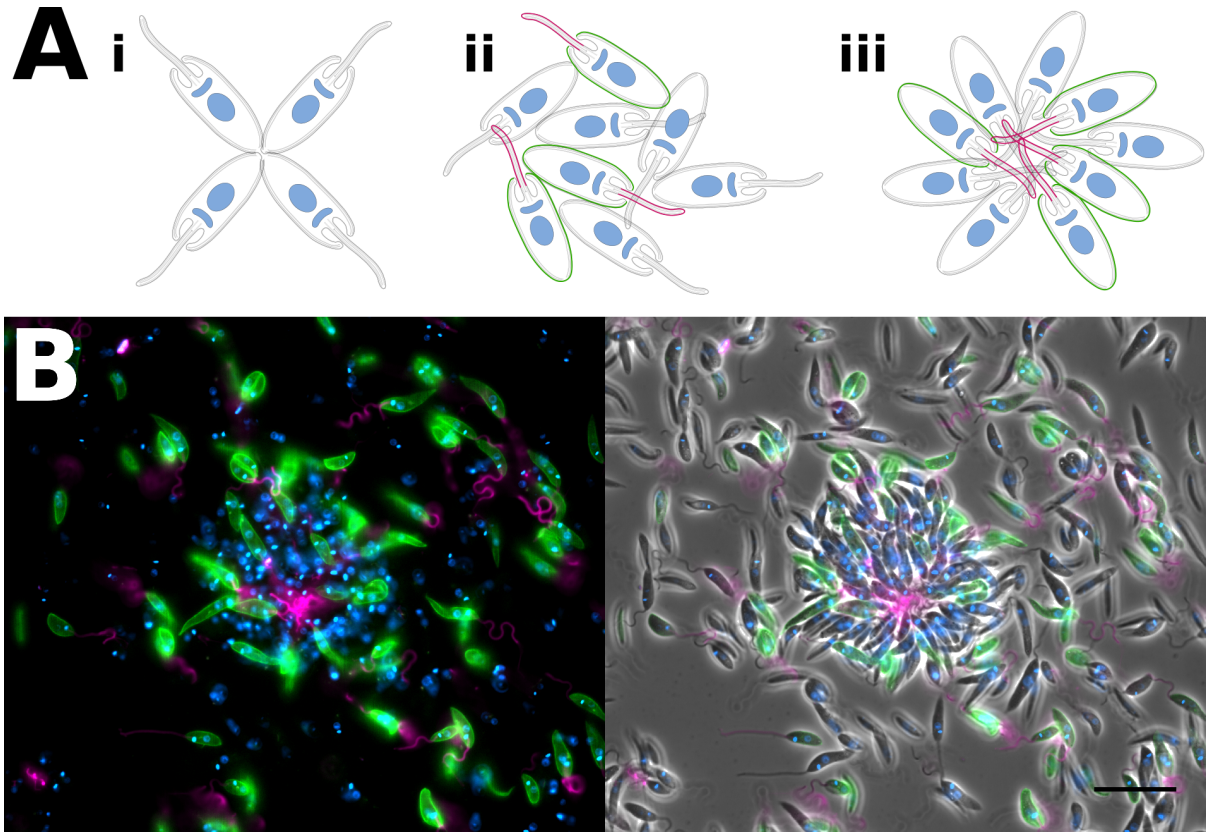


Figure 5.10 Clumps formed by BBS2 knockouts incorporate labelled cells in co-culture. (A) Potential mechanisms of clump formation: Cytokinesis defect resulting in cells attached by their posterior ends - clumps formed by this mechanism would not be expected to incorporate many fluorescent cells (i); or increase in adherent properties of ΔBBS2 cells, resulting in clumps able to incorporate labelled cells - either with cells adhering randomly with no uniform orientation (ii), or with cells adopting a rosette formation with their flagella in the centre (iii). **(B)** After 24h of co-culture, clumps contain both labelled and unlabelled cells, arranged in a rosette formation. Scale bars = 20 μm.

Further to the morphological changes, Western blots were used to probe for the presence of life cycle stage-specific proteins; promastigote-specific paraflagellar rod protein 1 (PFR1) (Gadelha et al., 2005; Kohl et al., 1999) and amastigote-specific hydrophilic acylated surface protein B (HASP B) (Flinn et al., 1994). Whole cell protein lysates were produced from log phase and stationary phase promastigotes, as well as axenic amastigotes 24 and 72 hours into differentiation. PFR1 appeared to be expressed at comparable levels in the double knockouts as in both the wild type and the single knockouts in log phase and stationary phase promastigotes (**Fig 5.11 B**). All cell lines showed an absence of protein by 72 hours into differentiation, but the 24-hour time point showed an interesting difference: wild type and single knockout cell lysates showed PFR1 expression, albeit at a reduced level compared to the promastigote stages, but this was notably absent in the knockout cell lines (**Fig 5.11 B**). HASP B, meanwhile, showed expression in all cell lines at 24 and 72 hours into differentiation, but exhibited some differences in the promastigote phases (**Fig 5.11 C**). Log phase promastigotes showed only a hint of HASP B signal, while stationary phase promastigotes showed stronger expression, but in both cases the double knockout cell lines appeared to express slightly higher levels of HASP B than the wild type or single knockouts (**Fig 5.11 C**). The differences in band intensities in the log phase promastigotes in each blot can be explained by the uneven loading of whole cell lysate samples, which can clearly be seen in the Ponceau stained membranes. Taken together, these results suggest that the BBS2 double knockout cell line may progress through differentiation at a slightly accelerated rate.

5.2.8 Individual components of the BBSome are not essential for the successful infection of murine bone marrow derived macrophages by *Leishmania mexicana* promastigotes or for their intracellular survival as amastigotes.

Finally, in order to determine whether individual components of the BBSome were required for survival of intracellular amastigotes and to see whether the striking phenotype observed in *L. major* after BBS1 knockout could be reproduced in *L. mexicana*, each ΔBBS cell line was tested for its ability to infect and persist inside of macrophages *in vitro*. The ΔKHARON1 (ΔKH1) cell line (see Chapter 4), was included as a control as this cell line was known to show impaired survival inside of macrophages. However, as this was not derived from the Cas9T7 cell line, the wild type parental from which it was produced was also included for comparison. Promastigotes of each cell line were grown into stationary phase and stained with CFSE before addition to murine bone marrow derived macrophages at a multiplicity of infection of 10:1. Macrophages from each infection were fixed at 0, 24, 48 and 72-hour time points and infection levels were assessed by flow cytometry (see section 2.7). This approach was selected over microscopy-based counting of infected macrophages, as it would allow for thousands rather than only

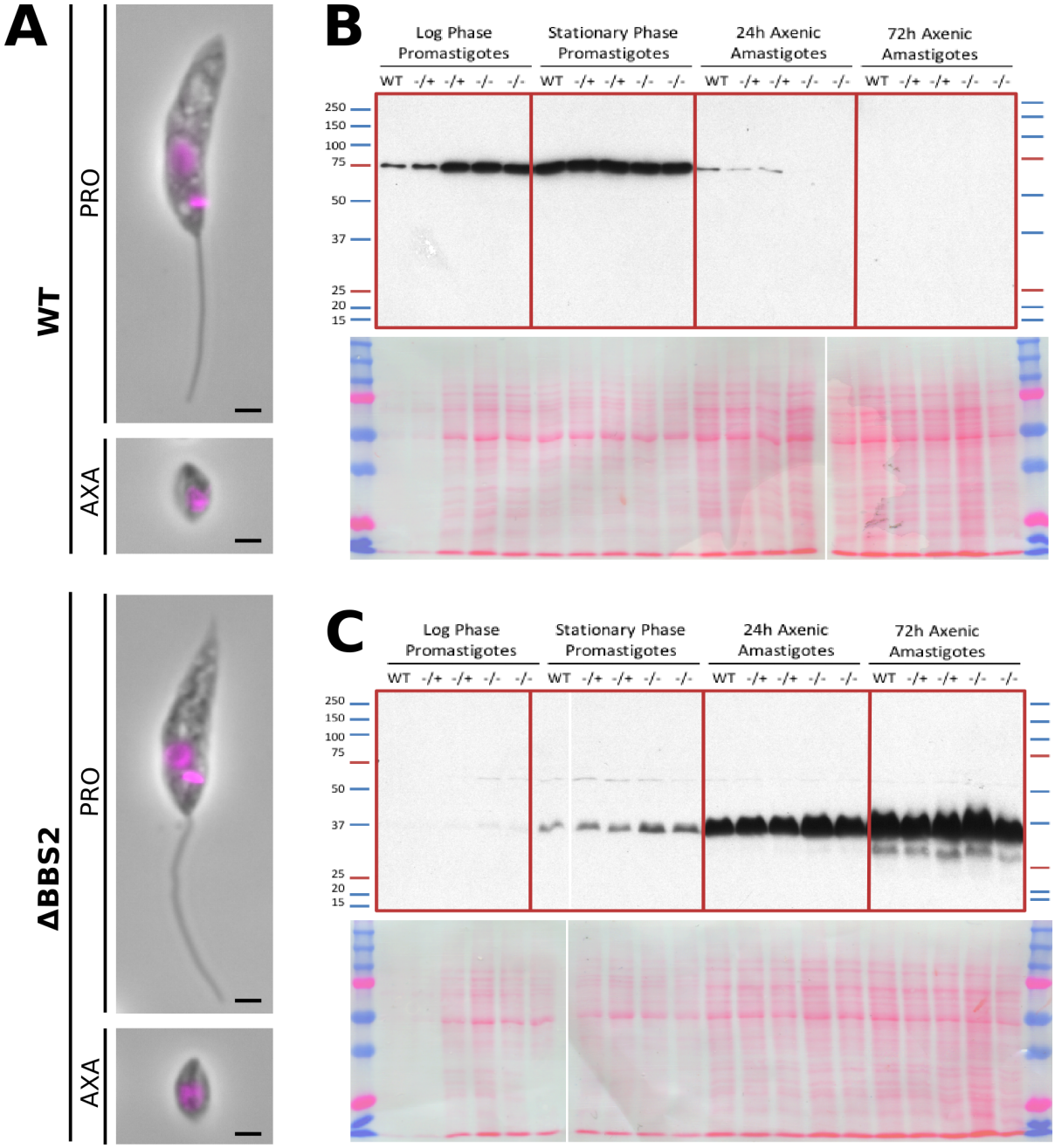


Figure 5.11 ΔBBS2 cells complete axenic differentiation but show changes in stage-specific markers at an accelerated rate. (A) ΔBBS2 cells successfully differentiate from promastigotes (PRO) to adopt an amastigote-like morphology (AXA) by 72 hours. Scale bars = 2 μm. **(B and C)** Western blots on whole cell lysates produced from wildtype (WT), and BBS2 single knockout (-/+) and double knockout (-/-) cells. Ponceau stained membranes show uneven protein lysate loading. **(B)** Detection of PFR1 using monoclonal antibody L13D6 **(Kohl et al., 1999)** and anti-mouse IgG HRP-conjugated secondary antibody (Sigma, A9044). **(C)** Detection of HASP B using anti-HASPB purified polyclonal serum **(Flinn et al., 1994)** and anti-mouse IgG HRP-conjugated secondary antibody (Sigma, A9044).

hundreds of macrophages to be included in the analysis, increasing the reliability of the results. However, this approach only provided a measure of percentage of infected macrophages, but not the number of amastigotes per infected macrophage. Forward scatter and side scatter data were gated to exclude cell debris and extracellular *Leishmania*, and uninfected controls were used to define the fluorescence intensity cut-off for uninfected cells. Each condition was performed in triplicate. However, one replicate showed duplicated populations in the scatter plots and was therefore excluded. The mean of the remaining two duplicates was calculated for each condition at each time point.

All of the measured cell lines showed a general decrease in percentage of infected macrophages over the 72 hour infection time course. Infection counts for each BBS knockout cell line were plotted against the infection counts for the parental Cas9T7 cell line, as well as the KHARON1 knockout and associated wild type (**Fig 5.12 A-H**). The downward trend for each knockout was generally very similar to that of the parental and most showed no obvious impairments in survival of amastigotes inside of macrophages (**Fig 5.12 A-H**). Overall, the wild type displayed the highest infectivity and the ΔKH1 cell line displayed the lowest infectivity. The Cas9T7 parental and all of the associated ΔBBS resided at intermediate levels of infectivity between these two cell lines (**Fig 5.12 A-H**), but ΔBBS5 appeared to show infectivity closest to the wild type (**Fig 5.12 E**), while ΔBBS7 showed infectivity closest to the impaired ΔKH1 (**Fig 5.12 F**). It is interesting that these two cell lines stand out from the rest as these both took slightly longer to reach stationary phase than the other cell lines (see section 5.2.3). However, it remains to be determined whether there is any causal link between these two factors. Previous work in *L. major* showed that while knockout of BBS1 did not impair the initial infection ability of the parasites, it resulted in a reduced ability of the amastigotes to survive inside of macrophages over 72 hours (Price et al., 2013). However, the decrease in percentage of infected macrophages was relatively minor, whereas the effect on *in vivo* mouse infections was more striking (Price et al., 2013). It would therefore be of interest to test the *L. mexicana* ΔBBS lines for their ability to persist in a mouse model of infection to determine whether these may produce any pronounced differences.

5.3 Discussion

The aims of these analyses were to determine the functions of the BBSome in *Leishmania mexicana*, and to identify any evidence of involvement of the complex in flagellar trafficking in this species.

The results showed localisations similar to those observed in other organisms, with the BBSome complex proteins localised to the base of the flagellum and the small GTPase, BBS3, localised throughout the flagellar membrane, with an additional strong signal in the basal body region. This basal body signal is interesting as such an intense signal is not characteristically present in flagellar membrane proteins (Burchmore et al., 2003; Tull et al., 2004) and may be related to the interaction of this small

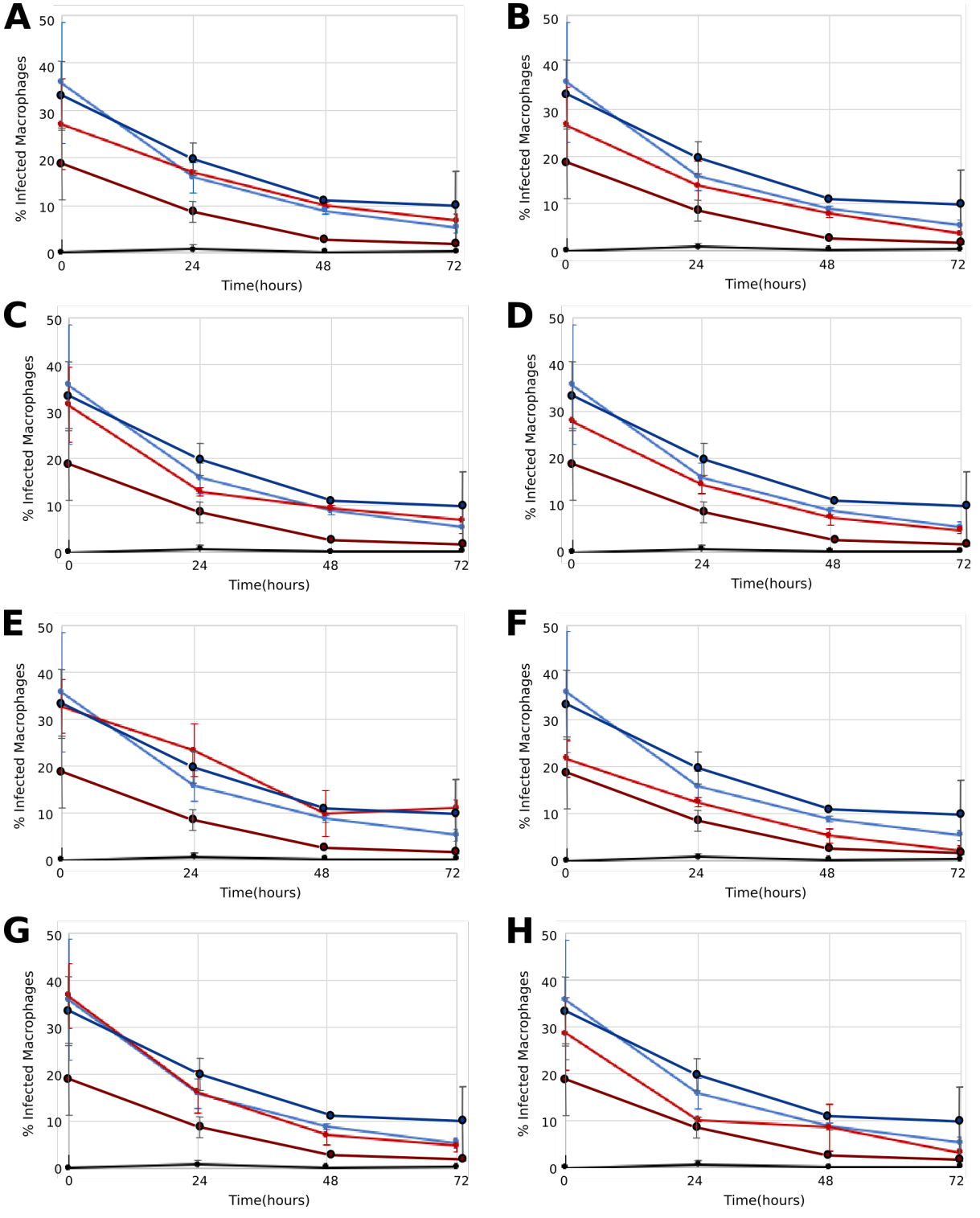


Figure 5.12. Knockout of individual BBS proteins does not severely impair the ability of *Leishmania mexicana* to infect or survive within macrophages. Number of infected macrophages was measured by flow cytometry over 72 hours. Each plot shows percentage infected macrophages for uninfected controls (●), KHARON1 knockout (●) and associated wild type (●), parental Cas9T7 (●), and BBS knockout (●): ΔBBS1 (A), ΔBBS2 (B), ΔBBS3 (C), ΔBBS4 (D), ΔBBS5 (E), ΔBBS7 (F), ΔBBS8 (G) and ΔBBS9 (H).

GTPase with the core complex. These localisations are consistent with the flagellar trafficking function that has been identified in other organisms, as is the observed conservation of various functional protein domains. This putative role is also consistent with the various phenotypes observed in the promastigote knockout cell lines.

The most compelling evidence in support of this role was that knockout of BBS3 resulted in mislocalisation of a putative flagellar calcium-binding protein (calflagin) in promastigotes, and that this phenotype was partially rescued by re-introduction of the BBS3 open reading frame. Knockout of both BBS2 and BBS7, meanwhile, caused an increase in localisation within the cell body and possibly on the plasma membrane, without as significant a reduction in flagellar signal. This result was particularly interesting as it closely resembled the localisation observed in the BBS3 add-back cell line. These results present strong evidence for the involvement of BBS3, and potentially the BBSome complex, in trafficking of the putative calflagin to the flagellar membrane. However, the difference in observed localisations between the BBS3 knockout and the BBS2 and BBS7 knockouts is somewhat curious. It therefore remains to be determined whether this trafficking is mediated by the interaction between BBS3 and the BBSome, or another as-yet unidentified function of BBS3 independent of the complex. Moreover, the results suggest that BBS3 may only be involved in trafficking of a subset of flagellar proteins, as the ΔBBS3 cell line showed no mislocalisation of SMP1 or the small GTPase, ARL-3A. Thus, while BBS3 appears to be involved in the trafficking of at least one flagellar membrane protein with putative sensory functions, it remains unclear whether this is part of a larger subset of proteins that are trafficked in a BBS3-dependent manner.

Further support for a role in trafficking comes from the effect of BBS gene knockout on flagellar length and the apparent change in flagellar adherence properties resulting in clumping of the ΔBBS2 cell line, as each of these phenotypes could imply a change in the trafficking of flagellar membrane proteins. Knockout of each individual BBSome component resulted in a statistically significant decrease in promastigote flagellum length. In *T. brucei*, RNAi knockdown of BBS3 has previously been linked to reduced flagellar length (Price et al., 2012), and this was compared to a similar phenotype observed during knockdown of another small GTPase, ARL-3 (Cuvillier et al., 2000; Sahin et al., 2008). However, taken together the presence of shorter flagella in all *L. mexicana* BBS knockout cell lines, and the lack of disrupted ARL-3A localisation in BBS3 knockouts, suggests that either the flagellar shortening observed herein may progress through a separate pathway, or that both ARL-3A and the BBSome contribute to a downstream mechanism regulating flagellar length.

The CRISPR-Cas9 produced BBS2 knockout and associated add-back cell line discussed in section 5.2.6, along with the parental Cas9T7 cell line have now been passed through the sandfly *Lutzomyia longipalpis* as part of a collaboration with the Petr Volf Group, Charles University in Prague, Czech Republic. These results showed that BBS2 knockout and add-back cell lines were able to replicate within the sandfly

midgut after defecation, at a rate comparable to the parental (Myskova et al., unpublished). All three cell lines were able to colonise the entire mesenteron, including the stomodeal valve, which is essential for transmission to the next host (Myskova et al., unpublished; Rogers et al., 2004). This suggests that the flagellar phenotypes observed in the ΔBBS2 promastigote, such as the increased clumping (section 5.2.6), do not interfere with the ability of these cells to adhere to the midgut epithelium and avoid clearance during sandfly defecation.

The knockout of individual BBSome components did not show evidence of a role in survival in the intracellular environment *in vitro*. Indeed, infections of murine bone marrow derived macrophages showed that none of the BBS protein knockouts caused impaired infection or survival. However, this may be due to redundancy and it is possible that knockout of multiple subunits in a single cell line may impair survival. This result was somewhat surprising as knockout of BBS1 in *Leishmania major* and of BBS1 and BBS9 in *Trypanosoma brucei* produced decreased virulence resulting in increased host survival and even complete clearance of detectable parasites in a mouse model of infection (Langousis et al., 2016; Price et al., 2013). This suggests that the BBSome does play a role in the survival of kinetoplastid species within mammalian hosts. It will therefore be important to determine whether knockout of BBSome components in *L. mexicana* impairs survival *in vivo*, or whether this represents an actual difference in this species.

CHAPTER 6

CONCLUSIONS AND OUTLOOK

6 Conclusions and Outlook

6.1 Addressing thesis aims

The aims of this thesis were to explore the putative roles of the *Leishmania mexicana* amastigote flagellum in parasite-host interactions; specifically in providing a platform for either receptor-ligand interactions or vesicular trafficking. The research presented herein provides comprehensive high-resolution models of intracellular *L. mexicana* amastigotes, allowing for precise definition of amastigote positioning within parasitophorous vacuoles, and of the connectivity between the parasite and the host cell. The use of 3D electron microscopy techniques allowed for reconciliation of previously contradictory evidence about amastigote positioning and revealed a previously unobserved amastigote orientation and associated vacuole shape. High-resolution 3D analysis of the connectivity between the amastigote flagellum and the PV membrane identified membranous extensions of the flagellar membranes as well as evidence suggestive of vesicular trafficking. To address the function of the amastigote flagellum, null mutants of components of the BBSome trafficking complex, and of the kinetoplastid-specific trafficking protein, KHARON1, were assessed for their ability to infect and replicate within macrophages to determine whether an intact flagellum, and a correctly populated flagellar membrane are required for survival within the intracellular environment. Analysis of ΔKHARON1 mutants revealed an intracellular-amastigote specific phenotype in the form of a striking alteration in amastigote cell shape and a cytokinesis defect. The constraint of this phenotype to the intracellular environment implies a crucial role for environmental sensing or parasite-host interaction in cell morphogenesis during amastigote adaptation. Further work will be required to determine flagellar involvement in these processes. Finally, analysis of null mutants for components of the BBSome trafficking complex highlighted potential differences between the roles of these components in different *Leishmania* species. The *L. mexicana* null mutants exhibited a number of flagellar phenotypes in the promastigote life cycle stage but did not show significantly impaired survival as intracellular amastigotes. Therefore, while the function of the amastigote flagellum remains obscure, the results presented in this thesis provide important evidence and uncover significant questions towards elucidating a role for this organelle.

6.2 A potential role for the amastigote flagellum in modulating PV formation?

The results presented in Chapter 3 demonstrate that amastigote contact with the parasitophorous vacuole membrane is more complex than had previously been defined. While posterior contact appears to remain constant, flagellum contact is only observed in vacuoles of a particular shape. Based on the

trends we observed in vacuole size and occupancy, we have proposed a model of amastigote positioning during vacuole development. In this model, amastigotes remain in contact with the parasitophorous vacuole membrane throughout vacuole development. However, we propose that while amastigotes are initially found within tight vacuoles with contact on all sides, vacuole size increase begins as a bulging volume away from the side of the amastigote, leaving both the posterior end and the flagellar tip in contact with the membrane, before opening out further with a resulting loss of flagellar contact.

This model predicts differences between *Leishmania* of the mexicana complex and other species; either in terms of *L. mexicana* promoting vacuole growth, or of other *Leishmania* species suppressing this. While *Leishmania* of the mexicana complex are located within large, shared vacuoles (Russell et al., 1992), other species, such as *L. major*, inhabit tight, individual vacuoles which undergo fission after parasite division (Castro et al., 2006; Real and Mortara, 2012). These different *Leishmania* species have different requirements for survival inside of parasitophorous vacuoles and must therefore be able to modulate their maturation in a species-specific fashion. Seminal studies assessing either re-infection of macrophages with a single *Leishmania* species (Real et al., 2008) or co-infection of macrophages with different *Leishmania* species (Real et al., 2010) have already vastly contributed to our understanding of these different requirements. *L. major* promastigotes phagocytosed by macrophages with established *L. amazonensis* infections were initially enclosed within tight vacuoles, but these were able to fuse with the large PVs containing *L. amazonensis* amastigotes (Real et al., 2010). Strikingly, upon incorporation in to the shared vacuoles, *L. major* cells failed to undergo differentiation, and instead survived and proliferated as promastigotes (Real et al., 2010). *L. major* cells that remained in their own individual vacuoles, meanwhile, differentiated into amastigotes (Real et al., 2010). This was in stark contrast to re-infection of macrophages with *L. amazonensis* amastigotes; upon incorporation into pre-established vacuoles containing the same species, *L. amazonensis* promastigotes differentiated to the amastigote form (Real et al., 2008). Moreover, co-infection of macrophages with pre-differentiated *L. major* and *L. amazonensis* amastigotes showed no fusion of vacuoles containing the different species (Real et al., 2010). However, while these studies have provided clear insight into the result of inter-species vacuole fusion after maturation of large, shared vacuoles, the use of similar models of co-infection could potentially provide answers to the question of parasite modulation of vacuole development. For example, if simultaneous co-infection of macrophages with *L. major* and *L. amazonensis* promastigotes resulted in fusion of vacuoles while both species were enclosed within tight PVs, analysis of the progression of shared-vacuole maturation could shed light on whether differential vacuole size results from parasite-induced inhibition or stimulation of growth. Also of interest would be analysis of the effect of infection with different *Leishmania* species on known regulators of mammalian lysosome size. The lysosomal trafficking regulator (LYST)/Beige gene has been implicated in both general lysosomal size regulation and in PV size regulation during *Leishmania* infection (Perou et al., 1997; Wilson et al., 2008). *Leishmania*

amazonensis-infection of bone marrow derived macrophages (BMDMs) from mice lacking this gene showed enhanced PV expansion, while infection of BMDMs from mice overexpressing the gene produced PVs of markedly reduced size {Wilson 2008}. Infection of wild type murine BMDMs with *L. amazonensis* caused increased expression of LYST/Beige (Wilson et al., 2008), suggesting that this may be a macrophage mechanism of fighting *Leishmania* infection. It would therefore be of interest to determine whether differences in expression levels occur with different *Leishmania* species, or whether any *Leishmania* virulence factors interact with the resulting protein.

Of particular relevance to the research question set out in this thesis, are two predictions from our model that raise interesting questions about potential roles for the amastigote flagellum:

1. Our model predicts that tip interactions occur frequently in early stages of vacuole maturation, but infrequently in later stages. This raises the interesting question of whether the amastigote flagellum could be involved in modulating vacuole size increase.

2. Our model also predicts that membrane must be delivered to the tight parasitophorous vacuoles to allow for growth into the bulging and open vacuole types. It will be of particular interest in future to determine whether all incorporated membrane is of host-origin, or whether fusion of parasite-derived vesicles, and in particular flagellar-derived vesicles, with the PV membrane could contribute to this process.

Both of these questions are particularly interesting in light of the flagellar membrane activity we observed by electron tomography and Airyscan detection (Chapter 3). These results showed long tubular extensions of the flagellar membrane which were still observed by live cell imaging 72 hours into an infection time course, suggesting that these are not simply remnants of flagellar shortening. Similarly, high-resolution tomography showed evidence of vesicular activity occurring on both the flagellar membrane and the parasitophorous vacuole membrane. A proposed function of the amastigote flagellum is in providing a platform for communication with the host, and these results would be consistent with a role for this organelle in vesicular trafficking.

Recent analyses on the secretion of *Leishmania* proteins have shown that only a small proportion of these contain classical secretion signals (Silverman et al., 2008). Moreover, many of the proteins in the *Leishmania* secretome had previously been associated with vesicles released from other eukaryotic cell types (Silverman et al., 2008). Together, these findings have led to the suggestion that the majority of *Leishmania*-secreted proteins are not exported via classical secretion systems but are instead released via an exosome-based mechanism (Silverman et al., 2010, 2008). Several *Leishmania*-secreted proteins have been implicated in parasite-host interactions; GP63, for example, has been shown to cleave multiple macrophage protein tyrosine phosphatases, causing alterations in host cell signalling (Gomez et al., 2009; Hallé et al., 2009). Incubation of macrophages with *Leishmania*-derived vesicles has shown

alterations in macrophage cytokine production (Silverman et al., 2010), providing support for the theory of vesicle-mediated delivery of virulence factors to the host cell. Furthermore, both the release and content of *Leishmania*-derived vesicles have been shown to be temperature- and pH-dependent (Hassani et al., 2011; Silverman et al., 2010). This portends a potential ability to manipulate delivery of virulence factors in response to changes in host environment. However, the subcellular origin of these bioactive vesicles remains to be determined. Flagellar-derived vesicles have been identified in other organisms, including in *Chlamydomonas reinhardtii* where vesicle-mediated delivery of the protease VLE from the flagella of daughter cells induces 'hatching' through degradation of the encapsulating mother cell wall (Wood et al., 2013), and in *Trypanosoma brucei* (Szempruch et al., 2016), where they have been implicated in parasite-parasite communication. This biological precedent has led to the hypothesis that virulence factor delivery-mediating vesicles could be released from the *Leishmania* flagellum. Within this context, this thesis provides intriguing findings, which may represent the first definitive structural evidence of membrane shedding and budding from the *Leishmania* flagellum.

6.3 Trafficking of flagellar membrane proteins

One of the key objectives of this thesis was to assess the link between flagellar membrane trafficking in the amastigote and survival within the intracellular environment. While our results do not definitively provide a link between these processes, they do provide intriguing results with potential implications for the role of flagellar membrane trafficking. This research addressed the importance of flagellar membrane protein trafficking by targeting the kinetoplastid specific protein, KHARON1, and the widely-conserved BBSome complex. The analysis of the BBSome complex components (Chapter 5) did not show evidence of a role in survival in the intracellular environment. This was somewhat surprising as knockout of components of the BBSome were shown to reduce virulence in both *Leishmania major* and *Trypanosoma brucei* (Langousis et al., 2016; Price et al., 2013). This suggests that the while the BBSome may play a role in the survival of some kinetoplastid species within mammalian hosts, these mechanisms may not be universal amongst the parasites. Our knockouts of the BBSome components did, however, highlight a number of flagellar phenotypes in the promastigote form. Knockout of BBS2, for example, caused a striking clumping phenotype in promastigotes. Analysis of the orientation of cells within the clumps and their ability to incorporate non-mutant cells showed that these were arranged in a rosette formation with attachment occurring via the flagellum and suggested a potential increase in the adherent properties of the flagellar membrane.

Moreover, knockout of each individual component resulted in a statistically significant decrease in promastigote flagellum length. A number of proteins involved in flagellar length regulation have been localised to the flagellum, including kinesin-13 (Blaineau et al., 2007) and the small GTPase ARL-3A (Cuvillier et al., 2000; Sahin et al., 2008). However, knockout of BBS3 did not affect the localisation of

ARL-3A, as shown by endogenous tagging. This does not necessarily preclude a role for flagellar protein trafficking in regulation of flagellar length, but further analysis will be required to determine whether the decreased flagellar length results directly from the mistrafficking of specific flagellar proteins. Interestingly, while the BBS3-null mutant did not cause mislocalisation of ARL-3A or of SMP1, it did cause a partial mislocalisation of a calflagin. BBS3 therefore appears to be involved in the trafficking of at least one flagellar membrane protein with putative sensory functions, but it remains unclear whether this is part of a larger subset of proteins that are trafficked in a BBS3-dependent manner. Given the existence of proteins other than the BBSome in kinetoplastids that are involved in flagellar membrane protein trafficking (e.g. KHARON1), it is plausible that these may each be involved in trafficking of specific subsets of flagellar proteins. It would therefore be of particular interest to determine whether proteins which are mis-targeted in knockouts of either KHARON1 or components of the BBSome are affected by knockout of the other. KHARON1 has now been shown to be involved in the trafficking of both the flagellar glucose transporter GT1 in *L. mexicana* and the calcium channel TbCaCh in *T. brucei* (Sanchez et al., 2016; Tran et al., 2013). Analysis of the localisation of these proteins in knockouts of components of the BBSome could therefore provide insight into different trafficking pathways for flagellar membrane proteins within kinetoplastids.

6.4 Specialisation of the amastigote posterior pole

Apart from the role of the amastigote flagellum in parasite-host interactions, the results presented in this thesis also suggest an interesting role for the amastigote posterior pole. The model of amastigote positioning during vacuole development presented in Chapter 3 predicts that there are molecular interactions between the parasite and the vacuole membrane that act as an anchoring point. Early studies using freeze fracture techniques suggested a specialisation of the plasma membrane at regions of interaction, characterised by aggregation of intra-membranous particles (Benchimol and de Souza, 1981). These aggregates were compared to the adhesions observed in freeze-fracture replicas of gap-junctions, albeit specifically identified on the parasite membrane rather than both membranes as would occur in a gap-junction (Benchimol and de Souza, 1981). The molecular components of such adhesions remain to be determined. Transmission electron microscopy studies in the early 1970s described an invagination of the amastigote plasma membrane at the posterior end in *L. donovani* and *L. tropica* (Gardener, 1974; Pham et al., 1970). These studies stated that no sub-pellicular microtubules were located in this region (Gardener, 1974), and suggested that these invaginations might represent pinocytic activity (Pham et al., 1970). As was the case with early studies of amastigote positioning, these results rely on observations from single ultrathin sections, and therefore may not represent the reality of the situation in a three-dimensional context. More recent studies have suggested that this might represent a route of entry for MHC class II molecules (Leao et al., 1995). MHC class II molecules are internalised by *Leishmania* amastigotes and degraded within megasomes (Leao et al., 1995), and studies

of their localisation in the PV membrane have shown them to congregate near the parasite posterior pole at the site of parasite adherence (Lang et al., 1994; Leao et al., 1995). This localisation, together with early reports of the posterior invagination, have led to the suggestion of endocytosis of the MHC class II molecules via this route (Leao et al., 1995). This would be a rather startling discovery, as the flagellar pocket has thus far represented the only known site of endocytosis in trypanosomatids (Coppens et al., 1987; Sengupta et al., 1999). Support for the hypothesis was based on the difficulty of determining a mechanism via which PV-membrane localised molecules could reach the flagellar pocket, when attachment occurred via the posterior pole (Leao et al., 1995). However, given the results presented in Chapter 3 of this thesis, it is easy to imagine how this might occur in earlier stages of vacuole formation. It will therefore be relevant to determine how internalisation and degradation of MHC class II molecules by intracellular parasites fits in with the progression of vacuole formation. The specialisation of the amastigote posterior pole and its role in parasite-host interactions represents an area that could benefit from the use of three-dimensional electron microscopy techniques. Of particular interest would be confirming whether the array of subpellicular microtubules ends in this region and determining whether the observed invaginations play a role in anchoring of the amastigotes to the PV membrane.

6.5 Future Work

The work presented in this thesis has made significant steps in addressing the role of the amastigote flagellum in survival within the parasitophorous vacuole environment. However, there remain a number of questions that could benefit from future analysis. The question of amastigote positioning within the parasitophorous vacuole would benefit from closer analysis of the parasite posterior pole. It would be of particular interest to determine whether this region of contact serves only to anchor the amastigote to the vacuole membrane, or whether it could have additional functions. Initial investigations of this could focus on ultrastructural investigations in order to determine whether the subpellicular microtubule network continues uninterrupted to the posterior pole, and to identify any evidence of activity in this region. However, these analyses could be further supplemented by an analysis of the molecular components in this region, and a search for mutants in which this contact was lost. Future work will also be required to confirm the model of amastigote positioning during parasitophorous vacuole development defined in this thesis. The key piece of evidence required for the confirmation of this model would take the form of live cell imaging examples of vacuoles progressing from a characteristically tight form to a bulging form, and from a bulging form to an open form. Live cell imaging could also be used to test predictions arising from this model, including that tip interactions are lost during transition from bulging to open vacuoles, and that vesicles of amastigote flagellum origin may fuse with and incorporate into the parasitophorous vacuole membrane. Finally, the role of the *Leishmania* parasite in modulating vacuole development could be investigated through analysis of the

differences between *Leishmania* species, in terms of their effects on known regulators of mammalian lysosome size, or the effect of co-infection with different species on vacuole development.

Future work will also be required to address open questions arising from the analysis of flagellar trafficking mutants included in this thesis. Key future experiments would include the identification of KHARON1 trafficking substrates in *L. mexicana* amastigotes, in order to assess how loss of this protein might impede flagellar function, and whether this may contribute to the poor intracellular survival. Insight into the underlying causes of poor survival in these knockouts could also be gained by analysis of the order in which the various phenotypes occur. Moreover, given the orientations of wild type amastigotes within parasitophorous vacuoles defined by the structural analyses described in Chapter 3, it would be of interest to determine whether ΔKHARON1 amastigotes maintain posterior contact with the parasitophorous vacuole membrane. In terms of the ΔBBS mutants, the key experiment that needs to be performed is an analysis of their survival in an *in vivo* mouse model of infection. However, certain *in vitro* analyses, including the assessment of flagellar length in the ΔBBS mutants could be strengthened by the inclusion of add-back cell lines. As with KHARON1, it would be beneficial to identify trafficking substrates of the BBSome in amastigotes, as these might provide insight into the role of the amastigote flagellum. Finally, it would be of particular interest to determine whether proteins which are mis-targeted in knockouts of either KHARON1 or the BBSome are affected by the knockout of the other, as this could provide insight into any redundancy that may exist between these trafficking pathways or conversely, whether each is responsible for the trafficking of a distinct subset of proteins.

6.6 Concluding Remarks

Cilia and flagella are crucial organelles with roles in both motility and signalling across eukaryotes. Revealing the diverse roles of these organelles and elucidating the underlying mechanisms therefore has important implications both for human disease research and our understanding of basic cell biology. Flagellar research in *Leishmania* species is particularly interesting due to the presence of both motile 9+2 flagella and immotile 9+0 flagella in the different life-cycle stages. While several roles have been defined for the motile promastigote flagellum, the importance of the amastigote flagellum has long eluded understanding. This thesis offers insight into the complexities and potential significance of amastigote positioning during vacuole maturation and provides evidence which ties in with the emerging field of flagellar vesicles as a delivery mechanism for virulence factors. This work has therefore contributed to the complex body of evidence towards finally defining the role of the *Leishmania* amastigote flagellum.

7 References

Alexander, J, Vickerman, K, 1975. Fusion of host cell secondary lysosomes with the parasitophorous vacuoles of *Leishmania mexicana*-infected macrophages. J Protozool 22, 502-8.

Abdelhamed, ZA, Natarajan, S, Wheway, G, Inglehearn, CF, Toomes, C, Johnson, CA, Jagger, DJ, 2015. The Meckel-Gruber syndrome protein TMEM67 controls basal body positioning and epithelial branching morphogenesis in mice via the non-canonical Wnt pathway. Dis Model Mech 8, 527-41.

Abdelhamed, ZA, Wheway, G, Szymanska, K, Natarajan, S, Toomes, C, Inglehearn, C, Johnson, CA, 2013. Variable expressivity of ciliopathy neurological phenotypes that encompass Meckel-Gruber syndrome and Joubert syndrome is caused by complex de-regulated ciliogenesis, Shh and Wnt signalling defects. Hum Mol Genet 22, 1358-72.

Adams, GM, Huang, B, Piperno, G, Luck, DJ, 1981. Central-pair microtubular complex of *Chlamydomonas* flagella: polypeptide composition as revealed by analysis of mutants. J Cell Biol 91, 69-76.

Afzelius, BA, 1959. Electron microscopy of the sperm tail; results obtained with a new fixative. J Biophys Biochem Cytol 5, 269-78.

Afzelius, BA, 1976. A human syndrome caused by immotile cilia. Science 193, 317-9.

Aigner, A, 2006. Gene silencing through RNA interference (RNAi) *in vivo*: strategies based on the direct application of siRNAs. J Biotechnol 124, 12-25.

Alberio, SO, Dias, SS, Faria, FP, Mortara, RA, Barbiéri, CL, Haapalainen, F.E., 2004. Ultrastructural and cytochemical identification of megasome in *Leishmania (Leishmania) chagasi*. Parasitol Res 92, 246-54.

Allen, RA, 1965. Isolated cilia in inner retinal neurons and in retinal pigment epithelium. J Ultrastruct Res 12, 730-47.

Alsford, S., Turner, D., Obado, S., Sanchez-Flores, A., Glover, L., Berriman, M., Hertz-Fowler, C., Horn, D., 2011. High-throughput phenotyping using parallel sequencing of RNA interference targets in the African trypanosome. Genome research 21, 915-24.

Ambit, A, Woods, KL, Cull, B, Coombs, GH, Mottram, JC, 2011. Morphological events during the cell cycle of *Leishmania major*. Eukaryot Cell 10, 1429-38.

Anderson, JR, Jones, BW, Watt, CB, Shaw, MV, Yang, JH, Demill, D, Lauritzen, JS, Lin, Y, Rapp, KD, Mastronarde, D, Koshevoy, P, Grimm, B, Tasdizen, T, Whitaker, R, Marc, RE, 2011. Exploring the retinal connectome. Mol Vis 17, 355-79.

Anderson, RG, 1974. Isolation of ciliated or unciliated basal bodies from the rabbit oviduct. J Cell Biol 60, 393-404.

Andrews, PM, Porter, KR, 1974. A scanning electron microscopic study of the nephron. Am J Anat 140, 81-115.

Ansley, SJ, Badano, JL, Blacque, OE, Hill, J, Hoskins, BE, Leitch, CC, Kim, JC, Ross, AJ, Eichers, ER, Teslovich, TM, Mah, AK, Johnsen, RC, Cavender, JC, Lewis, RA, Leroux, MR, Beales, PL, Katsanis, N, 2003. Basal body dysfunction is a likely cause of pleiotropic Bardet-Biedl syndrome. Nature 425, 628-33.

Antoine, JC, Jouanne, C, Ryter, A, Zilberfarb, V, 1987. *Leishmania mexicana*: a cytochemical and quantitative study of lysosomal enzymes in infected rat bone marrow-derived macrophages. Exp Parasitol 64, 485-98.

Antoine, JC, Prina, E, Jouanne, C, Bongrand, P, 1990. Parasitophorous vacuoles of *Leishmania amazonensis*-infected macrophages maintain an acidic pH. Infect Immun 58, 779-87.

Antoine, JC, Prina, E, Lang, T, Courret, N, 1998. The biogenesis and properties of the parasitophorous vacuoles that harbour *Leishmania* in murine macrophages. Trends Microbiol 6, 392-401.

Aslett, M., Aurrecoechea, C., Berriman, M., Brestelli, J., Brunk, B.P., Carrington, M., Depledge, D.P., Fischer, S., Gajria, B., Gao, X., Gardner, M.J., Gingle, A., Grant, G., Harb, O.S., Heiges, M., Hertz-Fowler, C., Houston, R., Innamorato, F., Iodice, J., Kissinger, J.C., Kraemer, E., Li, W., Logan, F.J., Miller, J.A., Mitra, S., Myler, P.J., Nayak, V., Pennington, C., Phan, I., Pinney, D.F., Ramasamy, G., Rogers, M.B., Roos, D.S., Ross, C., Sivam, D., Smith, D.F., Srinivasamoorthy, G., Stoeckert, C.J., Subramanian, S., Thibodeau, R., Tivey, A., Treatman, C., Velarde, G., Wang, H., 2010. TriTrypDB: a functional genomic resource for the Trypanosomatidae. Nucleic Acids Res. 38, D457-62.

Baccetti, B, Dallai, R, Fratello, B, 1973. The spermatozoon of arthropoda. XXII. The 12+0', 14+0' or aflagellate sperm of protura. J Cell Sci 13, 321-35.

Badano, J., Ansley, S., Leitch, C., Lewis, R., Lupski, J., Katsanis, N., 2003. Identification of a novel Bardet-Biedl syndrome protein, BBS7, that shares structural features with BBS1 and BBS2. The American Journal of Human Genetics 72, 650-8.

Bárcena, M., Koster, A.J., 2009. Electron tomography in life science. Semin. Cell Dev. Biol. 20, 920-30.

Bardet, G., 1920. Sur un syndrome d'obesité congénitale avec polydactylie et rétinite pigmentaire : contribution a l'étude des formes cliniques de l'obésité hypophysaire. Paris.

Barnes, BG, 1961. Ciliated secretory cells in the pars distalis of the mouse hypophysis. J Ultrastruct Res 5, 453-67.

Bastin, P, Matthews, KR, Gull, K, 1996. The paraflagellar rod of kinetoplastida: solved and unsolved questions. Parasitol Today 12, 302-7.

Bastin, P, Pullen, TJ, Sherwin, T, Gull, K, 1999. Protein transport and flagellum assembly dynamics revealed by analysis of the paralysed trypanosome mutant snl-1. J Cell Sci 112 (Pt 21), 3769-77.

Bates, PA, Rogers, ME, 2004. New insights into the developmental biology and transmission mechanisms of *Leishmania*. Curr Mol Med 4, 601-9.

Bates, P.A., 1994. Complete developmental cycle of *Leishmania mexicana* in axenic culture. Parasitology 108 (Pt 1), 1-9.

Bates, P.A., 2007. Transmission of *Leishmania* metacyclic promastigotes by phlebotomine sand flies. Int. J. Parasitol. 37, 1097-106.

Bates, P.A., Robertson, C.D., Tetley, L., Coombs, G.H., 1992. Axenic cultivation and characterization of *Leishmania mexicana* amastigote-like forms. Parasitology 105 (Pt 2), 193-202.

Baur, PS, Stacey, TR, 1977. The use of PIPES buffer in the fixation of mammalian and marine tissues for electron microscopy. J Microsc 109, 315-27.

Beales, PL, Katsanis, N, Lewis, RA, Ansley, SJ, Elcioglu, N, Raza, J, Woods, MO, Green, JS, Parfrey, PS, Davidson, WS, Lupski, JR, 2001. Genetic and mutational analyses of a large multiethnic Bardet-Biedl cohort reveal a minor involvement of BBS6 and delineate the critical intervals of other loci. Am J Hum Genet 68, 606-16.

Benchimol, M, de Souza, W, 1981. *Leishmania mexicana amazonensis*: attachment to the membrane of the phagocytic vacuole of macrophages *in vivo*. Z Parasitenkd 66, 25-9.

Beneke, T., Madden, R., Makin, L., Valli, J., Sunter, J., Gluenz, E., 2017. A CRISPR Cas9 high-throughput genome editing toolkit for kinetoplastids. Royal Society Open Science 4, 170095.

Berbari, NF, Lewis, JS, Bishop, GA, Askwith, CC, Mykytyn, K, 2008. Bardet-Biedl syndrome proteins are required for the localization of G protein-coupled receptors to primary cilia. Proc Natl Acad Sci U S A 105, 4242-6.

Berns, K, Hijmans, EM, Mullenders, J, Brummelkamp, TR, Velds, A, Heimerikx, M, Kerkhoven, RM, Madiredjo, M, Nijkamp, W, Weigelt, B, Agami, R, Ge, W, Cavet, G, Linsley, PS, Beijersbergen, RL, Bernards, R, 2004. A large-scale RNAi screen in human cells identifies new components of the p53 pathway. Nature 428, 431-7.

Bhogaraju, S, Engel, BD, Lorentzen, E, 2013. Intraflagellar transport complex structure and cargo interactions. Cilia 2, 10.

Biedl, A, 1922. Ein Geschwisterpaar mit adiposogenitaler dystrophie. Dtsch Med Wochenschr 48, 1630.

Binder, LI, Dentler, WL, Rosenbaum, JL, 1975. Assembly of chick brain tubulin onto flagellar microtubules from *Chlamydomonas* and sea urchin sperm. Proc Natl Acad Sci U S A 72, 1122-6.

Blaineau, C, Tessier, M, Dubessay, P, Tasse, L, Crobu, L, Pagès, M, Bastien, P, 2007. A novel microtubule-depolymerizing kinesin involved in length control of a eukaryotic flagellum. Curr Biol 17, 778-82.

Blanchette, J., Racette, N., Faure, R., Siminovitch, K.A., Olivier, M., 1999. *Leishmania*-induced increases in activation of macrophage SHP-1 tyrosine phosphatase are associated with impaired IFN-gamma-triggered JAK2 activation. Eur. J. Immunol. 29, 3737-44.

Boekhoff, I, Tareilus, E, Strotmann, J, Breer, H, 1990. Rapid activation of alternative second messenger pathways in olfactory cilia from rats by different odorants. EMBO J 9, 2453-8.

Borges, VM, Vannier-Santos, MA, de Souza, W, 1998. Subverted transferrin trafficking in *Leishmania*-infected macrophages. Parasitol Res 84, 811-22.

Borovsky, D., Schlein, Y., 1987. Trypsin and chymotrypsin-like enzymes of the sandfly *Phlebotomus papatasi* infected with *Leishmania* and their possible role in vector competence. Med. Vet. Entomol. 1, 235-42.

Brailov, I, Bancila, M, Brisorgueil, MJ, Miquel, MC, Hamon, M, Vergé, D, 2000. Localization of 5-HT(6) receptors at the plasma membrane of neuronal cilia in the rat brain. Brain Res 872, 271-5.

Briggman, KL, Helmstaedter, M, Denk, W, 2011. Wiring specificity in the direction-selectivity circuit of the retina. Nature 471, 183-8.

Broadhead, R, Dawe, HR, Farr, H, Griffiths, S, Hart, SR, Portman, N, Shaw, MK, Ginger, ML, Gaskell, SJ, McKean, PG, Gull, K, 2006. Flagellar motility is required for the viability of the bloodstream trypanosome. Nature 440, 224-7.

Brokaw, CJ, 1965. Non-sinusoidal bending waves of sperm flagella. J Exp Biol 43, 155-69.

Brokaw, CJ, 1972. Flagellar movement: a sliding filament model. Science 178, 455-62.

Brokaw, CJ, 2005. Computer simulation of flagellar movement IX. Oscillation and symmetry breaking in a model for short flagella and nodal cilia. Cell Motil Cytoskeleton 60, 35-47.

Brokaw, CJ, Luck, DJ, Huang, B, 1982. Analysis of the movement of *Chlamydomonas* flagella: the function of the radial-spoke system is revealed by comparison of wild-type and mutant flagella. J Cell Biol 92, 722-32.

Burchmore, RJ, Hart, DT, 1995. Glucose transport in amastigotes and promastigotes of *Leishmania mexicana mexicana*. Mol Biochem Parasitol 74, 77-86.

Burchmore, RJ, Landfear, SM, 1998. Differential regulation of multiple glucose transporter genes in *Leishmania mexicana*. J Biol Chem 273, 29118-26.

Burchmore, R., Rodriguez-Contreras, D., McBride, K., Merkel, P., Barrett, M., Modi, G., Sacks, D., Landfear, S., 2003. Genetic characterization of glucose transporter function in *Leishmania mexicana*. Proceedings of the National Academy of Sciences 100, 3901-3906.

Burge, 1973. Mechanisms of contrast and image formation of biological specimens in the transmission electron microscope. J Microsc 98, 251-285.

Cardoso, A.E., da Silva, R.A., de Carvalho, GC, Fraga, G.A., de Barbosa, C.M., dos Santos, S.A., Castro, HC, Lione, V, 2014. Leishmaniasis: History, Evolution of Treatment and the Need for New Drugs. Current Biotechnology 3, 279-288.

Carmi, R, Rokhlina, T, Kwitek-Black, AE, Elbedour, K, Nishimura, D, Stone, EM, Sheffield, VC, 1995. Use of a DNA pooling strategy to identify a human obesity syndrome locus on chromosome 15. Hum Mol Genet 4, 9-13.

Carrera, L., Gazzinelli, R.T., Badolato, R., Hieny, S., Muller, W., Kuhn, R., Sacks, D.L., 1996. *Leishmania* promastigotes selectively inhibit interleukin 12 induction in bone marrow-derived macrophages from susceptible and resistant mice. J. Exp. Med. 183, 515-26.

Carvalho-Santos, Z, Machado, P, Branco, P, Tavares-Cadete, F, Rodrigues-Martins, A, Pereira-Leal, JB, Bettencourt-Dias, M, 2010. Stepwise evolution of the centriole-assembly pathway. J Cell Sci 123, 1414-26.

Castro, R, Scott, K, Jordan, T, Evans, B, Craig, J, Peters, EL, Swier, K, 2006. The ultrastructure of the parasitophorous vacuole formed by *Leishmania major*. J Parasitol 92, 1162-70.

Cavalier-Smith, T, 1978. The evolutionary origin and phylogeny of microtubules, mitotic spindles and eukaryote flagella. Biosystems 10, 93-114.

Cavalier-Smith, T, 2002. The phagotrophic origin of eukaryotes and phylogenetic classification of Protozoa. Int J Syst Evol Microbiol 52, 297-354.

Cerutti, H, Casas-Mollano, JA, 2006. On the origin and functions of RNA-mediated silencing: from protists to man. Curr Genet 50, 81-99.

Chan, J., Fujiwara, T., Brennan, P., McNeil, M., Turco, S.J., Sibille, J.C., Snapper, M., Aisen, P., Bloom, B.R., 1989. Microbial glycolipids: possible virulence factors that scavenge oxygen radicals. Proc. Natl. Acad. Sci. U.S.A. 86, 2453-7.

Chang, KP, 1978. *Leishmania* infection of human skin fibroblasts *in vitro*: absence of phagolysosomal fusion after induced phagocytosis of promastigotes, and their intracellular transformation. Am J Trop Med Hyg 27, 1084-96.

Chang, KP, 1979. *Leishmania donovani*: promastigote-macrophage surface interactions *in vitro*. Exp Parasitol 48, 175-89.

Chang, KP, Dwyer, DM, 1976. Multiplication of a human parasite (*Leishmania donovani*) in phagolysosomes of hamster macrophages *in vitro*. Science 193, 678-80.

Chilvers, MA, Rutman, A, O'Callaghan, C, 2003. Ciliary beat pattern is associated with specific ultrastructural defects in primary ciliary dyskinesia. J Allergy Clin Immunol 112, 518-24.

Cole, DG, Diener, DR, Himelblau, AL, Beech, PL, Fuster, JC, Rosenbaum, JL, 1998. *Chlamydomonas* kinesin-II-dependent intraflagellar transport (IFT): IFT particles contain proteins required for ciliary assembly in *Caenorhabditis elegans* sensory neurons. J Cell Biol 141, 993-1008.

Coombs, GH, Tetley, L, Moss, VA, Vickerman, K, 1986. Three dimensional structure of the *Leishmania* amastigote as revealed by computer-aided reconstruction from serial sections. Parasitology 92 (Pt 1), 13-23.

Coppens, I, Opperdoes, FR, Courtoy, PJ, Baudhuin, P, 1987. Receptor-mediated endocytosis in the bloodstream form of *Trypanosoma brucei*. J Protozool 34, 465-73.

Cornillie, FJ, Lauweryns, JM, Corbeel, L, 1984. Atypical bronchial cilia in children with recurrent respiratory tract infections. A comparative ultrastructural study. Pathol Res Pract 178, 595-604.

Courret, N., Fréhel, C., Gouhier, N., Pouchelet, M., Prina, E., Roux, P., Antoine, J.-C.C., 2002. Biogenesis of *Leishmania*-harbouring parasitophorous vacuoles following phagocytosis of the metacyclic promastigote or amastigote stages of the parasites. J. Cell. Sci. 115, 2303-16.

Croft, SL, 2001. Monitoring drug resistance in leishmaniasis. Trop Med Int Health 6, 899-905.

Cruz, AK, Titus, R, Beverley, SM, 1993. Plasticity in chromosome number and testing of essential genes in *Leishmania* by targeting. Proc Natl Acad Sci U S A 90, 1599-603.

Cuvillier, A, Redon, F, Antoine, JC, Chardin, P, DeVos, T, Merlin, G, 2000. LdARL-3A, a *Leishmania* promastigote-specific ADP-ribosylation factor-like protein, is essential for flagellum integrity. J Cell Sci 113 (Pt 11), 2065-74.

Da Silva, MS, Monteiro, JP, Nunes, VS, Vasconcelos, EJ, Perez, AM, Freitas-Júnior, L.. H., Elias, MC, Cano, MI, 2013. *Leishmania amazonensis* promastigotes present two distinct modes of nucleus and kinetoplast segregation during cell cycle. PLoS One 8, e81397.

Dahl, HA, 1963. Fine structure of cilia in rat cerebral cortex. Z Zellforsch Mikrosk Anat 60, 369-86.

Dallai, R, Afzelius, Witalinski, W, 1995. The axoneme of the spider spermatozoon. Bolletino di zoologia 62, 335-338.

De Groot, D.M., 1988. Comparison of methods for the estimation of the thickness of ultrathin tissue sections. J Microsc 151, 23-42.

Dean, S, Sunter, J, Wheeler, RJ, 2017. TrypTag.org: A Trypanosome Genome-wide Protein Localisation Resource. Trends Parasitol 33, 80-82.

Dean, S, Sunter, J, Wheeler, RJ, Hodkinson, I, Gluenz, E, Gull, K, 2015. A toolkit enabling efficient, scalable and reproducible gene tagging in trypanosomatids. Open Biol 5, 140197.

Deerinck, TJ, Bushong, EA, Thor, A, Ellisman, MH, 2010. NCMIR methods for 3D EM: a new protocol for preparation of biological specimens for serial block face scanning electron microscopy. National Centre for Microscopy and Imaging Research 6-8.

Denk, W, Horstmann, H, 2004. Serial block-face scanning electron microscopy to reconstruct three-dimensional tissue nanostructure. PLoS Biol 2, e329.

Dentler, WL, Rosenbaum, JL, 1977. Flagellar elongation and shortening in *Chlamydomonas*. III. structures attached to the tips of flagellar microtubules and their relationship to the directionality of flagellar microtubule assembly. J Cell Biol 74, 747-59.

Deretic, D, Wang, J, 2012. Molecular assemblies that control rhodopsin transport to the cilia. Vision Res 75, 5-10.

Deretic, D, Williams, AH, Ransom, N, Morel, V, Hargrave, PA, Arendt, A, 2005. Rhodopsin C terminus, the site of mutations causing retinal disease, regulates trafficking by binding to ADP-ribosylation factor 4 (ARF4). Proc Natl Acad Sci U S A 102, 3301-6.

Desjardins, M, Descoteaux, A, 1997. Inhibition of phagolysosomal biogenesis by the *Leishmania* lipophosphoglycan. J Exp Med 185, 2061-8.

Desjardins, M, Huber, LA, Parton, RG, Griffiths, G, 1994. Biogenesis of phagolysosomes proceeds through a sequential series of interactions with the endocytic apparatus. J Cell Biol 124, 677-88.

Desjeux, P, 2001. Worldwide increasing risk factors for leishmaniasis. Med Microbiol Immunol 190, 77-9.

Devos, D, Dokudovskaya, S, Alber, F, Williams, R, Chait, BT, Sali, A, Rout, MP, 2004. Components of coated vesicles and nuclear pore complexes share a common molecular architecture. PLoS Biol 2, e380.

Dillon, R.J., Lane, R.P., 1993. Bloodmeal digestion in the midgut of *Phlebotomus papatasi* and *Phlebotomus langeroni*. Med. Vet. Entomol. 7, 225-32.

Dolan, MF, Melnitsky, H, Margulis, L, Kolnicki, R, 2002. Motility proteins and the origin of the nucleus. Anat Rec 268, 290-301.

Domire, JS, Green, JA, Lee, KG, Johnson, AD, Askwith, CC, Mykytyn, K, 2011. Dopamine receptor 1 localizes to neuronal cilia in a dynamic process that requires the Bardet-Biedl syndrome proteins. Cell Mol Life Sci 68, 2951-60.

Doudna, JA, Charpentier, E, 2014. Genome editing. The new frontier of genome engineering with CRISPR-Cas9. Science 346, 1258096.

Dutcher, SK, 2003. Long-lost relatives reappear: identification of new members of the tubulin superfamily. Curr Opin Microbiol 6, 634-40.

Dutcher, SK, Huang, B, Luck, DJ, 1984. Genetic dissection of the central pair microtubules of the flagella of *Chlamydomonas reinhardtii*. J Cell Biol 98, 229-36.

Dute, R, Kung, C, 1978. Ultrastructure of the proximal region of somatic cilia in *Paramecium tetraurelia*. J Cell Biol 78, 451-64.

Dwyer, DM, 1980. Isolation and partial characterization of surface membranes from *Leishmania donovani* promastigotes. J Protozool 27, 176-82.

Edelstein, A., Amodaj, N., Hoover, K., Vale, R., Stuurman, N., 2010. Computer control of microscopes using μManager. Curr Protoc Mol Biol Chapter 14, Unit14.20.

Eguether, T, Agustin, S.J., Keady, BT, Jonassen, JA, Liang, Y, Francis, R, Tobita, K, Johnson, CA, Abdelhamed, ZA, Lo, CW, Pazour, GJ, 2014. IFT27 links the BBSome to IFT for maintenance of the ciliary signaling compartment. Dev Cell 31, 279-90.

Elliott, DA, Clark, DP, 2000. *Cryptosporidium parvum* induces host cell actin accumulation at the host-parasite interface. Infect Immun 68, 2315-22.

Emmer, B., Maric, D., Engman, D., 2010. Molecular mechanisms of protein and lipid targeting to ciliary membranes. Journal of Cell Science 123, 529-536.

Engelmann, R, Weisshart, K, Zimmermann, B, Birkenbell, J, Tham, J, 2014. Airyscanning: A Novel Approach to Confocal Imaging. Carl Zeiss Microscopy GmbH.

Fan, Y, Esmail, MA, Ansley, SJ, Blacque, OE, Boroevich, K, Ross, AJ, Moore, SJ, Badano, JL, May-Simera, H, Compton, DS, Green, JS, Lewis, RA, van Haelst, MM, Parfrey, PS, Baillie, DL, Beales, PL, Katsanis, N, Davidson, WS, Leroux, MR, 2004. Mutations in a member of the Ras superfamily of small GTP-binding proteins causes Bardet-Biedl syndrome. Nat Genet 36, 989-93.

Feistel, K, Blum, M, 2006. Three types of cilia including a novel 9+4 axoneme on the notochordal plate of the rabbit embryo. Dev Dyn 235, 3348-58.

Fesenko, EE, Kolesnikov, SS, Lyubarsky, AL, 1985. Induction by cyclic GMP of cationic conductance in plasma membrane of retinal rod outer segment. Nature 313, 310-3.

Fiebig, M, Kelly, S, Gluenz, E, 2015. Comparative Life Cycle Transcriptomics Revises *Leishmania mexicana* Genome Annotation and Links a Chromosome Duplication with Parasitism of Vertebrates. PLoS Pathog 11, e1005186.

Fiebig, M., 2014. Characterisation of the Transcriptomes of *Leishmania mexicana* Promastigotes and Amastigotes. University of Oxford.

Figarella, K, Uzcategui, NL, Zhou, Y, LeFurgey, A, Ouellette, M, Bhattacharjee, H, Mukhopadhyay, R, 2007. Biochemical characterization of *Leishmania major* aquaglyceroporin LmAQP1: possible role in volume regulation and osmotaxis. Mol Microbiol 65, 1006-17.

Finn, R.D., Attwood, T.K., Babbitt, P.C., Bateman, A., Bork, P., Bridge, A.J., Chang, H.-Y.Y., Dosztányi, Z., El-Gebali, S., Fraser, M., Gough, J., Haft, D., Holliday, G.L., Huang, H., Huang, X., Letunic, I., Lopez, R., Lu, S., Marchler-Bauer, A., Mi, H., Mistry, J., Natale, D.A., Necci, M., Nuka, G., Orengo, C.A., Park, Y., Pesseat, S., Piovesan, D., Potter, S.C., Rawlings, N.D., Redaschi, N., Richardson, L., Rivoire, C., Sangrador-Vegas, A., Sigrist, C., Sillitoe, I., Smithers, B., Squizzato, S., Sutton, G., Thanki, N., Thomas, P.D., Tosatto, S.C., Wu, C.H., Xenarios, I., Yeh, L.-S.S., Young, S.-Y.Y., Mitchell, A.L., 2017. InterPro in 2017-beyond protein family and domain annotations. Nucleic Acids Res. 45, D190-D199.

Fire, A, Xu, S, Montgomery, MK, Kostas, SA, Driver, SE, Mello, CC, 1998. Potent and specific genetic interference by double-stranded RNA in *Caenorhabditis elegans*. Nature 391, 806-11.

Flinn, HM, Rangarajan, D, Smith, DF, 1994. Expression of a hydrophilic surface protein in infective stages of *Leishmania major*. Mol Biochem Parasitol 65, 259-70.

Forestier, CL, Machu, C, Loussert, C, Pescher, P, Späth, GF, 2011. Imaging host cell-*Leishmania* interaction dynamics implicates parasite motility, lysosome recruitment, and host cell wounding in the infection process. Cell Host Microbe 9, 319-30.

Forget, G., Gregory, D., Whitcombe, L., Olivier, M., 2006. Role of host protein tyrosine phosphatase SHP-1 in *Leishmania donovani*-induced inhibition of nitric oxide production. Infection and immunity 74, 6272-9.

Fournier, D, Palidwor, GA, Shcherbinin, S, Szengel, A, Schaefer, MH, Perez-Iratxeta, C, Andrade-Navarro, MA, 2013. Functional and genomic analyses of alpha-solenoid proteins. PLoS One 8, e79894.

Freitas-Junior, LH, Chatelain, E, Kim, HA, Siqueira-Neto, JL, 2012. Visceral leishmaniasis treatment: What do we have, what do we need and how to deliver it? Int J Parasitol Drugs Drug Resist 2, 11-9.

Friedrich, RW, Genoud, C, Wanner, AA, 2013. Analyzing the structure and function of neuronal circuits in zebrafish. Front Neural Circuits 7, 71.

Gadelha, C, Wickstead, B, de Souza, W, Gull, K, Cunha-e-Silva, N, 2005. Cryptic paraflagellar rod in endosymbiont-containing kinetoplastid protozoa. Eukaryot Cell 4, 516-25.

Gadelha, C, Wickstead, B, Gull, K, 2007. Flagellar and ciliary beating in trypanosome motility. Cell Motil Cytoskeleton 64, 629-43.

Gadelha, C., Wickstead, B., McKean, P.G., Gull, K., 2006. Basal body and flagellum mutants reveal a rotational constraint of the central pair microtubules in the axonemes of trypanosomes. J. Cell. Sci. 119, 2405–13.

Garcia-Gonzalo, F.R., Reiter, J.F., 2012. Scoring a backstage pass: mechanisms of ciliogenesis and ciliary access. J. Cell Biol. 197, 697-709.

Gardener, P.J., 1974. Pellicle-associated structures in the amastigote stage of *Trypanosoma cruzi* and *Leishmania* species. Ann Trop Med Parasitol 68, 167-76.

Garlapati, S, Dahan, E, Shapira, M, 1999. Effect of acidic pH on heat shock gene expression in *Leishmania*. Mol Biochem Parasitol 100, 95-101.

Geng, L, Okuhara, D, Yu, Z, Tian, X, Cai, Y, Shibazaki, S, Somlo, S, 2006. Polycystin-2 traffics to cilia independently of polycystin-1 by using an N-terminal RVxP motif. J Cell Sci 119, 1383-95.

Gherman, A, Davis, EE, Katsanis, N, 2006. The ciliary proteome database: an integrated community resource for the genetic and functional dissection of cilia. Nat Genet 38, 961-2.

Ghosh, M, Mukherjee, T, 2000. Stage-specific development of a novel adenosine transporter in *Leishmania donovani* amastigotes. Mol Biochem Parasitol 108, 93-9.

Gibbons, IR, 1965. Chemical dissection of cilia. Arch Biol (Liege) 76, 317-52.

Gibbons, IR, Grimstone, AV, 1960. On flagellar structure in certain flagellates. J Biophys Biochem Cytol 7, 697-716.

Gibbons, IR, Rowe, AJ, 1965. Dynein: A Protein with Adenosine Triphosphatase Activity from Cilia. Science 149, 424-6.

Gilula, NB, Satir, P, 1972. The ciliary necklace. A ciliary membrane specialization. J Cell Biol 53, 494-509.

Glaser, TA, Baatz, JE, Kreishman, GP, Mukkada, AJ, 1988. pH homeostasis in *Leishmania donovani* amastigotes and promastigotes. Proc Natl Acad Sci U S A 85, 7602-6.

Gluenz, E., Ginger, M., McKean, P., 2010a. Flagellum assembly and function during the *Leishmania* life cycle. Current Opinion in Microbiology 13, 473479.

Gluenz, E., Höög, J., Smith, A., Dawe, H., Shaw, M., Gull, K., 2010b. Beyond 9+0: noncanonical axoneme structures characterize sensory cilia from protists to humans. The FASEB Journal 24, 3117-3121.

Godsel, LM, Engman, DM, 1999. Flagellar protein localization mediated by a calcium-myristoyl/palmitoyl switch mechanism. EMBO J 18, 2057-65.

Gomez, MA, Contreras, I, Hallé, M, Tremblay, ML, McMaster, RW, Olivier, M, 2009. *Leishmania* GP63 alters host signaling through cleavage-activated protein tyrosine phosphatases. Sci Signal 2, ra58.

Gong, Z, Son, W, Chung, YD, Kim, J, Shin, DW, McClung, CA, Lee, Y, Lee, HW, Chang, DJ, Kaang, BK, Cho, H, Oh, U, Hirsh, J, Kernan, MJ, Kim, C, 2004. Two interdependent TRPV channel subunits, inactive and Nanchung, mediate hearing in *Drosophila*. J Neurosci 24, 9059-66.

González, C, Wang, O, Strutz, SE, González-Salazar, C, Sánchez-Cordero, V, Sarkar, S, 2010. Climate change and risk of leishmaniasis in north america: predictions from ecological niche models of vector and reservoir species. PLoS Negl Trop Dis 4, e585.

Gonzalez, V, Combe, A, David, V, Malmquist, NA, Delorme, V, Leroy, C, Blazquez, S, Ménard, R, Tardieux, I, 2009. Host cell entry by apicomplexa parasites requires actin polymerization in the host cell. Cell Host Microbe 5, 259-72.

Gossage, S.M., Rogers, M.E., Bates, P.A., 2003. Two separate growth phases during the development of *Leishmania* in sand flies: implications for understanding the life cycle. Int. J. Parasitol. 33, 1027-34.

Gray, J, 1955. The movement of sea-urchin spermatozoa. Journal of Experimental Biology 32, 775-801.

Gray, J., 1930. The Mechanism of Ciliary Movement. VI. Photographic and Stroboscopic Analysis of Ciliary Movement. Proceedings of the Royal Society of London. Series B, Containing Papers of a Biological Character 107, 313-332.

Gregory, D.J., Olivier, M., 2005. Subversion of host cell signalling by the protozoan parasite *Leishmania*. Parasitology 130 Suppl, S27-35.

Gueirard, P., Laplante, A., Rondeau, C., Milon, G., Desjardins, M., 2008. Trafficking of *Leishmania donovani* promastigotes in non-lytic compartments in neutrophils enables the subsequent transfer of parasites to macrophages. Cell. Microbiol. 10, 100-11.

Guesdon, A., Blestel, S., Kervrann, C., Chrétien, D., 2013. Single versus dual-axis cryo-electron tomography of microtubules assembled *in vitro*: limits and perspectives. J. Struct. Biol. 181, 169-78.

Gupta, N, Goyal, N, Singha, UK, Bhakuni, V, Roy, R, Rastogi, AK, 1999. Characterization of intracellular metabolites of axenic amastigotes of *Leishmania donovani* by 1H NMR spectroscopy. Acta Trop 73, 121-33.

Hall, DH, Russell, RL, 1991. The posterior nervous system of the nematode *Caenorhabditis elegans*: serial reconstruction of identified neurons and complete pattern of synaptic interactions. J Neurosci 11, 1-22.

Hallé, M, Gomez, MA, Stuible, M, Shimizu, H, McMaster, WR, Olivier, M, Tremblay, ML, 2009. The *Leishmania* surface protease GP63 cleaves multiple intracellular proteins and actively participates in p38 mitogen-activated protein kinase inactivation. J Biol Chem 284, 6893-908.

Händel, M, Schulz, S, Stanarius, A, Schreff, M, Erdtmann-Vourliotis, M, Schmidt, H, Wolf, G, Höllt, V, 1999. Selective targeting of somatostatin receptor 3 to neuronal cilia. Neuroscience 89, 909-26.

Hassani, K, Antoniak, E, Jardim, A, Olivier, M, 2011. Temperature-induced protein secretion by *Leishmania mexicana* modulates macrophage signalling and function. PLoS One 6, e18724.

Haynes, L, Yau, KW, 1985. Cyclic GMP-sensitive conductance in outer segment membrane of catfish cones. Nature 317, 61-4.

Henley, C, Costello, DP, Thomas, MB, Newton, WD, 1969. The “9+1” pattern of microtubules in spermatozoa of *Mesostoma* (Platyhelminthes, Turbellaria). Proc Natl Acad Sci U S A 64, 849-56.

Heuser, T, Raytchev, M, Krell, J, Porter, ME, Nicastro, D, 2009. The dynein regulatory complex is the nexin link and a major regulatory node in cilia and flagella. J Cell Biol 187, 921-33.

Hodges, M., Scheumann, N., Wickstead, B., Langdale, J., Gull, K., 2010. Reconstructing the evolutionary history of the centriole from protein components. Journal of Cell Science 123, 1407-1413.

Hoffmann-Berling, H, 1955. Flagellum models and adenosinetriphosphate (ATP). Biochim Biophys Acta 16, 146-54.

Holwill, M.E., 1965. The motion of *Strigomonas oncopelti*. Journal of Experimental Biology 42, 125-137.

Hu, Q, Milenkovic, L, Jin, H, Scott, MP, Nachury, MV, Spiliotis, ET, Nelson, WJ, 2010. A septin diffusion barrier at the base of the primary cilium maintains ciliary membrane protein distribution. Science 329, 436-9.

Huangfu, D, Anderson, KV, 2006. Signaling from Smo to Ci/Gli: conservation and divergence of Hedgehog pathways from *Drosophila* to vertebrates. Development 133, 3-14.

Huff, J., 2015. The Airyscan detector from ZEISS: confocal imaging with improved signal-to-noise ratio and super-resolution. Nat Meth 12.

Hughes, J, Ward, CJ, Peral, B, Aspinwall, R, Clark, K, Millán, S.J., Gamble, V, Harris, PC, 1995. The polycystic kidney disease 1 (PKD1) gene encodes a novel protein with multiple cell recognition domains. Nat Genet 10, 151-60.

Humbert, M.C., Weihbrecht, K., Searby, C.C., Li, Y., Pope, R.M., Sheffield, V.C., Seo, S., 2012. ARL13B, PDE6D, and CEP164 form a functional network for INPP5E ciliary targeting. Proc. Natl. Acad. Sci. U.S.A. 109, 19691-6.

Ishikawa, H, Thompson, J, Yates, JR, Marshall, WF, 2012. Proteomic analysis of mammalian primary cilia. Curr Biol 22, 414-9.

Ivens, AC, Peacock, CS, Worthey, EA, Murphy, L, Aggarwal, G, Berriman, M, Sisk, E, Rajandream, MA, Adlem, E, Aert, R, Anupama, A, Apostolou, Z, Attipoe, P, Bason, N, Bauser, C, Beck, A, Beverley, SM, Bianchettin, G, Borzym, K, Bothe, G, Bruschi, CV, Collins, M, Cadag, E, Ciarloni, L, Clayton, C, Coulson, RM, Cronin, A, Cruz, AK, Davies, RM, Gaudenzi, D.J., Dobson, DE, Duesterhoeft, A, Fazelina, G, Fosker, N, Frasch, AC, Fraser, A, Fuchs, M, Gabel, C, Goble, A, Goffeau, A, Harris, D, Hertz-Fowler, C, Hilbert, H, Horn, D, Huang, Y, Klages, S, Knights, A, Kube, M, Larke, N, Litvin, L, Lord, A, Louie, T, Marra, M, Masuy, D, Matthews, K, Michaeli, S, Mottram, JC, Müller-Auer, S, Munden, H, Nelson, S, Norbertczak, H, Oliver, K, O'neil, S, Pentony, M, Pohl, TM, Price, C, Purnelle, B, Quail, MA, Rabbinowitsch, E, Reinhardt, R, Rieger, M, Rinta, J, Robben, J, Robertson, L, Ruiz, JC, Rutter, S, Saunders, D, Schäfer, M, Schein, J, Schwartz, DC, Seeger, K, Seyler, A, Sharp, S, Shin, H, Sivam, D, Squares, R, Squares, S, Tosato, V, Vogt, C, Volckaert, G, Wambutt, R, Warren, T, Wedler, H, Woodward, J, Zhou, S, Zimmermann, W, Smith, DF, Blackwell, JM, Stuart, KD, Barrell, B, others , 2005. The genome of the kinetoplastid parasite, *Leishmania major*. Science 309, 436-42.

Jean, Y, Langlais, J, Roberts, KD, Chapdelaine, A, Bleau, G, 1979. Fertility of a woman with nonfunctional ciliated cells in the fallopian tubes. Fertil Steril 31, 349-50.

Jékely, G, Arendt, D, 2006. Evolution of intraflagellar transport from coated vesicles and autogenous origin of the eukaryotic cilium. Bioessays 28, 191-8.

Jenkins, PM, Hurd, TW, Zhang, L, McEwen, DP, Brown, RL, Margolis, B, Verhey, KJ, Martens, JR, 2006. Ciliary targeting of olfactory CNG channels requires the CNGB1b subunit and the kinesin-2 motor protein, KIF17. Curr Biol 16, 1211-6.

Jensen, CG, Davison, EA, Bowser, SS, Rieder, CL, 1987. Primary cilia cycle in PtK1 cells: effects of colcemid and taxol on cilia formation and resorption. Cell Motil Cytoskeleton 7, 187-97.

Jin, X, Mohieldin, AM, Muntean, BS, Green, JA, Shah, JV, Mykytyn, K, Nauli, SM, 2014. Cilioplasm is a cellular compartment for calcium signaling in response to mechanical and chemical stimuli. Cell Mol Life Sci 71, 2165-78.

Jin, H., White, S., Shida, T., Schulz, S., Aguiar, M., Gygi, S., Bazan, J., Nachury, M., 2010. The Conserved Bardet-Biedl Syndrome Proteins Assemble a Coat that Traffics Membrane Proteins to Cilia. Cell 141.

Johnson, KA, Rosenbaum, JL, 1992. Polarity of flagellar assembly in *Chlamydomonas*. J Cell Biol 119, 1605-11.

Joy, T, Cao, H, Black, G, Malik, R, Charlton-Menys, V, Hegele, RA, Durrington, PN, 2007. Alstrom syndrome (OMIM 203800): a case report and literature review. Orphanet J Rare Dis 2, 49.

Kamhawi, S., 2006. Phlebotomine sand flies and *Leishmania* parasites: friends or foes? Trends Parasitol. 22, 439-45.

Kamhawi, S., Modi, G.B., Pimenta, P.F., Rowton, E., Sacks, D.L., 2000. The vectorial competence of *Phlebotomus sergenti* is specific for *Leishmania tropica* and is controlled by species-specific, lipophosphoglycan-mediated midgut attachment. Parasitology 121 (Pt 1), 25-33.

Kane, M.M., Mosser, D.M., 2001. The role of IL-10 in promoting disease progression in leishmaniasis. J. Immunol. 166, 1141-7.

Katsanis, N, Beales, PL, Woods, MO, Lewis, RA, Green, JS, Parfrey, PS, Ansley, SJ, Davidson, WS, Lupski, JR, 2000. Mutations in MKKS cause obesity, retinal dystrophy and renal malformations associated with Bardet-Biedl syndrome. Nat Genet 26, 67-70.

Kee, HL, Dishinger, JF, Blasius, TL, Liu, CJ, Margolis, B, Verhey, KJ, 2012. A size-exclusion permeability barrier and nucleoporins characterize a ciliary pore complex that regulates transport into cilia. Nat Cell Biol 14, 431-7.

Kim, JC, Badano, JL, Sibold, S, Esmail, MA, Hill, J, Hoskins, BE, Leitch, CC, Venner, K, Ansley, SJ, Ross, AJ, Leroux, MR, Katsanis, N, Beales, PL, 2004. The Bardet-Biedl protein BBS4 targets cargo to the pericentriolar region and is required for microtubule anchoring and cell cycle progression. Nat Genet 36, 462-70.

Knott, G, Marchman, H, Wall, D, Lich, B, 2008. Serial section scanning electron microscopy of adult brain tissue using focused ion beam milling. J Neurosci 28, 2959-64.

Kohl, L, Robinson, D, Bastin, P, 2003. Novel roles for the flagellum in cell morphogenesis and cytokinesis of trypanosomes. EMBO J 22, 5336-46.

Kohl, L, Sherwin, T, Gull, K, 1999. Assembly of the paraflagellar rod and the flagellum attachment zone complex during the *Trypanosoma brucei* cell cycle. J Eukaryot Microbiol 46, 105-9.

Kozminski, KG, Beech, PL, Rosenbaum, JL, 1995. The *Chlamydomonas* kinesin-like protein FLA10 is involved in motility associated with the flagellar membrane. J Cell Biol 131, 1517-27.

Kozminski, KG, Johnson, KA, Forscher, P, Rosenbaum, JL, 1993. A motility in the eukaryotic flagellum unrelated to flagellar beating. Proc Natl Acad Sci U S A 90, 5519-23.

Krieger, V., Liebl, D., Zhang, Y., Rajashekar, R., Chlanda, P., Giesker, K., Chikkaballi, D., Hensel, M., 2014. Reorganization of the endosomal system in Salmonella-infected cells: the ultrastructure of *Salmonella*-induced tubular compartments. PLoS Pathog. 10, e1004374.

Krüger, T., Engstler, M., 2015. Flagellar motility in eukaryotic human parasites. Seminars in cell & developmental biology 46, 113-27.

Kulaga, HM, Leitch, CC, Eichers, ER, Badano, JL, Lesemann, A, Hoskins, BE, Lupski, JR, Beales, PL, Reed, RR, Katsanis, N, 2004. Loss of BBS proteins causes anosmia in humans and defects in olfactory cilia structure and function in the mouse. Nat Genet 36, 994-8.

Kwitek-Black, AE, Carmi, R, Duyk, GM, Buetow, KH, Elbedour, K, Parvari, R, Yandava, CN, Stone, EM, Sheffield, VC, 1993. Linkage of Bardet-Biedl syndrome to chromosome 16q and evidence for non-allelic genetic heterogeneity. Nat Genet 5, 392-6.

LaCount, DJ, Barrett, B, Donelson, JE, 2002. *Trypanosoma brucei* FLA1 is required for flagellum attachment and cytokinesis. J Biol Chem 277, 17580-8.

Lambertz, U, Silverman, JM, Nandan, D, McMaster, WR, Clos, J, Foster, LJ, Reiner, NE, 2012. Secreted virulence factors and immune evasion in visceral leishmaniasis. J Leukoc Biol 91, 887-99.

Lander, N, Li, ZH, Niyogi, S, Docampo, R, 2015. CRISPR/Cas9-Induced Disruption of Paraflagellar Rod Protein 1 and 2 Genes in *Trypanosoma cruzi* Reveals Their Role in Flagellar Attachment. MBio 6, e01012.

Lang, T, de Chastellier, C, Frehel, C, Hellio, R, Metezeau, P, Leao, S.. S., Antoine, JC, 1994. Distribution of MHC class I and of MHC class II molecules in macrophages infected with *Leishmania amazonensis*. J Cell Sci 107 (Pt 1), 69-82.

Langousis, G, Shimogawa, MM, Saada, EA, Vashisht, AA, Spreafico, R, Nager, AR, Barshop, WD, Nachury, MV, Wohlschlegel, JA, Hill, KL, 2016. Loss of the BBSome perturbs endocytic trafficking and disrupts virulence of *Trypanosoma brucei*. Proc Natl Acad Sci U S A 113, 632-7.

Laskay, T., van Zandbergen, G., Solbach, W., 2003. Neutrophil granulocytes--Trojan horses for *Leishmania major* and other intracellular microbes? Trends Microbiol. 11, 210-4.

Laurence, JZ, Moon, RC, 1995. Four cases of “retinitis pigmentosa” occurring in the same family, and accompanied by general imperfections of development. 1866. Obes Res 3, 400-3.

Leao, D.S., Lang, T, Prina, E, Hellio, R, Antoine, JC, 1995. Intracellular *Leishmania amazonensis* amastigotes internalize and degrade MHC class II molecules of their host cells. J Cell Sci 108 (Pt 10), 3219-31.

Lechtreck, KF, 2015. IFT-Cargo Interactions and Protein Transport in Cilia. Trends Biochem Sci 40, 765-78.

Lechtreck, KF, Brown, JM, Sampaio, JL, Craft, JM, Shevchenko, A, Evans, JE, Witman, GB, 2013. Cycling of the signaling protein phospholipase D through cilia requires the BBSome only for the export phase. J Cell Biol 201, 249-61.

Lechtreck, KF, Johnson, EC, Sakai, T, Cochran, D, Ballif, BA, Rush, J, Pazour, GJ, Ikebe, M, Witman, GB, 2009. The *Chlamydomonas reinhardtii* BBSome is an IFT cargo required for export of specific signaling proteins from flagella. J Cell Biol 187, 1117-32.

Leppert, M, Baird, L, Anderson, KL, Otterud, B, Lupski, JR, Lewis, RA, 1994. Bardet-Biedl syndrome is linked to DNA markers on chromosome 11q and is genetically heterogeneous. Nat Genet 7, 108-12.

Letunic, I, Bork, P, 2016. Interactive tree of life (iTOL) v3: an online tool for the display and annotation of phylogenetic and other trees. Nucleic Acids Res 44, W242-5.

Lidow, Menco, B.., 1984. Observations on Axonemes and Membranes of Olfactory and Respiratory Cilia in Frogs and Rats Using Tannic Acid-Supplemented Fixation and Photographic Rotation. Journal of Ultrastructural Research 86, 18-30.

Liem, KF, Ashe, A, He, M, Satir, P, Moran, J, Beier, D, Wicking, C, Anderson, KV, 2012. The IFT-A complex regulates Shh signaling through cilia structure and membrane protein trafficking. J Cell Biol 197, 789-800.

Liew, GM, Ye, F, Nager, AR, Murphy, JP, Lee, JS, Aguiar, M, Breslow, DK, Gygi, SP, Nachury, MV, 2014. The intraflagellar transport protein IFT27 promotes BBSome exit from cilia through the GTPase ARL6/BBS3. Dev Cell 31, 265-78.

Liew, F.Y., Millott, S., Parkinson, C., Palmer, R.M., Moncada, S., 1990. Macrophage killing of *Leishmania* parasite *in vivo* is mediated by nitric oxide from L-arginine. J. Immunol. 144, 4794-7.

Lodowski, KH, Lee, R, Ropelewski, P, Nemet, I, Tian, G, Imanishi, Y, 2013. Signals governing the trafficking and mistrafficking of a ciliary GPCR, rhodopsin. J Neurosci 33, 13621-38.

Loktev, AV, Zhang, Q, Beck, JS, Searby, CC, Scheetz, TE, Bazan, JF, Slusarski, DC, Sheffiled, VC, Jackson, PK, Nachury, MV, 2008. A BBSome Subunit Links Ciliogenesis, Microtubule Stability, And Acetylation. Dev Cell 15 (Pt 6), 854-65.

Lucas, JS, Leigh, MW, 2014. Diagnosis of primary ciliary dyskinesia: searching for a gold standard. Eur Respir J 44, 1418-22.

Lye, LF, Owens, K, Shi, H, Murta, SM, Vieira, AC, Turco, SJ, Tschudi, C, Ullu, E, Beverley, SM, 2010. Retention and loss of RNA interference pathways in trypanosomatid protozoans. PLoS Pathog 6, e1001161.

Maga, JA, Sherwin, T, Francis, S, Gull, K, LeBowitz, JH, 1999. Genetic dissection of the *Leishmania* paraflagellar rod, a unique flagellar cytoskeleton structure. J Cell Sci 112 (Pt 16), 2753-63.

Makin, L., 2017. TBC. University of Oxford.

Malone, AM, Anderson, CT, Tummala, P, Kwon, RY, Johnston, TR, Stearns, T, Jacobs, CR, 2007. Primary cilia mediate mechanosensing in bone cells by a calcium-independent mechanism. Proc Natl Acad Sci U S A 104, 13325-30.

Maric, D, McGwire, BS, Buchanan, KT, Olson, CL, Emmer, BT, Epting, CL, Engman, DM, 2011. Molecular determinants of ciliary membrane localization of *Trypanosoma cruzi* flagellar calcium-binding protein. J Biol Chem 286, 33109-17.

Martone, ME, Deerinck, TJ, Yamada, N, Bushong, E, Ellisman, MH, 2013. Correlated 3D Light and Electron Microscopy: Use of High Voltage Electron Microscopy and Electron Tomography for Imaging Large Biological Structures. Journal of Histotechnology 23.

Marx, V, 2013. Neurobiology: Brain mapping in high resolution. Nature 503, 147-52.

Mastronarde, DN, 1997. Dual-axis tomography: an approach with alignment methods that preserve resolution. J Struct Biol 120, 343-52.

Mastronarde, D., 2014. IMOD, PEET, and SerialEM from the Mastronarde Group University of Colorado, Boulder.

Matheoud, D., Moradin, N., Bellemare-Pelletier, A., Shio, M.T., Hong, W.J., Olivier, M., Gagnon, E., Desjardins, M., Descoteaux, A., 2013. *Leishmania* evades host immunity by inhibiting antigen cross-presentation through direct cleavage of the SNARE VAMP8. Cell Host Microbe 14, 15-25.

Mazareb, S., Fu, Z., Zilberstein, D., 1999. Developmental regulation of proline transport in *Leishmania donovani*. Experimental Parasitology 91, 341-8.

McComb, P, Langley, L, Villalon, M, Verdugo, P, 1986. The oviductal cilia and Kartagener's syndrome. Fertil Steril 46, 412-6.

McNeely, T.B., Rosen, G., Londner, M.V., Turco, S.J., 1989. Inhibitory effects on protein kinase C activity by lipophosphoglycan fragments and glycosylphosphatidylinositol antigens of the protozoan parasite *Leishmania*. Biochem. J. 259, 601-4.

McNeely, T.B., Turco, S.J., 1987. Inhibition of protein kinase C activity by the *Leishmania donovani* lipophosphoglycan. Biochem. Biophys. Res. Commun. 148, 653-7.

McNeely, T.B., Turco, S.J., 1990. Requirement of lipophosphoglycan for intracellular survival of *Leishmania donovani* within human monocytes. J. Immunol. 144, 2745-50.

Menco, B.P., 1984. Ciliated and microvillous structures of rat olfactory and nasal respiratory epithelia: A study using ultra-rapid cryo-fixation followed by freeze-substitution or freeze-etching . Cell and Tissue Research 235, 225-241.

Milenkovic, L, Scott, MP, Rohatgi, R, 2009. Lateral transport of Smoothened from the plasma membrane to the membrane of the cilium. J Cell Biol 187, 365-74.

Minocha, N, Kumar, D, Rajanala, K, Saha, S, 2011. Kinetoplast morphology and segregation pattern as a marker for cell cycle progression in *Leishmania donovani*. J Eukaryot Microbiol 58, 249-53.

Mitchell, D., 2004. Speculations on the evolution of 9+2 organelles and the role of central pair microtubules. Biology of the Cell 96, 691-696.

Mochizuki, T, Wu, G, Hayashi, T, Xenophontos, SL, Veldhuisen, B, Saris, JJ, Reynolds, DM, Cai, Y, Gabow, PA, Pierides, A, Kimberling, WJ, Breuning, MH, Deltas, CC, Peters, DJ, Somlo, S, 1996. PKD2, a gene for polycystic kidney disease that encodes an integral membrane protein. Science 272, 1339-42.

Moini, AR, Emamy, H, Asadian, A, 1975. The Laurence-Moon-Biedl syndrome. Six cases of obesity, short stature, mental retardation, small genitalia, and retinitis pigmentosa. Clin Pediatr (Phila) 14, 812-5.

Moncrieff, D.A., Robinson, V.N.E., Harris, L.B., 1978. Charge neutralisation of insulating surfaces in the SEM by gas ionisation. Journal of Physics D: Applied Physics 11, 2315-2325.

Mourão, A, Nager, AR, Nachury, MV, Lorentzen, E, 2014. Structural basis for membrane targeting of the BBSome by ARL6. Nat Struct Mol Biol 21, 1035-41.

Mozaffarian, G, Nakhjavani, MK, Farrahi, A, 1979. The Laurence-Moon-Bardet-Biedl syndrome: unresponsiveness to the action of testosterone, a possible mechanism. Fertil Steril 31, 417-22.

Muccio, D.T., Scalone, A, Bruno, A, Marangi, M, Grande, R, Armignacco, O, Gradoni, L, Gramiccia, M, 2015. Epidemiology of Imported Leishmaniasis in Italy: Implications for a European Endemic Country. PLoS One 10, e0129418.

Mukhopadhyay, S, Wen, X, Chih, B, Nelson, CD, Lane, WS, Scales, SJ, Jackson, PK, 2010. TULP3 bridges the IFT-A complex and membrane phosphoinositides to promote trafficking of G protein-coupled receptors into primary cilia. Genes Dev 24, 2180-93.

Muller, WA, Steinman, RM, Cohn, ZA, 1980a. The membrane proteins of the vacuolar system I. Analysis of a novel method of intralysosomal iodination. J Cell Biol 86, 292-303.

Muller, WA, Steinman, RM, Cohn, ZA, 1980b. The membrane proteins of the vacuolar system. II. Bidirectional flow between secondary lysosomes and plasma membrane. J Cell Biol 86, 304-14.

Munro, NC, Currie, DC, Lindsay, KS, Ryder, TA, Rutman, A, Dewar, A, Greenstone, MA, Hendry, WF, Cole, PJ, 1994. Fertility in men with primary ciliary dyskinesia presenting with respiratory infection. Thorax 49, 684-7.

Murray, H.W., Masur, H., Keithly, J.S., 1982. Cell-mediated immune response in experimental visceral leishmaniasis. I. Correlation between resistance to *Leishmania donovani* and lymphokine-generating capacity. J. Immunol. 129, 344-50.

Murray, H.W., Nathan, C.F., 1999. Macrophage microbicidal mechanisms *in vivo*: reactive nitrogen versus oxygen intermediates in the killing of intracellular visceral *Leishmania donovani*. J. Exp. Med. 189, 741-6.

Mykytyn, K, Braun, T, Carmi, R, Haider, NB, Searby, CC, Shastri, M, Beck, G, Wright, AF, Iannaccone, A, Elbedour, K, Riise, R, Baldi, A, Raas-Rothschild, A, Gorman, SW, Duhl, DM, Jacobson, SG, Casavant, T, Stone, EM, Sheffield, VC, 2001. Identification of the gene that, when mutated, causes the human obesity syndrome BBS4. Nat Genet 28, 188-91.

Mykytyn, K, Mullins, RF, Andrews, M, Chiang, AP, Swiderski, RE, Yang, B, Braun, T, Casavant, T, Stone, EM, Sheffield, VC, 2004. Bardet-Biedl syndrome type 4 (BBS4)-null mice implicate Bbs4 in flagella formation but not global cilia assembly. Proc Natl Acad Sci U S A 101, 8664-9.

Myskova, J., Leštinová, T., Volf, P., 2017. Development of *Leishmania mexicana* PF16 and BBS knock outs in *Lu. longipalpis*.

Nachury, MV, Loktev, AV, Zhang, Q, Westlake, CJ, Peränen, J, Merdes, A, Slusarski, DC, Scheller, RH, Bazan, JF, Sheffield, VC, Jackson, PK, 2007. A core complex of BBS proteins cooperates with the GTPase Rab8 to promote ciliary membrane biogenesis. Cell 129, 1201-13.

Nachury, M., Seeley, E., Jin, H., 2010. Trafficking to the Ciliary Membrane: How to Get Across the Periciliary Diffusion Barrier? Annu. Rev. Cell Dev. Biol. 26, 59-87.

Nakamura, T, Gold, GH, 1987. A cyclic nucleotide-gated conductance in olfactory receptor cilia. Nature 325, 442-4.

Nakata, K., Shiba, D., Kobayashi, D., Yokoyama, T., 2012. Targeting of Nphp3 to the primary cilia is controlled by an N-terminal myristoylation site and coiled-coil domains. Cytoskeleton (Hoboken) 69, 221-34.

Nandan, D., Lo, R., Reiner, N.E., 1999. Activation of phosphotyrosine phosphatase activity attenuates mitogen-activated protein kinase signaling and inhibits c-FOS and nitric oxide synthase expression in macrophages infected with *Leishmania donovani.* Infect. Immun. 67, 4055-63.

Nauli, SM, Alenghat, FJ, Luo, Y, Williams, E, Vassilev, P, Li, X, Elia, AE, Lu, W, Brown, EM, Quinn, SJ, Ingber, DE, Zhou, J, 2003. Polycystins 1 and 2 mediate mechanosensation in the primary cilium of kidney cells. Nat Genet 33, 129-37.

Neugebauer, DC, Neuwinger, J, Jockenhövel, F, Nieschlag, E, 1990. "9 + 0" axoneme in spermatozoa and some nasal cilia of a patient with totally immotile spermatozoa associated with thickened sheath and short midpiece. Hum Reprod 5, 981-6.

Nicastro, D, Fu, X, Heuser, T, Tso, A, Porter, ME, Linck, RW, 2011. Cryo-electron tomography reveals conserved features of doublet microtubules in flagella. Proc Natl Acad Sci U S A 108, E845-53.

Nishimura, DY, Searby, CC, Carmi, R, Elbedour, K, Maldergem, V.L., Fulton, AB, Lam, BL, Powell, BR, Swiderski, RE, Bugge, KE, Haider, NB, Kwitek-Black, AE, Ying, L, Duhl, DM, Gorman, SW, Heon, E, Iannaccone, A, Bonneau, D, Biesecker, LG, Jacobson, SG, Stone, EM, Sheffield, VC, 2001. Positional cloning of a novel gene on chromosome 16q causing Bardet-Biedl syndrome (BBS2). Hum Mol Genet 10, 865-74.

Nishimura, D., Fath, M., Mullins, R., Searby, C., Andrews, M., Davis, R., Andorf, J., Mykytyn, K., Swiderski, R., Yang, B., Carmi, R., Stone, E., Sheffield, V., 2004. Bbs2-null mice have neurosensory deficits, a defect in social dominance, and retinopathy associated with mislocalization of rhodopsin. Proceedings of the National Academy of Sciences of the United States of America 101, 16588-93.

Nonaka, S, Tanaka, Y, Okada, Y, Takeda, S, Harada, A, Kanai, Y, Kido, M, Hirokawa, N, 1998. Randomization of left-right asymmetry due to loss of nodal cilia generating leftward flow of extraembryonic fluid in mice lacking KIF3B motor protein. Cell 95, 829-37.

Oberholzer, M, Langousis, G, Nguyen, HT, Saada, EA, Shimogawa, MM, Jonsson, ZO, Nguyen, SM, Wohlschlegel, JA, Hill, KL, 2011. Independent analysis of the flagellum surface and matrix proteomes provides insight into flagellum signaling in mammalian-infectious *Trypanosoma brucei*. Mol Cell Proteomics 10, M111.010538.

Oda, T, Yagi, T, Yanagisawa, H, Kikkawa, M, 2013. Identification of the outer-inner dynein linker as a hub controller for axonemal dynein activities. Curr Biol 23, 656-64.

Ogbadoyi, EO, Robinson, DR, Gull, K, 2003. A high-order trans-membrane structural linkage is responsible for mitochondrial genome positioning and segregation by flagellar basal bodies in trypanosomes. Mol Biol Cell 14, 1769-79.

Olivier, M., Brownsey, R.W., Reiner, N.E., 1992. Defective stimulus-response coupling in human monocytes infected with *Leishmania donovani* is associated with altered activation and translocation of protein kinase C. Proc. Natl. Acad. Sci. U.S.A. 89, 7481-5.

Overath, P, Engstler, M, 2004. Endocytosis, membrane recycling and sorting of GPI-anchored proteins: *Trypanosoma brucei* as a model system. Mol Microbiol 53, 735-44.

Pan, A.A., 1984. *Leishmania mexicana*: serial cultivation of intracellular stages in a cell-free medium. Exp. Parasitol. 58, 72-80.

Pazour, GJ, Agrin, N, Leszyk, J, Witman, GB, 2005. Proteomic analysis of a eukaryotic cilium. J Cell Biol 170, 103-13.

Pazour, GJ, Dickert, BL, Witman, GB, 1999. The DHC1b (DHC2) isoform of cytoplasmic dynein is required for flagellar assembly. J Cell Biol 144, 473-81.

Pearson, RD, Sullivan, JA, Roberts, D, Romito, R, Mandell, GL, 1983. Interaction of *Leishmania donovani* promastigotes with human phagocytes. Infect Immun 40, 411-6.

Peddie, CJ, Collinson, LM, 2014. Exploring the third dimension: volume electron microscopy comes of age. Micron 61, 9-19.

Pedersen, H, 1983. Absence of dynein arms in endometrial cilia: cause of infertility? Acta Obstet Gynecol Scand 62, 625-7.

Pedersen, H, Rebbe, H, 1975. Absence of arms in the axoneme of immobile human spermatozoa. Biol Reprod 12, 541-4.

Penczek, P, Marko, M, Buttle, K, Frank, J, 1995. Double-tilt electron tomography. Ultramicroscopy 60, 393-410.

Peng, D., Kurup, S., Yao, P., Minning, T., Tarleton, R., 2015. CRISPR-Cas9-Mediated Single-Gene and Gene Family Disruption in *Trypanosoma cruzi*. MBio 6, e02097-14.

Peng, D., Tarleton, R., 2015. Eukaryotic Pathogen CRISPR guide RNA/DNA Design Tool. Microbial Genomics.

Perou, CM, Leslie, JD, Green, W, Li, L, Ward, DM, Kaplan, J, 1997. The Beige/Chediak-Higashi syndrome gene encodes a widely expressed cytosolic protein. J Biol Chem 272, 29790-4.

Pham, T.D., Azar, H.A., Moscovic, E.A., Kurban, A.K., 1970. The ultrastructure of *Leishmania tropica* in the oriental sore. Ann Trop Med Parasitol 64, 1-4.

Pickett-Heaps, J, 1974. The evolution of mitosis and the eukaryotic condition. Biosystems 6, 37-48.

Piperno, G, Mead, K, 1997. Transport of a novel complex in the cytoplasmic matrix of *Chlamydomonas* flagella. Proc Natl Acad Sci U S A 94, 4457-62.

Piperno, G, Mead, K, Henderson, S, 1996. Inner dynein arms but not outer dynein arms require the activity of kinesin homologue protein KHP1(FLA10) to reach the distal part of flagella in *Chlamydomonas*. J Cell Biol 133, 371-9.

Porter, KR, Claude, A, Fullam, EF, 1945. A study of tissue culture cells by electron microscopy: methods and preliminary observations. J Exp Med 81, 233-46.

Porter, ME, Bower, R, Knott, JA, Byrd, P, Dentler, W, 1999. Cytoplasmic dynein heavy chain 1b is required for flagellar assembly in *Chlamydomonas*. Mol Biol Cell 10, 693-712.

Porter, K.R., 1956. The submicroscopic morphology of protoplasm.

Praetorius, HA, Spring, KR, 2001. Bending the MDCK cell primary cilium increases intracellular calcium. J Membr Biol 184, 71-9.

Prensier, G, Vivier, E, Goldstein, S, Schrével, J, 1980. Motile flagellum with a “3 + 0” ultrastructure. Science 207, 1493-4.

Price, HP, Hodgkinson, MR, Wright, MH, Tate, EW, Smith, BA, Carrington, M, Stark, M, Smith, DF, 2012. A role for the vesicle-associated tubulin binding protein ARL6 (BBS3) in flagellum extension in *Trypanosoma brucei*. Biochim Biophys Acta 1823, 1178-91.

Price, H., Paape, D., Hodgkinson, M., Farrant, K., Doehl, J., Stark, M., Smith, D., 2013. The *Leishmania major* BBSome subunit BBS1 is essential for parasite virulence in the mammalian host. Molecular Microbiology 90, 597-611.

Prina, E, Antoine, JC, Wiederanders, B, Kirschke, H, 1990. Localization and activity of various lysosomal proteases in *Leishmania amazonensis*-infected macrophages. Infect Immun 58, 1730-7.

Radermacher, M, 1992. Weighted Back-Projection Methods, in: Frank, J (Ed.), Electron Tomography. Springer, Boston, MA.

Ralston, KS, Lerner, AG, Diener, DR, Hill, KL, 2006. Flagellar motility contributes to cytokinesis in *Trypanosoma brucei* and is modulated by an evolutionarily conserved dynein regulatory system. Eukaryot Cell 5, 696-711.

Ready, PD, 2010. Leishmaniasis emergence in Europe. Euro Surveill 15, 19505.

Real, F, Florentino, PT, Reis, LC, Ramos-Sanchez, EM, Veras, PS, Goto, H, Mortara, RA, 2014. Cell-to-cell transfer of *Leishmania amazonensis* amastigotes is mediated by immunomodulatory LAMP-rich parasitophorous extrusions. Cell Microbiol 16, 1549-64.

Real, F, Pouchelet, M, Rabinovitch, M, 2008. *Leishmania* (*L.*) *amazonensis*: fusion between parasitophorous vacuoles in infected bone-marrow derived mouse macrophages. Exp Parasitol 119, 15-23.

Real, F., Mortara, R., 2012. The diverse and dynamic nature of *Leishmania* parasitophorous vacuoles studied by multidimensional imaging. PLoS Neglected Tropical Diseases 6, e1518.

Real, F., Mortara, R., Rabinovitch, M., 2010. Fusion between *Leishmania amazonensis* and *Leishmania major* Parasitophorous Vacuoles: Live Imaging of Coinfected Macrophages. PLoS Negl Trop Dis 4.

Reiter, JF, Leroux, MR, 2017. Genes and molecular pathways underpinning ciliopathies. Nat Rev Mol Cell Biol 18, 533-547.

Rieder, CL, Jensen, CG, Jensen, LC, 1979. The resorption of primary cilia during mitosis in a vertebrate (PtK1) cell line. J Ultrastruct Res 68, 173-85.

Ringo, DL, 1967a. The arrangement of subunits in flagellar fibers. J Ultrastruct Res 17, 266-77.

Ringo, DL, 1967b. Flagellar motion and fine structure of the flagellar apparatus in *Chlamydomonas*. J Cell Biol 33, 543-71.

Rittig, MG, Schröppel, K, Seack, KH, Sander, U, N'Diaye, EN, Maridonneau-Parini, I, Solbach, W, Bogdan, C, 1998. Coiling phagocytosis of trypanosomatids and fungal cells. Infect Immun 66, 4331-9.

Robertis, D.E., 1956. Electron microscope observations on the submicroscopic organization of the retinal rods. J Biophys Biochem Cytol 2, 319-30.

Robinson, DR, Gull, K, 1991. Basal body movements as a mechanism for mitochondrial genome segregation in the trypanosome cell cycle. Nature 352, 731-3.

Robinson, KA, Beverley, SM, 2003. Improvements in transfection efficiency and tests of RNA interference (RNAi) approaches in the protozoan parasite *Leishmania*. Mol Biochem Parasitol 128, 217-28.

Robinson, V.N.E., 1975. The elimination of charging artefacts in the scanning electron microscope. Journal of Physics E: Scientific Instruments 8, 638-640.

Rodriguez-Contreras, D., Aslan, H., Feng, X., Tran, K., Yates, P.A., Kamhawi, S., Landfear, S.M., 2015. Regulation and biological function of a flagellar glucose transporter in *Leishmania mexicana*: a potential glucose sensor. FASEB J. 29, 11-24.

Rogers, ME, Chance, ML, Bates, PA, 2002. The role of promastigote secretory gel in the origin and transmission of the infective stage of *Leishmania mexicana* by the sandfly *Lutzomyia longipalpis*. Parasitology 124, 495-507.

Rogers, M.B., Hilley, J.D., Dickens, N.J., Wilkes, J., Bates, P.A., Depledge, D.P., Harris, D., Her, Y., Herzyk, P., Imamura, H., Otto, T.D., Sanders, M., Seeger, K., Dujardin, J.-C.C., Berriman, M., Smith, D.F., Hertz-Fowler, C., Mottram, J.C., 2011. Chromosome and gene copy number variation allow major structural change between species and strains of *Leishmania*. Genome Res. 21, 2129-42.

Rogers, M.E., Ilg, T., Nikolaev, A.V., Ferguson, M.A., Bates, P.A., 2004. Transmission of cutaneous leishmaniasis by sand flies is enhanced by regurgitation of fPPG. Nature 430, 463-7.

Rosenbaum, JL, Child, FM, 1967. Flagellar regeneration in protozoan flagellates. J Cell Biol 34, 345-64.

Rossman, CM, Forrest, JB, Lee, RM, Newhouse, AF, Newhouse, MT, 1981. The dyskinetic cilia syndrome; abnormal ciliary motility in association with abnormal ciliary ultrastructure. Chest 80, 860-5.

Roth, KE, Rieder, CL, Bowser, SS, 1988. Flexible-substratum technique for viewing cells from the side: some *in vivo* properties of primary (9+0) cilia in cultured kidney epithelia. J Cell Sci 89 (Pt 4), 457-66.

Russell, DG, Xu, S, Chakraborty, P, 1992. Intracellular trafficking and the parasitophorous vacuole of *Leishmania mexicana*-infected macrophages. J Cell Sci 103 (Pt 4), 1193-210.

Sacks, D.L., Modi, G., Rowton, E., Späth, G., Epstein, L., Turco, S.J., Beverley, S.M., 2000. The role of phosphoglycans in *Leishmania*-sand fly interactions. Proc. Natl. Acad. Sci. U.S.A. 97, 406-11.

Sacks, D.L., Pimenta, P.F., McConville, M.J., Schneider, P., Turco, S.J., 1995. Stage-specific binding of *Leishmania donovani* to the sand fly vector midgut is regulated by conformational changes in the abundant surface lipophosphoglycan. J. Exp. Med. 181, 685-97.

Sagan, L, 1967. On the origin of mitosing cells. J Theor Biol 14, 255-74.

Sahin, A, Espiau, B, Marchand, C, Merlin, G, 2008. Flagellar length depends on LdARL-3A GTP/GDP unaltered cycling in *Leishmania amazonensis*. Mol Biochem Parasitol 157, 83-7.

Saigusa, T, Bell, PD, 2015. Molecular pathways and therapies in autosomal-dominant polycystic kidney disease. Physiology (Bethesda) 30, 195-207.

Sale, WS, Satir, P, 1977. The termination of the central microtubules from the cilia of *Tetrahymena pyriformis*. Cell Biol Int Rep 1, 45-9.

Sanchez, MA, Tran, KD, Valli, J, Hobbs, S, Johnson, E, Gluenz, E, Landfear, SM, 2016. KHARON Is an Essential Cytoskeletal Protein Involved in the Trafficking of Flagellar Membrane Proteins and Cell Division in African Trypanosomes. J Biol Chem 291, 19760-73.

Santrich, C, Moore, L, Sherwin, T, Bastin, P, Brokaw, C, Gull, K, LeBowitz, JH, 1997. A motility function for the paraflagellar rod of *Leishmania* parasites revealed by PFR-2 gene knockouts. Mol Biochem Parasitol 90, 95-109.

Satir, P, 1965. STUDIES ON CILIA : II. Examination of the Distal Region of the Ciliary Shaft and the Role of the Filaments in Motility. J Cell Biol 26, 805-34.

Satir, P., Guerra, C., Bell, A., 2007. Evolution and persistence of the cilium. Cell Motility and the Cytoskeleton 64, 906-913.

Schlein, Y., Jacobson, R.L., 1998. Resistance of *Phlebotomus papatasi* to infection with *Leishmania donovani* is modulated by components of the infective bloodmeal. Parasitology 117 (Pt 5), 467-73.

Schlein, Y., Romano, H., 1986. *Leishmania major* and *L. donovani*: effects on proteolytic enzymes of *Phlebotomus papatasi* (Diptera, Psychodidae). Exp. Parasitol. 62, 376-80.

Schneider, C.A., Rasband, W.S., Eliceiri, K.W., 2012. NIH Image to ImageJ: 25 years of image analysis. Nat. Methods 9, 671-5.

Schwartz, EA, Leonard, ML, Bizios, R, Bowser, SS, 1997. Analysis and modeling of the primary cilium bending response to fluid shear. Am J Physiol 272, F132-8.

Scianimanico, S., Desrosiers, M., Dermine, J.F., Méresse, S., Descoteaux, A., Desjardins, M., 1999. Impaired recruitment of the small GTPase rab7 correlates with the inhibition of phagosome maturation by *Leishmania donovani* promastigotes. Cell. Microbiol. 1, 19-32.

Seger, R., Krebs, E.G., 1995. The MAPK signaling cascade. FASEB J. 9, 726-35.

Seiler, H, 1983. Secondary electron emission in the scanning electron microscope. Journal of Applied Physics 54.

Sengupta, S, Tripathi, J, Tandon, R, Raje, M, Roy, RP, Basu, SK, Mukhopadhyay, A, 1999. Hemoglobin endocytosis in *Leishmania* is mediated through a 46-kDa protein located in the flagellar pocket. J Biol Chem 274, 2758-65.

Seo, S, Baye, LM, Schulz, NP, Beck, JS, Zhang, Q, Slusarski, DC, Sheffield, VC, 2010. BBS6, BBS10, and BBS12 form a complex with CCT/TRiC family chaperonins and mediate BBSome assembly. Proc Natl Acad Sci U S A 107, 1488-93.

Severn, A., Wakelam, M.J., Liew, F.Y., 1992. The role of protein kinase C in the induction of nitric oxide synthesis by murine macrophages. Biochem. Biophys. Res. Commun. 188, 997-1002.

Shah, AS, Farmen, SL, Moninger, TO, Businga, TR, Andrews, MP, Bugge, K, Searby, CC, Nishimura, D, Brogden, KA, Kline, JN, Sheffield, VC, Welsh, MJ, 2008. Loss of Bardet-Biedl syndrome proteins alters the morphology and function of motile cilia in airway epithelia. Proc Natl Acad Sci U S A 105, 3380-5.

Shaner, NC, Lambert, GG, Chammas, A, Ni, Y, Cranfill, PJ, Baird, MA, Sell, BR, Allen, JR, Day, RN, Israelsson, M, Davidson, MW, Wang, J, 2013. A bright monomeric green fluorescent protein derived from *Branchiostoma lanceolatum*. Nat Methods 10, 407-9.

Sheffield, VC, Carmi, R, Kwitek-Black, A, Rokhlina, T, Nishimura, D, Duyk, GM, Elbedour, K, Sunden, SL, Stone, EM, 1994. Identification of a Bardet-Biedl syndrome locus on chromosome 3 and evaluation of an efficient approach to homozygosity mapping. Hum Mol Genet 3, 1331-5.

Shim, MS, Kwon, YJ, 2010. Efficient and targeted delivery of siRNA *in vivo*. FEBS J 277, 4814-27.

Silverman, JM, Chan, SK, Robinson, DP, Dwyer, DM, Nandan, D, Foster, LJ, Reiner, NE, 2008. Proteomic analysis of the secretome of *Leishmania donovani*. Genome Biol 9, R35.

Silverman, JM, Clos, J, de' Oliveira, CC, Shirvani, O, Fang, Y, Wang, C, Foster, LJ, Reiner, NE, 2010. An exosome-based secretion pathway is responsible for protein export from *Leishmania* and communication with macrophages. J Cell Sci 123, 842-52.

Simons, M, Gloy, J, Ganner, A, Bullerkotte, A, Bashkurov, M, Krönig, C, Schermer, B, Benzing, T, Cabello, OA, Jenny, A, Mlodzik, M, Polok, B, Driever, W, Obara, T, Walz, G, 2005. Inversin, the gene product mutated in nephronophthisis type II, functions as a molecular switch between Wnt signaling pathways. Nat Genet 37, 537-43.

Singh, N, Kumar, M, Singh, RK, 2012. Leishmaniasis: current status of available drugs and new potential drug targets. Asian Pac J Trop Med 5, 485-97.

Smith, EF, Lefebvre, PA, 1997. The role of central apparatus components in flagellar motility and microtubule assembly. Cell Motil Cytoskeleton 38, 1-8.

Sollelis, L, Ghorbal, M, MacPherson, CR, Martins, RM, Kuk, N, Crobu, L, Bastien, P, Scherf, A, Lopez-Rubio, JJ, Sterkers, Y, 2015. First efficient CRISPR-Cas9-mediated genome editing in *Leishmania* parasites. Cell Microbiol 17, 1405-12.

Sorokin, S, 1962. Centrioles and the formation of rudimentary cilia by fibroblasts and smooth muscle cells. J Cell Biol 15, 363-77.

Sorokin, SP, 1968. Reconstructions of centriole formation and ciliogenesis in mammalian lungs. J Cell Sci 3, 207-30.

Stephen, LA, Elmaghloob, Y, Ismail, S, 2017. Maintaining protein composition in cilia. Biol Chem.

Sterkers, Y, Lachaud, L, Crobu, L, Bastien, P, Pagès, M, 2011. FISH analysis reveals aneuploidy and continual generation of chromosomal mosaicism in *Leishmania major*. Cell Microbiol 13, 274-83.

Stuart, K, 1983. Kinetoplast DNA, mitochondrial DNA with a difference. Mol Biochem Parasitol 9, 93-104.

Sui, H, Downing, KH, 2006. Molecular architecture of axonemal microtubule doublets revealed by cryo-electron tomography. Nature 442, 475-8.

Summers, KE, Gibbons, IR, 1971. Adenosine triphosphate-induced sliding of tubules in trypsin-treated flagella of sea-urchin sperm. Proc Natl Acad Sci U S A 68, 3092-6.

Sunter, JD, Benz, C, Andre, J, Whipple, S, McKean, PG, Gull, K, Ginger, ML, Lukeš, J, 2015. Modulation of flagellum attachment zone protein FLAM3 and regulation of the cell shape in *Trypanosoma brucei* life cycle transitions. J Cell Sci 128, 3117-30.

Swanson, J, 1988. Fluorescent Labeling of Endocytic Compartments. Methods in Cell Biology 29, 137-151.

Szempruch, AJ, Sykes, SE, Kieft, R, Dennison, L, Becker, AC, Gartrell, A, Martin, WJ, Nakayasu, ES, Almeida, IC, Hajduk, SL, Harrington, JM, 2016. Extracellular Vesicles from *Trypanosoma brucei* Mediate Virulence Factor Transfer and Cause Host Anemia. Cell 164, 246-257.

Tapia, J.C., Kasthuri, N., Hayworth, K.J., Schalek, R., Lichtman, J.W., Smith, S.J., Buchanan, J., 2012. High-contrast en bloc staining of neuronal tissue for field emission scanning electron microscopy. Nat Protoc 7, 193-206.

Toledo, SP, Medeiros-Neto, GA, Knobel, M, Mattar, E, 1977. Evaluation of the hypothalamic-pituitary-gonadal function in the Bardet-Biedl syndrome. Metabolism 26, 1277-91.

Tran, KD, Vieira, DP, Sanchez, MA, Valli, J, Gluenz, E, Landfear, SM, 2015. Kharon1 null mutants of *Leishmania mexicana* are avirulent in mice and exhibit a cytokinesis defect within macrophages. PLoS One 10, e0134432.

Tran, K., Rodriguez-Contreras, D., Shinde, U., Landfear, S., 2012. Both sequence and context are important for flagellar targeting of a glucose transporter. J. Cell. Sci. 125, 3293-8.

Tran, K., Rodriguez-Contreras, D., Vieira, D., Yates, P., David, L., Beatty, W., Elferich, J., Landfear, S., 2013. KHARON1 mediates flagellar targeting of a glucose transporter in *Leishmania mexicana* and is critical for viability of infectious intracellular amastigotes. Journal of Biological Chemistry.

Tull, D, Vince, JE, Callaghan, JM, Naderer, T, Spurck, T, McFadden, GI, Currie, G, Ferguson, K, Bacic, A, McConville, MJ, 2004. SMP-1, a member of a new family of small myristoylated proteins in kinetoplastid parasites, is targeted to the flagellum membrane in *Leishmania*. Mol Biol Cell 15, 4775-86.

Tull, D., Heng, J., Gooley, P., Naderer, T., McConville, M., 2012. Acylation-dependent and-independent membrane targeting and distinct functions of small myristoylated proteins (SMPs) in *Leishmania major*. International journal for parasitology 42, 239-47.

Tyler, KM, Fridberg, A, Toriello, KM, Olson, CL, Cieslak, JA, Hazlett, TL, Engman, DM, 2009. Flagellar membrane localization via association with lipid rafts. J Cell Sci 122, 859-66.

Ueno, N, Wilson, ME, 2012. Receptor-mediated phagocytosis of *Leishmania*: implications for intracellular survival. Trends Parasitol 28, 335-44.

Van Zandbergen, G., Klinger, M., Mueller, A., Dannenberg, S., Gebert, A., Solbach, W., Laskay, T., 2004. Cutting edge: neutrophil granulocyte serves as a vector for *Leishmania* entry into macrophages. J. Immunol. 173, 6521-5.

Vaughan, S, Shaw, M, Gull, K, 2006. A post-assembly structural modification to the lumen of flagellar microtubule doublets. Curr Biol 16, R449-50.

Vickerman, K, 1962. The mechanism of cyclical development in trypanosomes of the *Trypanosoma brucei* sub-group: an hypothesis based on ultrastructural observations. Trans R Soc Trop Med Hyg 56, 487-95.

Vickerman, K, 1969. On the surface coat and flagellar adhesion in trypanosomes. J Cell Sci 5, 163-93.

Vihinen, H, Belevich, I, Jokitalo, E, 2013. Three dimensional electron microscopy of cellular organelles by serial block face SEM and ET. Microscopy and Analysis 27, 7-10.

Wall, MA, Coleman, DE, Lee, E, Iñiguez-Lluhi, JA, Posner, BA, Gilman, AG, Sprang, SR, 1995. The structure of the G protein heterotrimer Gi alpha 1 beta 1 gamma 2. Cell 83, 1047-58.

Waller, RF, McConville, MJ, 2002. Developmental changes in lysosome morphology and function *Leishmania* parasites. Int J Parasitol 32, 1435-45.

Wanner, A, Salathé, M, O'Riordan, TG, 1996. Mucociliary clearance in the airways. Am J Respir Crit Care Med 154, 1868-902.

Warburg, A, Tesh, RB, McMahon-Pratt, D, 1989. Studies on the attachment of *Leishmania* flagella to sand fly midgut epithelium. J Protozool 36, 613-7.

Warner, FD, Satir, P, 1973. The substructure of ciliary microtubules. J Cell Sci 12, 313-26.

Warner, FD, Satir, P, 1974. The structural basis of ciliary bend formation. Radial spoke positional changes accompanying microtubule sliding. J Cell Biol 63, 35-63.

Wei, D, Jacobs, S, Modla, S, Zhang, S, Young, CL, Cirino, R, Caplan, J, Czymmek, K, 2012. High-resolution three-dimensional reconstruction of a whole yeast cell using focused-ion beam scanning electron microscopy. Biotechniques 53, 41-8.

Wei, Q, Zhang, Y, Li, Y, Zhang, Q, Ling, K, Hu, J, 2012. The BBSome controls IFT assembly and turnaround in cilia. Nat Cell Biol 14, 950-7.

Weston, AE, Armer, HE, Collinson, LM, 2009. Towards native-state imaging in biological context in the electron microscope. J Chem Biol 3, 101-12.

Wheeler, R., 2012. Generation, regulation and function of morphology in *Leishmania* and *Trypanosoma*. University of Oxford.

Wheeler, R., Gluenz, E., Gull, K., 2011. The cell cycle of *Leishmania*: morphogenetic events and their implications for parasite biology Mol. Microbiol. 79, 647-662.

Wheeler, R., Gull, K., Gluenz, E., 2015. 9+2 to 9+0 axoneme conversion in *Leishmania*. Cilia 4, O5.

Wheeler, R., n.d. Circle Finder [WWW Document].

White, JG, Southgate, E, Thomson, JN, Brenner, S, 1986. The structure of the nervous system of the nematode *Caenorhabditis elegans*. Philos Trans R Soc Lond B Biol Sci 314, 1-340.

Wickstead, B, Gull, K, 2007. Dyneins across eukaryotes: a comparative genomic analysis. Traffic 8, 1708-21.

Wiens, CJ, Tong, Y, Esmail, MA, Oh, E, Gerdes, JM, Wang, J, Tempel, W, Rattner, JB, Katsanis, N, Park, HW, Leroux, MR, 2010. Bardet-Biedl syndrome-associated small GTPase ARL6 (BBS3) functions at or near the ciliary gate and modulates Wnt signaling. J Biol Chem 285, 16218-30.

Williams, CL, Li, C, Kida, K, Inglis, PN, Mohan, S, Semenec, L, Bialas, NJ, Stupay, RM, Chen, N, Blacque, OE, Yoder, BK, Leroux, MR, 2011. MKS and NPHP modules cooperate to establish basal body/transition zone membrane associations and ciliary gate function during ciliogenesis. J Cell Biol 192, 1023-41.

Wilsman, NJ, Farnum, CE, 1983. Arrangement of C-tubule protofilaments in mammalian basal bodies. J Ultrastruct Res 84, 205-12.

Wilson, J., Huynh, C., Kennedy, K., Ward, D., Kaplan, J., Aderem, A., Andrews, N., 2008. Control of parasitophorous vacuole expansion by LYST/Beige restricts the intracellular growth of *Leishmania amazonensis*. PLoS Pathogens 4, e1000179.

Wirschell, M, Olbrich, H, Werner, C, Tritschler, D, Bower, R, Sale, WS, Loges, NT, Pennekamp, P, Lindberg, S, Stenram, U, Carlén, B, Horak, E, Köhler, G, Nürnberg, P, Nürnberg, G, Porter, ME, Omran, H, 2013. The nexin-dynein regulatory complex subunit DRC1 is essential for motile cilia function in algae and humans. Nat Genet 45, 262-8.

Witman, GB, 1975. The site of *in vivo* assembly of flagellar microtubules. Ann N Y Acad Sci 253, 178-91.

Wolfe, J, 1970. Structural analysis of basal bodies of the isolated oral apparatus of *Tetrahymena pyriformis*. J Cell Sci 6, 679-700.

Wood, CR, Huang, K, Diener, DR, Rosenbaum, JL, 2013. The cilium secretes bioactive ectosomes. Curr Biol 23, 906-11.

Woods, K, a' Bhaird, N.N., Dooley, C, Perez-Morga, D, Nolan, DP, 2013. Identification and characterization of a stage specific membrane protein involved in flagellar attachment in *Trypanosoma brucei*. PLoS One 8, e52846.

Woods, MO, Young, TL, Parfrey, PS, Hefferton, D, Green, JS, Davidson, WS, 1999. Genetic heterogeneity of Bardet-Biedl syndrome in a distinct Canadian population: evidence for a fifth locus. Genomics 55, 2-9.

World Health Organisation, 2016. Status of endemicity of visceral leishmaniasis.

World Health Organization, 2016. Status of endemicity of cutaneous leishmaniasis [WWW Document].

World Health Organization, 2017. Leishmaniasis Fact Sheet [WWW Document].

Yagi, T, Kamiya, R, 2000. Vigorous beating of *Chlamydomonas* axonemes lacking central pair/radial spoke structures in the presence of salts and organic compounds. Cell Motil Cytoskeleton 46, 190-9.

Yamaguchi, T., Wallace, D., Magenheimer, B., Hempson, S., Grantham, J., Calvet, J., 2004. Calcium restriction allows cAMP activation of the B-Raf/ERK pathway, switching cells to a cAMP-dependent growth-stimulated phenotype. The Journal of biological chemistry 279, 40419-30.

Yamamoto, S., 2012. The role of the BBSome in *Trypanosoma brucei*. University of Oxford.

Yokota, T, Ohno, N, Tamura, K, Seita, M, Toshimori, K, 1993. Ultrastructure and function of cilia and spermatozoa flagella in a patient with Kartagener's syndrome. Intern Med 32, 593-7.

Young, TL, Penney, L, Woods, MO, Parfrey, PS, Green, JS, Hefferton, D, Davidson, WS, 1999. A fifth locus for Bardet-Biedl syndrome maps to chromosome 2q31. Am J Hum Genet 64, 900-4.

Zhang, F, Wen, Y, Guo, X, 2014. CRISPR/Cas9 for genome editing: progress, implications and challenges. Hum Mol Genet 23, R40-6.

Zhang, Q, Nishimura, D, Seo, S, Vogel, T, Morgan, DA, Searby, C, Bugge, K, Stone, EM, Rahmouni, K, Sheffield, VC, 2011. Bardet-Biedl syndrome 3 (Bbs3) knockout mouse model reveals common BBS-associated phenotypes and Bbs3 unique phenotypes. Proc Natl Acad Sci U S A 108, 20678-83.

Zhang, Q, Yu, D, Seo, S, Stone, EM, Sheffield, VC, 2012. Intrinsic protein-protein interaction-mediated and chaperonin-assisted sequential assembly of stable bardet-biedl syndrome protein complex, the BBSome. J Biol Chem 287, 20625-35.

Zhang, WW, Matlashewski, G, 2015. CRISPR-Cas9-Mediated Genome Editing in *Leishmania donovani*. MBio 6, e00861.

Zilberstein, D, Shapira, M, 1994. The role of pH and temperature in the development of *Leishmania* parasites. Annu Rev Microbiol 48, 449-70.

8 Appendix

8.1 List of Supplementary Materials

Supplementary Video S3.1. 3View image stack.avi
Video showing a 3View image stack of *Leishmania*-infected macrophages fixed 72 hours post-infection. Magnification: x5,000. Lateral resolution: 5.6 nm. Slice number: 398. Slice thickness: 50 nm. Total volume: 40.49 μm x 42.00 μm x 19.90 μm. Video shows stack binned by 2 in xy and in z dimensions. Scale bar = 5 μm.

Supplementary Video S3.2. Tomogram of flagellar membrane streamer 1.avi
Three joined serial dual axis tomograms showing the interface between the *Leishmania mexicana* amastigote flagellum and the macrophage parasitophorous vacuole membrane at 24 hours post infection. The flagellum possesses a narrow, tubular extension of the flagellar membrane, closely followed in contour by the parasitophorous vacuole membrane. Reconstruction can be found in **Figure 3.8 C**. Magnification: x13,000. Resolution: 0.85 nm. Total tomogram volume: 4.11 μm x 3.86 μm x 0.28 μm. Video shows cropped region of tomogram binned by 4 in z. Scale bar = 200 nm.

Supplementary Video S3.3. Tomogram of flagellar membrane streamer 2.avi
Five joined serial dual axis tomograms showing the interface between the *Leishmania mexicana* amastigote flagellum and the macrophage parasitophorous vacuole membrane at 24 hours post infection. The flagellum possesses a narrow, tubular extension of the flagellar membrane, closely followed in contour by the parasitophorous vacuole membrane. Reconstruction can be found in **Figure 3.8 D**. Magnification: x13,000. Resolution: 0.85 nm. Total tomogram volume: 3.74 μm x 3.99 μm x 0.35 μm. Video shows cropped region of tomogram binned by 4 in z. Scale bar = 200 nm.

Supplementary Video S3.4. Tomogram of vesicular activity.avi
Six joined serial dual axis tomograms showing the interface between the *Leishmania mexicana* amastigote flagellum and the macrophage parasitophorous vacuole membrane at 72 hours post infection. Vesicular structures can be seen on both the flagellar and parasitophorous vacuole membranes, which appear to bridge the gap between these two structures. Vesicular activity on the parasitophorous vacuole appears to be particularly focused in the region nearest the flagellum. Reconstruction can be found in **Figure 3.10 B & C**. Magnification: x13,000. Resolution: 0.85 nm. Total tomogram volume: 4.42 μm x 3.71 μm x 0.60 μm. Video shows cropped region of tomogram binned by 2 in xy and by 4 in z. Scale bar = 200 nm.